Impacts of convective treatment on tropical rainfall variability in realistic and idealized simulations

Zur Erlangung des akademischen Grades eines

DOKTORS DER NATURWISSENSCHAFTEN
(Dr. rer. nat.)
von der KIT-Fakultät für Physik des

Karlsruher Instituts für Technologie (KIT)

genehmigte

DISSERTATION

von

M. Sc. Hyunju Jung

aus Seoul

Tag der mündlichen Prüfung: 26.05.2023

Referent: Prof. Dr. Peter Knippertz

Korreferentin: Prof. Dr. Corinna Hoose

KIT

Karlsruher Institut für Technologie

Abstract

The prediction of precipitation in the tropics is a challenge for numerical weather prediction (NWP), meaning very low practical predictability there. However, previous studies indicated that intrinsic predictability in the tropics is up to a few weeks and thus longer than in the extratropics. Equatorial waves (EWs) from the linear shallow-water theory are considered the source of this long predictability. Most weather and climate models still struggle to accurately capture EWs, which is often attributed to parameterized convection. With advanced computing power, model development is moving toward high-resolution models with explicit convection. To evaluate the value of these high-resolution models, this thesis aims to provide important insights into the behavior of tropical precipitation due to the treatment of deep and shallow convection using the ICOsahedral Nonhydrostatic (ICON) model.

First, we examine the sensitivity of EWs to model configuration using realistic ICON simulations with varying horizontal grid spacings (80–2.5 km) and with different convective treatments between parameterized versus explicit deep and shallow convection. To robustly identify wave signals, we use two objective methods, one filtering rainfall using a fast Fourier transform and the other projecting two-dimensional wind and geopotential onto theoretical wave patterns. The results demonstrate that large-scale EWs are surprisingly consistent in terms of phase speed and wave amplitude with little sensitivity to model resolution, convective treatment and wave identification method. Rainfall signals of westward inertio-gravity waves (WIGs), however, show a large difference between parameterized and explicit convection with the latter showing marked rainfall signals but with no corresponding wind patterns. A composite analysis to link rainfall and wind fields of waves reveals that the identified signals in rainfall appear to be associated with mesoscale convective systems, the spatiotemporal scales of which overlap with those of WIGs, and thus are isolated as waves through space-time filtering.

Secondly, we analyze idealized ICON simulations in a tropical aquachannel configuration with zonally symmetric sea surface temperatures and with rigid walls at 30°N/S. The aquachannel simulations vary in the representation of deep and shallow convection but with the same horizontal grid spacing of 13 km. All aquachannel simulations have maximum rainfall at the equator, showing an intertropical convergence zone (ITCZ) there, but the rainfall amount increases by 35 % with explicit deep convection. To physically understand this difference, we adapt a diagnostic based on a conceptual model by Emanuel (2019), assuming boundary-layer quasi-equilibrium (BLQE), the weak temperature gradient approximation, and mass and energy

conservation. BLQE implies that moist entropy is in balance between surface enthalpy fluxes, which import high moist entropy to the BL, and convective downdrafts, which transport low moist entropy from the free troposphere into the BL. The results reveal that the rainfall differences are primarily associated with surface enthalpy fluxes through BLQE, while precipitation efficiency is surprisingly constant in the ITCZ. Further detailed analysis demonstrates that mean surface wind speed, which is closely related to the large-scale circulation, contributes most to the differences in surface enthalpy fluxes. Thus, the treatment of deep convection alters mean rainfall through tight links between surface winds, associated surface fluxes and convective mass flux.

Lastly, variability associated with EWs is examined in the aquachannel simulations by using the same wave identification methods used for the realistic simulations. All simulations show prominent signals of Kelvin waves (KWs) with large variations among them. Parameterized deep convection produces various eastward propagation with speeds of 5–27 $\mathrm{m\,s^{-1}}$, while explicit deep convection exhibits a dominance of KWs with a zonal wavenumber of one and with a propagation speed of 24 $\mathrm{m\,s^{-1}}$. Furthermore, explicit deep convection causes more pronounced structures of zonal wind and temperature in the lower stratosphere and a stronger link of wind-induced surface enthalpy flux exchange to the development of convection. Meanwhile, the treatment of shallow convection plays a role for temperature variation below 2.5 km. However, BL warming is in phase with maximum rainfall associated with KWs, which is opposite to observations. Parameterized deep convection generates a feature sharing similarities with the Madden Julian Oscillation, which is not found in the other aquachannel simulations.

The novelty of this thesis lies in understanding the behavior of tropical rainfall in both realistic and idealized simulations by using diagnostics adapted for systematic comparisons between different simulations, mainly due to different convective treatments. This allows us to obtain valuable insights into the sensitivity of tropical rainfall and its variability to model configuration, ultimately paving the way for developing more accurate weather and climate predictions in the tropics.

Kurzfassung

Die Vorhersage von Niederschlägen in den Tropen stellt eine Herausforderung für die numerische Wettervorhersage (NWP) mit sehr geringer praktischer Vorhersagbarkeit dar. Frühere Studien haben jedoch darauf hingewiesen, dass die intrinsische Vorhersagbarkeit in den Tropen bis zu einigen Wochen reicht und damit länger ist als in den Extratropen. *Equatorial waves* (EWs) aus der linearen Flachwasserdynamik gelten als Quelle dieser langen Vorhersagbarkeit. Die meisten Wetter- und Klimamodelle haben immer noch Schwierigkeiten, EWs genau zu erfassen, was oft auf parametrisierte Konvektion zurückzuführen ist. Mit fortschreitender Rechenleistung bewegt sich die Modellentwicklung hin zu hochauflösenden Modellen mit expliziter Konvektion. Um den Nutzen dieser hochauflösenden Modelle zu bewerten, zielt diese Arbeit darauf ab, wichtige Einblicke in das Verhalten von tropischen Niederschlägen aufgrund der Behandlung von hochreichender und flacher Konvektion mithilfe des ICOsahedral Nonhydrostatic (ICON)-Modells zu geben.

Zunächst untersuchen wir die Sensitivität der EWs gegenüber der Modellkonfiguration unter Verwendung realistischer ICON-Simulationen mit unterschiedlichen horizontalen Gitterauflösungen (80–2.5 km) und mit unterschiedlichen konvektiven Behandlungen zwischen parametrisierter und expliziter hochreichende und flache Konvektion. Zur robusten Identifizierung von Wellensignalen verwenden wir zwei objektive Methoden, von denen eine den Niederschlag mit Hilfe einer Fast Fourier Transformation filtert und die andere zweidimensionale Wind- und Geopotenzialdaten auf theoretische Wellenmuster projiziert. Die Ergebnisse zeigen, dass großräumige EWs in Bezug auf Phasengeschwindigkeit und Wellenamplitude erstaunlich konsistent sind und kaum von der Modellauflösung, der konvektiven Behandlung und der Wellenidentifikationsmethode abhängen. Die Niederschlagssignale von *westward inertio-gravity waves* (WIGs) zeigen jedoch einen großen Unterschied zwischen parametrisierter und expliziter Konvektion, wobei explizite Konvektion deutliche Niederschlagssignale, jedoch keine entsprechenden Windmuster enthält. Eine zusammengesetzte Analyse zur Verknüpfung von Niederschlags- und Windfeldern von Wellen zeigt, dass die identifizierten Signale im Niederschlag mit mesoskaligen konvektiven Systemen verbunden zu sein scheinen, deren raum-zeitliche Skalen sich mit denen von WIGs überschneiden und daher durch Raum-Zeit-Filterung als Wellen isoliert werden.

Zweitens analysieren wir idealisierte ICON-Simulationen in einer tropischen Aquachannel-Konfiguration mit zonal symmetrischen Meeresoberflächentemperaturen zwischen 30°N/S. Die Simulationen variieren in der Darstellung der hochreichende und flache Konvektion, jedoch mit

dem gleichen horizontalen Gitterauflösungen von 13 km. Bei allen Aquachannelsimulationen liegt das Niederschlagsmaximum am Äquator, was auf eine intertropische Konvergenzzone (ITCZ) dort hindeutet, aber die Niederschlagsmenge nimmt bei expliziter hochreichende Konvektion um 35 % zu. Um diesen Unterschied physikalisch zu verstehen, passen wir eine Diagnostik an, die auf einem konzeptionellen Modell von Emanuel (2019) basiert und von einem *boundary-layer quasi-equilibrium* (BLQE), einer *weak temperature gradient approximation* und der Erhaltung von Masse und Energie ausgeht. BLQE impliziert, dass die feuchte Entropie im Gleichgewicht zwischen den Oberflächen-Enthalpieflüssen, die hohe feuchte Entropie in die BL einbringen, und konvektiven Abwinden, die niedrige feuchte Entropie aus der freien Troposphäre in die BL transportieren. Die Ergebnisse zeigen, dass die Niederschlagsunterschiede in erster Linie mit den Oberflächenenthalpieflüssen durch die BLQE zusammenhängen, während die Niederschlagseffizienz in der ITCZ erstaunlich konstant ist. Eine weitere detaillierte Analyse zeigt, dass die mittlere Oberflächenwindgeschwindigkeit, die eng mit der großräumigen Zirkulation zusammenhängt, am meisten zu den Unterschieden in den Oberflächenenthalpieflüssen beiträgt. Somit verändert die Behandlung der hochreichende Konvektion die mittlere Niederschlagsmenge durch enge Verbindungen zwischen den Oberflächenwinden, den damit verbundenen Oberflächenflüssen und dem konvektiven Massenfluss.

Schließlich wird die mit den EWs verbundene Variabilität in den Aquachannelsimulationen untersucht, indem dieselben Methoden zur Wellenidentifizierung wie bei den realistischen Simulationen verwendet werden. Alle Simulationen zeigen auffällige Signale von Kelvinwellen (KWs) mit großen Variationen zwischen ihnen. Parametrisierte hochreichende Konvektion erzeugt verschiedene Ausbreitungen nach Osten mit Geschwindigkeiten von 5–27 m s^{-1}, während explizite hochreichende Konvektion eine Dominanz von KWs mit einer zonalen Wellenzahl von eins und mit einer Ausbreitungsgeschwindigkeit von 24 m s^{-1} aufweist. Darüber hinaus führt explizite hochreichende Konvektion zu ausgeprägteren Strukturen des zonalen Windes und der Temperatur in der unteren Stratosphäre und zu einer stärkeren Verknüpfung des windinduzierten Austauschs des Oberflächenenthalpieflusses mit der Entwicklung der Konvektion. Unterdessen spielt die Behandlung der flache Konvektion eine Rolle für die Temperaturschwankungen unterhalb von 2.5 Metern. Allerdings ist die BL-Erwärmung mit einem Niederschlagsmaximum in Verbindung mit KWs verbunden, was im Gegensatz zu den Beobachtungen steht. Die parametrisierte hochreichende Konvektion erzeugt ein Merkmal, das Ähnlichkeiten mit der Madden-Julianischen Oszillation aufweist, die in den anderen Aquachannelsimulationen nicht zu finden ist.

Die Neuheit dieser Arbeit besteht darin, das Verhalten des tropischen Niederschlags sowohl in realistischen als auch in idealisierten Simulationen zu verstehen, indem Diagnostiken verwendet werden, die für systematische Vergleiche zwischen verschiedenen Simulationen geeignet sind, vor allem aufgrund unterschiedlicher konvektiver Behandlungen. Dadurch erhalten wir wertvolle Einblicke in die Empfindlichkeit des tropischen Niederschlags und seiner Variabilität gegenüber der Modellkonfiguration, was letztlich den Weg für die Entwicklung genauerer Wetter- und Klimavorhersagen in den Tropen ebnet.

Preface

The PhD candidate confirms that the research presented in this thesis contains significant scientific contributions by herself. This thesis reuses material from the following publications:

Jung, H., and P. Knippertz, 2023: Link between the time-space behavior of rainfall and 3D dynamical structures of equatorial waves in global convection-permitting simulations. *Geophys. Res. Lett.*, 50 (2), e2022GL100 973, doi: 10.1029/2022GL100973.

Jung, H., P. Knippertz, Y. Ruckstuhl, R. Redl, T. Janjic, and C. Hoose, 2023: Understanding the dependence of mean precipitation on convective treatment in tropical aquachannel experiments (under review). *Weather Clim. Dynam. Discuss.*, 4 (1), 249–264, doi: 10.5194/wcd-4-249-2023.

The candidate confirms that appropriate credit has been given within the thesis where reference has been made to the work of others. This copy has been supplied on the understanding that this is copyright material and that no quotation from the thesis may be published without proper acknowledgment.

Acronyms

AEJ	African easterly jet
AEW	African easterly wave
BL	Boundary layer
BLQE	Boundary-layer quasi-equilibrium
CAPE	Convective available potential energy
CIN	Convective inhibition
CISK	Conditional Instability of the Second Kind
CTL	Cloud top level
DKRZ	Deutsches Klimarechenzentrum (German Climate Computing Centre)
DWD	Deutscher Wetterdienst (German weather service)
DYAMOND	DYnamics of the Atmospheric general circulation Modeled On Non-hydrostatic Domains
ECMWF	European Centre for Medium-Range Weather Forecasts
EIG	Eastward inertio-gravity wave
EL	Equilibrium level
ER	Equatorial Rossby wave
EW	Equatorial wave
ICON model	ICOsahedral Nonhydrostatic model
IG	Inertio-gravity wave
IMERG	Integrated Multi-Satellite Retrievals for Global Precipitation Measurement
KIT	Karlsruhe Institute of Technology
KW	Kelvin wave
LCL	Lifting condensation level
LFC	Level of free convection
LFS	Level of free sink
MCS	Mesoscale convective system

MJO	Madden Julian Oscillation
MPAS	Model for Prediction Across Scales
MPI-M	Max Plank Institute for Meteorology
MRG	Mixed-Rossby gravity wave
NWP	Numerical weather forecast
OLR	Outgoing longwave radiation
PW	Precipitable water
RRTM	Rapid Radiative Transfer Model
SST	Sea surface temperature
TOGA COARE	Tropical Ocean and Global Atmosphere Coupled Ocean–Atmosphere Response Experiment
TRMM	Tropical Rainfall Measuring Mission
WIG	Westward inertio-gravity wave
WISHE	Wind-induced surface heat exchange
WK method	Wheeler and Kiladis (1999)'s method
YP method	Yang et al. (2003)'s method

Symbols

D Detrainment

E Entrainment

F_h Surface enthalpy fluxes

L_f Latent heat for freezing

L_v Latent heat for vaporization

M_d Convective downdraft mass flux

M_u Convective updraft mass flux

S Dry stability

$\dot{Q}$ Radiative cooling

ϵ_p Precipitation efficiency

Pr   Precipitation rate

$\overline{U}_h$ Surface horizontal wind speed

ϕ Geopotential

ρ Air density

V_h Horizontal wind velocity

c_E Surface exchange coefficient for latent heat

c_H Surface exchange coefficient for sensible heat

c_p Specific heat at constant pressure

d Boundary layer height

g Gravitational acceleration

h_b Moist static energy in the boundary layer

h_m Moist static energy in the lower troposphere

h_e Equivalent depth

h Moist static energy

k Zonal wavenumber

n Meridional wavenumber

q_* Saturated specific humidity

q_i Specific ice content

q_v Specific humidity

u Zonal wind

v Meridional wind

w_e Environmental vertical velocity

w Large-scale vertical velocity

y_0 Trapping scale

T Temperature

Contents

1   Introduction

The climate of the tropics is unique because it is characterized by a warm, moist environment with little seasonal variability compared to midlatitudes and abundant rainfall exceeding surface evaporation (Webster, 2020a). This area hosts approximately 80 % of the world's terrestrial biodiversity as well as most of its marine diversity (Barlow et al., 2018), and is critical for global food production such as maize, rice and other staple crops (FAO, 2022). However, practical predictability of rainfall at these latitudes remains low and accurate weather forecasts are notoriously challenging (Haiden et al., 2012; Privé and Errico, 2013; Vogel et al., 2020), making it essential to improve forecast skills in the tropics for socio-economic development, health and food security.

A number of factors can contribute to these difficulties. First, numerical weather forecast (NWP) models have been developed with a strong focus on midlatitude weather systems, and atmospheric dynamics in the tropics differs from higher latitudes due to the small values of the Coriolis parameter in the former. This means that the geostrophic balance between the pressure gradient force and the Coriolis force, which dominates weather systems in the midlatitues (Holton, 2004), does not apply to describe dynamics in the tropics. Secondly, the observational network in the tropics is sparse, since more than 70 % of the tropics is covered by ocean as well as very few radiosonde stations cover the tropical land masses (Parker et al., 2008; Ferreira et al., 2019) due to limited infrastructure and political will. This provides lack of adequate data of temperature and humidity, including winds which is indirectly measured. Moisture measurements from microwave frequency or infrared channel are also insufficient, particularly at low levels (Medeiros et al., 2010; Stevens et al., 2018). Lastly, data assimilation, a technique used in NWP to obtain the best estimate of the atmospheric state by incorporating observation data, is often tailored to the dominance of geostrophic balance in the extratropics (Privé and Errico, 2013). In other words, current data assimilation algorithms are suboptimal for the tropics (Žagar et al., 2004; Zagar et al., 2005; Gleiter et al., 2022), providing poor estimate of initial conditions. As a result, large initial uncertainty can rapidly deprecate weather forecasts through the butterfly effect (Lorenz, 1963).

Despite these difficulties, intrinsic predictability in the tropics has been found to be greater than that in the extratropics. Figure 1.1 demonstrates that given the same initial condition uncertainty, predictability is longer in the tropics by 2–4 days than in the midlatitudes, suggesting that the low practical predictability must result not only from initial condition problems but also from
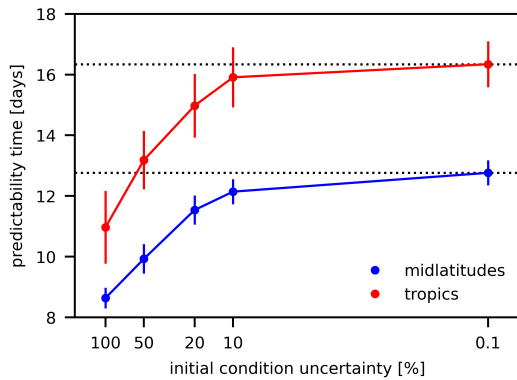
Figure 1.1: Predictability times as a function of initial condition uncertainty, estimated from "perfect model" experiments (Selz et al., 2022). The predictability times are defined as the time when the 300 hPa difference kinetic energy reaches half the climatological variance. The dotted lines indicate the estimated intrinsic limits for the midlatitudes and tropics, respectively. Source from Bardachova (2022) ©The Author(s). Used with permission.

model errors (Selz and Craig, 2015). Judt (2020) found that error, defined by difference kinetic energy between his identical twin experiments, grows more slowly at low latitudes than at higher latitudes. In the latter, error reaches its limit at around day 17, but the former exhibits a time scale beyond the simulation period of 20 days. Note that the simulation period is limited because it was the first attempt to assess predictability using a global high-resolution model. Furthermore, Ying and Zhang (2017) showed that forecast skill in the tropics can be achievable beyond two weeks with improvements in model error and initial and boundary conditions. Both studies suggested that the source of predictability in the tropics lies in equatorial waves (EWs), which are east- and westward disturbances trapped near the equator and modulate a substantial fraction of rainfall variability in the tropics (Kiladis et al., 2009). Additionally, longer predictability in the tropics not only means better forecast of tropical weather, but also has the potential to improve weather forecasts in the midlatitudes (Vitart, 2013; Pante and Knippertz, 2019).

EWs appear to be a crucial source of predictability in the tropics. However, it is widely recognized that current NWP models face significant challenges in accurately capturing the variability associated with them, particularly at longer lead times (Dias et al., 2018; Yang et al., 2021). One critical factor in improving the representation of this variability is the coupling between large-scale circulations and convection, which is often affected by most NWP models through convection parameterization. Such parameterization relies on many physical assumptions to represent a collective impact of several subgrid-scale convective systems on a model grid box, which can lead to significant uncertainties and biases. Not surprisingly, many studies have attributed the poor representation of EW variability in NWP models to the limitations of convection parameterization (Randall, 2013; Tomassini, 2020). Addressing these uncertainties and improving the accuracy of convection parameterization remains a key area of focus for improving the representation of tropical rainfall and its variability in weather and climate models.

With advancing computing resources, high-resolution NWP models are becoming feasible, implying no need for *deep* convection parameterization that controls rainfall generation and vertical energy transport through latent heat release and mixing with ambient air (Emanuel, 1994; Bechtold, 2017). Thus, the vertical distribution of heat, moisture and momentum due to deep convection is not calculated through the physical assumptions in a scheme but computed

from dynamical equations (Stensrud, 2007). This case is called an explicit representation of deep convection. Meanwhile, even finer resolution is required to resolve *shallow* convection that plays an important role for the exchange of heat and moisture between the boundary layer (BL) and the free troposphere, particularly in the subtropics (Schlemmer et al., 2017; Naumann et al., 2019; Sakradzija et al., 2020). The explicit representation of convection allows the models to capture the details of moist processes, including the development of individual convective cells (e.g., thunderstorms), potentially leading to the improvement of coupling between the large-scale circulation and convection such as convectively coupled EWs (Judt and Rios-Berrios, 2021). However, the explicit representation of deep convection requires high computational power due to fine model resolution. Therefore, added values of running those models should be adequately addressed.

The primary focus of this dissertation is to investigate how convective treatment, in particular parameterized versus explicit convection, affects the processes of moist convection. The processes include mean rainfall, its variability and convectively coupled EWs. To assess global impacts, the study area of interest is the equatorial belt (30°N–30°S). The overarching research aim is to obtain insight into the sensitivities of atmospheric processes in the tropics to convective treatment.

The thesis is structured as follows: Chapter 2 provides a comprehensive overview of the existing research on tropical large-scale circulations, moist convection and their representations in numerical models. Chapter 3 outlines research questions and Chapter 4 presents the realistic and idealized simulations and data analyzed in this thesis. Chapter 5 describes the methods used to analyze the model simulations and data. The results are divided into three chapters: Chapter 6 shows rainfall variability associated with EWs in global realistic simulations, Chapter 7 investigates the mean state in idealized simulations by using a new concept to unveil physical reasons behind changes due to different convective treatments and Chapter 8 presents results about internal variability, such as EWs, of the idealized simulations. Finally, Chapter 9 summarizes the main results and Chapter 10 provides suggestions and remarks for future research.

2   Theoretical background

Atmospheric dynamics in the tropics differs from the midlatitudes, in particular due to the very weak Coriolis effect in the tropics. In other words, geostrophic balance between the Coriolis force and the pressure gradient force does not govern the flow dynamics in the tropics. Furthermore, there is a lack of high-frequency and large-coverage of observational data in the tropics, which makes it difficult to obtain a true state of the atmosphere there. This chapter first provides an overview of important large-scale flows in the tropics, including tropical circulations in section 2.1 and modes of variability in section 2.2. Moist convection and representation of it in a model are addressed in section 2.3. How the coupling between large-scale circulation and moist convection is represented in models is explained in section 2.4.

2.1   Tropical circulations

2.1.1   Intertropical Convergence Zone

The intertropical convergence zone (ITCZ) is a narrow rainfall belt encircling the Earth near the equator (Webster, 2020a). The ITCZ is formed where the easterly trade winds of the northern and southern hemispheres meet and rise. The region of the ITCZ is characterized by frequent thunderstorms and heavy rainfall, while the trade wind belts exhibit the characteristics of relative inactivity and stagnation with a typical wind speed of 2–5 $\mathrm{m\,s^{-1}}$. Yearly precipitation accumulation shows that the location of the ITCZ is slightly shifted to the northern hemisphere (Fig. 2.1) with seasonal migration further north in boreal summer. The migration of the ITCZ redistributes large amounts of moisture and is an important source of rainfall over lands, making it crucial for the global water balance.

The ITCZ also plays an important role in global circulation, as it is coupled with other large-scale features. The rising motion of the ITCZ coincides with the low-level convergence of the Hadley circulation (Johnson et al., 1999). The ascending branch of the Hadley circulation over high sea surface temperatures (SSTs) in the western Pacific warm pool is difficult to separate from the ascent motion of an east-west overturning circulation in the equatorial Pacific (Schwendike et al., 2014), which forms the Walker circulation. Thus, the ITCZ is related to the Walker circulation through its coupling to the Hadley circulation. The position of the ITCZ is an important factor in understanding seasonal reversals in low-level wind patterns, which are called the monsoon circulations, as the seasonal migration of its position changes wind patterns (Schneider et al., 2014; Geen et al., 2020).
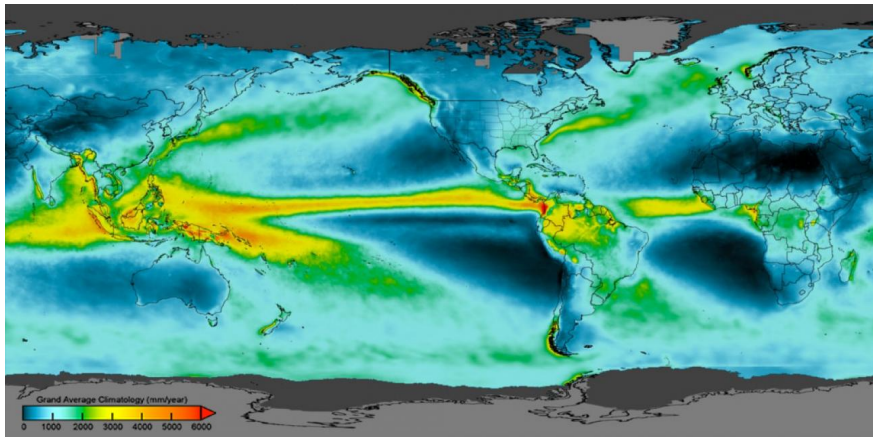
Figure 2.1: The average amount of precipitation [mm/year] from June 2000 - May 2019. The data is retrieved from satellite observations. The narrow zonal rainfall belt illustrates the ITCZ. In the South Pacific, a prominent rainfall deviates from the ITCZ, indicating the South Pacific Convergence Zone. The image is obtained from the NASA's website `https://gpm.nasa.gov/data/imerg/precipitation-climatology`.

Despite its importance, state-of-the-art general circulation models still struggle to accurately represent many characteristics of the ITCZ, including the double-ITCZ problem that the models simulate excessive rainfall in the southern hemisphere (Fiedler et al., 2020; Tian and Dong, 2020). Even in an idealized aquaplanet configuration, which avoids complexities associated with the land-sea distribution and orography, the spatial and temporal distributions of mean precipitation are sensitive to type of numerical model (Stevens and Bony, 2013; Rajendran et al., 2013; Landu et al., 2014; Benedict et al., 2017), vertical and horizontal resolution (Li et al., 2011; Retsch et al., 2017, 2019), and representation of convection (Möbis and Stevens, 2012; Nolan et al., 2016; Retsch et al., 2019; Rios-Berrios et al., 2022).

2.1.2 Hadley circulation

The Hadley circulation is a meridional overturning circulation in both hemispheres with the ascending branch around the equator. The air from the ascending branch moves poleward near the tropopause, eventually sinking back down to the surface. Halley (1686) and Hadley (1735) proposed that the solar heating difference between the tropics and extratropics is the main driver of global circulation when they attempted to explain the easterly trade winds. In their hypothesis, trade winds resulted from the temperature gradient between the equator with warm air rising and the poles with cold air sinking, which would form a single overturning circulation in each hemisphere through mass conservation, as illustrated in Fig. 2.2a, but actually not observed on Earth. Rather, the rising air from the equator subsides at around 30°N/S. As the air moves poleward, the Coriolis effect becomes larger and the wind turns to the right in the northern hemisphere. At 30°N/S the poleward air flow turns into a strong westerly by angular momentum conservation (Held and Hou, 1980), which is called subtropical jets, and the poleward flow descends there. The effect of the Coriolis force in the lower troposphere is found in trade winds that are easterlies towards the equator. Thus, the equator–pole energy imbalance and angular
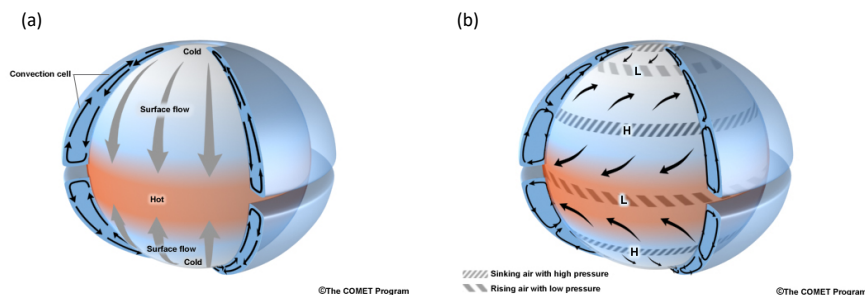
Figure 2.2: Schematics of overturning circulations (a) without the Earth's rotation and (b) with the Earth's rotation. The color on the globe indicates solar heating on the surface. The arrows depict the wind flows. The letter "H" and "L" indicate high pressure and low pressure systems, respectively. The source of this material is COMET® of the University Corporation for Atmospheric Research (UCAR), sponsored in part through cooperative agreement(s) with the National Oceanic and Atmospheric Administration (NOAA), U.S. Department of Commerce (DOC). ©1997-2022 University Corporation for Atmospheric Research. All Rights Reserved.

momentum conservation result in the Hadley circulation constrained between 30°N/S illustrated in Fig. 2.2b.

How does this large-scale meridional overturning circulation relate to the ITCZ? In boreal summer, the ascending branch of the Hadley cell is located in the northern hemisphere, which coincides with the ITCZ. The ascending branch of the Hadley cell can interact with the upward motion through latent heat release within the ITCZ, leading to strengthening the large-scale circulation and intensifying rainfall (Schneider et al., 2014). The Hadley circulation transports mass and energy in the form of moist static energy, which is a thermodynamic variable to describe the sum of gravitational potential energy, heat content and potential energy from latent heating, from the tropics to the extratropics through the collocation of its ascending branch and the ITCZ (Adam et al., 2016), thus they are responsible for meridional energy transports on Earth.

2.1.3 Walker circulation

The Walker circulation is a zonal overturning circulation that occurs over the entire tropical belt. Here we explain it by focusing on the Pacific Walker circulation that spans the tropical Pacific Ocean, from the eastern to the western Pacific. It is characterized by the sinking motion in the eastern Pacific and the rising motion in the western Pacific (Fig. 2.3). These features can be explained by trade winds, the existence of continents around the Pacific Ocean and inhomogeneous sea surface temperatures (SSTs). The tropical ocean is subject to the easterly trade winds, which drive the equatorial current in the mixed layer to the west, causing warm surface water to pile up on the western side of the ocean basin bounded by the Maritime Continent and Australia. Meanwhile, the North and South Pacific Gyres transport cold water from the higher latitudes to the equator and wind-driven Ekman transports bring colder subsurface water to the surface, decreasing the SSTs in the east of the tropical Pacific Ocean (Marshall and Plumb,
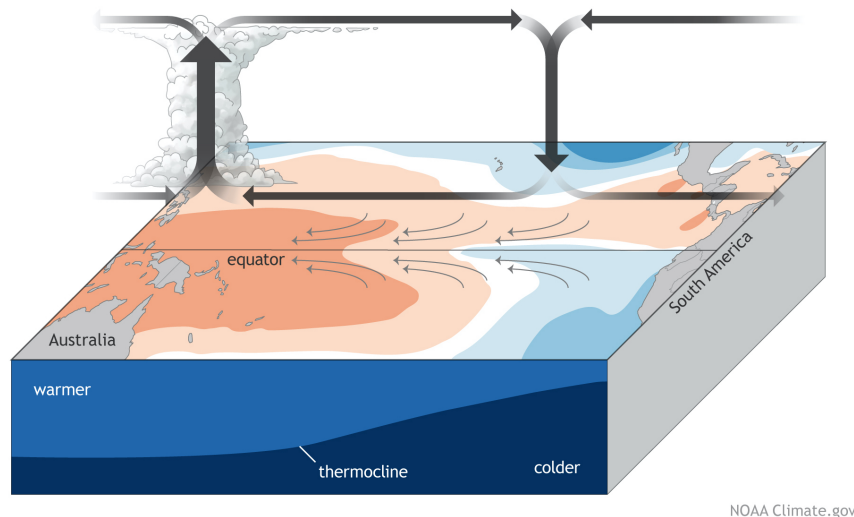
Figure 2.3: Schematic of the Walker circulation across the tropical Pacific Ocean. The SST distribution is shown in color together with the ocean layers. The reddish and bluish colors on the ocean surface illustrate relatively warm and cold SST, respectively. The thick arrows depict the zonal overturning circulation and the thin arrows on the surface depict the surface horizontal winds. The vertical cross section of the ocean is shown with warmer and colder water divided by the thermocline, a transition zone between the surface layer and the abyssal water with a sharp vertical gradient of temperature. Illustrated by NOAA/climate.gov.

2016). This east-west equatorial SST gradient drives a zonal overturning circulation, which was first argued by Bjerknes (1969) and he called the Walker circulation (Fig. 2.3) named after Gilbert Walker. Figure 2.3 illustrates how the Walker circulation is driven by the SST gradient. Over the higher SSTs, the atmosphere is unstable, so deep convection and rainfall frequently occur, indicating an ascent of air. The subsidence occurs in the regions with lower SSTs and the circulation consists of the lower branch of the easterlies, ascent in the west Pacific and descent in the east Pacific, closed by westerlies in the upper troposphere.

The Walker circulation and the ITCZ are also closely linked to each other. The sinking motion of the Walker circulation suppresses convection in the eastern Pacific, while the rising motion enhances convection and rainfall in the western Pacific. The zonal extension of the Walker circulation influences the extension of the ITCZ (Yuan, 2004). When the central Pacific gets warmer (an El Niño condition), the ascending branch of the Walker circulation is shifted to the east and becomes narrower as the sinking motion is bounded to the eastern Pacific. This leads to the development of convection in the central Pacific, altering the pattern of the ITCZ.

2.1.4 Monsoon circulation

A monsoon circulation is characterized by a seasonal reversal of winds between winter and summer. The word monsoon origins from the Arabic word *mausim* meaning season. As the origin of the term, the essential feature of a monsoon system is differential heating between land and sea (Webster, 1987) and it is a unified planetary-scale circulation associated with the global divergent circulation (Trenberth et al., 2000). Figure 2.4 demonstrates the global scale monsoon circulation, in which regional monsoons are embedded such as the Asia-Australia,
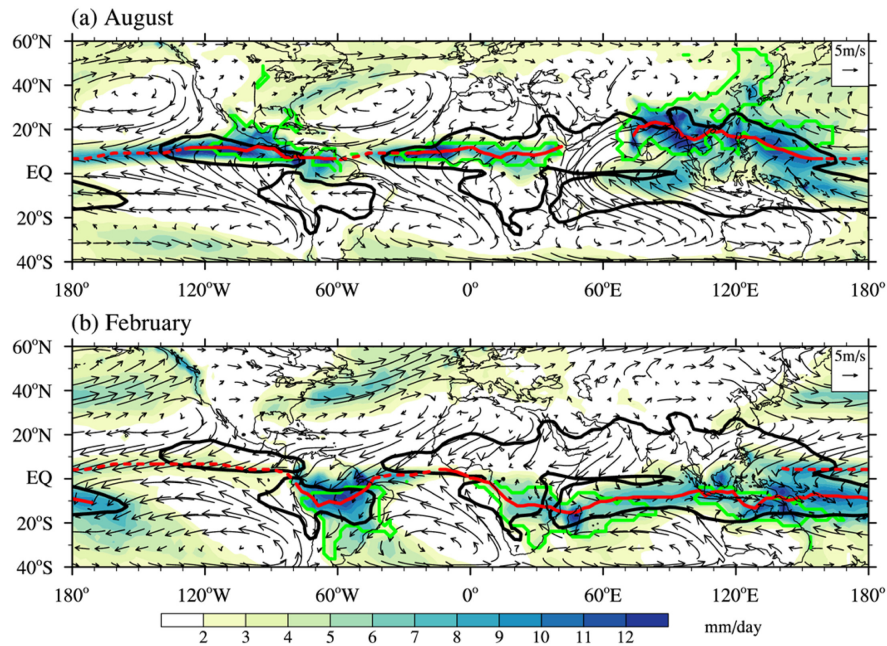
Figure 2.4: Climatological low-level (850 hPa) winds (arrows) and precipitation rate (shading) in (a) August and (b) February. The green lines outline the monsoon domains defined by precipitation characteristics and the black lines outline the tropical monsoon domains defined by the seasonal reversal of zonal wind. The red lines indicate the ITCZ positions (solid for monsoon trough and dashed for trade wind convergence). Reproduced from Wang et al. (2017). ©2017 Published by Elsevier B. V.

tropical African and Indian Ocean monsoons (Webster et al., 1998). For example, there are consistent changes in tropical South America, west Africa, southeast Asia and east Asia from August to February, including low-level wind directions and high rainfall migrating from north to south.

Another important aspect in Fig. 2.4 is that the seasonal change of the low-level wind pattern follows the position of the ITCZ (red lines). In boreal summer, the ITCZ shifts northward, specifically in the eastern Hemisphere, which supports southwesterly flows in the low level over the Indian Ocean. This low-level flow carries warm, moist air from the Indian Ocean to south and southeast Asia and partly east Asia (Wang, 2002). The ITCZ migration and meridional ocean heat transport in the Indian Ocean control the monsoon system over India (Loschnigg and Webster, 2000; Gadgil, 2003). For east Asia, an east-west temperature gradient becomes important, such that heating by the Tibetan Plateau in the east and cool Pacific Ocean create a strong gradient (Yihui and Chan, 2005). The north-south temperature gradient is also important for the monsoon system in east Asia due to the warm western Pacific Ocean and cool Australia (Chang et al., 2005). From mid-May to mid-June the monsoon progresses northeastward, forming monsoon fronts when approaching eastern China, Korea and Japan. This frontal system is called Mei-Yu in China, Changma in Korea and Baiu in Japan. Changma, which begins in late June and ends in late July, contributes to about half of the total annual precipitation in the Korean Peninsula (Oh et al., 1997).

2.2 Modes of variability

The tropics manifest different modes of variability, of which temporal scales range from days to years (Ortega et al., 2017). The variability in the troposphere can be largely characterized by EWs which are derived from the shallow water equations on an equatorial beta plane. Also, the Madden Julian Oscillation (MJO) and easterly waves are important features in the tropics, although they cannot be explained by the shallow water equations. This section will explain how EWs are derived from the shallow water equation and their characteristics in section 2.2.1, the MJO in section 2.2.2 and easterly waves in section 2.2.3.

2.2.1 Equatorial waves

EWs are east- or westward propagating disturbances trapped in the equatorial region. They can couple with deep convection and thus control a considerable fraction of tropical rainfall variability (Takayabu, 1994a; Yasunaga and Mapes, 2012; Kiladis et al., 2009). Figure 2.5 shows the evolution of rainfall averaged over the equatorial region (5°N–5°S). This clearly illustrates that rainfall is abundant in the tropics, and is non-stationary but propagates eastward and westward. One of the distinctive features is convectively coupled Kelvin waves (KWs) over the central and eastern Pacific. For example, a strong rainfall event ($> 1 \, \mathrm{mm \, h^{-1}}$), observed in Africa (0°E) at around day 59, propagates eastward over the Indian Ocean, Maritime Continent and Pacific Ocean with a propagation speed of around $15 \, \mathrm{m \, s^{-1}}$. Eastward propagation with a similar speed is frequently observed in Fig. 2.5 and some of these signals encircle the globe. In addition, westward propagating disturbances are evident over the Atlantic and Africa. The westward-propagating rainfall events are relatively faster than the eastward propagation and their period is around two days.

Before the satellite era, Riehl (1945) first recognized periodic disturbances propagating westward in the Caribbean. The patterns of the waves were documented with attempts to understand the dynamics behind them (Palmer, 1952; Riehl, 1954). Later, some studies realized these types of waves are trapped along the equator (Rosenthal, 1965; Stern, 1963; Bretherton, 1964). It is the seminal paper by Matsuno (1966) in which the motion of EWs was first derived from the shallow water equations on an equatorial beta plane. The solutions describe horizontal and temporally-varying structures of normal modes of the atmosphere. The horizontal behavior is related to vertical structures via a mathematical constant, the so-called equivalent depth h_e. The solutions of the shallow water equations satisfy the relationship

$$\frac{\sqrt{gh_e}}{\beta} \left(\frac{\omega^2}{gh_e} - k^2 - \frac{k}{\omega}\beta \right) = 2n + 1; \quad n = 0, 1, 2, ... \tag{2.1}$$

where g is the gravitational acceleration, ω is the frequency, k is the zonal wavenumber and n is the number of meridional mode. The formula relates ω and k which is called a dispersion relationship. A detailed derivation of the solution is shown in Appendix A. Solutions of Eq. 2.1 can be obtained with some approximations. For example, the term ω^2/gh_e on the left-hand side can be neglected at low frequencies. Then, the dispersion relation becomes
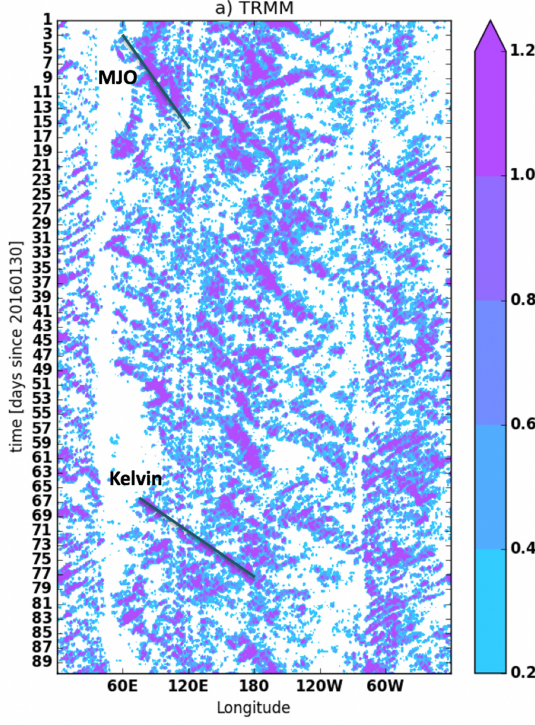
Figure 2.5: Hovmöller diagram of precipitation [mm h^{-1}] averaged over 5°N/S from satellite observations for the period January 30–April 29 2016. Lines indicate typical phase speeds associated with MJO ($\sim$7 m s^{-1}) and Kelvin wave ($\sim$15 m s^{-1}) propagation. The Tropical Rainfall Measuring Mission 3B42 product (TRMM; Huffman et al., 2007) are used for the satellite products. Reprinted from Bengtsson et al. (2021). ©The Authors, CC BY-NC-ND 4.0 ©①⊜⑤

$$\omega_{\text{Rossby}} \approx \frac{-\beta k}{k^2 + (2n+1)\beta/\sqrt{gh_e}}. \tag{2.2}$$

This wave class corresponds to equatorial Rossby waves (ERs). On a resting atmosphere, i.e., no background wind, they always propagate westward because ω is of opposite sign to k.

At high frequencies, the term $k/\omega\beta$ in Eq. 2.1 can be neglected, resulting in

$$\omega_{\text{IG}} \approx \pm\left[(2n+1)\beta\sqrt{gh_e} + k^2 gh_e\right]^{1/2}. \tag{2.3}$$

These wave classes corresponding to the roots represent the inertio-gravity (IG) wave types. The positive and negative roots are called eastward inertio-gravity (EIG) and westward inertio-gravity (WIG) waves, respectively.

Note that the aforementioned solutions are for $n \geq 1$. For $n = 0$, the dispersion relation can be obtained directly from Eq. 2.1 as

$$\omega_{n=0} = k\sqrt{gh_e}\left[\frac{1}{2} \pm \frac{1}{2}\left(1 + \frac{4\beta}{k^2\sqrt{gh_e}}\right)^{1/2}\right]. \tag{2.4}$$

The negative root corresponds to mixed-Rossby gravity waves (MRGs), while the positive root corresponds to EIGs with $n = 0$.

KWs have no meridional wind component, so the dispersion relationship can be obtained by setting the meridional wind component to zero (Appendix A). Thus, the solution for KWs
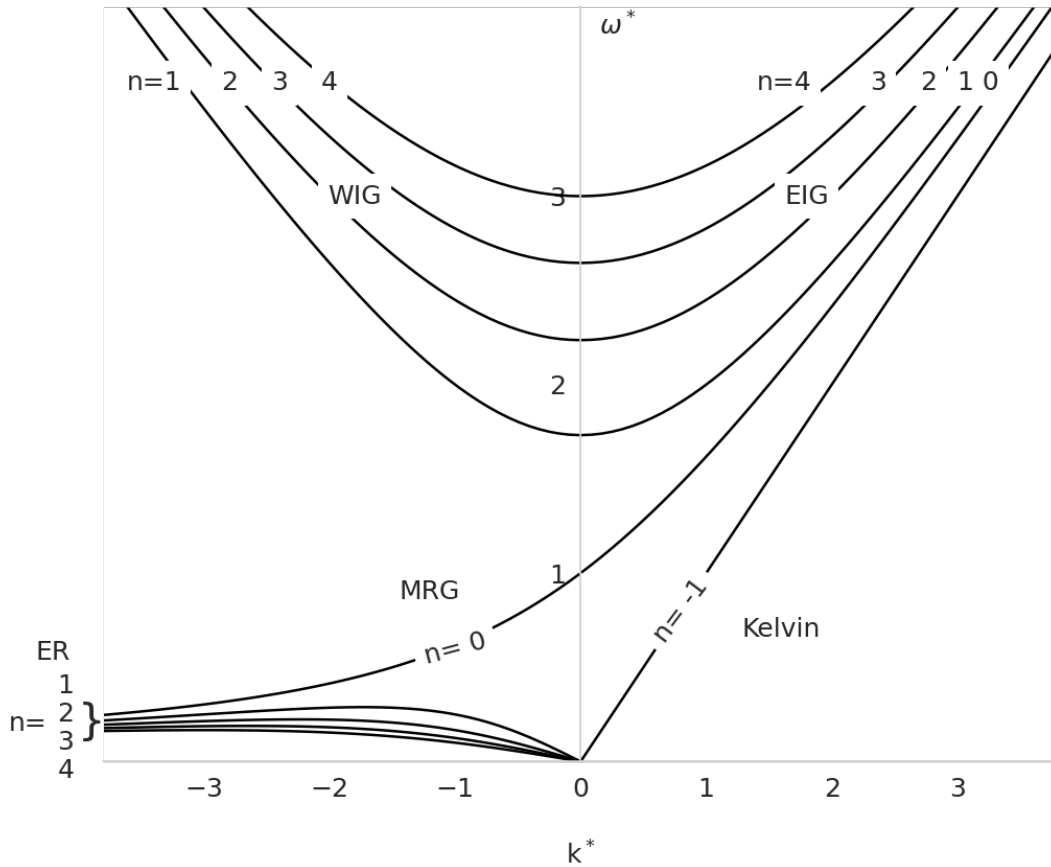
Figure 2.6: Dispersion curves for EWs ($n = -1, 0, 1, 2, 3, 4$) as a function of the nondimensional frequency ω^* and zonal wave number k^* as $\omega^* = \omega/(\beta(\sqrt{gh_e})^{1/2}$ and $k^* = k(\sqrt{gh_e}/\beta)^{1/2}$.

follows as

$$\omega_{KW} = k\sqrt{gh_e}. \tag{2.5}$$

This solution corresponds to Eq. 2.1 with $n = -1$. The phase speed of KW ($= \omega/k$) is identical to the group speed ($= \partial\omega/\partial k$). The dispersion relationship of frequency and wavenumber for each wave type is illustrated in Fig. 2.6.

Matsuno's solution is constructed based on the resting atmosphere, so EWs in reality may deviate from his solution by the background zonal flow and vertical wind shear (Yang et al., 2003; Dias and Kiladis, 2014). Nonetheless, studies using satellite observation of outgoing longwave radiation (OLR) and infrared brightness temperature, as a proxy of convection, of several years found that the spectrum of cloud patterns is indeed aligned with the dispersion curves (Takayabu, 1994a; Wheeler and Kiladis, 1999) and those waves are called convectively coupled EWs.

In the following, the characteristics of EWs and their importance will be discussed. For the remainder of the thesis, an ER denotes that of the first meridional mode ($n = 1$) and an EIG denotes that of $n = 0$, the dispersion curve of which is closely related to MRGs (Fig. 2.6).
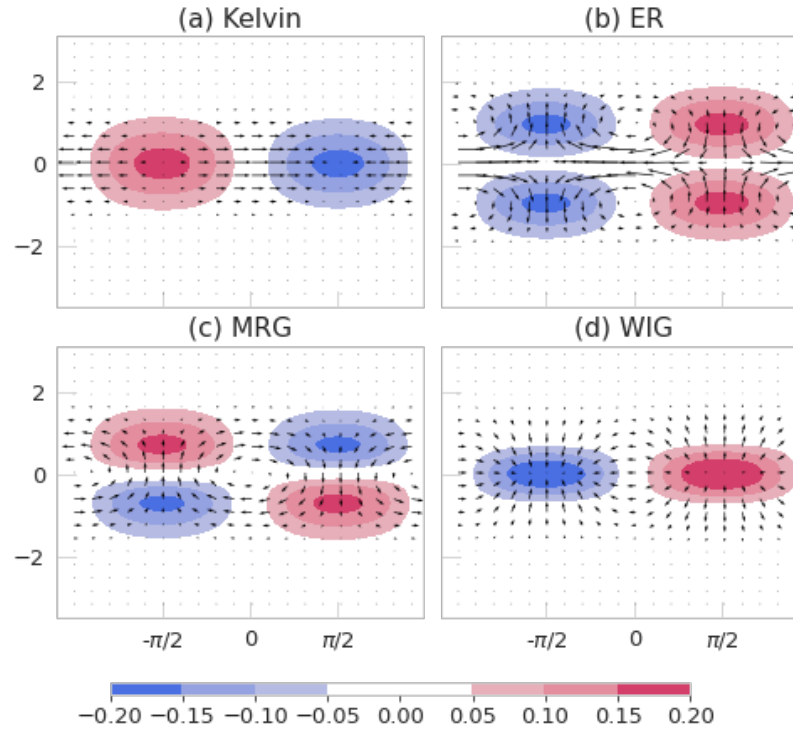
Figure 2.7: Theoretical patterns of (a) KW, (b) ER with $n = 1$, (c) MRG and (d) WIG with $n = 1$ in the lower troposphere. All scales and fields have been nondimensionalized. The vectors and shading show horizontal winds and divergence, respectively.

a. Kelvin waves

KWs are eastward-propagating disturbances, the propagation speed of which is typically 12–25 m s^{-1} when they are coupled to convection, while dry KWs propagate much faster at speeds of 30–60 m s^{-1} (Wheeler et al., 2000; Straub and Kiladis, 2003b). The eastward propagating rainfall at 15 m s^{-1}, discussed in the context of Fig. 2.5, is related to convectively coupled KWs. The theoretical pattern of KWs is shown in Fig. 2.7a. The structure is symmetric about the equator and is composed of only zonal wind with the maximum variance at the equator. Correspondingly, observed KWs are largely symmetric with respect to the equator at the zonal scale of 3300–6600 km (Straub and Kiladis, 2003b) and possibly up to 10,000 km. The vertical structure of zonal winds can be characterized by an elbow or boomerang shape (Fig. 2.8a): Prior to a maximum activity of convectively coupled KWs, easterly anomalies in the lower troposphere are dominant with a westward tilt with height but with an eastward tilt in the lower stratosphere (Wheeler et al., 2000; Straub and Kiladis, 2003b; Yang et al., 2003; Kiladis et al., 2009). Mid-tropospheric warming over low-level cooling is in phase with KWs (Fig. 2.8b), showing a first baroclinic mode in temperature associated with KWs. The specific humidity structure (Fig. 2.8c) shows that the lower troposphere is moistened two days before the maximum wave activity. During the active phase, moistening rapidly deepens throughout the atmospheric column, except for the dry BL. Although they occur at almost any time of the year, KWs have a seasonality with maximum activity in February–August (Wheeler et al., 2000).
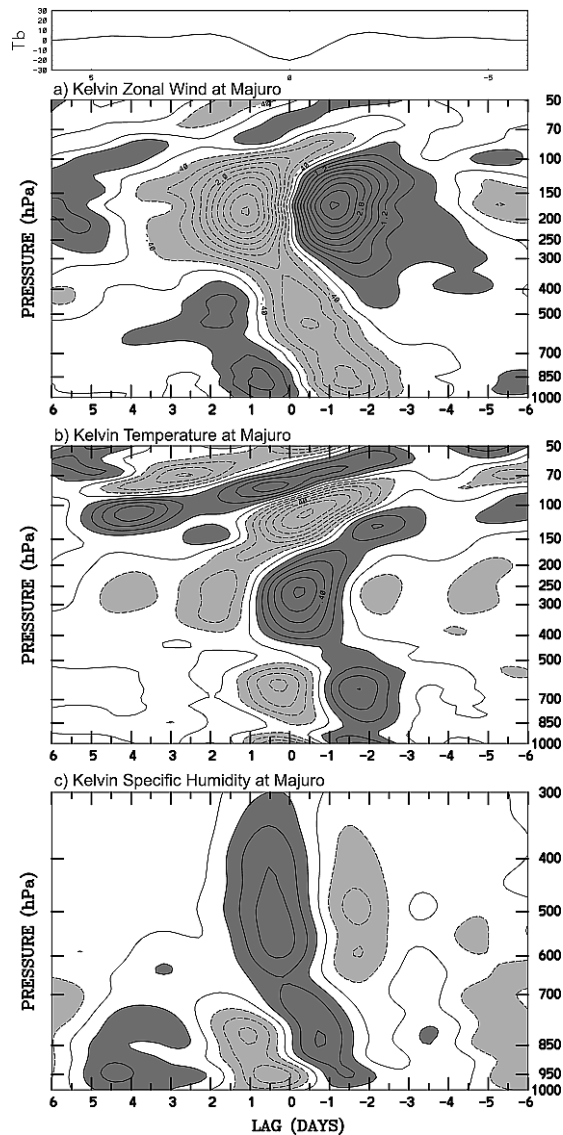
Figure 2.8: Time-height sections of anomalies of (a) zonal wind, (b) temperature, and (c) specific humidity at Majuro (7.1°N, 171.4°E), scaled to a −20 K perturbation in KW-filtered brightness temperature at the nearest grid point on day 0. Contour interval is 0.4 m s^{-1} for wind, 0.1 K for temperature, and 0.1 g kg^{-1} for specific humidity, with negative contours dashed. Dark shading represents positive perturbations. Note that time increases from right to left. Reprinted from Kiladis et al. (2009). ©2009, American Geophysical Union.

KWs are crucial for weather predictions in various ways. KWs modulate upper-level wind variability and capturing this well in an NWP model can translate into obtaining accurate upper-level wind variability, which in turn can improve weather forecasts (Žagar et al., 2021). Their upper-level dynamics also influence the propagation of cold surges over South America, impacting temperature variability and precipitation associated with a cold front (Liebmann et al., 2009). KWs are strongly coupled to the ITCZ (Straub and Kiladis, 2002; Dias and Pauluis, 2011), as the former is characterized by the maximum variance of the upper-level divergence at the equator and the latter exhibits the maximum rainfall near the equator. Convectively coupled KWs substantially contribute to the modulation of rainfall variability over equatorial Africa on a day-to-day scale (Schlueter et al., 2019; Ayesiga et al., 2021). Heavy rainfall over Southeast Asia is associated with the active phase of KWs (Ferrett et al., 2020). Furthermore, KW activity in the central Pacific is associated with extratropical Rossby wave disturbances by exciting a lower tropospheric pressure surge (Straub and Kiladis, 2003a).

b. Equatorial Rossby waves

ERs are westward-propagating disturbances, the propagation speed of which is 5–7 m s^{-1} when they are coupled to convection. Dry ERs propagate much faster at speeds of 10–20 m s^{-1} (Kiladis et al., 2009). From linear wave theory, ERs are characterized by a pair of cyclonic wind patterns in both hemispheres with low-level convergence in phase with poleward wind anomalies and in quadrature with equatorial zonal wind (Fig. 2.7b). The typical wavenumber of ERs is 4–5 with a zonal scale of 4000–11,000 km. ERs can be found at almost any time of the year with a maximum wave activity in the southern hemisphere in boreal winter (Wheeler et al., 2000). The vertical structure of ERs is fundamentally different from KWs. The temperature structure of ERs is rather barotropic with a different temperature profile from KWs (Inoue et al., 2020; Nakamura and Takayabu, 2022). ERs can be categorized into the rotational type, while KWs are more divergent or non-rotational (Yasunaga and Mapes, 2012). This rotational flow may be associated with an improvement in predictability (Raymond et al., 2015). Indeed, predictability associated with ER waves is around a week (Li and Stechmann, 2020; Yang et al., 2021), which is longer than KWs.

c. Mixed-Rossby gravity waves

MRGs are westward-propagating disturbances with a phase speed of 8–10 m s^{-1}, while their wave packet can propagate to the east with an average speed of 5 m s^{-1} (Wheeler and Kiladis, 1999). The theoretical pattern of MRGs is characterized by cross-equatorial meridional flow with a maximum wind anomaly at the equator (Fig. 2.7c). Corresponding low-level convergence is off-equatorial and in phase with the maximum meridional wind anomaly. The longitudinal scale is 1000–4000 km and the seasonal cycle of the waves can be found with strong wave activity in August–November (Wheeler et al., 2000). The vertical structures of meridional wind and temperature for MRGs exhibit an elbow shape as for KWs. Phase speeds of MRGs can greatly differ over the Indian Ocean where the Walker circulation can strongly influence the horizontal wind fields in the upper and lower levels (Takasuka et al., 2019; Suematsu and Miura, 2022). As well as the aforementioned waves, MRGs are an important source of predictability in the tropics (Li and Stechmann, 2020; Yang et al., 2021). Furthermore, they substantially contribute to subseasonal variability (Stephan et al., 2021).

d. Westward inertio-gravity waves

Westward inertio-gravity waves of the first meridional mode (WIG1) propagate westward with phase speeds of 10–30 m s^{-1} and with a spatial scale of 200–2000 km (Takayabu, 1994b; Tulich and Kiladis, 2012). The first meridional mode refers to $n = 1$ in Eq. 2.1. Figure 2.7d shows that the pattern of divergence and convergence is maximized at the equator with the corresponding horizontal wind pattern. Note that the spatial structure of WIG1 is symmetric with respect to the equator, while westward inertio-gravity waves of the second meridional mode (WIG2) exhibit an antisymmetric pattern (not shown). Due to their period, WIG1 are also called 2-day waves (Haertel and Kiladis, 2004; Haertel et al., 2008). The structures of the 2-day waves were well

documented during the Tropical Ocean and Global Atmosphere Coupled Ocean–Atmosphere Response Experiment (TOGA COARE; Webster and Lukas, 1992; Takayabu et al., 1996; Haertel and Kiladis, 2004), observational and modeling focus of which is on understanding the fields of the atmosphere, the ocean and their coupling in the western Pacific warm pool over the period of November 1992–February 1993. Corresponding to the period of TOGA COARE, Wheeler et al. (2000) reported that convective activity associated with WIG1 can be found in December, January and February. The 2-day periodicity is related to the diurnal cycle, leading to a combined effect on the life cycle of convective systems, which is crucial for the organization of convection within a larger-scale circulation (Chen and Houze, 1997; Johnson and Ciesielski, 2013). WIG1 share similarities with squall line systems in terms of structure, spatial and temporal scales and propagation (Takayabu et al., 1996; Tulich and Kiladis, 2012). For example, African squall lines travel at $50\,\mathrm{km\,h^{-1}}$ ($\sim 14\,\mathrm{m\,s^{-1}}$) and their maximum spatial scale can overlap the low bar of the spatial scale of WIG1.

2.2.2 Madden Julian Oscillation

The MJO is a planetary-scale disturbance that slowly propagates eastward with a speed of $5\,\mathrm{m\,s^{-1}}$ and is mainly observed in the Indian and Pacific Oceans. It was first documented by Madden and Julian (1971, 1972). They found an alternating zonal wind signal with a period of 40–50 days when they were investigating temperature and pressure patterns in the tropics. In fact, the MJO is characterized by its intraseasonal variability (30–90 days). It contains a large-scale pattern consisting of an enhanced rainfall (or convection) phase and a suppressed rainfall phase (Zhang, 2005). Figure 2.9 illustrates the structure of the MJO when the enhanced phase is located over the Indian Ocean where the low-level convergence is evident with corresponding upper-level divergence, leading to strong upward motion, thus heavy rainfall. The enhanced phase is accompanied by the suppressed phase over the west-central Pacific Ocean where it is characterized by low-level divergence, leading to sunny and relatively dry weather there. This coupled large-scale circulation slowly propagates to the east, which changes local weather.

The MJO is also evident in Fig. 2.5 which is marked in the first couple of weeks over $60°–100°\mathrm{E}$. The organized rainfall system propagates eastward at a speed of $7\,\mathrm{m\,s^{-1}}$. Again, the MJO does not derive from Matsuno's wave solutions, but it is an important intraseasonal variability in the global climate system, as it substantially shapes weather patterns such as rainfall and temperature around the world (Woolnough, 2019). The frequency of rainfall extremes in the Indian Ocean, the Maritime Continent and the western Pacific becomes higher during the active phase of the MJO (Jones et al., 2004). The MJO can modulate temperature variability in the northern hemisphere through MJO-induced Rossby wave propagation (Seo et al., 2016). Its role in influencing temperature can lead to heat waves in Australia (Parker et al., 2014). The list of the MJO impact is non-exhaustive, but is summarized in Fig. 2.10. For practical reasons, the low frequency of the MJO creates implications for climate prediction as it interacts with other climate variabilities such as El Niño events (Lin et al., 2006; Zavala-Garay et al., 2005), and its interactions with EWs indirectly impact predictability for shorter time windows (Roundy and Frank, 2004; Zhang et al., 2020; Adames and Wallace, 2014; Johnson and Ciesielski, 2013).
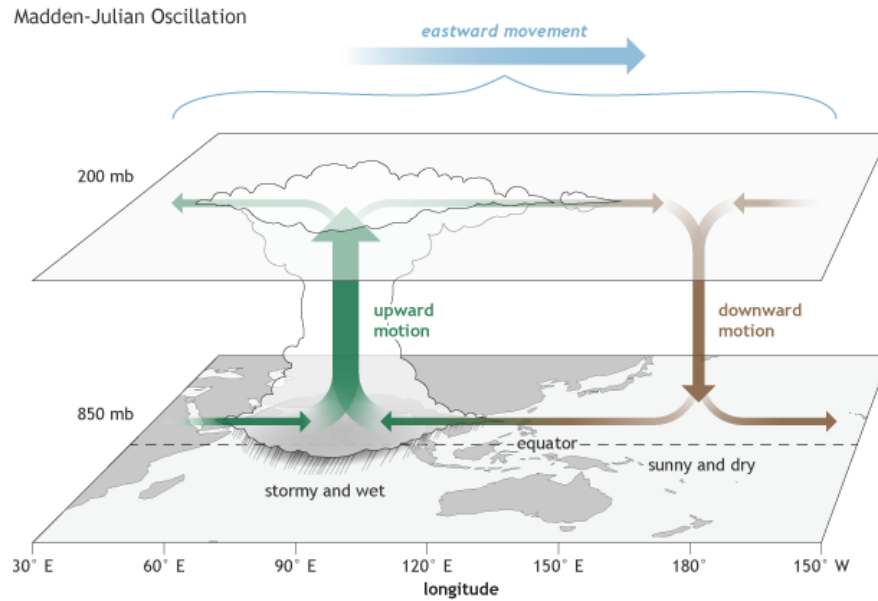
Figure 2.9: Schematics of the MJO when the enhanced convective phase is centered across the Indian Ocean and the suppressed convective phase is centered over the west-central Pacific Ocean NOAA/climate.gov drawing by Fiona Martin.

2.2.3 Easterly waves

The previous subsections explored EWs, which derive from the shallow water equation on an equatorial beta plane, and the MJO, which is a planetary-scale disturbance. Easterly waves are also frequently observed in the Pacific, the east Atlantic and West Africa (Reed and Recker, 1971; Thompson Jr et al., 1979; Carlson, 1969) but do not have a linear solution. Easterly waves are synoptic-scale disturbances with wavelengths of 2500–3500 km, with phase speeds of $8 \, \mathrm{m \, s^{-1}}$ on average and with periods of 2–10 days. African easterly waves (AEWs), which propagate over Africa to the tropical Atlantic, have a period of 3–5 days. AEWs can force 40 % of the formation of squall lines from May to October over West Africa (Fink and Reiner, 2003). They are induced by baroclinic disturbances of the African easterly jet (AEJ) in the mid-troposphere (Burpee, 1972). Easterly waves in the eastern Pacific are associated with around half of seasonal rainfall in boreal summer (Dominguez et al., 2020), and modulate deep convection as well as dynamic and thermodynamic conditions within the eastern Pacific ITCZ (Huaman et al., 2021).

2.2.4 Identification of modes of variability

Objectively extracting signals of the aforementioned modes of variability can be challenging (Knippertz et al., 2022; Žagar et al., 2022). A recent methodological intercomparison study (Knippertz et al., 2022) found differences in identified signals of EWs, mainly between approaches based on wavenumber-frequency filtering (e.g., Wheeler and Kiladis, 1999; Gehne and Kleeman, 2012; Kikuchi et al., 2018) and spatial projection (e.g., Yang et al., 2003; Žagar et al., 2009), and proposed to use two fundamentally different wave identification methods to check robustness of detected signals. In the following, we describe the concept of two wave
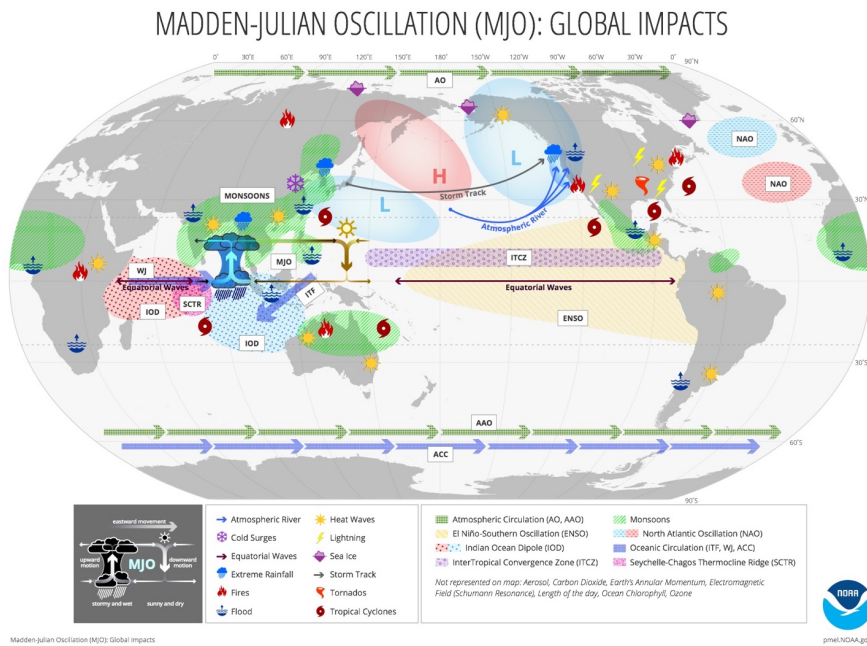
Figure 2.10: Schematics of the global impacts of the MJO. Further reading refers to Zhang (2013). Reprinted from Yoneyama and Zhang (2020). ©The Authors, CC BY-NC 4.0 ⓒ①⑤

identification methods, focusing on Wheeler and Kiladis (1999) and Yang et al. (2003), and their strengths and weaknesses.

a. Wavenumber-frequency filtering

This method is based on time-space filtering introduced by Takayabu (1994a) and Wheeler and Kiladis (1999, hereafter WK), who used satellite-measured OLR. This method is arguably the most widely used[1]. It characterizes EWs based on the dispersion relationship discussed in section 2.2.1 using two-dimensional horizontal fields such as OLR, infrared brightness temperature, rainfall, horizontal divergence or other proxies for deep convection. Observed signals are related to the shallow water equations through h_e which is a mathematical constant to relate horizontal and vertical structures. The range of h_e for the troposphere is 10–250 m, while convectively couple EWs typically exhibit h_e of 12–50 m (Kiladis et al., 2009; Wheeler and Nguyen, 2015). The general steps of the WK approach involve: (1) transforming a time-domain signal into a wavenumber-frequency domain using a fast Fourier transform, (2) selecting a window of wavenumber and frequency for each wave type according to their dispersion relationship (illustrated in Fig. 2.6) and removing signals outside of the window and (3) applying an inverse fast Fourier transform to retrieve a signal corresponding to the wave type.

One of the major advantages of this approach is that one is flexible to define waves in a way that it can filter out not only EWs but also the MJO and easterly waves which are not solutions of the shallow water equations, i.e., no dispersion relationship. When their characteristic wavenumber and frequency are defined, these values can be constrained in the wavenumber-frequency domain

---

[1]The paper of Wheeler and Kiladis (1999) has been cited by 1867 as of April 17, 2023. Soure: Google Scholar

to return the wave signals. Additionally, both model and observational data can be used for the WK method such as rainfall, infrared brightness temperature and other fields that can represent convective clouds (Yasunaga and Mapes, 2012). However, there are some drawbacks to using this method. One issue is that a long time integration is required to best utilize the benefits of the method, such that the time length of data should be longer than a period of an EW of interest to avoid spectral leakage (Wheeler and Weickmann, 2001). Furthermore, spurious oscillation can occur in the filtered data near discontinuities, such as the first and last time steps, which is called a ringing effect. Therefore, its utilization is limited for real-time applications.

b. 2D spatial projection

This method was introduced by Yang et al. (2003, hereafter YP) and characterizes horizontal structures of EWs based on theoretical patterns (Fig. 2.7) using two-dimensional fields of horizontal winds and geopotential at a pressure level. To identify the horizontal structures easily, new variables q and r are introduced as $q = (g/c)\phi + u$ and $r = (g/c)\phi - u$, where u is the zonal wind and ϕ is the geopotential height, according to Gill (1980). Then, q, v and r can be projected onto corresponding parabolic cylinder functions D_n as follows:

$$\{q, v, r\} = \sum_{n=0}^{n=\infty} \{q_n, v_n, r_n\} D_n. \tag{2.6}$$

As D_n is closely related to a Hermite polynomial of order n which is a key component to define the meridional structure of v for the solutions of Matsuno (1966) (see Appendix A). The meridional structure is constrained by a trapping scale $y_0 = \sqrt{c/2\beta}$, which is proportional to the fourth root of h_e. The YP method uses $y_0 = 6°$, which is empirically deduced and equivalent to $h_e = 43$ m. The horizontal structures obtained using Eq. 2.6 correspond to wave patterns shown in Fig. 2.7.

The general steps for the YP method involve: (1) computing q, v and r from the dynamical fields (u, v and ϕ), (2) filtering q, r and v in a broad window of wavenumber and frequency using the fast Fourier transform, which isolates east- and westward-moving components and thus removes stationary and high-frequency waves, (3) projecting the Fourier coefficients of q, r and v onto the meridional structures of EWs defined by parabolic cylinder functions and (4) transforming the Fourier coefficients back into the physical space. The wavenumber-frequency window loosely constrains characteristic phase speeds, but the projection is the key component of this approach. Thus, the YP method is fundamentally different from the WK method.

One of the main advantages of using the YP method is that it is suitable for real-time applications (Yang et al., 2021). As the projection is done on instantaneous fields, the detected waves are not affected much by the length of input data. Thus, forecast data can be used with incorporation with analysis data. However, the YP method requires global two-dimensional fields of u, v and ϕ. This restricts the application only to analysis and model data because no observations globally cover these variables. Furthermore, the projection is done onto theoretical patterns, which means that easterly waves and the MJO cannot be identified by the YP method.
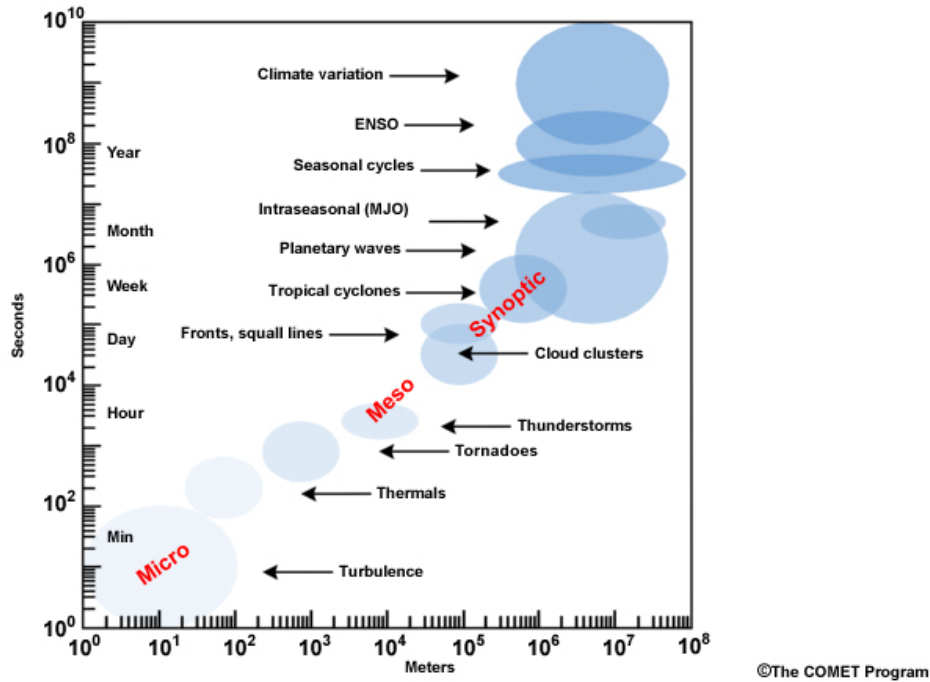
Figure 2.11: Conceptual description of spatial and temporal scale of various atmospheric processes in the tropics. One of the examples for multiscale interactions is coupling between thunderstorms (moist convection) and the MJO. The source of this material is COMET® of the University Corporation for Atmospheric Research (UCAR), sponsored in part through cooperative agreement(s) with the National Oceanic and Atmospheric Administration (NOAA), U.S. Department of Commerce (DOC). ©1997-2022 University Corporation for Atmospheric Research. All Rights Reserved.

2.2.5 Representation in numerical models

Despite their abundance in the tropics and their importance of predictability, weather and climate models often fail to correctly capture EWs and the MJO (Bengtsson et al., 2019; Dias et al., 2018; Lin et al., 2006). Their representation is sensitive to model type (Rios-Berrios et al., 2020; Blackburn et al., 2013), boundary condition (Williamson et al., 2013), simulation geometry (Blanco et al., 2016) and treatment of convection (Judt and Rios-Berrios, 2021; Rios-Berrios et al., 2022). However, the reasons behind the large discrepancies are not fully understood.

EWs are characterized by their synoptic scales on time scales of days to weeks and the MJO is a planetary scale on intraseasonal time scales. These large-scale features are coupled to mesoscale convection. Figure 2.11 summarizes this wide spectrum of spatial and temporal scales of atmospheric processes in the tropics. Thus, multiscale interactions between convection and large-scale circulations (Fig. 2.11) are the key to accurately representing EWs. Yet, it is a nontrivial exercise to pinpoint the sources of uncertainty (Gehne et al., 2022). To start this discussion, we first explore how convection is represented in a model in the following section.

Figure 2.12: Photo of different spatial scales of thunderstorms over southern Borneo (photo center point: 3.0°S, 114.0°E) taken by the International Space Station on August 5, 2014. ©the Earth Science and Remote Sensing Unit, NASA Johnson Space Center.

2.3 Moist convection

Deep convection is ubiquitous in the tropics and occurs at many scales from hourly and kilometers (thunderstorms) to daily and hundreds of kilometers (mesoscale convective systems) to subseasonal and planetary scales (MJO). This wide range of spatial scales of tropical deep convection is illustrated in Fig. 2.12. Individual thunderstorms with extensive anvil clouds are developed along a coastline and a larger convective system is formed in the center of the island. These distributions of deep convective clouds can be random, but the pattern and propagating features of clouds in this area are highly modulated by the diurnal cycle, the MJO and EWs (e.g., Peatman et al., 2021; Zhou et al., 2022). Previously, the focuses were spatially large scales and temporally long scales. This section focuses on individual convective processes (km-scale) in section 2.3.1, organized forms of individual convection (mesoscale) in section 2.3.2, and the representation of moist convective processes in a numerical model in section 2.3.3.

2.3.1 Process of moist convection

Convection comes from the Latin word convectiō, meaning "carrying" which describes a buoyancy-driven overturning movement of rising warm air and subsiding cold air. The life cycle of moist convection as a single convective cell can be classified into three stages (Weisman and Klemp, 1986):

- An unsaturated air parcel is lifted in an unstable condition such as surface warming during the daytime in summer. The parcel adiabatically moves upward and the adiabatic expansion cools the parcel. As the parcel becomes cooler as it rises, it reaches the saturated mixing ratio, thus forming a cloud (cumulus stage in Fig. 2.13).
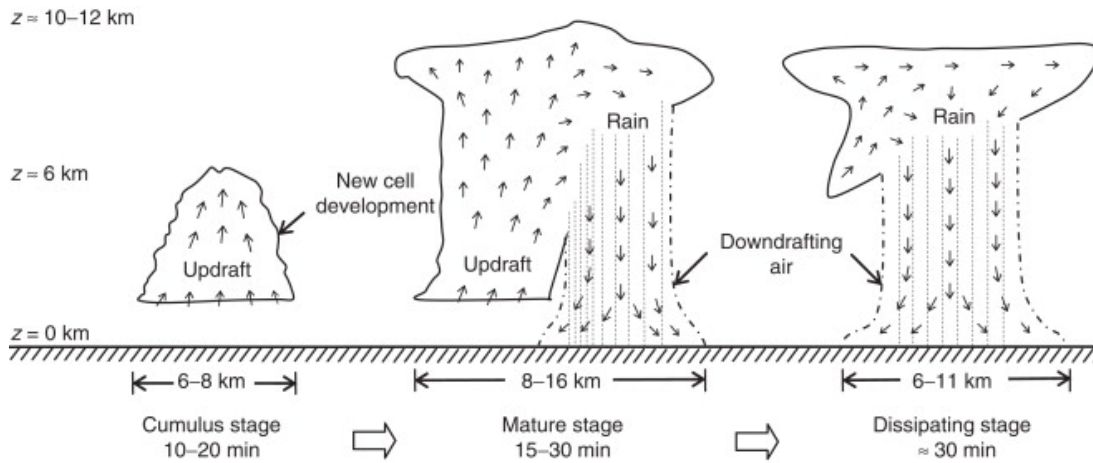
Figure 2.13: Evolution of moist convection with no vertical wind shear. Reprinted from Koutsoyiannis and Langousis (2011). ©2011 Published by Elsevier B.V.

- The parcel rises until it reaches the equilibrium level (EL) where the parcel's virtual temperature equals the ambient air virtual temperature. Since the upward motion of the parcel carries the upward momentum, the air can shoot slightly higher than the EL. Over time, parcels in the ascent gain water droplets or ice, depending on temperature, and the convective cloud becomes mature. At the EL, ice particles are distributed laterally, creating an anvil. As the process repeats, raindrops and ice particles become too heavy, so that updrafts cannot hold them in the air. Thus, those liquid and solid particles eventually precipitate in the form of rain, graupel or even hail (mature stage in Fig. 2.13).

- Precipitation brings down not only moisture but also air, which forms downdrafts. This process is accompanied by the entrainment of dry air at mid levels (3–5 km above the ground), which cools the downdrafts. While falling down, rain evaporation and ice melting happen, which cools down the surroundings. The entrainment of dry air and evaporative cooling by rain accelerates the downdrafts. This cold downdraft arrives at the surface, forming a cold pool. As the precipitation cools the surface and the boundary layer (BL), the convective cloud loses instability and eventually dissipates (dissipating stage in Fig. 2.13).

This convective process is accompanied by condensation and evaporation and it describes the life cycle of moist convection.

The maximum buoyancy of a lifted air parcel can be quantified by convective available potential energy (CAPE), which measures the total amount of buoyancy by integrating the difference in temperature between the parcel and environment at the levels where the former is warmer than the latter (Holton, 2004). Figure 2.14 illustrates how to quantify CAPE by lifting an unsaturated air parcel. An unsaturated air parcel ascents from the ground and follows the dry adiabat. When this dry adiabat meets the line of constant mixing ratio, the parcel becomes saturated and this level is called the lifting condensation level (LCL in Fig. 2.14). Now the saturated parcel follows the pseudoadiabat which is an irreversible process because condensates
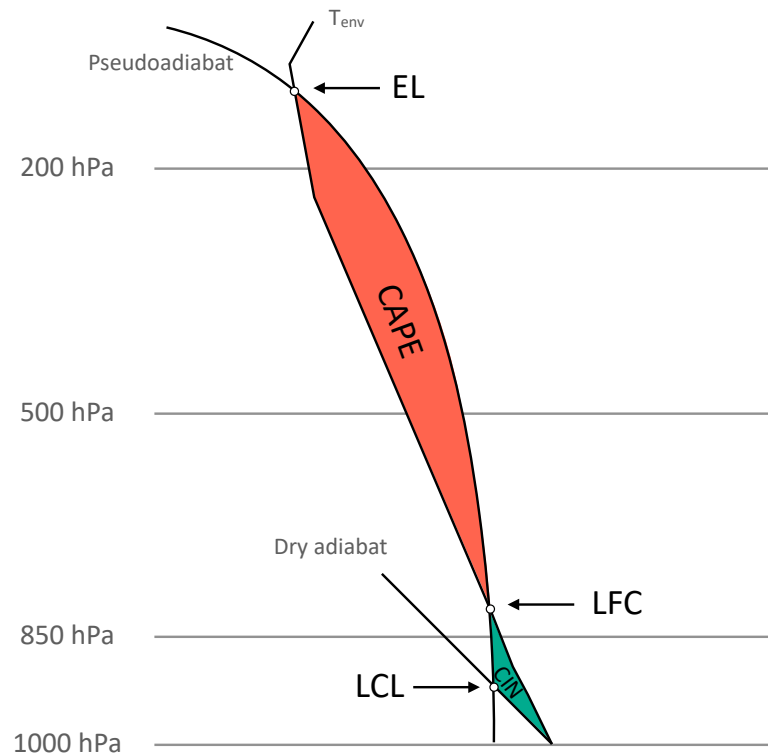
Figure 2.14: Schematics of a skew T-P diagram to illustrate convective available energy (CAPE) and convective Inhibition (CIN). The parcel at 1000 hPa rises adiabatically until it reaches the lifting condensation level (LCL). From here it follows a curve of pseudoadiabat (or moist adiabat). When the parcel reaches the level of free convection (LFC), it rises with no lifting until the equilibrium level (EL) is reached.

are assumed to be immediately removed from the air parcel. At the LCL, the parcel is cooler than the ambient air, so it should be lifted until it reaches the level of free convection (LFC in Fig. 2.14). The LFC is the level where the parcel is neutrally buoyant to the environment. The closed area in green represents convective inhibition (CIN) which is the energy barrier that the rising air parcel has to overcome so that convection occurs. A dry BL and large stability increase CIN, so extra lifting forcing is needed to lift an air parcel. Solar heating during the daytime, lifting of an air parcel when it passes a mountain, or other lifting mechanisms can reduce CIN, which triggers convection more easily than a case of large CIN. Above the LFC, the parcel freely moves upward under the condition that it is warmer than the ambient air. The air parcel cannot ascend anymore above the EL where it is cooler than the ambient air, except for parcel overshoots.

For CAPE, the difference in virtual temperature between the pseudoadiabat and ambient air at each level is calculated and integrated from the level of the LCL to the EL, indicated as the sketched area in orange in Fig. 2.14. The typical value of CAPE for thunderstorms in the Midwest of North America is around 2000–3000 J kg^{-1}, leading to a strong maximum updraft

velocity up to $50 \, \text{m s}^{-1}$. In contrast, the warm, humid environment in the tropics limits the difference in virtual temperature with a typical value of CAPE being around $500 \, \text{J kg}^{-1}$. This leads to relatively moderate updraft velocities for tropical thunderstorms compared to those in the midlatitudes (Holton, 2004).

2.3.2 Organized convection

In the tropics, large clusters of convection are found more frequently than isolated convection. These clusters often consist of deep convective showers and stratiform heavy rain (Cheng and Houze, 1979; Houze, 1989) and are called mesoscale convective systems (MCSs) with spatial scales of $100 \, \text{km}$ to $1000 \, \text{km}$ and with temporal scales of several hours to more than a day (e.g., Houze, 2004, 2018; Feng et al., 2021). Note that a single deep convective cell grows and dies within an hour or so. MCSs account for more than half of tropical rainfall (Nesbitt et al., 2006; Tao and Moncrieff, 2009; Yuan and Houze, 2010) with even higher frequency (around $90 \, \%$) over tropical lands (Yuan and Houze, 2010). The rainfall amount associated with MCSs is greater over lands than oceans in the tropics (Fiolleau and Roca, 2013). Furthermore, rainfall tends to be more extreme over tropical oceans when convection is organized into MCSs (Angulo-Umana and Kim, 2023).

Types of MCSs can be categorized largely into squall lines (Zipser, 1977) and non-squall tropical clusters (Leary and Houze, 1979), depending on vertical wind shear (LeMone et al., 1998; Weisman and Rotunno, 2004). These types differ in terms of propagation speed and longevity, but they both share typical structures (Fig. 2.15). At the leading edge of the system, deep convective clouds are dominant with a narrow region of $O(1$–$10 \, \text{km})$. This narrow region is followed by an extensive area of anvil stratiform clouds with a horizontal scale of $O(10$–$500 \, \text{km})$. The anvil stratiform clouds partly originate from the leading convective clouds and are partly formed through internal dynamics, generating stratiform precipitation (Zipser, 1977; Houze et al., 1980). Over the tropical belt, the rainfall rate by convective precipitation ($7.3 \, \text{mm h}^{-1}$) is four times greater than that by stratiform precipitation ($1.8 \, \text{mm h}^{-1}$), whereas stratiform rainfall explains about $70 \, \%$ of the rain area in the tropics (Schumacher and Houze, 2003). The area ratio of convective to stratiform precipitation is greater over land than over ocean.

The vertical profile of heating differs between the convective and stratiform parts (Houze, 1982; Johnson and Young, 1983). Strong updrafts in the convective precipitation part is shown in Fig. 2.15. This strong upward motion means positive total heating throughout the troposphere, dominated by condensation. In contrast, the stratiform part is characterized by a top-heavy heating profile. The upper troposphere is dominated by net heating by old, weak updrafts from the convective region and sublimation of water vapor, while evaporation of stratiform precipitation cools the lower troposphere. Furthermore, the cloud base in the stratiform area is located at around $5 \, \text{km}$ or $500 \, \text{hPa}$ where melting and evaporation of precipitating particles are dominant and thus contribute to net cooling.

The top-heavy heating profile of an MCS has global impacts. When the fraction of stratiform rain increases, the heating profile is elevated and intensified (Schumacher et al., 2004), which
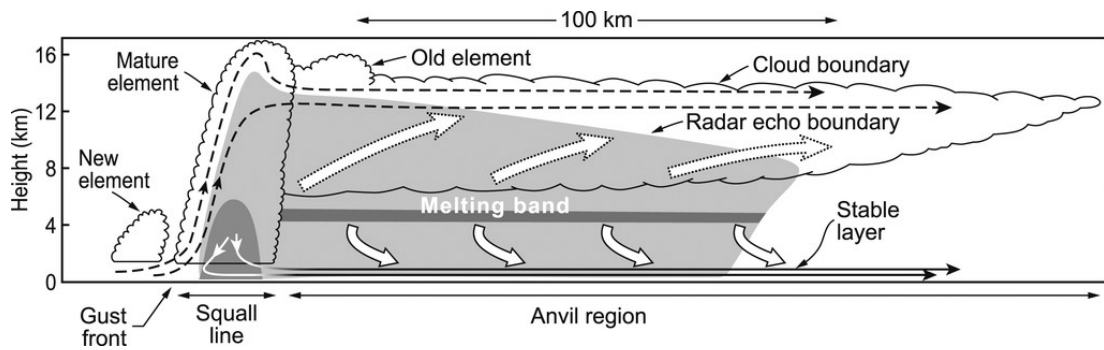
Figure 2.15: Schematic cross section through a squall-line system observed over the eastern tropical Atlantic Ocean. New convection is developed in front of the gust front, followed by a small area of deep convection. A large fraction of the system is covered by a stratiform cloud. This vertical structure of a squall line represents the general structure of a MCS. Adapted from Houze (1977); Houze and Betts (1981). Reprinted from Houze (2018). ©American Meteorological Society. Used with permission.

increases the vertical gradient of net heating in the upper troposphere. The increased gradient of net heating can change the upper-level divergence, and thus impact the large-scale circulations (Haynes and McIntyre, 1987; Mapes and Houze, 1995) and further midlatitude dynamics (Schumacher et al., 2004).

Another characteristics is that an MCS propagates. Tropical MCSs tend to propagate westward and the speed is faster over land than over ocean (Feng et al., 2021), specifically over Africa with a substantial speed up to $17\,\mathrm{m\,s}^{-1}$ (Hodges and Thorncroft, 1997). One of the explanations is that a cold pool at the leading edge of an MCS can trigger new convection. As a cold pool spreads out from its parent system, it lifts positive-buoyant air upward, leading to the formation of new convection. Other studies showed that low-level wind shear is as important as cold pools to explain MCS propagation (Rotunno et al., 1988; Weisman and Rotunno, 2004). With no wind shear, the MCS dissipates quickly since negative buoyancy by the cold pools is placed below updrafts. With no cold pool, a low-level wind shear tilts the MCS forward or rearward, depending on its profile. A tilted structure does not support the longevity of an MSC without a cold pool. With a rearward tilt and a cold pool, however, positive buoyancy by the cold pool occurs in the leading edge of an MCS, maintaining the propagation of the MCS (see Fig. 18 in Rotunno et al., 1988).

Tropical MCSs are often embedded within large-scale features such as the ITCZ (Khouider and Moncrieff, 2015), EWs (Mapes et al., 2006; Haertel and Kiladis, 2004; Cheng et al., 2023), tropical disturbances (Schumacher and Houze, 2006) and the MJO (Zuluaga and Houze, 2013). This indicates that MCSs are modulated by the large-scale features and affect them through changing the vertical distribution of heat, moisture and momentum. Amongst the aforementioned large-scale features, WIG1 share similar characteristics with MCSs in terms of their spatial scale and propagation speed and direction, marking the importance of wave-convection coupling (Tulich and Kiladis, 2012).

2.3.3 Convection parameterization

Convection parameterization is a method to represent the collective or averaged effects of convective motions on a large-scale environment. It calculates grid-scale variables such as convective heating and moisture tendencies from the subgrid-scale activity in a model column. Grid resolution of climate and weather models are relatively coarse to correctly resolve the process of moist convection, so these subgrid-scale processes are simulated through convection parameterization that describes its average effects on the local and large-scale variables (such as temperature, moisture and winds) on the model grid (Stensrud, 2007). The typical horizontal grid spacing for current operational global models is $O(10\,\text{km})$. The horizontal grid spacings of 13 and 9 km are used by the German Weather Service (DWD)[2] and the European Centre for Medium-Range Weather Forecasts (ECMWF)[3], respectively. Horizontal grid spacing with $\Delta x = 1$–$10\,\text{km}$ can resolve some deep convection but not all deep convection. Additionally, it is argued that horizontal resolution of 100 m would be required to accurately resolve deep convection (Kwon and Hong, 2017; Jeevanjee, 2017). Thus, the km-scale resolution is referred to as a convective gray zone (Weisman et al., 1997; Hong and Dudhia, 2012; Prein et al., 2015).

There are many convection parameterization schemes that physically represent the subgrid-scale processes in models (Arakawa, 2004) and one of its kinds is based on mass flux approaches (e.g., Tiedtke, 1989). One of the common features of these convection schemes is to evaluate CAPE at every grid point to determine whether or not convection should be triggered, as explained in section 2.3.1.

Convection paramerization largely includes three steps:

(a) triggering convection,

(b) modifying the vertical distribution of heat, moisture and momentum together with a cloud model and,

(c) determining the amount of convective heating.

Below, the numerical process of convection parameterization is demonstrated using a mass flux approach (Tiedtke, 1989), which is currently used by the NWP model by DWD and ECMWF.

The first step involves finding convective columns and testing for shallow convection and then deep convection. The LCL and the cloud top level (CTL), which can actually lie higher than the EL, are determined for shallow and deep convection. For shallow convection, the ascent is examined with strong entrainment, a process that mixes surrounding air into convective clouds. If the pressure level difference between the LCL and CTL is less than 200 hPa, shallow convection is activated. For deep convection, cloud ascent is examined with small entrainment and moisture loss. If the pressure level difference between the LCL and CTL is greater than 200 hPa, deep convection is activated. If neither of the criteria is met in a convective column,

---

[2] https://www.dwd.de/EN/research/weatherforecasting/num_modelling/01_num_weather_prediction_modells/icon_description.html

[3] https://www.ecmwf.int/en/forecasts/documentation-and-support

mid-level (congestus) convection is formed under conditions of prevalent large-scale ascent with the relative humidity being greater than 80 %. Although different types of convection can occur at the same time in reality, the scheme allows only one convection type in a time step.

The second step determines the vertical distribution of heat, moisture and momentum by incorporating a cloud model. The large-scale equations for heat and moisture contain the vertical eddy transports which are divided into contributions from convective updraft mass flux, convective downdraft mass flux and the environmental subsidence. Convective mass flux M is calculated using bulk properties of entrainment E and detrainment D as follows:

$$\frac{\partial M}{\partial z} = E - D. \tag{2.7}$$

M represents both convective updrafts and downdrafts. A simple entraining plume model is used to calculate the entrainment and detrainment as the sum of a mixing term by the turbulent exchange of mass through cloud edges and an organized term by the lateral mass exchange through large-scale convergence. For the calculation of E, the free-trospospheric humidity is considered, which improved the representation of EWs and the MJO in the NWP model (Bechtold et al., 2008). The entrainment and detrainment are used to solve the updraft and downdraft equations model level by model level. For updrafts, the iteration starts from the LCL, while the computation for downdraft mass flux starts from the level of free sink (LFS) where a saturated mixture of cloud and environmental air becomes negatively buoyant due to evaporation of cloud condensate and melting. The initial downdraft at the LFS is assumed to be proportional to the updraft mass flux at the cloud base, and then the steps are repeated from one model level to another, similarly to the updraft mass flux.

The last step of convection parameterization is to determine the total strength of convective heating which requires the estimate of the mass flux at the cloud base, which is called a convective closure. Different closure assumptions are used, depending on type of convection, determined at the first step. For deep convection, the large-scale and BL forcings generate CAPE, which is consumed by convection for stabilization over a time scale of one hour (Bechtold et al., 2014). The concept is similar to convective quasi-equilibrium in a way that a large-scale disturbance is balanced by convection (Arakawa and Schubert, 1974). The shallow convection closure assumes a quasi-equilibrium of moist static energy in the subcloud layer with an adjustment time scale of 3 hours (Grant, 2001). Lastly, the closure for midlevel convection is achieved by simply formulating the updraft mass flux at the cloud base as a product of updraft velocity and air density at the cloud base.

Precipitation is an important product of a convection scheme through a simple microphysics scheme. The total precipitation flux is obtained, considering condensation in updrafts through a saturation adjustment, evaporation in downdrafts and in the subcloud layer, and conversion from cloud condensate to precipitation which depends on updraft mass flux and velocity (Sundqvist, 1978).

There are limits to the mass flux scheme. The mass flux approach heavily relies on the single parameter of entrainment, but there is no universal formulation of entrainment rates despite many attempts by previous studies (Siebesma and Cuijpers, 1995; Lin and Arakawa, 1997; Carpenter et al., 1998). For computation of updrafts, the cloud-scale pressure gradient is neglected in the model. This suppresses upgradient momentum transport, which increases vertical shear which might be important to organize convective systems. Nonetheless, models with the mass flux approach can provide reasonable distributions of rainfall, heat and moisture (e.g., Slingo et al., 1996; Bechtold et al., 2001).

2.4   Convection-circulation coupling

Tropical circulations (section 2.1) and variability (section 2.2) are the characteristic large-scale features in the tropics, and they often have a tight link to convection. Section 2.3 demonstrated processes of moist convection, which tends to form into an organized structure, and how these processes are represented in a numerical model. One of the main tasks of convection parameterization is to represent interactions between moist convection and large-scale features. For example, spatial and temporal scales differ considerably between thunderstorms and EWs or the MJO (Fig. 2.11). The efforts to improve the multiscale interactions in the mass flux scheme include the increased sensitivity of entrainment to relative humidity for tropical variability (Bechtold et al., 2008), the consideration of BL forcing in convective instability for the diurnal cycle over land (Bechtold et al., 2014) and the improvement of convection coupled to mesoscale dynamics for rainfall features (Becker et al., 2021).

Another approach to improve convection-circulation coupling is a stochastic convection scheme, rather than the deterministic version, described in section 2.3.3. The goal of a stochastic convection scheme is to increase the variability of subgrid-scale variables on a grid column using statistical distributions. Plant and Craig (2008) adapted the mass flux scheme with statistical distributions of the occurrence of plumes and plume mass fluxes for deep convection, while Sakradzija et al. (2020) implemented probability distributions of new cloud population and lifetime mass flux for shallow convection. Bengtsson et al. (2021) suggested a stochastic cellular automata approach, in which the degree of convective organization on a grid box determines probabilities of subgrid-scale properties on its neighboring grid boxes. These stochastic methods enhance the variability of convective mass flux on a grid column.

A computationally demanding approach would be a high-resolution model with explicit convection as parameterized convection has been considered a barrier for multi-scale interactions between convection and large-scale circulations (Randall, 2013; Tomassini, 2020). Explicit deep convection shows promising results, particularly in the tropics where baroclinic instability is of little relevance for weather systems. Explicit convection captures the spatial and temporal variability of tropical rainfall more realistically compared to parameterized convection (Stevens et al., 2020). Wind-induced surface exchange of heat and moisture is also improved, as shown for the tropical Atlantic Ocean by Paccini et al. (2021). Moreover, explicit deep convection performs better in terms of convectively coupled EWs (Judt and Rios-Berrios, 2021) and gravity

wave momentum fluxes, which are often triggered by convection in the tropics and subtropics (Stephan et al., 2019).

Despite these many improvements, models with explicit deep convection do not outperform those with parameterizations in every aspect. Parameterized deep convection is in better agreement with observations than explicit deep convection in terms of mean rainfall distribution (Wedi et al., 2020). Furthermore, Becker et al. (2021) demonstrated that their new convection parameterization scheme, which improves the coupling of convection to mesoscale dynamics, outperformed explicit deep convection in terms of both mean and intensity of rainfall over tropical Africa. Some aspects of convective systems are improved with explicit convection, but deep convective and MCS systems largely deviate from satellite observations (Feng et al., 2023). These results indicate that resolving convection does not necessarily translate into the improvement of the multi-scale interactions in the atmosphere, but accurate representations of physical processes and links between them are crucial.

One can untangle these important links by employing a simple framework. Emanuel (2019), for example, presented a conceptual framework to obtain an understanding of the complex processes in the tropics. This framework is built around boundary-layer quasi-equilibrium (BLQE), the weak temperature gradient approximation, and mass and energy conservation. BLQE describes a balance of moist entropy in the subcloud layer. The balance is achieved between surface enthalpy fluxes, which transport warm, moist air into the subcloud layer, and convective downdrafts and environmental subsidence, which transport cool, dry air from the free troposphere into the subcloud layer (Emanuel et al., 1994; Raymond, 1995). The weak temperature gradient approximation neglects horizontal temperature advection implying a balance between diabatic heating and vertical advection (Sobel et al., 2001). Emanuel (2019)'s framework considers processes on a time scale longer than that associated with the redistribution of energy by internal gravity waves. A key parameter of the conceptual model is precipitation efficiency that summarizes the collective effects of turbulent and microphysical processes. Despite its relative simplicity, the framework is able to explain fundamental characteristics of the tropical atmosphere such as the exponential relationship between rainfall and column relative humidity (Bretherton et al., 2004), convective self-aggregation (Bretherton et al., 2005) and the horizontal structures of the Walker and Hadley circulations.

3 Research Questions

In the previous chapter, we have extensively examined various atmospheric phenomena linked to moist convection in the tropics. However, representing these complex processes in weather and climate models is challenging, as they require making several physical assumptions on the grid scale (e.g, parameterized convection). Therefore, it is essential to investigate how the simulations perform when moist convection processes are explicitly represented in the models. For that, the ICOsahedral Nonhydrostatic (ICON) model (Zängl et al., 2015) in the NWP configuration is used to investigate the impact of treatment of deep and shallow convection on tropical rainfall variability in this dissertation. Both realistic and idealized simulations using the ICON-NWP model are examined here to provide a comprehensive perspective on the sensitivity of tropical rainfall to the treatment of deep and shallow convection. In the following, the research questions are outlined with motivation for three main studies.

EWs control a considerable portion of tropical rainfall variability. However, weather and climate models still struggle to accurately represent EWs, and convection parameterizations are thought to be an important reason for that (Dias et al., 2018; Bengtsson et al., 2019; Lin et al., 2006). Increased computing power now enables global simulations with explicit deep convection (Satoh et al., 2017; Stevens et al., 2019). Recently, Judt and Rios-Berrios (2021) demonstrated that explicit convection produces more realistic EWs than parameterized convection using the Model for Prediction Across Scales-Atmosphere (MPAS-A; Skamarock et al., 2012) from the DYAMOND project (Dynamics of the Atmospheric general circulation Modeled On Non-hydrostatic Domain; Stevens et al., 2019), in which nine numerical models are simulated on global realistic configuration that includes continents, orography and initial and boundary conditions from reanalysis data. Here, we use ICON simulations from the DYAMOND project to examine if the results using the ICON-NWP model are consistent with the MPAS results. While the previous study used one wave filtering method, EWs in the ICON simulations are identified by using two different wave identification methods (outlined in section 2.2.4): one filtering rainfall based on space-time spectral analysis and the other projecting wind and geopotential onto theoretical wave patterns. The first part of this dissertation in Chapter 6 explores the sensitivity of simulated EWs to model configuration in realistic ICON-NWP simulations and addresses the following research questions:

> **RQ 1a** How do model resolution and convective treatment in ICON impact unfiltered precipitation patterns compared to satellite observations and MPAS?
>
> **RQ 1b** How sensitive are EWs to model configuration such as model resolution, convective treatment and model type?
>
> **RQ 1c** Are the identified EWs robust when using two complementary wave identification methods?

While Chapter 6 focuses on exploring the realistic simulations, we shift the focus to idealized simulations, i.e, tropical aquachannel simulations, in Chapters 7 and 8. The idealized simulations are designed to avoid complexity associated with continents, orography, zonal asymmetries and influences of the extratropics on the tropical conditions. The symmetric nature of configuration provides better statistics than the realistic ones, as all longitudes can be treated equivalently. The horizontal grid spacing is 13 km. The only difference among the simulations is the treatment of deep and shallow convection.

The ITCZ is a key circulation and precipitation feature in the tropics, but there has been a large spread in the representation of the ITCZ in global weather and climate models (Fiedler et al., 2020; Tian and Dong, 2020; Wedi et al., 2020). Even, idealized modeling frameworks, such as aquaplanet simulations, showed a high sensitivity of tropical rainfall to various factors (e.g., Rajendran et al., 2013). However, the reasons for that remain unclear. Here, we use a novel approach with which we disentangle different physical processes responsible for the changeable behavior of the ITCZ in numerical models. The diagnostic tool is built upon the conceptual framework developed by Emanuel (2019) based on boundary-layer quasi-equilibrium (Raymond, 1995), weak temperature gradient approximation (Sobel et al., 2001) and mass and energy conservation. The following research questions are developed to guide this part of the study in Chapter 7 that utilizes the diagnostics to analyze the idealized simulations:

> **RQ 2a** How does the mean state differ with altering the treatment of deep and shallow convection in the aquachannel simulations?
>
> **RQ 2b** What diagnostic framework is suitable to understand the differences in rainfall between parameterized and explicit convection?
>
> **RQ 2c** What processes are responsible for differences in mean rainfall in the ITCZ between the experiments?

The behavior of EWs depends on the mean state (Yang et al., 2003; Dias and Kiladis, 2014), so the thorough analysis of the mean state in Chapter 7 establishes an important first step to understand EWs in the aquachannel simulations. Moreover, rainfall variability and convectively coupled EWs are also highly sensitive to model configuration (Blackburn et al., 2013; Williamson et al., 2013; Blanco et al., 2016). This means that the sensitivity of EWs to convective treatment that we obtain using the realistic simulations in Chapter 6 does not necessarily remain the same

when using the aquachannel simulations, although both cases use the ICON-NWP model. EWs in the aquachannel simulations are identified using the complementary methods as done in Chapter 6. The final part of the study in Chapter 8 addresses the following research questions:

> **RQ 3a** What characterizes the large-scale variability of rainfall and horizontal winds in the aquachannel simulations?
>
> **RQ 3b** How strongly do EWs contribute to variability of rainfall and horizontal winds?
>
> **RQ 3c** How consistent are waves in the aquachannel simulations with their real-world counterparts?

By tackling the listed questions, we can gain insights into the fundamental dynamics of tropical phenomena and improve our understanding of EWs and their impact on climate variability, ultimately contributing to more accurate weather and climate predictions in the future.

4 Model and data

The ICON model (Zängl et al., 2015) has been developed through a joint project between the Deutscher Wetterdienst (DWD), the Max Planck Institute for Meteorology (MPI-M), the Deutsches Klimarechenzentrum (DKRZ) and the Karlsruhe Institute of Technology (KIT). The model equations are discretized on an icosahedral-triangular Arakawa-C grid which equally treats an area of a horizontal grid cell over the globe, compared to the conventional lat-lon grid. The model solves the fully compressible nonhydrostatic atmospheric equations of motion. This allows ICON to be applicable for NWP purposes from regional to global scales.

4.1 Realistic simulations

4.1.1 Simulation setup

We use global ICON simulations which were performed under the DYAMOND initiative (Stevens et al., 2019), which is the first intercomparison project of global convection-permitting models. Nine different models, including ICON and MPAS, are available, which simulated the atmosphere over the same period of 1 August – 10 September 2016. The atmospheric state is initialized on the first day at 0UTC using the global (9 km) analysis of ECMWF. Sea surface temperatures and sea ice cover are prescribed using the ECMWF daily operational data. There is no assimilation of meteorological variables.

The experiments using the ICON model version 2.1.02 follow the DYAMOND protocol which is described above. They consist of nine simulations with varying horizontal grid spacings of 2.5, 5, 10, 20, 40 and 80 km. Deep and shallow convection parameterizations (Tiedtke, 1989; Bechtold et al., 2008) are experimentally turned off for all six resolutions. For the three grid spacings between 20 and 80 km additional three runs are conducted with parameterized deep and shallow convection. The number of vertical levels is 90 with the model top at 75 km. Schemes of physical parameterization include the Rapid Radiative Transfer Model (RRTM) scheme (Mlawer et al., 1997), one-moment microphysics scheme with graupel as well as cloud water, rain water, cloud ice and snow (Baldauf et al., 2011) and interactive surface flux scheme and soil model (Schrodin and Heise, 2002). A further detailed description of the ICON model and experimental setup can be found in Hohenegger et al. (2020).

Here we briefly describe the MPAS experiments which follow the DYAMOND protocol and which we compare the ICON experiments with in Chapter 6. MPAS is a global fully-compressible nonhydrostatic model (Skamarock et al., 2012). The nonhydrostatic solver is

discretized using centroidal Voronoi meshes and a C-grid staggering. The scale-aware convection parameterization based on the mass flux scheme (Tiedtke, 1989) is incorporated in MPAS (Wang, 2022). The portion of precipitation from the scheme decreases with increasing horizontal grid resolution. Judt and Rios-Berrios (2021), for example, demonstrated that more than 70 % of precipitation in the tropics is resolved when the horizontal grid spacing is ≤ 7.5 km. (Less than 5 % of tropical precipitation is resolved with the horizontal grid spacing greater than 7.5 km.) The grid mesh and the new scheme make MPAS another useful tool to explore the atmospheric processes from regional to global scales.

Ten simulations using MPAS are available from the DYAMOND protocol. The simulations differ in horizontal grid spacing from 480 km down to 3.75 km. Rainfall variability and EWs were investigated in each MPAS simulation using a space-time filter by Judt and Rios-Berrios (2021), who demonstrated that explicit convection is key to accurately representing EWs and rainfall variability in MPAS.

4.1.2   Data for evaluation of realistic simulations

a. IMERG

The globally gridded rainfall product Integrated Multi-Satellite Retrievals for Global Precipitation Measurement (GPM) V6 final version (IMERG; Hou et al., 2014; Huffman et al., 2015) is used for rainfall. The temporal resolution of the original product is 30 minutes but we use rainfall accumulation over the past 6 hours from IMERG (0, 6, 12 and 18UTC). The high-resolution rainfall product at 0.1° is remapped to 1° lat-lon grid. The spatial and temporal resolutions for our purpose are fine enough to characterize EWs and capture MCSs. In the remainder of the dissertation, we refer to this dataset as IMERG.

b. ERA5

The global coverage wind observation data for the period covering August 1–September 10, 2016 is not available, so as observation alternatives we use the ERA5 reanalysis dataset by ECMWF (Hersbach et al., 2020). Horizontal winds and geopotential at 200 and 850 hPa are used for the spatial projection method. To construct 3D structures modulated by EWs, dynamical and thermodynamical fields (horizontal winds and temperature) on model levels are obtained from the ERA5 reanalysis dataset. ERA5 data are instantaneous fields every 6 hours and interpolated to 1° lat-lon grid.

4.2   Idealized simulations

We use version 2.6.3 of the ICON model in the NWP configuration. Radiation is computed using RRTM (Mlawer et al., 1997). A single-moment microphysical scheme is used to predict cloud water, rain water, cloud ice and snow without graupel (Seifert, 2008). A turbulent kinetic energy scheme is used for the representation of turbulent mixing and surface-to-atmosphere

transfer (Raschendorfer, 2001; Mellor and Yamada, 1982). Our model configuration closely follows the operational setup, including a full non-linear Coriolis parameter, but some aspects are different for the specific purpose of our study. The surface of the entire model domain is covered by water (aquaplanet or aquachannel simulation) to exclude complexities associated with topography and the diurnal cycle has fixed equinoctial insolation over the whole simulation period. Zonally symmetric SSTs are prescribed with a maximum of 27 °C at the equator dropping to approximately 5 °C at 60°N/S. This SST distribution has been used in other studies and is called the "Qobs" profile (Neale and Hoskins, 2000). There is no feedback of the atmosphere on the ocean and the underlying water surface, effectively making the ocean an indefinite energy source.

To spin up our aquachannel simulations, we adapt the modeling practice used in Bretherton and Khairoutdinov (2015). First we conduct a global aquaplanet simulation with a horizontal grid spacing of 40 km and a time step of 300 s. The initialization of the 40 km aquaplanet run follows the Qobs case of Neale and Hoskins (2000). The number of vertical levels is 90 with the model top at 75 km. Deep and shallow convection are parameterized using a bulk mass-flux scheme (Bechtold et al., 2008; Tiedtke, 1989). The 40 km global aquaplanet experiment is run for 120 simulation days (gray solid line in Fig. 4.1), after which the grid spacing is reduced to 26 km with a time step of 225 s and the simulation is continued for another 90 days. Finally, the model domain is restricted to a channel geometry between 30°N and 30°S and the horizontal grid spacing is reduced to 13 km with a time step of 112.5 s (black solid line in Fig. 4.1). The domain encloses the entire globe and forms a closed ring in the zonal direction. Walls closed by setting the meridional wind component to zero are introduced at the latitudinal boundaries where virtual potential temperature, water vapor mixing ratio, air density, and zonal and vertical winds are prescribed by zonally and temporally averaging them at 30°N and 30°S from the 26 km aquaplanet simulation. The prescribed variables at the closed walls are time-invariant, zonally constant but vertically variant. Except for the aforementioned quantities, all other variables are set to zero at the walls. The setup for the aquachannel run is identical to the aquaplanet runs except for the simulation geometry and the horizontal resolution. The coarser aquaplanet simulations thus serve to obtain the boundary conditions and to spin up the aquachannel run with reduced computational cost. The total simulation period of the 13 km aquachannel run is 102 days, consisting of spin-up at the beginning of 62 days and the analysis period of 40 days. The output time step is hourly. Output variables are remapped from the original triangular grid to a regular grid at 0.2° grid spacing.

To illustrate the modelling approach, Fig. 4.1 depicts the evolution of the probability density distribution of precipitable water (PW) in the equatorial belt (20 °N/S) over the entire run time from day 0 to 314. In the beginning of the 40 km aquaplanet simulation, PW is distributed narrowly around $40 \, \text{kg} \, \text{m}^{-2}$ but by day 50 the distribution has widened with a broad dry maximum around $25 \, \text{kg} \, \text{m}^{-2}$ and a narrower secondary maximum near $55 \, \text{kg} \, \text{m}^{-2}$. After that, the bimodal shape remains stable, even when the grid spacing is reduced from 40 km to 26 km on day 120. The moist maximum corresponds to the actual ITCZ region, while the dry maximum represents the large area of subsidence in the cooler outer tropics with relatively few intermediate values
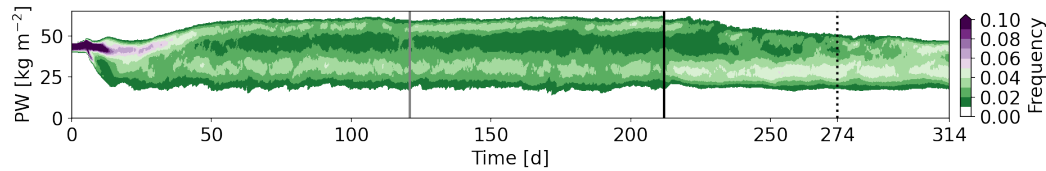
Figure 4.1: Evolution of the frequency density distribution of precipitable water in the equatorial belt between 20°N/S over a successive set of the aquaplanet and aquachannel simulations. The gray solid line indicates when the 26 km aquaplanet run begins, the black solid line when the 13 km aquachannel run begins and the dotted line marks when the analysis period of 40 days begins. Reprinted from Jung et al. (2023). ©The Authors, CC BY 4.0 ⓒⓘ

of PW in between. Such a rapid evolution into a stable bimodal structure was seen in other aquaplanet simulations with Coriolis force (e.g., Arnold and Randall, 2015; Khairoutdinov and Emanuel, 2018), as the large-scale circulation redistributes moisture from the relatively homogeneous initial conditions.

When the 13 km aquachannel experiment begins on day 210, a considerable change can be observed. The range of PW slowly decreases due to a reduction of the moist columns and an increase in the frequency of dry areas despite little change in magnitude. This drift slows down but still continues into the investigation period after day 274, suggesting that a full equilibrium has not been reached yet. Towards the end of the simulation around day 314, there are some indications of a bimodal distribution again, yet much closer to each other than in the global simulation before day 210. The reason for this behavior lies in the prescribed properties at the closed walls. While in the global configuration, the Hadley cells span over 30°N/S, in the aquachannel configuration the model creates its own limited Hadley circulation away from the walls with subsidence around 15°N/S (discussed in detail in section 7.1). The narrower overturning circulation reduces the amount of moisture converging into the ITCZ (not shown). It is also conceivable that the suppression of exchange with the higher latitudes reduces moisture uptake through surface fluxes triggered by dry intrusions from the midlatitudes (Bretherton and Khairoutdinov, 2015). Nonetheless, the PW evolution over the entire simulation period exhibits smooth transitions not only from the coarse to high resolutions but also from the aquaplanet and aquachannel geometries.

Our original intention to prescribe zero meridional wind, and constant zonal and vertical winds from the 26 km aquaplanet experiment at the rigid walls was to simulate a Hadley circulation with descending branches near 30°N/S as in the global runs, but the model develops its own Hadley circulation rather than connecting its dynamical fields with the boundaries. We suspect that a possible reason is the suppression of eddy transport between the tropics and extratropics at the boundaries, forcing the model to develop its own subtropical jets internally. Ultimately, this also leads to distortions in the fields of cloud, radiation and surface fluxes in the outer tropics. We presume that a wider channel or a two-way nested channel within a global domain would simulate jets at a more realistic location. However, the channel geometry suppresses tropical-extratropical interactions and thus reduces complexity. Furthermore, the advantage of having jets at more realistic location does not outweigh the merit of our configuration that is

Exp. name	Deep conv.	Shallow conv.
P13	On	On (deterministic)
S13	Off	On (deterministic)
SS13	Off	On (stochastic)
E13	Off	Off

Table 4.1: Treatment of deep and shallow convection schemes for each aquachannel experiment.

still able to reproduce a complex structure of dynamics and thermodynamics of the tropical atmosphere with affordable computational resource. To give as little weight as possible to the artifacts from the channel approach, we restrict our analysis to an equatorial belt between 20°N/S (corresponds to area used in Fig. 4.1). We are confident that our analysis for this area can give useful insights into how convective treatment affects ITCZ processes, at least in a qualitative sense.

We experimentally modify the representation of deep and shallow convection in the 13 km aquachannel configuration in the following way: (a) an experiment named P13 where the deterministic deep and shallow convection schemes are turned on (already shown in the context of Fig. 4.1), (b) S13 where only the deep convection scheme is turned off, (c) SS13 where the standard deterministic shallow convection scheme (Bechtold et al., 2008; Tiedtke, 1989) is replaced by a stochastic scheme (Sakradzija et al., 2015, 2020), and (d) E13 where both deep and shallow convection schemes are turned off. The different convective treatments are summarized in Table 4.1. In the stochastic shallow convection scheme, the shallow-cloud ensemble is represented based on the theory of Craig and Cohen (2006). The number of new clouds is set using a Poisson distribution and the lifetime average mass flux using a Weibull distribution. In the stochastic scheme there are two constraints: the mass flux closure of the deterministic scheme to constrain the ensemble average mass flux and the surface Bowen ratio to control the average mass flux per cloud (Sakradzija and Hohenegger, 2017). All aquachannel experiments share the same aquaplanet runs as spin-up. The different convective treatment is introduced when the channel geometry is introduced (black solid line in Fig. 4.1 at day 210). Other than the different representations of convection, the setups remain identical among the 13 km aquachannel experiments.

In Chapters 7 and 8, we analyze the last 40 days of each aquachannel experiment, i.e., after spin-up (day 274–314). For the remainder of the manuscript, the beginning of the analysis period is referred to as day 0, corresponding to the dotted line in figure 4.1.

5 Methods

5.1 Objective identification of equatorial waves based on linear theory

As outlined in section 2.2.4, we use two different wave identification methods to check the robustness of detected wave signals: one filtering rainfall using space-time filtering and the other projecting 2D horizontal winds and geopotential onto spatial patterns. Sections 5.1.1 and 5.1.2 describe the technical details of how we apply these approaches to our data.

5.1.1 Wavenumber-frequency filtering

Rainfall data is used for the WK method to identify EWs in all datasets including IMERG satellite observations and realistic (DYAMOND) and idealized (aquachannel) runs. The data padding approach slightly differs due to the availability of the observations prior to the study period, which is explained below. The wavenumber-frequency window selection for each wave type is identical for all cases, which is summarized in Fig. 5.1 and Table 5.1.

Before filtering the DYAMOND data, a latitudinal average between 5–15°N is applied to rainfall fields because rainfall mostly occurred in this latitudinal band during the study period (see Fig. 5 in Stevens et al., 2019). Additionally, this choice of the latitudinal band is consistent with Judt and Rios-Berrios (2021), who identified equatorial waves in the MPAS model from DYAMOND using the WK method. As the 40-day integration of the DYAMOND data (August 1–September 10, 2016) is rather short to apply the WK method, we use a padding method (Janiga et al., 2018) such that two-year IMERG data are padded before the simulation period and zeros afterward. To treat data consistently, the IMERG data after September 10, 2016 are also replaced by zeros for wave filtering. The padding method allows us to minimize spectral leakage (Wheeler and Weickmann, 2001). A zero-padding modification before and after the study period is applied to the DYAMOND dataset and the main conclusions do not change (not shown).

For data from the aquachannel (or idealized) simulations, a zero-padding technique is used as there is no long time integration of "observations" for the aquachannel simulations. The 40-day rainfall data of the aquachannel simulations are padded with 40-day zeros before and after, such that the total length of time after the zero-padding is 120 days for the WK method. The focus of the study is on the second chunk of 40 days when the actual data from the aquachannel runs are used to minimize spectral leakage (Wheeler and Weickmann, 2001) and maximize signals after filtering.
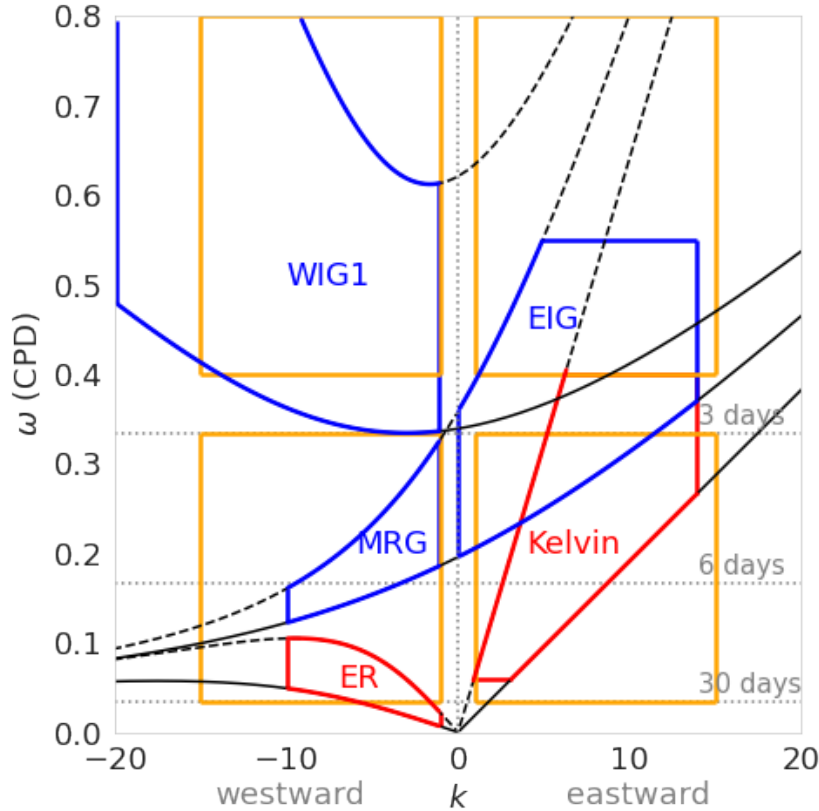
Figure 5.1: Dispersion relation of the linear wave solutions for equivalent depths of 8 m (black solid lines) and 90 m (black dashed lines). Boxes for red and blue solid lines indicate wavenumber-frequency windows for symmetric and antisymmetric waves, respectively, which are used for the WK method. The orange boxes refer to the broad windows that are used for the YP approach. See Table 5.1.

5.1.2 2D spatial projection

Knippertz et al. (2022) focused on large-scale KWs, ERs and MRGs with a broad window of periods of 2–15 days. To identify small-scale IGs, we set time windows of 3–30 days and 1.25–2.5 days for the large-scale and small-scale waves, respectively (see Fig. 5.1 and Table 5.1). The results for IG waves do not change when we cover a longer period (up to 5 days) or use 3-hourly fields of horizontal winds and geopotential.

A trapping scale y_0 of 6° is used for the ERA5 data and DYAMOND data following previous studies (e.g., Yang et al., 2003, 2021). For the aquachannel experiments, y_0 of 5° is used because it is the best compromise for the narrow channel geometry. For smaller y_0, the parabolic cylinder functions are strongly constrained near the equator. For greater y_0, the values near the equator deviate from the east- or westward moving component there.

5.2 Composite analysis

A composite technique is used to link EWs detected by the WK and YP approaches. Unfiltered rainfall is composited on the basis of the YP wave-filtered dynamical structures, and 3D struc-

	WK			YP	
	k	T [d]	h_e [m]	k	T [d]
KW	1–14	2.5–17	8–90	1–15	3–30
MRG	1–10	2.5–10	8–90	1–15	3–30
ER	1–10	6.25–96	1–90	1–15	3–30
EIG	0–14	1.82–5	8–90	1–15	3–30
WIG1	1–20	1.25–2.5	8–90	1–15	1.25–2.5
WIG2	1–15	1.25–2.5	8–90	1–15	1.25–2.5

Table 5.1: Filter windows of zonal wavenumber k, period T and equivalent depth h_e for each wave type when using the WK and YP methods

tures of unfiltered winds and temperature are composited on the basis of the WK wave-filtered rainfall.

For YP, two dynamical variables in quadrature to each other are selected to characterize the wave propagation as in Yang et al. (2021). For example, an MRG in the upper troposphere would show a theoretical spatial structure such that a maximum of equatorial northerly winds is in quadrature with a maximum of off-equatorial westerly winds and coincides with the upper-level divergence. (Note that with a first baroclinic vertical structure, the upper-level wind patterns would mirror the low-level counterpart and the sign of the divergence would be the opposite, Fig. 2.7c). Thus, as a westward-propagating MRG approaches, a person standing at the equator would observe decreasing upper-level southerly winds right above and increasing upper-level westerly winds to the north (Phase 1–3 in Fig. 5.2b). As the upper-level divergence of the wave approaches, the person observes increasing upper-level northerly winds at the equator with decreasing westerly winds (Phase 3–5 in Fig. 5.2b). With no background flow or vertical shear, the upper-level divergence, which coincides with the maximum of upper-level northerly winds, would be expected to be in phase with maximum rainfall (Phase 5). Thus, v at $0°$ and u at $10°$N are chosen for the composite analysis of MRG in the realistic simulations. Similarly, v at $8°$ and u at $0°$ are selected for ER, and v at $10°$N and u at $0°$ are selected for WIG1. As KWs do not have meridional wind components, du/dx and u at $0°$ are chosen for the composite. The exemplary selection for each type of waves using ERA5 reanalysis data, which is comparable to the realistic simulations, is summarized in Fig. 5.2. The signs and placements are carefully selected, such that a phase evolves clockwise for all east- and westward propagation and the upper-level divergence is expected in Phase 5 for convenient comparison.

For the idealized simulations y_0 is narrower than the realistic cases. Thus, different choices are made for the off-equatorial components based on the standard deviation of time and longitude fields of horizontal winds: v at $0°$ and u at $7°$N for MRG, v at $6°$ and u at $0°$ for ER, and v at
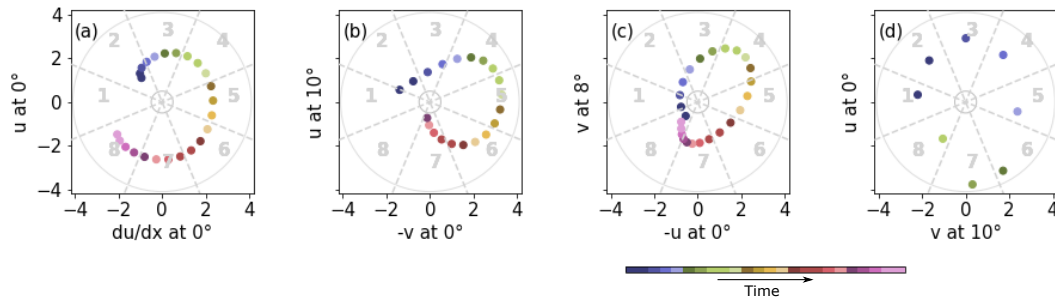
Figure 5.2: Exemplary visualization of how a composite analysis is constructed for (a) KW, (b) MRG, (c) ER and (d) WIG1 at a longitude at every 6 hours, and representative variables are denoted on the abscissa and ordinate axes. The inner and outer circles indicate when the amplitude of the wave activity is equal to a half and four standard deviations, respectively. Adapted from Jung and Knippertz (2023).

7°N and u at 0° for WIG1. KWs involve no off-equatorial components, so the same components of du/dx and u at 0° are chosen for the idealized simulations.

For WK, normalized fields of filtered rainfall and its tendency are used as in Schlueter et al. (2019), Yasunaga and Mapes (2012) and Riley et al. (2011). The filtered rainfall maximum is in Phase 5 and a phase number increases clockwise. For the composite analysis on the basis of a WK-filtered wave, the same metrics are used for all wave types.

In summary, the composites are based on eight characteristic phases for both WK and YP cases, with Phase 5 indicating maximum rainfall in WK and maximum divergence in YP. The variables of interest are averaged in each phase. For example, unfiltered rainfall is composited on a basis of a YP-filtered wave and then is averaged in each phase. This method enables to examine how the YP-filtered wave modulates rainfall.

5.3   Correlation analysis

Schlueter et al. (2019) showed that the influence of different EWs depends on time scale. Following their analysis, the variability of rainfall and horizontal winds at 200 and 850 hPa is calculated by applying a running average of one, three and seven days. Additionally, 6-hourly data is used to be compared. Thus, we obtain variability on time scales of 6 hours, one day, three days and one week. First, an average over a certain latitudinal band (0°–10°N for aquachannel simulations) is applied, and then a time average over 40 days is removed at each longitude to obtain anomalies. (The main results do not change when anomalies are first obtained and then a latitudinal average is applied.) The squared correlation coefficient between a wave signal and corresponding background variability on a given time scale is calculated at each longitude and then averaged over all longitudes. By doing so, we achieve an estimate that represents how much variability of rainfall or horizontal winds at a given time scale is explained by a certain wave type.

The correlation analysis is only applied to the aquachannel simulations since the 40-day study period limits the statistics. The zonally symmetric nature of the simulation setup allows us

to obtain a fair sample size by averaging the estimates over all longitudes in the aquachannel simulations. In contrast, the simulation period and geographical characteristics in the realistic simulations hinder meaningful statistics since each wave type has a preferable location where it is more highly correlated with variability of rainfall and horizontal winds than another location (Schlueter et al., 2019; Knippertz et al., 2022). Furthermore, time scales longer than a week imply poor sampling for correlation analysis for the aquachannel simulations. Thus, the longest time scale for the correlation analysis is set to a week.

5.4 Subjective identification of modes of variability

The WK and YP methods have their own limitations as discussed earlier in section 2.2.4. Wavenumber-frequency filtering of the WK method requires a long time integration of data, which should be longer than the period of EW of interest. While the length of the data is a minor concern for the YP method, it only identifies waves, the patterns of which are defined by the normal modes of the linearized shallow water equations on an equatorial beta plane. Thus, it is challenging to characterize the MJO (30–90 days) by applying the two wave identification methods to our datasets, which cover only 40 days.

Here we propose to identify the MJO by using its characteristic propagation speed and fluctuations in OLR, which is strongly correlated with cloudiness and precipitation. The MJO produces high amplitude signals in OLR with low and high values indicating the MJO active and suppressed phases, respectively (Hendon and Salby, 1994; Roundy, 2012; Sobel and Kim, 2012). Thus, the MJO signal is defined by lowest values of unfiltered OLR at a time step and this signal should propagate slowly eastward at around $5\,\mathrm{m\,s^{-1}}$. To find the lowest OLR values, we use a Hovmöller diagram of OLR averaged over $0°$–$10°$N. Using the detected OLR signal, we composite variables of interest, such as rainfall, horizontal wind fields, vertically integrated radiative fluxes and surface enthlapy fluxes, and compare these with the MJO characteristics from previous studies.

Additionally, we characterize KWs using raw data as for the MJO and compare the composite analysis of the MJO to that of KWs, although the latter can be more objectively carried out by using the WK and YP methods. Lowest values of surface pressure are used to characterize KWs (Milliff and Madden, 1996; Sobel and Kim, 2012). Except for that, the identification method is identical to that for the MJO.

5.5 Diagnostic for the intertropical convergence zone

This section presents the diagnostic based on Emanuel (2019)'s framework, which we apply in Sect. 7.2 to output from the four aquachannel experiments to further explore the discussed differences in rainfall and large-scale circulation.

5.5.1 Emanuel (2019)'s framework

In the framework of Emanuel (2019), the large-scale vertical velocity at the top of the BL w is written as

$$\rho w = M_u - M_d - \rho w_e, \tag{5.1}$$

where M_u and M_d are convective upward and downward mass fluxes of water vapor in kg m^{-2} s^{-1}, respectively, w_e the environmental vertical velocity away from convection, and ρ the air density at the top of the BL. Note that Emanuel (2019) uses dimensionless mass flux and vertical velocity fields, but we prefer utilizing them in physical units in order to apply the conceptual model to the simulated fields. Microphysical processes are not treated explicitly but formulated through one constant parameter, the so-called precipitation efficiency ϵ_p, which represents the fraction of all condensate that reaches the ground as precipitation. Also, ϵ_p is used to parameterize convective downdraft mass flux M_d as a function of M_u in the following way: $M_d = (1 - \epsilon_p)M_u$. For $\epsilon_p = 1$, all condensate precipitates, such that there is no evaporation and thus no downdraft mass flux. For $\epsilon_p = 0$, all condensate eventually evaporates again such that downdraft and updraft mass fluxes balance.

Moist static energy is a conserved thermodynamic variable under adiabatic processes and is defined as $h = \phi + c_p T + L_v q_v - L_f q_i$ with ϕ being geopotential, c_p the specific heat at constant pressure, T temperature, L_v the latent heat of vaporization, L_f the latent heat of freezing, q_v specific humidity and q_i specific ice content. With conservation of moist static energy, h budget for the BL becomes:

$$\int_b \left(\rho \frac{\partial h}{\partial t} + \rho V \cdot \nabla h \right) dz = F_h - \int_b \dot{Q} dz, \tag{5.2}$$

where V is the 3-dimensional wind velocity, F_h the surface enthalpy flux, $\dot{Q}$ the radiative cooling and the subscription b indicates the integral over the depth of the BL. In a well-mixed BL the vertical advection of h occurs at the top of the BL, and BLQE assumes that the injection of low-h air by convective downdrafts (M_d) and large-scale subsidence (w_e) is balanced by the uptake of high h through surface enthalpy fluxes (Raymond, 1995). Therefore, the vertical advection can be represented by a simple difference between characteristic values of h for the BL (h_b) and the free troposphere (h_m), here denoted by $h_b - h_m$. In quasi-equilibrium, the local time derivative vanishes and Eq. 5.2 becomes

$$\mathrm{d}\rho V_h \cdot \nabla h = F_h - \mathrm{d}\,\dot{Q}_b - (M_d + \rho w_e)(h_b - h_m), \tag{5.3}$$

where d is the BL height, V_h is the horizontal velocity and $\dot{Q}_b$ is the radiative cooling at the top of the BL, which is assumed to be characteristic for the entire BL, i.e., constant. In addition, advection is assumed to be approximately constant throughout the BL. Assuming that d is small, net radiative cooling at the top of the BL and the horizontal advection of h will be small and can be neglected. Then, Eq. 5.3 becomes

$$0 = F_h - (M_d + \rho w_e)(h_b - h_m). \tag{5.4}$$

The weak temperature gradient approximation implies that horizontal advection in the thermodynamic equation can be neglected, and time changes also vanish in quasi-equilibrium or steady state, such that thermodynamic balance is between vertical advection and diabatic heating (Sobel et al., 2001). In an ascending region, condensational heating is balanced by adiabatic cooling by an ascending parcel. In a descending region, of which the area fraction is far larger than an ascending region, adiabatic warming by subsidence is balanced by radiative cooling. The thermodynamic balance in the descending region can be formulated as $\rho w_e S = \dot{Q}$, where $S \equiv c_p \frac{dT}{dz} + g$ is closely related to dry static stability with g the gravitational acceleration. Using Eq. 5.1, this can be further written as

$$(\epsilon_p M_u - \rho w) = \frac{\dot{Q}}{S}, \tag{5.5}$$

which illustrates the limitation of convection by longwave cooling in the environment.

For simplicity, Emanuel (2019) assumed that the average of the tropospheric $\dot{Q}$ can be approximated with the radiative cooling at the top of the BL $\dot{Q}_b$ in order to couple the budget of h and the large-scale thermodynamic balance. Using Eqs. 5.1, 5.4 and 5.5, we can then derive a diagnostic expression for M_u as

$$M_u = \frac{1}{1 - \epsilon_p}\left(\frac{F_h}{h_b - h_m} - \frac{\dot{Q}}{S}\right). \tag{5.6}$$

Equation 5.6 demonstrates that the convective updraft mass flux increases with increasing surface enthalpy flux, with decreasing the vertical difference in moist static energy, with decreasing radiative cooling and with increasing dry static stability.

Raymond et al. (2015) suggested using a lower tropospheric quasi-equilibrium instead of the entire tropospheric adjustment because when h_b increases from its equilibrium, the lower troposphere responds to the deviation on a convective time scale. We thus average h in the lower troposphere between 0.5 and 5 km to obtain a typical value h_m, and the same layer is considered for $\dot{Q}$, which is an averaged quantity, and S, which represents the vertical gradient of dry static energy. For computing h_b, we average h from the lowest atmospheric level of 10 m to an approximate BL top of 500 m. We tested alternatives for the BL in the range from 0.4 to 1.5 km and for the troposphere from 4 to 9.5 km, and found the main findings to be rather insensitive to the exact choice of altitudes (not shown).

5.5.2 Formulation of convective updraft mass flux and precipitation efficiency

To relate this conceptual framework to the ICON model output, we need to find a relation between the modelled precipitation (either explicit or parameterized) to convective mass flux. We assume that precipitation rate Pr is directly proportional to M_u and ϵ_p:

$$\text{Pr} = \epsilon_p M_u \langle q_v \rangle \tag{5.7}$$

with $\langle q_v \rangle$ being the column specific humidity. The notation $\langle X \rangle$ indicates the mass-weighted column mean quantity, $\int \rho X \, dz / \int \rho \, dz$. In the conceptual model of Emanuel (2019), normalized Pr is proportional to normalized M_u multiplied by ϵ_p.

Using Eqs. 5.6 and 5.7, we have two unknowns, M_u and ϵ_p, because the other quantities can be readily obtained from the model output, and thus we can solve for them. In principle M_u could be calculated from w for each simulation, but the resolved vertical motions of explicit and parameterized convection contain different processes. In a convection scheme, the subgrid-scale quantities of M_u and ϵ_p are represented as their averages over a cloud ensemble on a grid column. With explicit convection, a grid column would be filled with one cloud by construction. Therefore, comparing these subgrid-scale quantities directly from the model output is a comparison of apples and oranges. The same principle applies to ϵ_p which is related to M_u. In our diagnostic, M_u and ϵ_p are not obtained directly from vertical motion but indirectly using other quantities. In this way, results are physically consistent across the experiments with different convective treatments.

Equation 5.6 is obtained by neglecting the horizontal advection in the BL. We also test the sensitivity of the diagnostic when the advection term is included. A scale analysis for the h budget of the BL (Eq. 5.3) reveals that the BL radiative cooling term can safely be ignored while the advection term is not fully negligible ($\mathrm{d}\dot{Q}_b \sim 1 \, \mathrm{W \, m^{-2}}$, $\mathrm{d}\rho V_h \cdot \nabla h \sim 10 \, \mathrm{W \, m^{-2}}$, $F_\mathrm{h} \sim 100 \, \mathrm{W \, m^{-2}}$). With this, Eq. 5.6 can be expressed as:

$$M_u = \frac{1}{1 - \epsilon_p} \Big(\frac{F_\mathrm{h} - \mathrm{d}\rho V_h \cdot \nabla h}{h_\mathrm{b} - h_\mathrm{m}} - \frac{\dot{Q}}{S} \Big). \tag{5.8}$$

where d is the BL height and V_h is the horizontal velocity. Here, only meridional advection is taken into account because BL meridional and zonal gradients are in the order of 10 and $0.1 \, \mathrm{J \, kg^{-1} \, km^{-1}}$, respectively, while BL meridional and zonal winds are comparable in magnitude. The advection term is calculated by integrating the meridional advection of h from the lowest atmospheric layer at 10 m to the BL top at 500 m, and assuming an air density of $1.2 \, \mathrm{kg \, m^{-2}}$.

5.6 Analyses of surface enthalpy fluxes

The ITCZ diagnostic (section 5.5) reveals that surface enthalpy fluxes play an important role for mean rainfall in aquachannel simulations. To understand their role in depth, we conduct further detailed analyses.

5.6.1 Decomposition of surface enthalpy fluxes

In a standard air-sea bulk formula, surface enthalpy fluxes can be written as

$$F_\mathrm{h} = \rho L_v c_E \overline{\mathrm{U}}_\mathrm{h} \Delta q + \rho c_p c_H \overline{\mathrm{U}}_\mathrm{h} \Delta T \tag{5.9}$$

where ρ is the air density at the lowest model level, L_v is the latent heat for vaporization, c_p is the specific heat at constant pressure, c_E and c_H are the surface exchange coefficient for latent

and sensible heat, respectively, $\overline{U}_h$ is the surface horizontal wind speed, and Δq and ΔT are the air-sea moisture and temperature contrasts. For our analysis, we define $\Delta q = q_*(SST) - q_v(z_1)$ and $\Delta T = SST - T(z_1)$, where $q_*(SST)$ is the saturated specific humidity for a given SST where z_1 indicates the lowest model level of the atmosphere, which equals to $10\,\text{m}$ in our case.

Surface enthalpy fluxes can be modulated by mean winds or thermodynamics and local perturbations of those components. To quantify this, the time and zonal mean of surface enthalpy fluxes are separated into mean contribution and local perturbation contribution by surface horizontal wind speed and thermodynamic variables. Assuming X is a temporally and spatially varying variable, we define $X = \{X\} + X'$ where $\{X\}$ indicates the horizontal mean (latitude and longitude) and X' the anomaly from the horizontal mean, and $X = [X] + X^*$ where $[X]$ indicates the time mean and X^* the anomaly from the time mean. If a field Y is a product of X_1 and X_2, i.e., $Y = X_1 X_2$, then $\{Y\} = \{X_1\}\{X_2\} + \{X_1' X_2'\}$ for the longitudinal mean (similarly for the time mean).

In the turbulence scheme used in ICON (Raschendorfer, 2001; Mellor and Yamada, 1982), the turbulent exchange coefficients are proportional to the turbulent kinetic energy and so we expect the coefficients to depend on surface wind speed (as well as vertical stability). This creates an overall more than linear dependence of the surface fluxes on wind speed. For simplicity, we combine the coefficients and surface wind speed, i.e., $c_E \overline{U}_h$ for the surface latent heat flux and $c_H \overline{U}_h$ for the surface sensible heat flux. Here we derive turbulent exchange coefficients from the other variables in Eq. 5.9. We set the air density in Eq. 5.9 to a constant value of $1.2\,\text{kg m}^{-2}$. Then, the surface latent and sensible heat fluxes vary with $c_E \overline{U}_h$ and Δq, and $c_H \overline{U}_h$ and ΔT, respectively. For example, a zonal mean of the surface latent heat flux can be expressed by the longitudinal mean and its fluctuation as $\{F_{\text{latent heat}}\} = \rho_s L_v \{c_E \overline{U}_h\}\{\Delta q\} + \rho_s L_v \{(c_E \overline{U}_h)' \Delta q'\}$. Thus, the zonal and time mean of F_h can be expressed as

$$
\begin{aligned}
[\{F_h\}] = \ &\rho_s L_v [\{c_E \overline{U}_h\}][\{\Delta q\}] \ + \ \rho_s c_p [\{c_H \overline{U}_h\}][\{\Delta T\}] \\
&+ \ \rho_s L_v [\{(c_E \overline{U}_h)' \Delta q'\}] \ + \ \rho_s c_p [\{(c_H \overline{U}_h)' \Delta T'\}] \\
&+ \ \rho_s L_v [\{c_E \overline{U}_h\}^* \{\Delta q\}^*] \ + \ \rho_s c_p [\{c_H \overline{U}_h\}^* \{\Delta T\}^*].
\end{aligned}
\tag{5.10}
$$

The first and second terms on the right-hand side in each row are from the surface latent and sensible heat fluxes, respectively. In the first row $[\{X_1\}][\{X_2\}]$ indicates the contributions of time and zonally averaged surface wind speed combined with the turbulent coefficients and thermodynamic effects to the time and zonal mean of F_h. In the second row $[\{X_1' X_2'\}]$ indicates a product of local fluctuations which is averaged over time and longitude, i.e., the covariance which indicates the contributions of local perturbations. In the last row $[\{X_1\}^* \{X_2\}^*]$ indicates the time mean of a product of temporal fluctuations of spatial means, which is close to near-zero (not shown). Equation 5.10 represents fields that are averaged over longitude first, and then time. Averaging, which is carried out over time and then longitude, is also tested (not shown) and does not change the results that are shown in section 7.2.1.

5.6.2 Two-dimensional histogram for latent heat flux

The latitudinal distributions of mean F_h are examined together with the method presented in Sect. 5.6.1. We here construct statistical distributions of surface horizontal wind speed, thermodynamic disequilibrium and surface fluxes (Hsu et al., 2022) to provide a complementary view. This does not require considering the turbulent exchange coefficients and allows us to examine how dependent surface fluxes are on surface wind speed and thermodynamic disequilibrium. Specifically, we ignore the surface sensible heat flux, which accounts for only about 10 % of surface enthalpy fluxes, and focus on the surface latent heat flux. Surface latent heat flux is grouped by bins of $\overline{U}_h$ and Δq to outline distributions of the variables and the surface flux in one figure. We sample the surface latent heat flux by bins of $\overline{U}_h$ and Δq at every output time step of one hour and at every grid point. The bin size for sampling is $1\,\mathrm{m\,s^{-1}}$ for $\overline{U}_h$ and $1\,\mathrm{g\,kg^{-1}}$ for Δq as in Hsu et al. (2022).

6 Results: Equatorial waves in realistic simulations

This chapter investigates the representation of EWs in state-of-the-art global convection-permitting simulations using the ICON-NWP model. The results from the simulations are compared to IMERG satellite observations and ERA5 reanalysis data for verification. First, section 6.1 illustrates Hovmöller diagrams of rainfall over the study period (1 August – 10 September 2016). Detected EWs using the WK and YP approaches are shown and qualitatively compared in section 6.2. Section 6.3 qualitatively and quantitatively links the waves identified by the two methods using composite technique.

6.1 Unfiltered rainfall

Figure 6.1 illustrates different characteristic behaviors of unfiltered rainfall from IMERG and the ICON simulations. IMERG shows well defined propagating and stationary features with large dry gaps in between, leading to an average rainfall of $0.28 \, \mathrm{mm \, h^{-1}}$ (Fig. 6.1a). There are fast westward propagating features over Africa and the downstream Atlantic as well as the eastern Pacific and indications of slow propagation over the western Pacific and Maritime Continent. In the ICON simulations (Fig. 6.1b–j) rainfall is considerably more widespread, leading to an overestimation of averaged rainfall by 10–30 %. For explicit convection (Fig. 6.1b–g), the clear westward propagation over Africa and the downstream Atlantic is well captured. However, the coarsest runs (40–80 km) unrealistically sharpen these structures, possibly due to some kind of wave-CISK mechanism (Conditional Instability of the Second Kind; Charney and Eliassen, 1964; Houze, 2004), leading to a large overestimation in mean rainfall and variance. Parameterized convection (Fig. 6.1h–j) favors rainfall over the Maritime Continent and Indian Ocean, with some indication for westward propagation. Mean rainfall and variance are relatively consistent across the parameterized runs with the latter only about half that observed.

Judt and Rios-Berrios (2021) also found an overall overestimation of mean rainfall in MPAS and an underestimation of variance with a marked degradation for parameterized convection. A noticeable difference to ICON is that in MPAS all wave propagation is weakened when parameterized convection is used, indicating an overall lower sensitivity to resolution and convective treatment in ICON that we will analyze further in the following subsections.
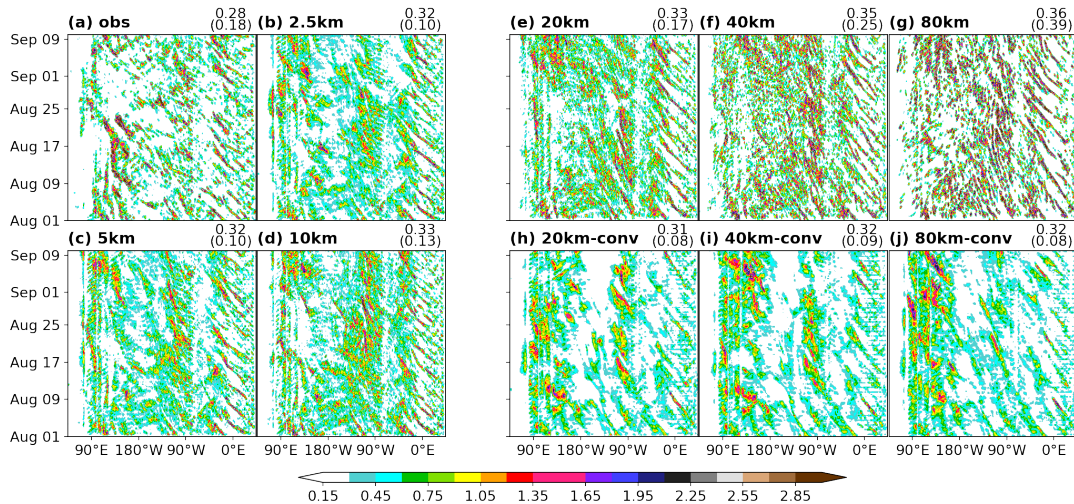
Figure 6.1: Hovmöller diagrams covering the period 1 August – 10 September 2016 of unfiltered precipitation averaged over 5–15°N [mm h^{-1}] from IMERG satellite data (obs) and ICON model simulations. Bold numbers indicate the horizontal grid spacing of each run; `conv` marks the runs with parameterized convection. The numbers on the top right denote the mean precipitation averaged over the simulation period and latitudinal belt (5–15°N) [mm h^{-1}] and their variance in time and longitude [mm^2 h^{-2}] are denoted in parenthesis. Reprinted from Jung and Knippertz (2023). ©The Authors, CC BY 4.0 ©①.

6.2 Equatorial waves

Figure 6.2 shows a superposition of the results based on WK applied to rainfall and on YP using dynamical fields at 200 hPa for the different wave types, allowing for a qualitative comparison between the two methods. In section 6.3, the WK and YP waves are linked by composite analyses. We begin with a discussion of KWs in section 6.2.1.

6.2.1 Kelvin waves

In the observations (Fig. 6.2a), several well developed KWs are discernible with propagation speeds of 10–12 m s^{-1}, particularly over the Pacific Ocean. Rainfall signals should be expected in areas of maximum upper-level divergence, and thus with easterlies shifted by a quarter wavelength to the west (and westerlies to the east, not shown). Rainfall activity in the central Pacific in late August is in fact accompanied by such anomalies, but that is not true for all KWs identified from rainfall. One possible reason is that according to theory, KWs are symmetric about the equator with maximum zonal wind anomalies and divergence there. During our study period, rainfall maxima are shifted far into the northern hemisphere, which may lead to a general mismatch between the WK and YP results.

The corresponding ICON simulations (Fig. 6.2b–f) all show KW structures in rainfall with consistent phase speed (10–12 m s^{-1}) but with some — rather unsystematic — variation in intensity and geographical occurrence. Physically consistent phase relationships to zonal wind can be detected in the simulations, broadly similar to the observations. Occasionally, KW wind signals propagate faster than the signals in rainfall (e.g. in the 20-km run with
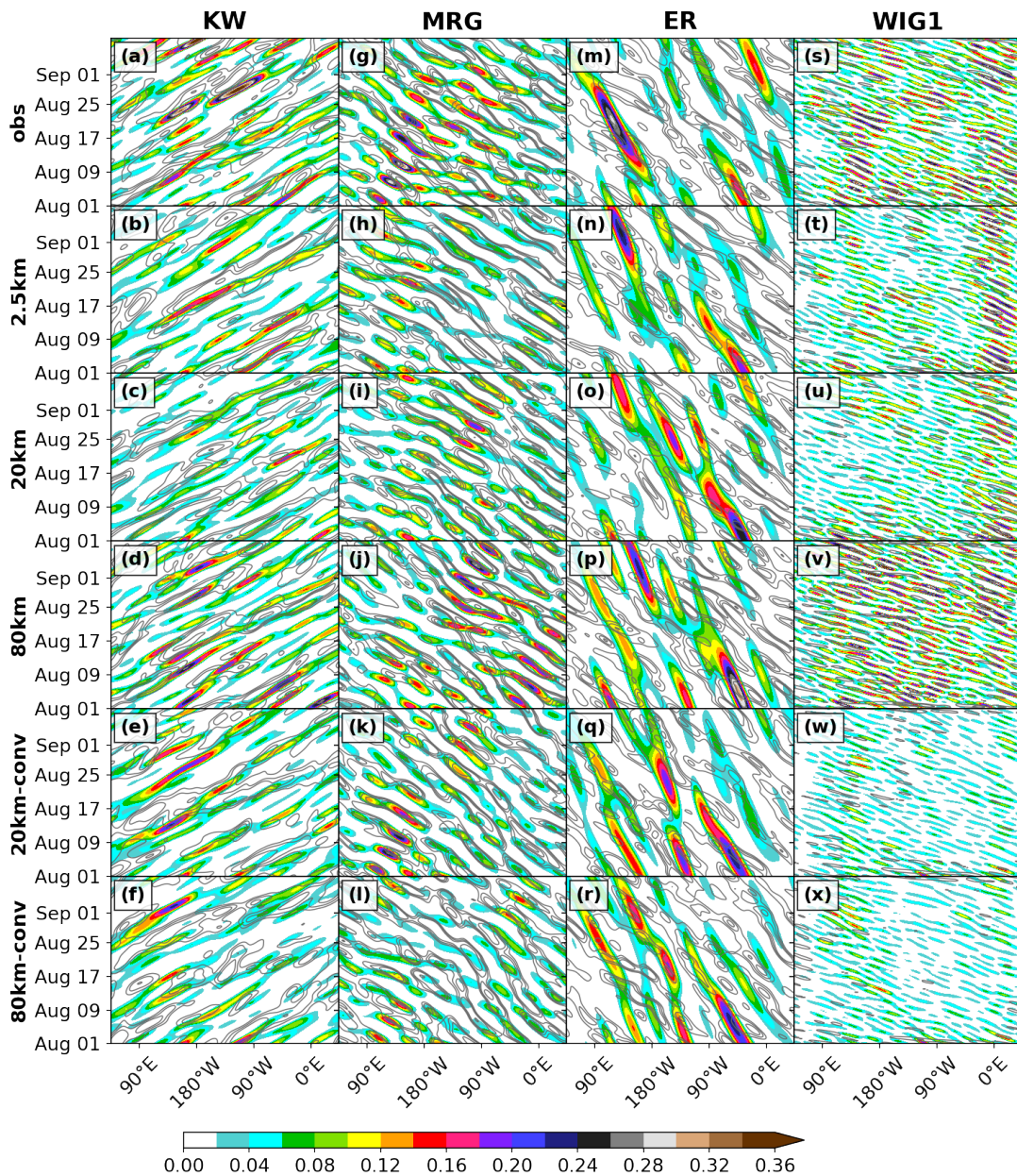
Figure 6.2: Hovmöller diagrams covering the period 1 August – 10 September 2016 of filtered precipitation averaged over 5–15°N [mm h^{-1}] (shading) and filtered upper-level wind (contour) from IMERG satellite data and ERA5 (obs), respectively, as well as corresponding ICON model simulations. The contour lines show easterly wind anomalies for KW and WIG1 and northerly wind anomalies for MRG and ER, with contours of 1, 3, 5 and 10 m s^{-1}. Bold numbers indicate the horizontal grid spacing of each run; `conv` marks the runs with parameterized convection. Reprinted from Jung and Knippertz (2023). ©The Authors, CC BY 4.0 ⓒⓘ.
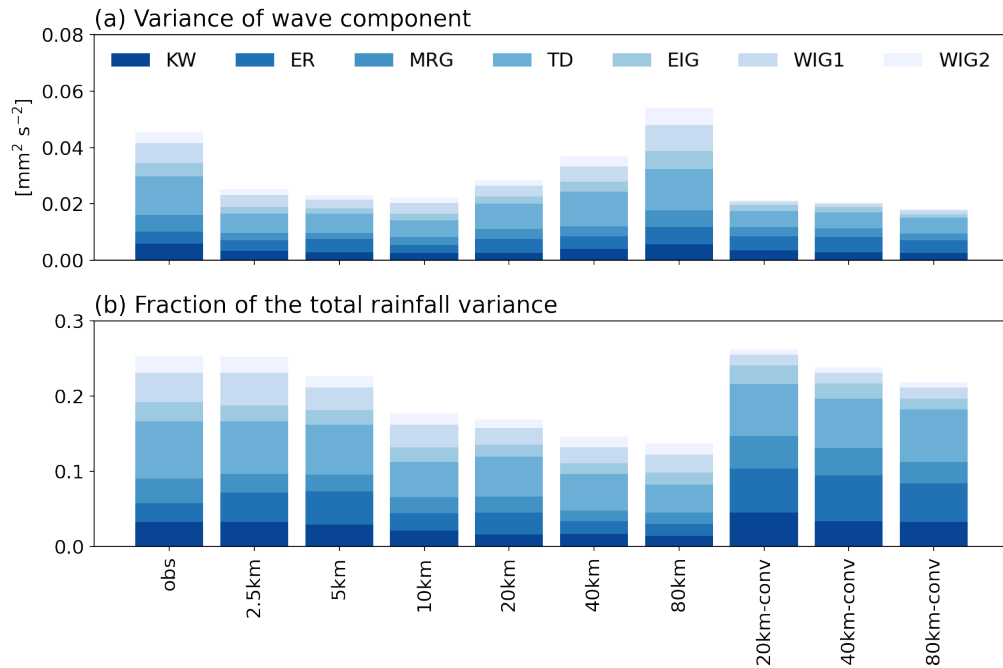
Figure 6.3: (a) Variance of WK-filtered precipitation [mm² h⁻²] for each wave type and (b) corresponding fraction of the total variance. ©The Authors, CC BY 4.0 ⓒⓘ.

parameterized convection), possibly indicating dry propagation with a larger equivalent depth. Rainfall variances of KW (Fig. 6.3a) are robust across the runs but underestimated relative to observations, except for the 80-km explicit run, while their wind variances are slightly overestimated (Fig. 6.4a). For both rain and wind, the fraction of the total variance is consistent with the observations (3–4 % for rainfall in Fig. 6.3b and 6–9 % for wind in Fig. 6.4b). An exception is for rainfall variance when the horizontal grid is too coarse to explicitly represent deep convection ($\Delta x \geq 20$ km).

6.2.2 Mixed-Rossby gravity waves

In observations MRG-filtered rainfall signals propagate westward with a fast speed of 15–20 m s⁻¹ (Fig. 6.2g). MRG activity is mostly restricted to the Indian and Pacific Oceans, and weakens in the course of the study period. There are also indications for a slow eastward group propagation consistent with MRG theory. MRG rainfall signals tend to move faster over the Pacific than Indian Ocean, which may be associated with a Doppler shift caused by the opposing low-level winds related to the Walker circulation (Takasuka et al., 2019). The theoretical structure of an MRG as used in YP implies that equatorial northerlies are accompanied by divergence at 10°N, favoring convection there. This is consistent with Fig. 6.2g showing frequent overlap between northerly wind anomalies and enhanced rainfall in 5–15°N. The propagation speeds of MRG identified by the YP method are largely consistent with those by the WK method.

MRGs in the ICON runs (Fig. 6.2h–l) largely agree with those in the observations in terms of their phase speed and wind-rain relation, but there are also some considerable differences. The
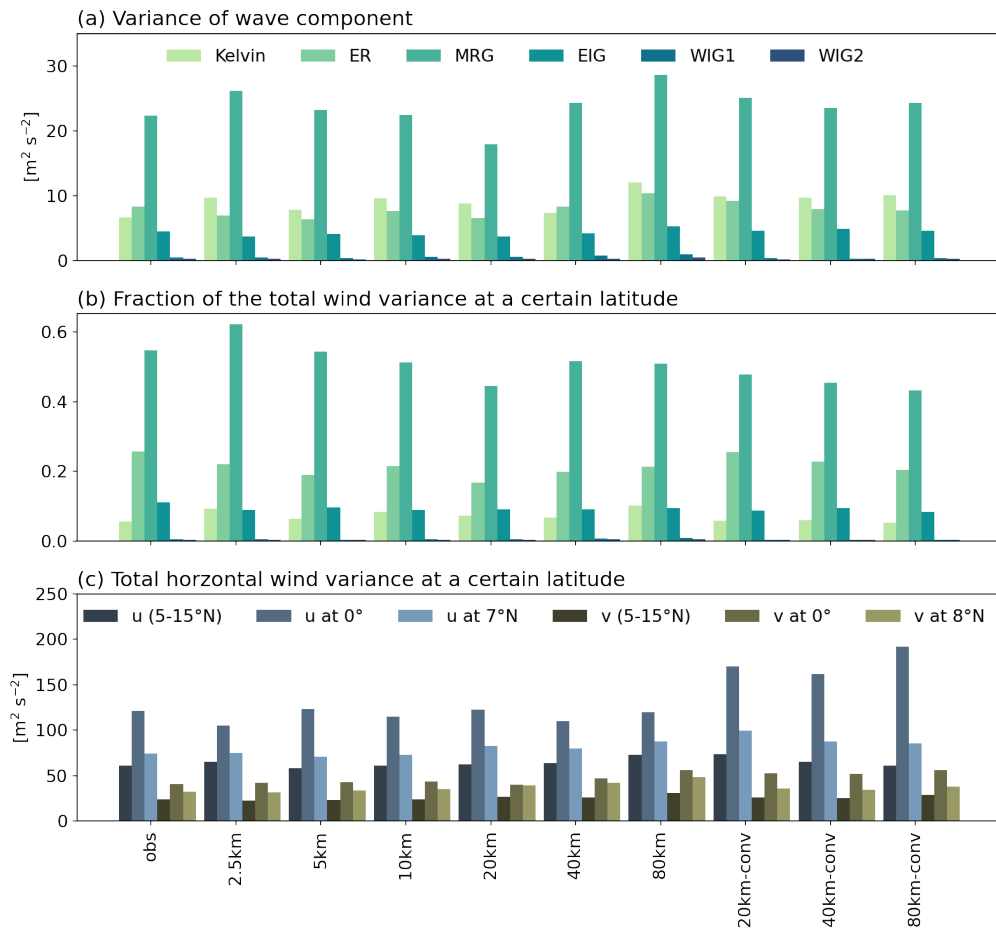
Figure 6.4: (a) Variance of YP-filtered 200-hPa zonal (*u*) or meridional (*v*) wind at a reference latitude and YP-filtered horizontal wind at 200 hPa [$m^2 s^{-2}$] and (b) corresponding fraction of the horizontal wind variance (KW: *u* at 0°, ER: *v* at 8°N, MRG: *v* at 0°, EIG: *v* at 0°, WIG1: *u* at 0°, WIG2: *u* at 7°). (c) Total horizontal wind variance at the reference latitude and latitudinal band averaged over 5–15°N. ⓒThe Authors, CC BY 4.0 ⓒⓘ.

20-km parameterized run matches better with the observations than the 2.5-km run in terms of geographical locations of rainfall activity and fraction of the total rainfall variance (Fig. 6.3b). The other runs show various deviations from the observations, including an eastward shift of the activity (even all the way to Africa in the 80-km explicit run) and a mismatch of rain and wind propagation in the 80-km parameterized run. These differences demonstrate that high resolution and explicit convection are no simple cure to representing EWs and that it is the subtle coupling of dynamical and thermodynamical effects that need to be represented well in the model.

6.2.3   Equatorial Rossby waves

Figure 6.2m shows ER identified in observations by the two methods. Five significant signals in rainfall can be detected to propagate westward with a speed of 3–5 m s^{-1}, with an outstanding signal over the Indian Ocean in the middle of the investigation period. According to the ER spatial structure used in YP, meridional wind at 8°N coincides with divergence around this latitude and thus should favor convection. However, this relationship is hardly evident from Fig. 6.2m, where the wind signals propagate much faster (10–12 m s^{-1}). This may be related to wave variability coupled to convection in WK and uncoupled in YP. Also, the Asian summer monsoon might influence the meridional structures of ER. Finally it is worth noting that the lower limit for wave periods is 6.25 days for WK and 3 days for YP, such that fast signals are suppressed by the WK filter.

Interestingly, the explicit runs (Fig. 6.2n–p) consistently show a very similar behavior, i.e., marked individual events at almost all longitudes with a slow propagation in rainfall and a fast propagation in winds. In contrast, parameterized convection generally exhibits a closer alignment in propagation between wind and rainfall (Fig. 6.2q–r). Furthermore, ER significantly contributes to the total rainfall variance in the parameterized runs (5–6 %), even more than for the observations (2 %) (Fig. 6.3b). This indicates that somehow parameterized convection responds more sensitively to the rotational (or balanced) flow of ERs than the more chaotic explicit convection (Raymond et al., 2015). Nevertheless, the results from the explicit runs closely match the observed variability and propagation speed.

6.2.4   Westward inertio-gravity waves

Finally for WIG1, the observations (Fig. 6.2s) show strong and frequent rainfall signals over the Maritime Continent, downstream of Africa and occasionally elsewhere with 4 % contribution to the total rainfall variance (Fig. 6.3b), while the corresponding u wind signals based on YP are very weak with 0.4 % contribution (Fig. 6.4b). (WIG2 shows the same tendency of strong rainfall signals but weak wind signals, Figs. 6.3 and 6.4). This strongly suggests that the signals WK identifies do not show theoretical dynamical structures (further discussed in section 6.3).

For WIG1, the ICON runs show a significant difference of rainfall signal between explicit and parameterized convection. For the former WIG1 contributes 2–4 % to the total rainfall variance and for the latter only 1 % (Fig. 6.3b). Explicit runs with 2.5- and 20-km grid spacing

show a strong activity over the African-Atlantic area but not over the Maritime Continent. The 80-km run with explicit convection has unrealistically strong signals at all longitudes, as already evident in the unfiltered rainfall. Moreover, in all ICON runs WIG1 hardly contributes to the total equatorial meridional wind variance ($< 1\,\%$ in Fig. 6.4b). It is therefore questionable if WK isolates random small-scale features of rainfall as WIG1. We address this with composite analyses in section 6.3.

6.2.5   Comparison to results using another model

The results described above have shown that the relationship between EWs, model resolution and convective treatment are complex in ICON. To first order, ICON consistently produces KW, MRG and ER signals across all considered resolutions and convective treatments, despite underestimation of rainfall variance, and variations in geographical distribution and wind-rain relationship. An exception is the somewhat unrealistic 80-km run with explicit convection that produces large wave-related variance in rainfall but a low relative contribution by EWs. Only WIG1-filtered rainfall demonstrates a fundamental difference between explicit and parameterized runs with the latter showing very little activity overall. Again, the 80-km explicit run appears somewhat overdoing activity.

How does that relate to the results of Judt and Rios-Berrios (2021)? For KW, they found that convective parameterization slows down the propagation speed, which we do not observe for ICON. This means that to represent KW, MPAS benefits from resolving convection, while little sensitivity is found in ICON. In MPAS, MRGs are consistent across different model configurations with some variations in variance, geographical maxima and propagation speed, broadly similar to our findings. For ER, they also found rather consistent results across all model configurations in close agreement with ICON. Finally WIG1 in ICON confirms a behavior shown in MPAS that associated rainfall signals are very weak with parameterized convection, while explicit convection emphasizes the activity over Africa and the Atlantic. (This geographical preference is also observed in tropical depression in both models, see Fig. B.1.) Why the phase speed and variance of KW are more robust in ICON than in MPAS is unclear, as both in principle use a similar convection scheme (Tiedtke, 1989) but only the latter adapts the portion of parameterized convection depending on grid resolution (Wang, 2022). It is possible that couplings with other parameterizations or with the dynamical core create this difference but such links are hard to disentangle.

6.3   Composite analysis

Previously, section 6.2 has revealed some striking differences between EWs detected using WK applied to rainfall and using YP applied to dynamical fields. Here we link the two methods using compositing techniques to shed some light into the structures of the identified signals. We concentrate on MRGs, for which we saw a good correspondence in Hovmöller diagrams, and WIG1 with very little wind signals overall. (The entire analyses can be found in Figs. B.4– B.7.)
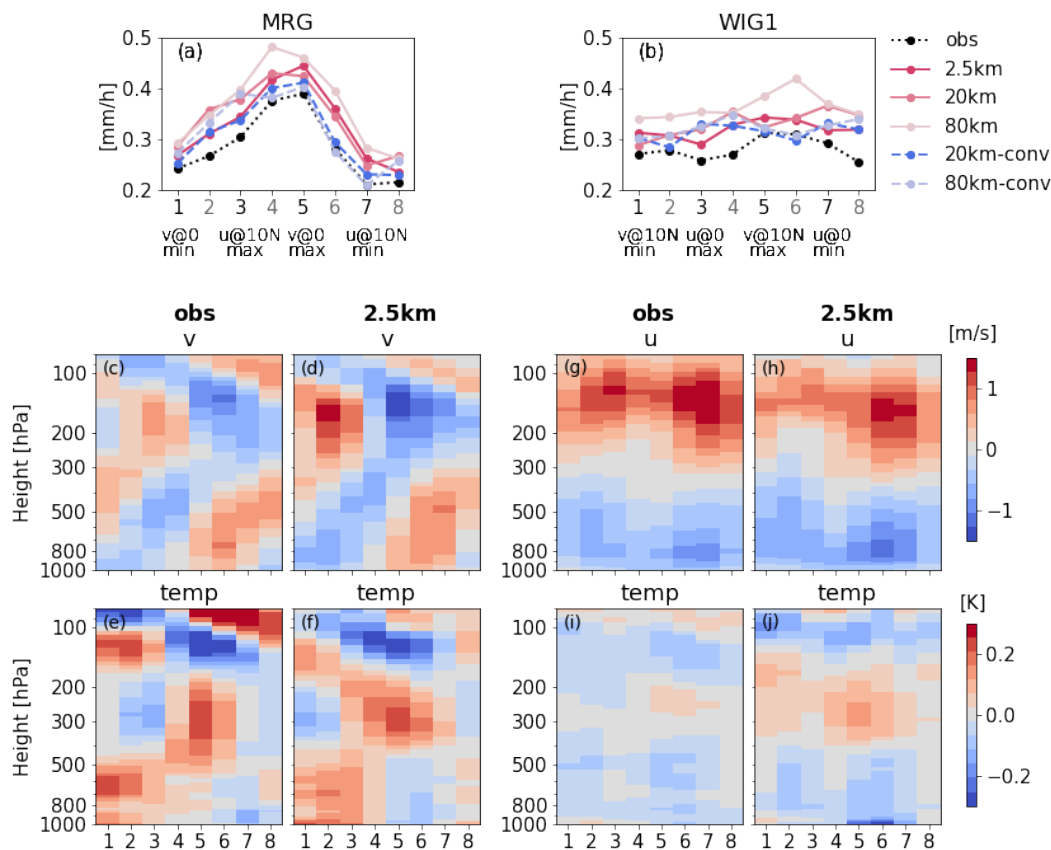
Figure 6.5: Composite of unfiltered rainfall on the basis of (a) MRG and (b) WIG1 wave phase identified by the YP method. Composite of unfiltered horizontal wind and temperature anomalies on the basis of (c–f) MRG and (g–j) WIG1 wave phase identified by the WK method. Composited variables are averaged over 5–15°N. Reprinted from Jung and Knippertz (2023). ©The Authors, CC BY 4.0 ⓒⓘ.

Using the wind fields of YP as the basis, we can see a strong modulation of rainfall through MRGs (Fig. 6.5a). The amplitude is similar across all configurations but shifted to higher values in ICON compared to IMERG. Maxima occur in Phase 5 (equatorial northerlies), as predicted by theory, in all runs but the two coarse-resolution explicit runs, where it occurs in Phase 4. This demonstrates that despite some subtle differences in the Hovmöller diagrams the mean relationships are robust. In strong contrast, the corresponding analysis for WIG1 (Fig. 6.5b) shows no meaningful variation and inconsistencies between the model configurations, likely related to the overall weak wind signals.

When we take the opposite perspective and composite meteorological fields averaged over 5–15°N on the basis of wave phases from WK-filtered rainfall at the same latitudes, robust MRG structures become evident. For the wet Phase 5, northerly wind anomalies at 200 hPa are found (Fig. 6.5c) as theory predicts. Wind structures then tilt towards lower phases below and above that level, forming an elbow structure. The corresponding analysis for temperature (Fig. 6.5e) shows a baroclinic structure with warm anomalies in the lower troposphere before Phase 5 and at 300 hPa in Phase 5 with an opposite tilt in the lower stratosphere. These vertical structures

resemble those described in other observational studies (Wheeler et al., 2000; Kiladis et al., 2009).

The vertical structures of wind and temperature from the 2.5-km run correspond well to those in the observations despite an underestimation of the lower-stratospheric temperature anomalies (Fig. 6.5d and f). The other runs also exhibit realistic vertical structures (Fig. B.4), indicating that MRG-rainfall coupling is produced well by ICON, irrespective of convective treatment and wave-identification method.

For WIG1 both observations and the ICON model show a weak modulation of temperature and zonal wind with the wave phase based on WK-filtered rainfall (Fig. 6.5g–j). If WIG1 existed during the study period, the composite analyses would present some sinusoidal patterns as for MRG. An intriguing point is that the associated signals are not small but show a westerly anomaly at high levels and an easterly anomaly at low levels, while the temperature shows a trimodal structure (cold-warm-cold). Such structures are typical for African Easterly Waves (Kiladis et al., 2006), which are active during this time of year over the area where we find WIG1 (Fig. 6.2). These environmental conditions are typical for the formation of westward moving mesoscale convective systems (MCSs), the rainfall signature of which then projects into the WIG1 wavenumber-frequency window without showing the corresponding dynamical structures. The modulations indeed are consistent with this interpretation. After the rainfall maximum in Phase 5, low-level easterlies increase, caused by downward momentum transport from the African easterly jet. Meanwhile, low-level cooling is caused by cold pools and midlevel heating by latent heat release in the stratiform part of the MCS. It is well known that models with parameterized convection struggle to realistically represent the complicated convective dynamics of MCSs (Marsham et al., 2013; Pantillon et al., 2015; Pante and Knippertz, 2019).

6.4 Summary and discussions

Judt and Rios-Berrios (2021) reported that resolved deep convection provides more realistic simulations of EWs, particularly the inertio-gravity type of waves, than parameterized deep convection in the MPAS simulations from DYAMOND (Stevens et al., 2019). Inspired by their work, we have characterized EWs in the corresponding ICON simulations by employing a combination of two different filtering approaches for a robust comparison of EWs: one based on a wavenumber-frequency method using rainfall (Wheeler and Kiladis, 1999) and the other based on a spatial-projection method using upper-level wind and geopotential (Yang et al., 2003) (see detail in section 5.1).

The main conclusions are summarized as follows:

1. All ICON runs produce westward propagating features in unfiltered rainfall, broadly corresponding to observations. Compared to the observations, ICON produces more widespread rainfall patterns, leading to an overestimation of mean rainfall, which was also found for MPAS. Rainfall variance is underestimated for parameterized convection but overestimated for the experimental coarse-resolution explicit ICON runs ($\Delta x > 20$ km).

A discernible distinction between the two models is that the westward propagation was suppressed for parameterized convection in MPAS (Judt and Rios-Berrios, 2021).

2. In the ICON model, KW, MRG and equatorial ER waves are largely consistent in terms of propagation speed and variance, irrespective of resolution, convective treatment and wave-identification method. Wave-related variances in rainfall are generally underestimated, but their contributions to the total rainfall variance is realistic, except for the explicit runs with coarse resolutions ($\Delta x \geq 20\,\mathrm{km}$). Variances in horizontal winds are consistent with the observations. Furthermore, we demonstrate that MRG robustly modulates rainfall and vertical structures of winds and temperature. Our results of wave-filtered rainfall largely agree with Judt and Rios-Berrios (2021) but KW phase speed is less sensitive to model configuration in ICON than MPAS.

3. Westward inertio-gravity waves (WIG1) exhibit a big difference between explicit and parameterized convection in both ICON and MPAS when using the WK approach. However, their wind signals (YP) are very feeble, irrespective of convective treatment, indicating no corresponding dynamical structure of WIG1. A composite analysis, which links the two approaches, reveals that this spurious signal is not a classical EW but likely signal from mesoscale convective systems, amongst others associated with African Easterly Waves, which are in fact better represented with explicit convection, as previous studies have shown.

Given the limited simulation period available, the main conclusions presented here may not hold for other seasons, as each wave type has its own annual cycle (Wheeler et al., 2000). Slow-moving waves such as ER in particular might be different over a longer time integration. A new generation of convection-permitting climate models will become available for better sampling in the foreseeable future (Palmer and Stevens, 2019). Despite these caveats, our application of both the WK and YP tools ensures detected EWs from two complementary perspectives and helps avoid misinterpretation of signals from one method (see Knippertz et al., 2022, for a detailed discussion). The robustness of large-scale EWs to model configuration in ICON is encouraging. This bodes well for a successful use of ICON in different resolutions for weather and climate predictions in the future.

7   Results: Mean state in idealized tropical aquachannel simulations

The previous chapter presented the sensitivities of EWs to model configuration in the realistic ICON-NWP simulations. In this chapter, we move our attention to the idealized ICON-NWP simulations which are another valuable tool to understand the complex system. Our simulations involve the tropical aquachannel configuration with full-blown physics and vary with different treatments of deep and shallow convection (described in section 4.2). This chapter explores the mean state of aquachannel simulations with a particular focus on rainfall using a novel diagnostic, described in section 5.5 before we delve into EWs in the aquachannel simulations in Chapter 8.

7.1   Mean state

To illustrate the overall structure of our experiments, this section presents an analysis of precipitation and circulation features for the last 40 simulation days.

7.1.1   Rainfall

The latitudinal distributions of zonally and time averaged precipitation are shown in Fig. 7.1a for the four different convective treatments. All experiments present a distinct ITCZ region with high mean precipitation concentrating between 5°N/S, where the SST maximum is prescribed. Explicit deep convection (S13, SS13 and E13) yields greater mean precipitation in the ITCZ than parameterized deep convection (P13) by about 35 %. (Between 5°N/S the time and zonally averaged precipitation is 7.28, 9.86, 9.73 and 9.84 mm d^{-1} for P13, S13, SS13 and E13, respectively.) P13 also produces a narrower, more pointy rainfall distribution. The treatment of shallow convection does not appear to have a large influence on the ITCZ structure. Outside of the ITCZ or the outer tropics, the overall rainfall amount and the differences between the experiments are relatively small. Rainfall decreases to less than or equal to 1 mm d^{-1} at around 10°N/S and beyond this slightly increases with latitude. This pattern of rainfall in the outer tropics is also observed in other aquaplanet, aquachannel and aquapatch simulations (e.g., Nolan et al., 2016; Rios-Berrios et al., 2022). It is due to rainfall embedded in filaments of high PW being sheared off from the ITCZ into the outer tropics (see Figs. B.8 and B.9).
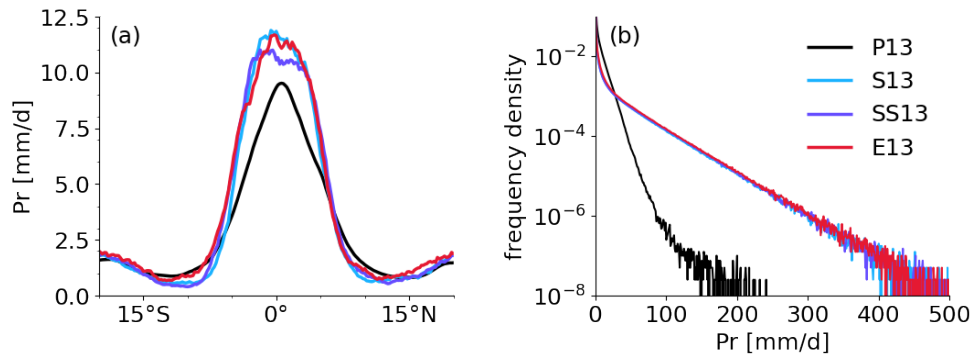
Figure 7.1: Distributions of (a) time and zonal mean of precipitation rate (Pr) and (b) precipitation intensity between 20°N/S. For the intensity distribution daily precipitation is grouped in model grids with the bin size of $1\,\mathrm{mm\,d^{-1}}$. Note the logarithmic vertical axis in (b). Reprinted from Jung et al. (2023). ©The Authors, CC BY 4.0

The rainfall intensity distribution further underlines the substantial difference between explicit and parameterized deep convection (Fig. 7.1b). Light and moderate rains ($< 30\,\mathrm{mm\,d^{-1}}$) occur more frequently in P13 than the others, which produce extreme rainfall rates of $400\,\mathrm{mm\,d^{-1}}$ and more, leading to the overall larger precipitation in the ITCZ. Correspondingly, Figs. B.8 and B.9 depict that large-scale systems of precipitation with weak intensity are formed in P13, whereas intense, localized storms are formed in S13, SS13 and E13. The much higher intensities also lead to a more wiggly zonal average as shown in Fig. 7.1a. It is speculative that extreme rainfalls with explicit deep convection are due to underresolved convective heating and mixing at 13 km grid spacing, generating strong updrafts and consequently extreme rainfall to remove instability in columns, which is somewhat in line with grid-point storms but rather found in convection parameterizations (Giorgi, 1991; Scinocca and McFarlane, 2004; Chan et al., 2014). This difference in rainfall intensity between parameterized versus explicit deep convection was also observed in realistic simulations (Pante and Knippertz, 2019; Judt and Rios-Berrios, 2021; Becker et al., 2021).

7.1.2 Dynamical structure

Figure 7.2 shows a cross section of the time mean meridional-height mass stream function and zonal wind. The meridional-height mass stream function is calculated by integrating the meridional wind from the surface level to a certain altitude. Volumetric flux is conserved along a line of a constant meridional-height mass stream function. P13 features a largely equator-symmetric troposphere-deep Hadley circulation with low-level convergence and corresponding upper-level divergence in the ITCZ (Fig. 7.2a). The remaining small asymmetries, which occur despite the symmetric nature of our simulation setup, are a further indication that the simulations may not have fully reached equilibrium. The descending branches occur around 15°N/S, which is narrower than the climatological Hadley circulation in the real atmosphere (Webster, 2020b) and in global aquaplanet simulations (not shown). The narrower Hadley circulation in the aquachannel experiments is because the exchange between the tropics and extratropics is suppressed at the closed walls of the tropical channel (discussed in section 4.2).
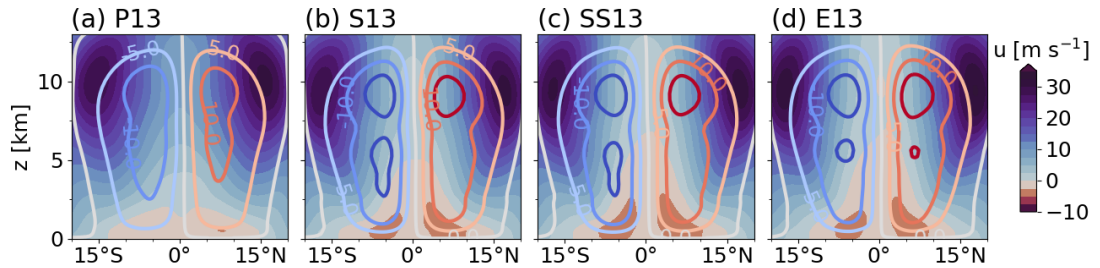
Figure 7.2: Time and zonal mean of zonal wind $[\mathrm{m\,s^{-1}}]$ (shading) and meridional-height mass stream function $[10^{10}\,\mathrm{kg\,s^{-1}}]$ (contour lines) for the analysis period in (a) P13, (b) S13, (c) SS13 and (d) E13. The interval for the colored contours is $5 \times 10^{10}\,\mathrm{kg\,s^{-1}}$. Reprinted from Jung et al. (2023). ©The Authors, CC BY 4.0 ⓒⓘ

Strong westerly upper-tropospheric jets occur at the outer edges of these narrow Hadley cells reaching an averaged speed of $30\,\mathrm{m\,s^{-1}}$. These in principle resemble the subtropical jets of the real atmosphere but shifted closer to the equator and weaker. The low-level easterly trade wind belt starts at about 14°N/S and reaches about 2 km, above which westerlies dominated. This creates a considerable westerly shear for the ITCZ convection (see Figs. B.8 and B.9).

The other experiments (Fig. 7.2b–d) generally produce similar large-scale dynamical features as P13. However, the overturning circulation and accompanying jets are strengthened. The maximum value of the mass stream function is 1.3×10^{11}, 1.81×10^{11}, 1.82×10^{11} and $1.84 \times 10^{11}\,\mathrm{kg\,s^{-1}}$ for P13, S13, SS13 and E13, respectively. This means that volumetric flux is greater with explicit deep convection, indicating stronger large-scale circulation. The strength of the simulated circulation is in agreement with other aquaplanet studies (Medeiros et al., 2016; Rios-Berrios et al., 2020), but P13 is at the lower end of the range found in the other studies. The stronger large-scale circulation with explicit deep convection is accompanied by stronger trade winds, with an increase of surface wind speed to about $4\,\mathrm{m\,s^{-1}}$. Such an increase of surface winds was also shown by a study using the ICON-NWP in a realistic setup (Paccini et al., 2021). Furthermore, the runs with explicit deep convection exhibit equatorial easterlies in the middle troposphere up to 5–7 km, while P13 exhibits equatorial westerlies there. Possibly the explicit deep convection produces more upward convective momentum transport. This mechanism may also weaken the westerlies in the upper troposphere, leading to an overall much enhanced horizontal wind shear compared to E13. The vertical shear in contrast is reduced in the ITCZ with potential consequences for the movement and organization of convective systems (see Figs. B.8 and B.9). There are some subtle differences in the strength and depth of the trade wind layer, supporting the idea that vertical momentum transport may play a role.

Another interesting aspect is that the runs with explicit deep convection (S13, SS13 and E13) generate a bimodal structure in the mass stream function, indicating a secondary shallow circulation that diverges polewards at around 7.5 km (Fig. 7.2b–d). We speculate that this could be related to a better representation of the convective lifecycle comprising shallow, congestus and cumulonimbus clouds (Johnson et al., 1999; Khairoutdinov et al., 2009), which is not the case for P13 (not shown). Local temperature gradients due to stronger net cooling by congestus
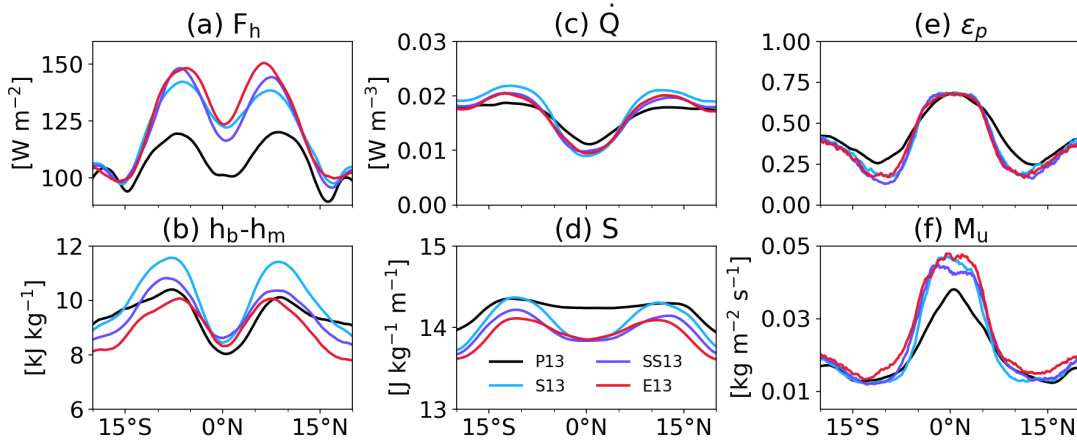
Figure 7.3: Time and zonal mean of (a) the surface enthalpy flux, (b) the vertical difference in moist static energy, (c) the lower tropospheric radiative cooling, (d) the dry static stability, (e) estimated precipitation efficiency and (f) estimated convective mass flux. Reprinted from Jung et al. (2023). ©The Authors, CC BY 4.0 ⓒⓘ

clouds in the vicinity of the ITCZ might create horizontal pressure gradients, which can in turn generate the secondary circulation. Furthermore, freezing and melting are substantial at around this level, which can be another source of local temperature gradients. As for P13, smaller hemispheric asymmetries are evident in the mass stream function and zonal wind for S13, SS13 and E13, indicating remaining imbalances.

Overall, the analysis in this and the previous subsection reveals that physically consistent differences in precipitation amount and the large-scale circulation exist between explicit and parameterized deep convection with only smaller modulation by the treatment of shallow convection.

7.2 Understanding differences in mean state

Section 7.1 showed substantial differences in the mean state among the different convective treatments, mainly between parameterized and explicit deep convection. Section 5.2 presented a diagnostic tool to compare these differences in a fair manner. Here we apply the diagnostic to averaged fields over the last 40 simulation days with a particular focus on mean rainfall. Given the zonal symmetry of our tropical channel, we will mostly consider zonal means. Figure 7.3 shows each quantity in Eq. 5.6 for the four different convective treatments. In the following, we will discuss the different aspects of the conceptual model one after another: Surface enthalpy fluxes (section 7.2.1), vertical structure of moist static energy (section 7.2.2), radiative cooling (section 7.2.3), stability (section 7.2.4), precipitation efficiency and convective mass flux (section 7.2.5), and finally meridional advection in the BL (section 7.2.6).

7.2.1 Surface enthalpy fluxes

The time and zonal mean of surface enthalpy fluxes is shown in Fig. 7.3a. P13 has F_h maxima in the trades and a local minimum in the ITCZ (black line in Fig. 7.3a), similar to the situation over real-world tropical oceans but confined to a narrower latitudinal stretch. The other experiments with explicit deep convection (S13, SS13 and E13) share similar latitudinal distributions but F_h increases compared to P13, in particular between 10°N/S (by 20–25 %). Note that shallow convection is represented by the deterministic shallow convection scheme for S13, by the stochastic shallow convection scheme for SS13 and explicitly for E13 (section 4.2). This indicates that the main difference in F_h is due to the treatment of deep convection rather than shallow convection. This is consistent with the differences in Hadley circulation and thus surface winds discussed in section 7.1.2. The difference between explicit and parameterized convection remains smaller outside of the subsidence region (about 15°N/S) than in the inner tropics. To investigate whether also thermodynamic effects play a role for these differences in surface enthalpy fluxes, we conduct a more detailed analysis. We decompose surface fluxes into their contributing factors and examine their statistical distribution.

a. Decomposition of surface fluxes

Figure 7.4a–c shows zonally and time averaged values of the individual terms of Eq. 5.9. The surface wind speed (Fig. 7.4a) mirrors the patterns in surface enthalpy fluxes (Fig. 7.3a) with maxima in the trade winds and with minima at the equator and in the area of the subsiding branches of the Hadley cells (Fig. 7.2). Winds then increase again further away from the equator. P13 shows considerably weaker surface winds by about $1\,\mathrm{m\,s^{-1}}$ than the other three runs out to about 10° from the equator, while the agreement in the rest of the domain is remarkably good. The treatment of shallow convection appears to have a rather small influence on surface winds.

The moisture contrast shows a much smoother latitudinal distribution and considerable contrasts between all four simulations (Fig. 7.4b). In P13 Δq is almost constant around $6.60\,\mathrm{g\,kg^{-1}}$ within 15°N/S and then sharply falls off towards higher latitudes as q_* quickly drops at these latitudes. The explicit treatment of deep convection (S13, SS13 and E13) appears to allow for more vigorous downdrafts injecting dry air from the mid-troposphere into the BL. In contrast to other fields discussed so far, the treatment of shallow convection also plays a significant role. S13, which uses the same shallow convection scheme as P13 but no parameterization of deep convection, shows only slightly enhanced Δq, particularly in the trade wind zone, where shallow mixing is important. The change to the stochastic treatment (SS13) from the deterministic treatment (S13) has little effect in the moist ITCZ area but further enhances Δq in the trades, eventually lining up with E13 at around 10°N/S.

Figure 7.4c shows that for ΔT the latitudinal structure and dependence on convective treatment is complex in contrast to the other two surface properties. All simulations have a local maximum at the equator, probably related to cool downdrafts from convection, but some have prominent maxima near the subsiding branches of the Hadley cells before all runs show a drop-off towards
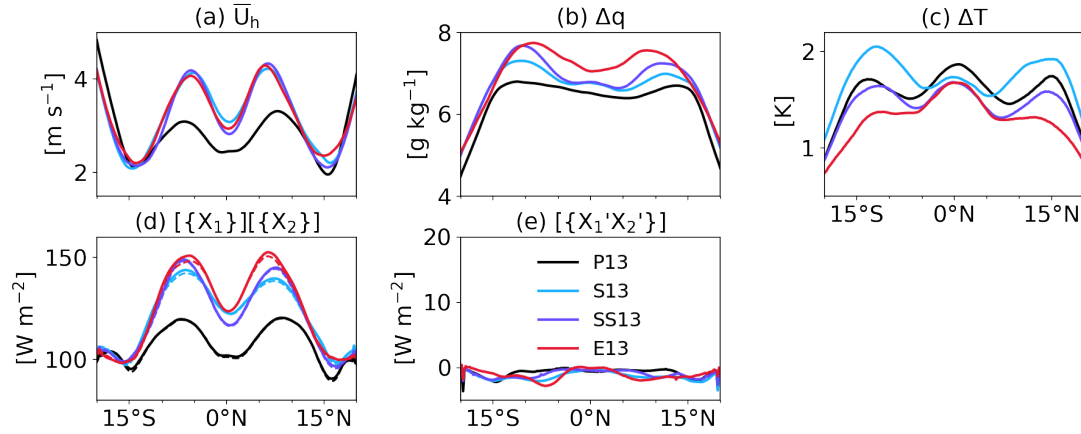
Figure 7.4: Time and zonal mean of surface properties: (a) the surface horizontal wind speed, (b) specific humidity contrast between the air and the ocean surface, and (c) temperature contrast between the air and the ocean surface. The bottom panels show contributions of (d) mean terms and (e) covariance terms (Eq. 5.10) to time and zonally averaged F_h. Here X represents the components of F_h such as $c_E \overline{U}_h$, $c_H \overline{U}_h$, Δq and ΔT. Dashed lines in (d) denote actual F_h from the model output (as in Fig. 7.3a) to facilitate the comparison. Reprinted from Jung et al. (2023). ©The Authors, CC BY 4.0 ©①

higher latitudes. E13 shows the overall smallest ΔT, possibly because it produces deeper convective downdrafts, leading to more adiabatic warming during the descent. The two simulations with parameterized shallow convection (S13 and SS13) largely agree with E13 near the equator but show considerably larger ΔT in the outer tropics, in particular S13. The reasons for this are not entirely clear. Finally P13 has the highest ΔT at the equator and intermediate values in the outer tropics. However, these differences in ΔT have little impact on the surface enthalpy fluxes, since the surface sensible heat flux contributes only about 10 % of the surface enthalpy fluxes. (In the latitudinal belt of 20°N/S the time and domain mean of the latent heat flux accounts for 97.4–115.7 W m^{-2}, while the surface sensible heat flux is 9.4–11.3 W m^{-2}.)

Figure 7.4d shows latitudinal variations of contributions of the time-zonal mean values (the terms in the first row of Eq. 5.10). Overall, the contributions of the time-zonal mean values follow the patterns of the actual F_h (solid and dashed lines in Fig. 7.4d). The differences between the contributions of the time-zonal mean values and the actual mean F_h are very small for P13 and SS13, showing that the time-zonal mean components shape the mean F_h, whereas some departures are found in E13 and S13.

Figure 7.4e shows latitudinal variations of contributions of the covariance terms (the terms in the second row of Eq. 5.10) to the time-zonal mean of F_h. Despite small magnitudes of the covariance terms compared to the mean contributions (Fig. 7.4d), E13 and S13 exhibit negative contributions to the mean F_h in the trades. The negative contributions indicate that $(c_E \overline{U}_h)' > 0$ coincides with $\Delta q' < 0$, meaning large q_v with a fixed q_* due to the prescribed SSTs, and vice versa for $(c_E \overline{U}_h)' < 0$ and $\Delta q' > 0$. Thus, the negative contribution can be interpreted as strong horizontal winds in a humid area or weak horizontal winds in a dry area.
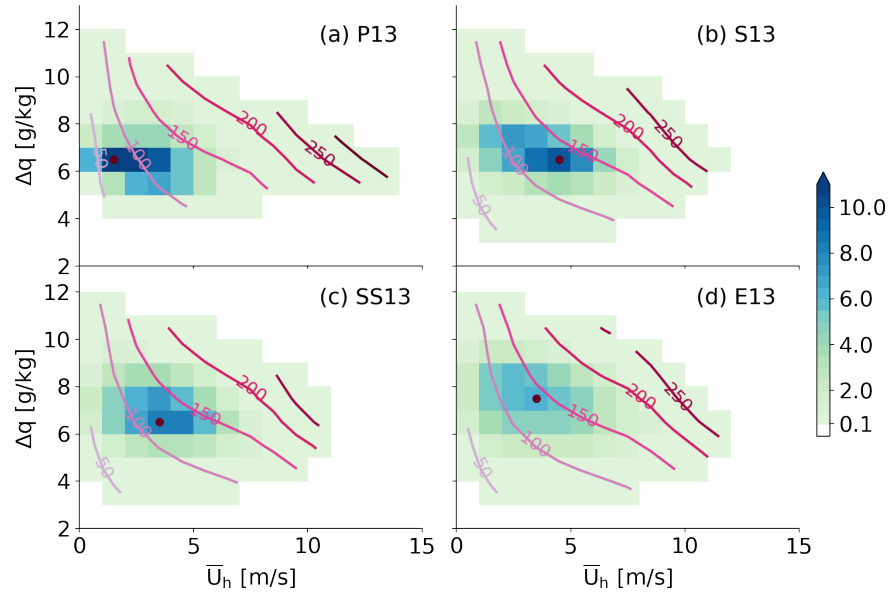
Figure 7.5: Two-dimensional histogram of surface wind speed and moisture contrast between the ocean and atmosphere in density (shading) with dots indicating the maxima. The minimum frequency density is 0.1 for shading. Contour lines indicate corresponding surface latent flux [W m^{-2}] binned by the wind speed and moisture contrast. Contour interval is 50 W m^{-2} increasing from lighter to darker colors. Reprinted from Jung et al. (2023). ©The Authors, CC BY 4.0 @①

To summarize, the time-zonal mean of $c_E \overline{U}_h$ and Δq is the main contributor to shape the mean F_h for all experiments (Fig. 7.4d), although for E13 and S13 the covariance terms have small negative contributions to F_h (Fig. 7.4e). The covariance terms might not be small if the horizontal resolution is fine enough to resolve cold pools (Marsham et al., 2013). Lastly, the temporal anomalies of the zonal mean components (the terms in the last row of Eq. 5.10) are very small compared to the aforementioned components (not shown).

b. Statistical distribution

Figure 7.5 depicts a two-dimensional histogram of $\overline{U}_h$ and Δq, and corresponding values of the surface latent heat flux (contour). For P13, the density distributions of both $\overline{U}_h$ and Δq are positively skewed with an extensively long tail for the former (Fig. 7.5a). The bin of $\overline{U}_h$ of 1–2 m s^{-1} and Δq of 6–7 g kg^{-1} contains the maximum frequency density of 14.9 % (colored dot). Contour lines, which indicate corresponding surface latent heat flux, demonstrate that the surface latent heat flux is more strongly dependent on $\overline{U}_h$ than on Δq. The maximum frequency density for $\overline{U}_h$ and Δq (colored dot) is located between the surface latent heat contour lines of 50–100 W m^{-2}.

E13 (Fig. 7.5d) exhibits the largest contrast to P13, showing relatively evenly distributed $\overline{U}_h$ and Δq. The maximum density (colored dot) accounts for 6.0 %, which is less than a half of that for P13, and is in the bin of $\overline{U}_h$ of 3–4 m s^{-1} and Δq of 7–8 g kg^{-1}, showing a greater surface wind and greater moisture contrast (seen also in Fig. 7.4a and b). The surface latent heat flux (contour

lines) increases strongly with increasing $\overline{U}_h$, while to lesser extent but noticeably it increases with increasing Δq. As expected from high F_h (Fig. 7.3a), the maximum density bin is located between the surface latent heat contour lines of 100–$150\,\text{W}\,\text{m}^{-2}$.

The distributions of S13 and SS13 (Fig. 7.5b and c) are in closer agreement with E13 than P13. The maximum frequency density (colored dot) lies between the contour lines of 100–$150\,\text{W}\,\text{m}^{-2}$ consistent with small differences in F_h among the explicit deep convection runs (Fig. 7.3a). Additionally, the surface latent heat flux varies strongly with $\overline{U}_h$ and relatively weakly with Δq. The distributions are concentrated to the highest frequency density of $10\,\%$ for S13 and $8.4\,\%$ for SS13, showing some intermediate density distributions between P13 and E13.

In summary, the decomposition analysis revealed that the time and zonal mean of $c_E\overline{U}_h$ and Δq mainly modulates the mean F_h and the statistical distributions showed that $\overline{U}_h$ is the dominant component for F_h distribution with the secondary role of Δq. These two different analyses demonstrate that mean $\overline{U}_h$ primarily modulates mean F_h.

7.2.2   Vertical difference of moist static energy

Figure 7.3b shows the vertical difference in h between the BL and the lower troposphere described by $h_b - h_m$ (Eq. 5.6). This contrast is key for the BLQE, as it determines the reduction of h in the BL through convective downdrafts and large-scale subsidence. Contrasts are smallest in the moist ITCZ region with relatively small differences among the four simulations with P13 showing the smallest values. Vertical h contrasts then increase markedly in the trade wind belt with much larger dependence on convective treatment, followed by a gradual fall-off towards higher latitudes. In the trade wind area, $h_b - h_m$ is smallest for E13 indicating deep mixing and conditions closer to moist neutrality. On the other hand, S13 shows much increased contrasts, suggesting that here deep mixing may be suppressed at the cost of more subtle shallow mixing. SS13 lies in the middle between these two extremes. P13 shows a fundamentally different behavior with a much slower fall-off towards higher latitudes.

Profiles of h provide a deeper insight into the $h_b - h_m$ pattern. The solid lines in Fig 7.6 demonstrate h profiles below $8\,\text{km}$ at characteristic latitudes for the ITCZ ($0°$), trades ($8°$N/S) and subsidence areas ($15°$N/S). Overall, h shifts to lower values from the equator to higher latitudes, following the prescribed SST pattern. The dashed lines in Fig. 7.6 show corresponding profiles of dry static energy ($s = \phi + c_p T$) with hardly any difference between the experiments. Therefore, lower h with increasing latitude is largely equivalent to a drier air.

In the ITCZ (Fig. 7.6a), the BL is fairly shallow ($\sim 400\,\text{m}$) and h_b differs little, changing by 0.1–$0.3\,\%$ (see Table 7.1). Note that the BL height is fixed for diagnostic to the layer of 10–$500\,\text{m}$. This is higher than the ITCZ BL but does not impact the results. E13 shows the lowest value, possibly related to more frequent and or more intense convective downdrafts in line with more intense rainfall (Fig. 7.1b). In the lower free troposphere, more distinct differences are evident, particularly between 1–$3\,\text{km}$. E13 has again the overall lowest values, such that downdrafts can more effectively reduce h_b. Retsch et al. (2019) also found a drier lower troposphere for
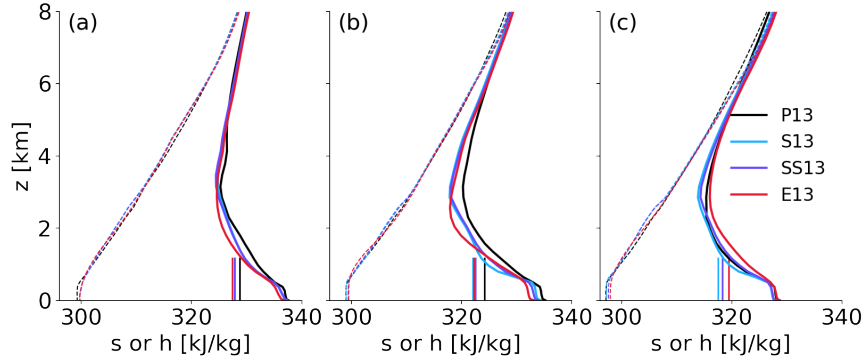
Figure 7.6: Profiles of the time and zonal mean of dry static energy (dashed) and moist static energy (solid) [kJ kg^{-1}] at (a) 0°, (b) 8 °N/S and (c) 15 °N/S. Those latitudes are chosen since they are representative of the ITCZ, the trade wind belt and the subsiding areas (see section 7.1). The vertical bars represent the calculated h_m (average over 0.5 to 5 km). Reprinted from Jung et al. (2023). ©The Authors, CC BY 4.0 ©①

their explicit deep convection cases than for parameterized ones. S13 and SS13 show enhanced values relative to E13 around 2 km, while P13 has higher h throughout most of the layer up to 5 km. Applying a vertical average over 0.5 to 5 km, we obtain h_m, which varies between 327.4 and 328.7 kJ kg^{-1} (Table 7.1). Given that differences within and above the BL are largely consistent between the runs, $h_b - h_m$ in the ITCZ increases by 3–6 % from P13 to S13, SS13 and E13 as also evident from Fig. 7.3b.

In the trade wind belt, differences among the four experiments in $h_b - h_m$ are larger than in the ITCZ (Figure 7.3b). This corresponds with more marked differences in the vertical profiles of h (Fig. 7.6b). The profiles are shifted to lower h from the ITCZ to the trade wind belt. Overall the shift is more evident for the explicit deep convection runs (S13, SS13 and E13) than P13 which shows a moderate h decrease in the trade wind belt. The variations of h_b among the four experiments are systematic with decreasing from P13 to S13 or SS13 to E13 by 0.83–1.36 kJ kg^{-1} (see Table 7.1). Also, E13 has a higher BL height by around 100 m or one model level than P13. Meanwhile, h_m varies small among the explicit deep convection runs (S13, SS13 and E13; colored vertical bars in Fig. 7.6b) but largely decreases from P13 to any run with explicit deep convection by 1.64–2.07 kJ kg^{-1} (Table. 7.1). Yet, the profiles among the explicit deep convection runs in the lower troposphere do not show a perfect match but rather subtle differences. SS13 exhibits somewhat an intermediate behavior of h between S13 and E13, such that SS13 alternates the patterns of h similar to S13 in the BL, E13 between 0.5–1.5 km and again S13 above 1.5 km. This intermediate behavior indicates that the stochastic scheme for shallow convection (SS13) mixes the air between the BL and lower troposphere more efficiently than the deterministic version (S13) but not as deeply as the explicit one (E13). Consequently, this results in some unsystematic behavior of $h_b - h_m$ from one to another with E13 showing the lowest value, then P13 and SS13 and finally with S13 showing the highest value (Fig. 7.3b).

In the subsidence region (Fig. 7.6c), the BL height is 500 m in all four experiments and h_b is fairly similar among the runs where E13 shows the largest value unlike the other latitudinal

	lat (°)	h_b	h_m	$h_b - h_m$	S
	P13	336.78	328.72	8.06	14.24
0	S13	336.34	327.88	8.45	13.85
	SS13	336.37	327.75	8.62	13.84
	E13	335.70	327.37	8.32	13.86
	P13	334.35	324.12	10.23	14.29
8	S13	334.5	322.05	11.48	14.25
	SS13	333.06	322.48	10.58	14.08
	E13	332.16	322.16	10.00	14.07
	P13	327.81	318.31	9.51	14.27
15	S13	327.27	317.51	9.76	14.17
	SS13	327.34	318.22	9.12	14.06
	E13	327.96	319.42	8.54	13.92

Table 7.1: Time and zonal average of the moist static energy [kJ kg^{-1}] and dry stability [J kg^{-1} m^{-1}] at three different latitudes. The layer of 10–500 m and 0.5–5 km are used for the quantities in the BL h_b and in the lower troposphere h_m and dry stability S, respectively.

regions. The maximum difference between two runs in h_b is 0.69 kJ kg^{-1} (Table. 7.1). Also, E13 shows the largest value of h_m, indicating more moisture columns than the others as profiles for dry static stability show no substantial differences. This is the opposite of the results by Retsch et al. (2019) who showed that the lower troposphere in the subsidence region is drier with explicit deep convection than parameterized deep convection. Given that the strength of the Hadley circulation is largely consistent with explicit deep convection (discussed in section 7.1.2), lower-tropospheric moisture is presumably dominated by local mixing rather than large-scale subsidence effects. Likewise, local mixing between S13 and SS13 fundamentally differs in that vertical mixing, mainly in the lower atmospheric layer, is more efficient for the stochastic version (SS13) (Sakradzija et al., 2020). Accordingly, h_m for SS13 increases from S13 by more than 0.5 kJ kg^{-1}, which is less than 0.5 kJ kg^{-1} in other latitudinal regions (Table. 7.1). Thus, we see a systematic change of $h_b - h_m$ in the subsidence region, representing some effects of local mixing.

In summary, h_b and h_m in the ITCZ and the trade wind belt show some systematic changes from parameterized to explicit deep convection, but the resulting pattern of $h_b - h_m$ varies with different convective treatments. The impact of shallow convective treatment is evident in profiles of h, particularly in the trade wind belt. The stochastic version of shallow convection (SS13) exhibits the intermediate behavior of h between the deterministic version (S13) and explicit version (E13), consequently reflected on the latitudinal distribution of $h_b - h_m$ (Fig. 7.3b).
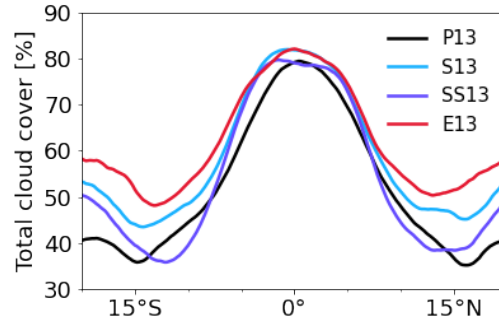
Figure 7.7: As in Fig. 7.3c but for total cloud cover. Reprinted from Jung et al. (2023). ©The Authors, CC BY 4.0 ©①

7.2.3 Radiative cooling

Figure 7.3c shows the time and zonal mean of radiative cooling in the lower troposphere (0.5–5 km). P13 exhibits the overall flattest latitudinal distribution with a minimum radiative cooling in the ITCZ and larger cooling in the outer tropics (Fig. 7.3c). S13, SS13 and E13 show a similar pattern but less cooling in the ITCZ and stronger cooling in the outer tropics, the latter particularly true for S13. In the following, we will discuss this result in the context of total cloud cover (Fig. 7.7) and the latitudinal-height distribution of the radiative temperature tendency (Fig. 7.8).

Figure 7.7 shows that amongst all runs, P13 has the overall smallest cloud cover, peaking at about 80 % at the equator and falling off gradually to 37 % at 15°N/S beyond which there is a slight increase again. Consequently, radiative cooling in the troposphere shows a marked contrast between the ITCZ region and the outer tropics (Fig. 7.8a). In the former, radiative cooling is generally reduced and there is even a slight warming below the tropopause, likely related to longwave absorption by optically thick cirrus (Senf et al., 2020). This is consistent with the fact that for P13 cloud ice in the upper troposphere is spread over a deeper layer by 1 km than in the other experiments (not shown). Note that the near-tropopause warming is not included in $\dot{Q}$ (Fig. 7.3c), which is averaged over 0.5–5 km (section 5.5). In the outer tropics, radiative cooling increases and is quite homogeneous across most of the free troposphere decreasing gently above about 9 km (Fig. 7.8a). The top of the BL stands out as an area of enhanced cooling associated with longwave emission from the top of shallow clouds into the relatively dry free troposphere above it.

The cloud cover and the radiative cooling in E13 show the largest contrast to P13. The cloud cover increases from P13 to E13 by 6 % in the ITCZ and by 34 % in the outer tropics (Fig. 7.7). Correspondingly, there are some differences in pattern of radiative cooling (Fig. 7.8d). Overall radiative cooling above the BL weakens due to increased vertical mixing around BL top by explicit deep and shallow convection. In the ITCZ, E13 exhibits only net radiative cooling, whereas P13 shows radiative warming near the tropopause. Longwave cooling is stronger when deep convection is explicitly represented because explicit deep convection releases more latent
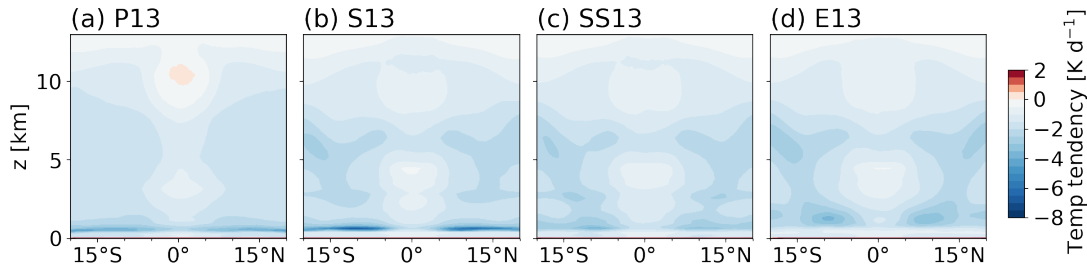
Figure 7.8: As in Fig. 7.2 but for net radiative temperature tendency. Reprinted from Jung et al. (2023). ©The Authors, CC BY 4.0 ©①

heat through microphysical processes than parameterized deep convection (can be inferred from more frequent extreme rainfall in explicit deep convection in Fig. 7.1b), which increases temperature of the atmospheric columns and consequently emits more longwave radiation. In the outer tropics, where the total cloud cover substantially increases from P13 to E13, radiative cooling in E13 shows signatures of shallow and congestus convection (Fig. 7.8d), which is hardly seen in the mean radiative cooling in P13 (Fig. 7.8a). The delicate structure demonstrates that E13 is able to construct a trimodal structure of deep, congestus and shallow clouds (Johnson et al., 1999; Khairoutdinov et al., 2009), consistent with the relatively high cloud cover. The weak BL radiative cooling reduces $\dot{Q}$ in the ITCZ and the mid-level clouds increase $\dot{Q}$ in the outer tropics from P13 to E13 (Fig. 7.3c).

S13 exhibits similar features to E13 in terms of cloud cover and radiative cooling (including $\dot{Q}$) in the ITCZ, but there are marked differences in the outer tropics. Cloud cover in S13 (47.7 %) is intermediate between P13 (39.8 %) and E13 (53.2 %) (Fig. 7.7). While the free-tropospheric cooling by radiation is consistent with E13, S13 (Fig. 7.8b) reveals that radiative cooling above the BL is substantially enhanced and very concentrated, creating a gap in cooling above that. This leads to the largest $\dot{Q}$ of all runs in the outer tropics (Fig. 7.3c).

Surprisingly, SS13 shows the closest cloud cover to P13 amongst all runs with explicit deep convection (Fig. 7.7). Free-tropospheric radiative cooling remains similar to S13 and E13, but the BL top cooling in the outer tropics is much reduced with slight enhancement at around 3 km (Fig. 7.8c). This is due to the fact that the stochastic version (SS13) allows for efficient mixing between the BL and the lower troposphere and for efficient BL convective heating (Sakradzija et al., 2020; Senf et al., 2020). Consequently, this leads to overall similar $\dot{Q}$ to E13 (Fig. 7.3c), despite the very different vertical structures of radiative temperature tendency.

7.2.4 Dry stability

In the conceptual framework, the effects of radiative cooling need to be considered relative to the dry stability S (Eq. 5.6), which is shown in Fig. 7.3d. For P13, S is almost constant between 15°N/S with a value of 14.2 J kg^{-1} m^{-1} beyond which it drops slightly. The other experiments exhibit some noteworthy differences. In the ITCZ, explicit deep convection appears to create a somewhat lower stability by about 0.4 J kg^{-1} m^{-1} compared to P13 (Table 7.1). This may

be related to the fact that parameterized convection is triggered a little more easily and can therefore more effectively stabilize the atmosphere in a convectively active region. This subtle difference is also evident from Fig. 7.6a. (The slope of s in the lower troposphere represents S.) In the outer tropics, the treatment of shallow convection has some effect on S, increasing S by about $0.1 \, \text{J} \, \text{kg}^{-1} \, \text{m}^{-1}$ from one experiment to another (Table 7.1): E13 likely produces the least shallow mixing and is thus least stable, followed by SS13 and S13. Finally, the largest stability is found in P13 to which both parameterized shallow and deep convection contribute. As in the ITCZ, differences are overall subtle and evident from profiles of s (Fig. 7.6b and c).

In the conceptual model the ratio of radiative cooling in the lower troposphere $\dot{Q}$ and dry stability S are regarded (second term in Eq. 5.6). As radiation and stability in all four runs largely compensate each other, the ratio is almost identical and also relatively constant over latitudes, accounting for $1.2 \pm 0.2 \, \text{g} \, \text{m}^{-2} \, \text{s}^{-1}$. In contrast, the effect of surface enthalpy fluxes and vertical contrast of h (first term in Eq. 5.6) accounts for 11.3–$13.7 \, \text{g} \, \text{m}^{-2} \, \text{s}^{-1}$ with standard deviation of 1.4–$1.6 \, \text{g} \, \text{m}^{-2} \, \text{s}^{-1}$. This demonstrates that despite all the details discussed above, the overall effect of radiation and stability to drive differences among the four simulations is minor.

7.2.5 Convective updraft mass flux and precipitation efficiency

Up to this point, we have examined the distributions of each term on the right-hand side in Eq. 5.6. To close our diagnostic, here we discuss M_u, ϵ_p and $\langle q_v \rangle$ which are directly related to rainfall (Eq. 5.7), and then link this discussion to the entire framework. We start with those quantities in the ITCZ. Figure 7.3e shows that ϵ_p has the maxima there with almost constant values of 0.629–0.648 in all four experiments (Table. 7.2). Meanwhile, $\langle q_v \rangle$ marginally decreases from P13 to S13 and SS13 to E13 by around 2–$6 \, \%$ (Table. 7.2), indicating that P13 has the moistest atmospheric column in the ITCZ, as also seen in profiles of h (Fig. 7.6a). Given the almost identical ϵ_p and the decreasing $\langle q_v \rangle$ from parameterized to explicit convection, M_u must increase from parameterized (P13) to explicit deep convection (S13, SS13 and E13) to increase rainfall accordingly (Eq. 5.7). Correspondingly, M_u increases from P13 to E13 by $37.2 \, \%$ (Fig. 7.3f and Table. 7.2). A similar increase in M_u by about $29 \, \%$ is shown for S13 and SS13. These differences in M_u are similar to those in Pr (33.7–$35.2 \, \%$).

In the outer tropics, ϵ_p sharply decreases from the ITCZ with a minimum at around 9–$12°$N/S and beyond this increases with latitude (Fig. 7.3e). The differences among the runs are substantial in the outer tropics, with ϵ_p varying between 0.214–0.306 (highest in P13). Mean values of $\langle q_v \rangle$ slightly vary with P13 marking the greatest value of $2.77 \, \text{g} \, \text{kg}^{-1}$ and with S13 marking the smallest value of $2.51 \, \text{g} \, \text{kg}^{-1}$ (not shown). From the ITCZ to the outer tropics M_u sharply decreases to about $0.015 \, \text{kg} \, \text{m}^{-2} \, \text{s}^{-1}$ (with E13 showing the upper limit of the range) and beyond the minimum slightly increases with latitude (Fig. 7.3f). These patterns of the minimum and marginal increase in ϵ_p and M_u are also observed in Pr (Fig. 7.1a), yet the differences in Pr in the outer tropics among the runs do not vary as much as those in ϵ_p due to low ϵ_p, low M_u and low $\langle q_v \rangle$ there.

	P13	S13	SS13	E13
Pr [mm d^{-1}]	7.28	9.87	9.75	9.85
$\langle q_v \rangle$ [g kg^{-1}]	4.0	3.92	3.92	3.75
M_u [kg m^{-2} s^{-1}]	0.0320 (0.0315)	0.0412 (0.0392)	0.0413 (0.0389)	0.0440 (0.0407)
ϵ_p	0.63 (0.64)	0.649 (0.693)	0.648 (0.692)	0.64 (0.694)
F_h [W m^{-2}]	105.7	129.5	127.2	135.1
Adv [W m^{-2}]	4.4	22.8	22.7	29.3

Table 7.2: The averaged precipitation rate (Pr), column specific humidity ($\langle q_v \rangle$), convective updraft mass flux (M_u), precipitation efficiency (ϵ_p), surface enthalpy flux (F_h) and BL merdional advection (Adv) between 5°N/S for each experiment. The quantities in parentheses indicate those when the BL meridional advection is included (Eq. 5.8).

To summarize, we show that in the ITCZ, M_u substantially increases from parameterized (P13) to explicit deep convection (S13, SS13 and E13), while ϵ_p is almost identical among them and $\langle q_v \rangle$ marginally decreases from P13 to S13 and SS13 to E13. Surprisingly, the increase in Pr is not associated with ϵ_p but M_u. In radiative convective equilibrium (RCE), where the large-scale circulation is absent, ϵ_p would be strongly linked to rainfall (Emanuel, 2019). Intuitively, an increase in rainfall would be strongly related to increasing precipitation efficiency (Narsey et al., 2019; Muller and Takayabu, 2020) but this is not the case in our simulations.

When revisiting all input variables in Eq. 5.6 for our diagnostic (Fig. 7.3), it is evident that in the ITCZ, F_h exhibits the same increasing tendency as M_u, while $h_b - h_m$ shows small differences. Meanwhile, $\dot{Q}$ and S compensate each other (section 7.2.4), which consequently have almost no effect on M_u. Therefore, M_u and F_h are strongly related to each other, which is explained by BLQE. Given constant ϵ_p in the ITCZ, an increase in M_u increases M_d, through $M_u = (1 - \epsilon_p)M_u$, which carries low h from the lower troposphere into the BL to balance enhanced F_h. The change in F_h is associated with changing $\overline{U}_h$ (section 7.2.1) which is closely linked to the Hadley circulation (section 7.1.2). Thus, a different convective treatment changes a large-scale circulation and surface horizontal wind, which alters associated surface fluxes that are in balance with convective mass flux, which is directly related to rainfall.

In the outer tropics, differences in ϵ_p (Fig. 7.3e) become evident between P13 and the other explicit deep convection runs (S13, SS13 and E13). However, Pr (Fig. 7.1a) is relatively small and does not vary much between the runs because of low absolute values of ϵ_p as well as the sharp decreases in M_u and $\langle q_v \rangle$ from the ITCZ. Beyond about 9–12°N/S, ϵ_p increases with increasing latitude, which is related to increasing Pr with latitude there. Nonetheless, differences in Pr remain small in the outer tropics compared to the ITCZ due to small absolute values of related terms (ϵ_p, M_u and $\langle q_v \rangle$; see Eq. 5.7).
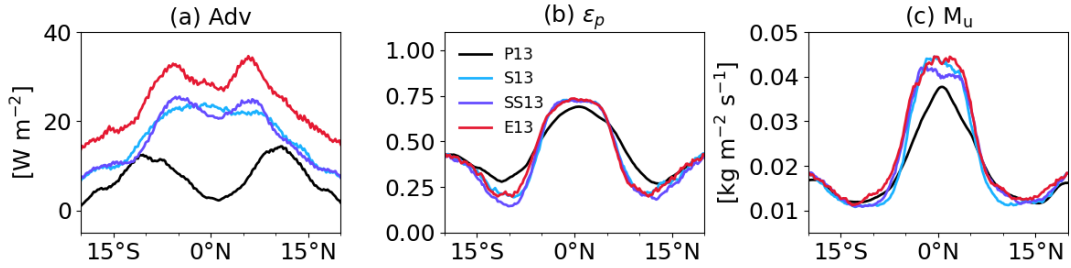
Figure 7.9: Time and zonal mean of (a) the meridional advection term ($\mathrm{d}\rho V_h \cdot \nabla h$), (b) estimated precipitation efficiency and (c) estimated convective mass flux using Eqs. 5.7 and 5.8. Reprinted from Jung et al. (2023). ©The Authors, CC BY 4.0 ⓒⓘ

7.2.6 Meridional advection

Figure 7.9 shows the latitudinal distribution of BL meridional advection and the impact of including it on precipitation efficiency and convective updraft mass flux. The meridional term for P13 has near-zero values at the equator that increases away from the equator, leading to an average of $4.4\,\mathrm{W\,m^{-2}}$ in the ITCZ (Table 7.2). The small advection term in the ITCZ decreases M_u by $0.0005\,\mathrm{kg\,m^{-2}\,s^{-1}}$ and increases ϵ_p by 0.01 compared to the advection-free diagnostic (section 7.2.5). At about 10°N/S, BL meridional advection reaches the maximum of $13.4\,\mathrm{W\,m^{-2}}$ and beyond that decreases with increasing latitude, leading to an increase in ϵ_p by 0.022 and an decrease in M_u by $0.001\,\mathrm{kg\,m^{-2}\,s^{-1}}$ which are considerably small.

In contrast to P13, E13 exhibits a large contribution of BL meridional advection (Fig. 7.9a). The averaged advection in the ITCZ is $29.3\,\mathrm{W\,m^{-2}}$, consequently reducing M_u by $0.0033\,\mathrm{kg\,m^{-2}\,s^{-1}}$ but increasing ϵ_p by 0.054 (Table 7.2). At around 7°N/S the advection term shows local maxima of $33.8\,\mathrm{W\,m^{-2}}$ and then sharply decreases with increasing latitude. The overall large meridional advection term for E13 is consistent with intensified $\overline{\mathrm{U}}_\mathrm{h}$ (Fig. 7.4a) and greater h shift in the BL with latitude (Fig. 7.6). Consequently, M_u marginally decreases by $0.0024\,\mathrm{kg\,m^{-2}\,s^{-1}}$ and ϵ_p increases by 0.037 in the outer tropics.

Similarly, SS13 shows large BL meridional advection in the ITCZ and has local maxima at around 7°N/S but overall weaker advection by around $6\,\mathrm{W\,m^{-2}}$ than E13 (Fig. 7.9a). The advection consideration leads to a decrease in M_u by $0.0025\,\mathrm{kg\,m^{-2}\,s^{-1}}$ and an increase in ϵ_p by 0.043 in the ITCZ (Table 7.2), which changes less strongly in the outer tropics (Fig. 7.9b and c). For S13 meridional advection closely follows that for SS13 (Fig. 7.9a), leading to averaged advection of $22.8\,\mathrm{W\,m^{-2}}$ in the ITCZ (Table 7.2). However, the maximum value is located in the ITCZ rather than at around 7°N/S. The minor increase from SS13 to S13 in $\overline{\mathrm{U}}_\mathrm{h}$ in the ITCZ (Fig. 7.4a) and the slightly reduced meridional h gradient for S13 (Fig. 7.6a and b) lead to the different shapes between S13 and SS13. Despite this difference, M_u and ϵ_p in S13 and SS13 change by the almost same degree when considering meridional advection.

In summary, the meridional advection inclusion slightly increases ϵ_p and slightly decreases M_u for all four cases. The former in the ITCZ increases by 8 % from P13 to the other explicit deep convection runs (S13, SS13 and E13), which was almost identical without considering the

advection term (section 7.2.5). However, the close association between M_u and rainfall remains strong, showing that the increase in M_u from P13 is by 22.9–28.9 %, which contributes most strongly to the increased Pr. Therefore, the two cases with and without BL horizontal advection demonstrate tight links between rainfall and convective mass flux, which is in balance with surface enthalpy fluxes through BLQE. Furthermore, surface enthalpy fluxes are substantially modulated by surface horizontal winds, which are intimately linked to the large-scale circulation in our case.

7.3   Summary and discussions

This study explored rainfall differences in aquachannel simulations with different convective treatment using a novel diagnostic tool, presented in section 5.5, to disentangle the processes important for rainfall in a fully coupled and physically consistent way. The innovation of our diagnostic is the application of the conceptual framework by Emanuel (2019) to output from a numerical model. Amongst other things, the framework assumes mass and energy conservation and the boundary-layer quasi-equilibrium (BLQE) approach (Raymond, 1995). BLQE describes the balance of moist static energy in the BL between surface enthalpy fluxes and vertical advection through convective downdrafts and large-scale subsidence. We applied our diagnostic to tropical aquachannel experiments with different treatments of shallow and deep convection in the ICON-NWP model (in section 4.2) to disentangle processes important for rainfall.

All four experiments show an ITCZ at the equator and a Hadley circulation with an ascending branch at the equator and descending branches at 15°N/S – somewhat narrower than the Hadley circulation in reality – and accompanying easterly trade winds at the flanks of the ITCZ. The narrower Hadley circulation is because the model develops its own internal circulation, at least partly related to suppressed eddy fluxes at the rigid walls. Despite the similar structures among the experiments, there are differences, mainly by deep convective treatment. From parameterized to explicit deep convection, the maximum precipitation in the ITCZ increases by 35 %, and the Hadley circulation and trade winds are also strengthened.

A physically consistent diagnostic was presented to understand the differences. Our diagnostic revealed important links for the differences when modifying a convective treatment. Figure 7.10 illustrates how variables relevant to rainfall change from parameterized to explicit deep convection. The changes can be summarized as follows:

- In the ITCZ, where the rainfall amount changes substantially, the large-scale circulation and surface horizontal winds get stronger with explicit deep convection. Strong surface winds enhance surface enthalpy fluxes by 20.2–27.7 %. The vertical difference in moist static energy between the BL and the lower troposphere is relatively small in response to changing convective treatment. Somewhat surprisingly, precipitation efficiency is little sensitive to the representation of convection with almost constant values of 0.629–0.648. In contrast, convective updraft mass flux increases by 29–37 % with explicit deep
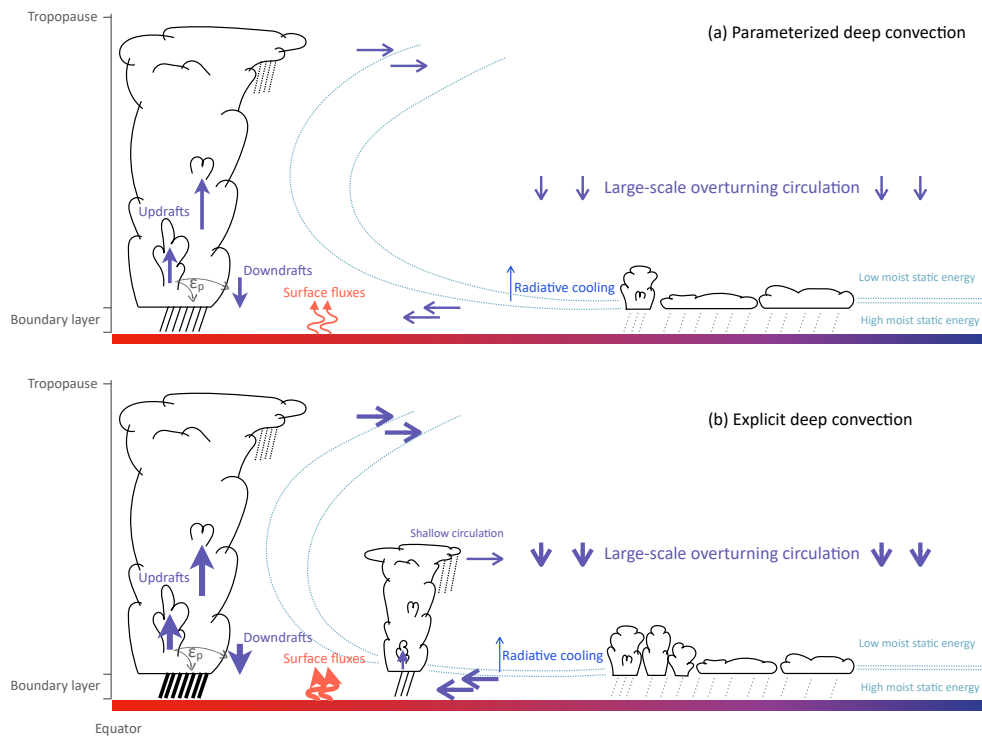
Figure 7.10: Schematic depiction of the important processes associated with rainfall for (a) parameterized deep convection and (b) explicit deep convection. The thick (thin) arrows and lines indicate large (small) quantities. The dotted curves indicate contour lines for constant values of moist static energy. See section 7.3 for a detailed discussion. Reprinted from Jung et al. (2023). ©The Authors, CC BY 4.0 ⓒⓘ

convection. The constant value of precipitation efficiency indicates that convective updraft mass flux increases proportionally to increasing convective downdraft mass flux, which is balanced by enhancing surface enthalpy fluxes to maintain BLQE. Thus, the rainfall change in response to convective treatment is due to the tight links among dynamical fields, surface fluxes and convective mass flux.

- In the trade wind belt, surface enthalpy fluxes and surface horizontal winds remain stronger with explicit deep convection. However, the vertical contrast of moist static energy between the BL and the lower troposphere greatly varies, depending on representation of shallow convection. Precipitation efficiency and convective updraft mass flux sharply decrease from the ITCZ, but the former is greater with parameterized deep convection (0.306) than with explicit one (0.214), while the latter shows little dependence on convective treatment. Despite this difference, the small values of precipitation efficiency and convective updraft mass flux do not change rainfall significantly from one experiment to another.

In all latitudes, a change in radiative cooling is compensated by altering dry stability, so having a very small net effect on convective mass flux. Note that radiative cooling was found to be crucial

for the RCE case without a large-scale circulation (Emanuel, 2019), but this is not the case for our experiments with full physics and dynamics. Moreover, explicit deep convection can produce more delicate distributions of convection, such as deep, shallow and congestus clouds, than parameterized convection but again mean rainfall is insensitive to a change in radiative cooling associated with these structures. In our case column specific humidity does not play an important role for rainfall changes. With explicit deep convection, the meridional advection of moist static energy in the BL is not negligible, leading to a slight increase of precipitation efficiency from 0.64 to 0.69. However, convective updraft mass flux still exhibits the strongest association with rainfall. A caveat of this diagnostic is that the effects of entrainment and detrainment are not considered, which might be important for convective updraft mass flux (Zipser, 2003; Möbis and Stevens, 2012). Somewhat indirectly, these effects are included in $h_\mathrm{b} - h_\mathrm{m}$ through lower-tropospheric h and in ϵ_p through indirect effects of re-evaporation.

The merit of our diagnostic lies in a fair comparison of simulations with different representations of convection to examine the processes potentially linked to rainfall. Since those processes are strongly coupled to each other, it is not trivial to disentangle what processes are ultimately responsible for rainfall. Furthermore, explicit and parameterized convection treats vertical motion differently, so it is not fair to compare convective updraft mass flux obtained directly from the modelled vertical wind field. Thus, we emphasize that the diagnostic presented here provides a physically consistent, fair comparison between explicit and parameterized convection and helps obtain a quantitative and qualitative view on important links in the system. Lastly, this tool also has potential to specify sources of uncertainty in NWP models and to identify the reasons behind the large spread in ITCZ behavior among different global climate models.

8 Results: Equatorial waves in idealized tropical aquachannel simulations

In the previous chapter, we examined the mean state of our aquachannel simulations. The mean rainfall is characterized by an ITCZ at the equator, with intensified rainfall with explicit deep convection. The large-scale circulation also gets stronger with explicit deep convection. This chapter explores internal variability. Section 8.1 presents the evolution of unfiltered rainfall and wind fields and section 8.2 shows EWs presented in the aquachannel simulations by using the complementary wave identification methods (section 5.1). Section 8.3 presents how EWs modulate related fields using the composite technique. Finally, section 8.4 shows evidence of the MJO in one of the aquachannel simulations.

8.1 Unfiltered fields

8.1.1 Precipitation

Figure 8.1 illustrates different rainfall patterns in the four aquachannel simulations. P13, in which both deep and shallow convection are parameterized, shows prominent eastward propagating features with different propagation speeds (Fig. 8.1a). Intense rainfall ($> 0.75\,\mathrm{mm\,h^{-1}}$) occurs in the western hemisphere at day 3 (dotted line A) and in the eastern hemisphere at day 12 (dotted line B), and both signals propagate eastward with speeds of 12–$18\,\mathrm{m\,s^{-1}}$. (Note that the aquachannel setup is zonally symmetric, so there are no geographical differences in longitude.) The intense rainfall along with dotted line B slows down substantially at day 15, appearing in the western hemisphere with a propagation speed of $5\,\mathrm{m\,s^{-1}}$ (dotted line D). This slowly propagating feature persists until the end of the simulation period. In addition, there are much faster east- and westward propagating features in the background with less intense rainfall of around $0.35\,\mathrm{mm\,h^{-1}}$. The fast eastward propagation exhibits speeds of 23–$27\,\mathrm{m\,s^{-1}}$ (around dotted line C).

This pattern of unfiltered rainfall in P13 (Fig. 8.1a) demonstrates different modes of variability. A wide range of eastward propagation speeds is evident. Intense rainfall is related to eastward propagation with a speed of 12–$18\,\mathrm{m\,s^{-1}}$ (lines A and B), while moderate rainfall is associated with fast propagation with a speed of 23–$27\,\mathrm{m\,s^{-1}}$ (line C). The propagation speeds of the former and the latter are in the range of convectively coupled and dry KWs, respectively, as discussed
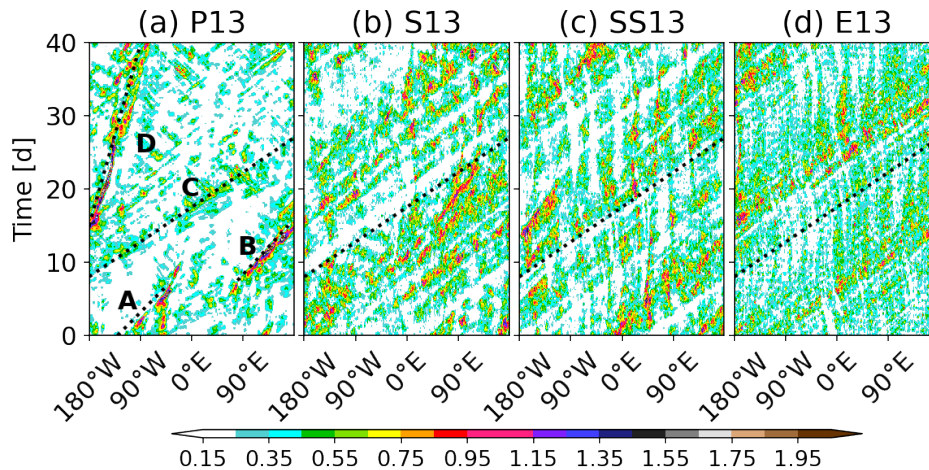
Figure 8.1: Hovmöller diagrams of unfiltered precipitation averaged over 0–10°N [mm h^{-1}] covering the analysis period over 40 days for (a) P13, (b) S13, (c) SS13 and (d) E13. The latitudinal band of 0–10°N is chosen not only to capture both symmetric and anti-symmetric patterns with respect to the equator but also to include the maximum rainfall in the ITCZ (Chapter 7). The dotted lines indicate phase speeds. A: 17 m s^{-1}, B: 15 m s^{-1}, C: 24 m s^{-1} and D: 5 m s^{-1}. Note that only line C is illustrated in S13, SS13 and E13.

earlier (section 2.2.1). The slow eastward-moving rainfall feature with the speed of 5 m s^{-1} (line D) shares characteristics with the MJO in terms of propagation speed. The relation between precipitation and modes of variability will be discussed in more detail in the following sections.

The largest contrast to P13 is found in E13, in which both deep and shallow convection are explicitly represented (Fig. 8.1d). E13 yields a distinctive eastward propagating rainfall event (> 0.45 mm h^{-1}) with a zonal wavenumber of one and a propagation speed of 23–25 m s^{-1}. This event is present throughout the simulation period of 40 days. Inbetween the wavenumber-one feature, rainfall of around 0.35 mm h^{-1} frequently occurs and this rainfall exhibits characteristics of standing waves or slow westward drifts.

S13 and SS13 (Fig. 8.1b and c) share similar rainfall patterns with E13. Note that deep convection is explicitly represented for S13, SS13 and E13, but shallow convection is represented differently using the deterministic (S13) and stochastic (SS13) schemes, while it is explicitly represented in E13 (Table 4.1). In S13 and SS13, eastward propagating features are evident with a zonal wavenumber of one and with propagation speeds of 23–25 m s^{-1} as in E13. Within the wavenumber-one packet, S13 and SS13 exhibit some substructures. Moreover, there are standing-wave features, which are more evident in SS13 than in S13. Another noticeable difference from E13 is that there are larger dry gaps between rainfall features. Additionally, rainfall systems slow down, e.g., at around 80°E at day 18 in S13 and at 80°W at day 15 in SS13, although they are not as dramatic as those in P13.

The wavenumber-one features in the runs with explicit deep convection (S13, SS13 and E13) propagate eastward (23–25 m s^{-1}) and this propagation speed is at the high end of the phase speed of convectively coupled KWs (section 2.2.1). Interestingly, propagating rainfall events are less intense for explicit deep convection (> 0.45 mm h^{-1}) than parameterized deep convection

($> 0.75\,\mathrm{mm\,h^{-1}}$), although mean rainfall in the ITCZ is greater with explicit deep convection by 35 % (Chapter 7). The different characteristics in mean rainfall and its variability indicate that convective treatment solely alters wave-convection coupling, and somewhat surprisingly that parameterized deep convection seems to generate more intense rainfall associated with wave-convection coupling in our case. Note that the realistic (DYAMOND) simulations demonstrated that explicit deep convection produces higher mean rainfall and higher rainfall variance (Fig. 6.1).

8.1.2 Horizontal winds

Figure 8.2 shows the averaged horizontal wind fields at 200 and 850 hPa. The zonal wind at 200 hPa (Fig. 8.2a–d) shows that westerly winds in the upper troposphere are more dominant in parameterized deep convection (P13) than explicit deep convection (S13, SS13 and E13), where easterlies occur occasionally. In contrast, the latter group exhibits dominant easterly winds at 850 hPa with some periods of weak westerlies, while P13 has a mixture of easterly and westerly winds at this level (Fig. 8.2e–h). These characteristics of zonal winds were briefly discussed in section 7.1.2 where we hypothesized that explicit deep convection allows more upward convective momentum transport in the ITCZ, leading to the weakening of the vertical shear. Note that the mean zonal wind at 200 hPa is westerly with speeds of 13.0, 7.44, 6.04 and 5.02 m s^{-1} for P13, S13, SS13 and E13, respectively, and the mean zonal wind at 850 hPa is easterly with speeds of 0.08, 1.66, 1.96 and 1.89 m s^{-1} for P13, S13, SS13 and E13, respectively.

Section 8.1.1 showed clear eastward propagations in the unfiltered precipitation fields of all four experiments. Correspondingly, Fig. 8.2 also shows eastward propagating signatures except for the meridional wind at 850 hPa. In the upper troposphere of P13 (Fig. 8.2a), a strong westerly wind of around 30 m s^{-1} propagates at the speed of 27 m s^{-1}, which is faster than line C suggests. This propagation persists during the first 20 days, encircling the simulation domain, and after that, the westerly wind weakens to around 10 m s^{-1}. In contrast, E13 (Fig. 8.2d) exhibits a consistent propagation of westerly wind with a zonal wavenumber of one. The westerly wind speed is approximately 15 m s^{-1}, which is half of the speed of the strong westerly in P13. This westerly wind propagates at the speed of 24 m s^{-1}, which is aligned with line C and corresponds to the speed of the eastward propagating rainfall in Fig. 8.1d. The zonal wind patterns at 200 hPa in S13 and SS13 (Fig. 8.2b and c) follow more closely that of E13 than P13, showing a wavenumber-one pattern in the westerly wind. However, there are some differences from E13, such that higher zonal wavenumbers are superimposed onto the wavenumber-one structure. Furthermore, the easterly wind at 200 hPa is stronger in S13 and SS13 than in E13.

The zonal wind pattern at 850 hPa of P13 (Fig. 8.2e) largely differs from that at 200 hPa. In the first 20 days, no persistent propagation is observed, but low-level westerly winds propagate eastward at 12–18 m s^{-1} (around lines A and B). This slow propagation coincides with the intense rainfall events. In contrast, explicit deep convection shows that the low-level zonal winds are largely opposed to the upper-level one (Fig. 8.2f–h), such that easterly winds are predominant with a zonal wavenumber-one structure. However, the features of standing waves are evident in SS13 and E13 (Fig. 8.2 g and h), which are not observed in the zonal wind at
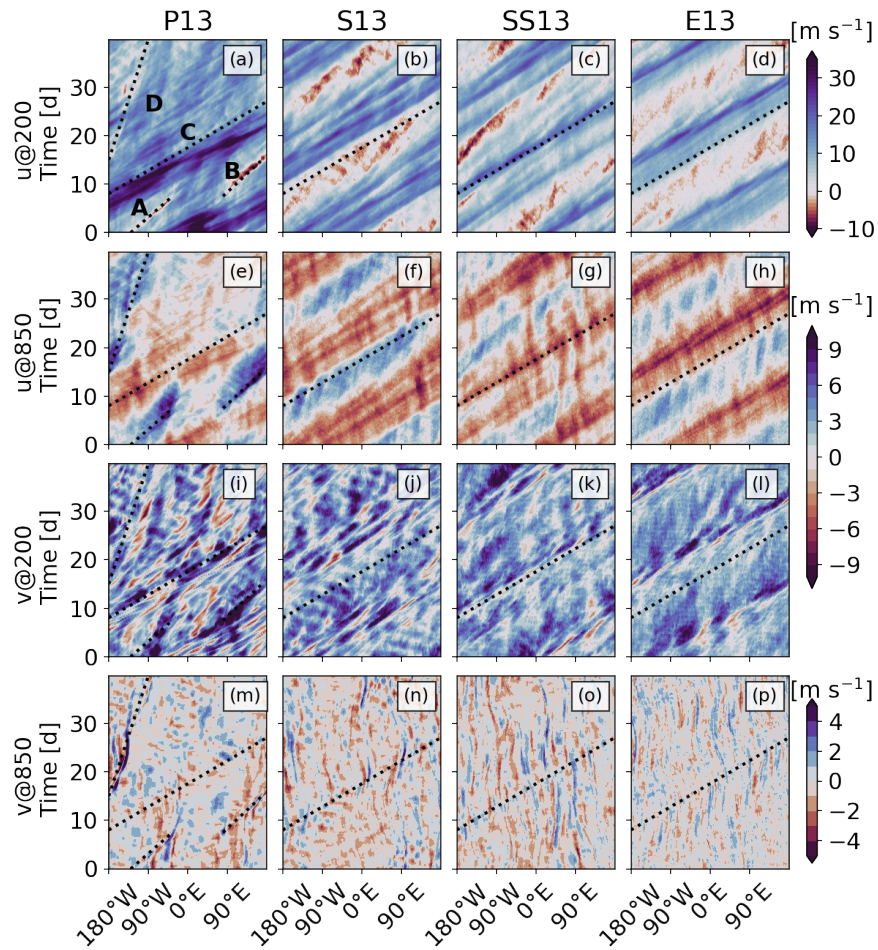
Figure 8.2: Hovmöller diagrams of unfiltered horizontal winds averaged over 0–10°N [m s^{-1}] covering the analysis period over 40 days for each aquachannel experiment: (a–d) zonal wind at 200 hPa, (e–h) zonal wind at 850 hPa, (i–l) meridional wind at 200 hPa and (m–p) meridional wind at 850 hPa. The dotted lines indicate phase speeds. A: 17 m s^{-1}, B: 15 m s^{-1}, C: 24 m s^{-1} and D: 5 m s^{-1}. Note that only line C is illustrated in S13, SS13 and E13.

200 hPa. The evidence of standing waves in the low-level wind and precipitation suggests that persistent structures may be associated with congestus or shallow clouds.

Figure 8.2i–l shows that southerly winds at 200 hPa are predominant in the northern hemisphere in all four runs, corresponding to the Hadley circulation in the ITCZ in Section. 7.1.2. (Note that northerly winds are predominant when the average is carried out in the southern hemisphere.) P13 (Fig. 8.2i) shows evidence of a fast eastward propagation of $27\,\mathrm{m\,s^{-1}}$, which slightly deviates from line C. Eastward propagation is also observed (e.g., west of line D), but the propagation speed is slower at $7\,\mathrm{m\,s^{-1}}$. In the other runs with explicit deep convection (Fig. 8.2j–l), strong southerly winds ($\geq 8\,\mathrm{m\,s^{-1}}$) are aligned with the westerly winds at 200 hPa. E13 exhibits a zonal wavenumber of one in the meridional wind pattern at 200 hPa. This is also evident in SS13 but to a lesser extent. The meridional wind pattern at 200 hPa in S13 shows higher zonal wavenumbers than one.

Figure 8.2m–p shows the meridional winds at 850 hPa. In P13, two delicate meridional wind patterns are observed aligned with lines A and D. Both reveal eastward-propagating characteristics with the one aligned with line A at around $12\,\mathrm{m\,s^{-1}}$, as it deviates from line A, and the other aligned with line D at around $5\,\mathrm{m\,s^{-1}}$, which coincide with the intense rainfall in Fig. 8.1a. Meanwhile, the meridional wind at this level rather shows a standing pattern with explicit deep convection (Fig. 8.2n–p).

To summarize this section, we explored the unfiltered fields of rainfall and horizontal winds. All fields illustrated prominent eastward propagation, except for the meridional wind at 850 hPa. As seen in the mean state (section 7.1), the largest differences are found between parameterized and explicit deep convection. In the following section, the two wave identification methods are applied to examine if the propagation is consistent with EWs.

8.2 Equatorial waves

Section 8.2 presents the variability of precipitation and horizontal winds and their relation with EWs. First, we explore the total variance of precipitation and horizontal winds and their variations on different time scales (6, 24, 72 and 168 hourly), and then how much of the variability on different time scales is explained by each wave type in section 8.2.1. After that, we focus on KWs, the contribution of which is the largest among EWs in section 8.2.2.

8.2.1 Variability related to equatorial waves

a. Precipitation

Figure 8.3 shows rainfall variability on different time scales and how it is correlated with wave-filtered rainfall (WK). The numbers on the x-axes denote the variance of unfiltered precipitation on different time scales, showing that the smoothing reduces total rainfall variance. For example, the total rainfall variance in E13 is reduced by half from one to the next longer time scale. A decrease of variance with a longer time scale is also substantial in P13, S13 and SS13 but not as

dramatic as seen in E13. One intriguing aspect is that rainfall variability on the 6-hourly time scale changes unsystematically with convective treatment, leading to 0.037, 0.045, 0.041 and 0.036 $mm^2 h^{-2}$ for P13, S13, SS13 and E13, respectively. Moreover, the runs with parameterized shallow convection (P13, S13 and SS13) share similar values of precipitation variance on the longer time scales, while explicit shallow convection (E13) marks the lowest variance compared to its counterparts. Note that ICON in the realistic global configuration produces higher total rainfall variance with explicit deep and shallow convection than with parameterized one. For example, the 20-km runs exhibit rainfall variance of 0.08 $mm^2 h^{-2}$ for parameterized deep and shallow convection and 0.17 $mm^2 h^{-2}$ for explicit deep and shallow convection (Fig. 6.1). This suggests that extratropical forcings and convection-triggering processes over land can change the sensitivity of rainfall variability to convective treatment. Additionally, the mean state analysis (Fig. 7.1) showed the differences in mean precipitation and its intensity clearly lie between parameterized and explicit deep convection. Given the results in the previous chapters, the differences in precipitation variability between the runs are unexpected and indicate an important role of shallow convection for rainfall variability, presumably through the moisture exchange between the BL and the free troposphere.

When paying attention to how much rainfall variability is explained by each wave type, the relative importance of EWs to explain rainfall variability varies with different time scales and different convective treatments. On the 6-hourly time scale (Fig. 8.3a), the total fraction of rainfall variability explained by EWs shows a substantial difference between parameterized and explicit shallow convection (46.3, 45.5, 43.9 and 29.4 % for P13, S13, SS13 and E13, respectively). At this scale, rainfall variability is dominated by KWs, leading to correlation coefficients of 21.5, 20.9, 22.1 and 12.3 % for P13, S13, SS13 and E13, respectively. Once again, E13 marks the lowest value, although the unfiltered field of precipitation (Fig. 8.1d) clearly illustrates eastward-propagating patterns. This again demonstrates the important role of shallow convection for wave-convection coupling. For E13, triggering convection is hard without the aid of the convection scheme, leading to the localization of rainfall, the evidence of this may be the standing-wave features, previously seen in the unfiltered fields. This applies to deep convection in S13 and SS13, but shallow convection is parameterized, which facilitates the exchange of moist static energy between the BL and free troposphere, such that triggering convection becomes easier, consequently increasing rainfall variance and KW activity.

The second largest contribution to precipitation variability on the 6-hourly time scale (Fig. 8.3a) is explained by EIGs (7.4–11.8 %), except for SS13 where rainfall variability is slightly more strongly correlated with ERs (R^2 = 8.6 %) than EIGs (R^2 = 8.3 %). Note that the spatial pattern of EIGs is antisymmetric about the equator. It is indicative that despite the symmetric nature of the simulation setup, our aquachannel simulations produce different modes of variability. Following EIGs, the next highest fraction of the total precipitation variance is contributed by ERs (5.4–8.6 %). WIG1s are slightly more important for rainfall variability (2.6–4 %) than MRGs (1.8–3.2 %).
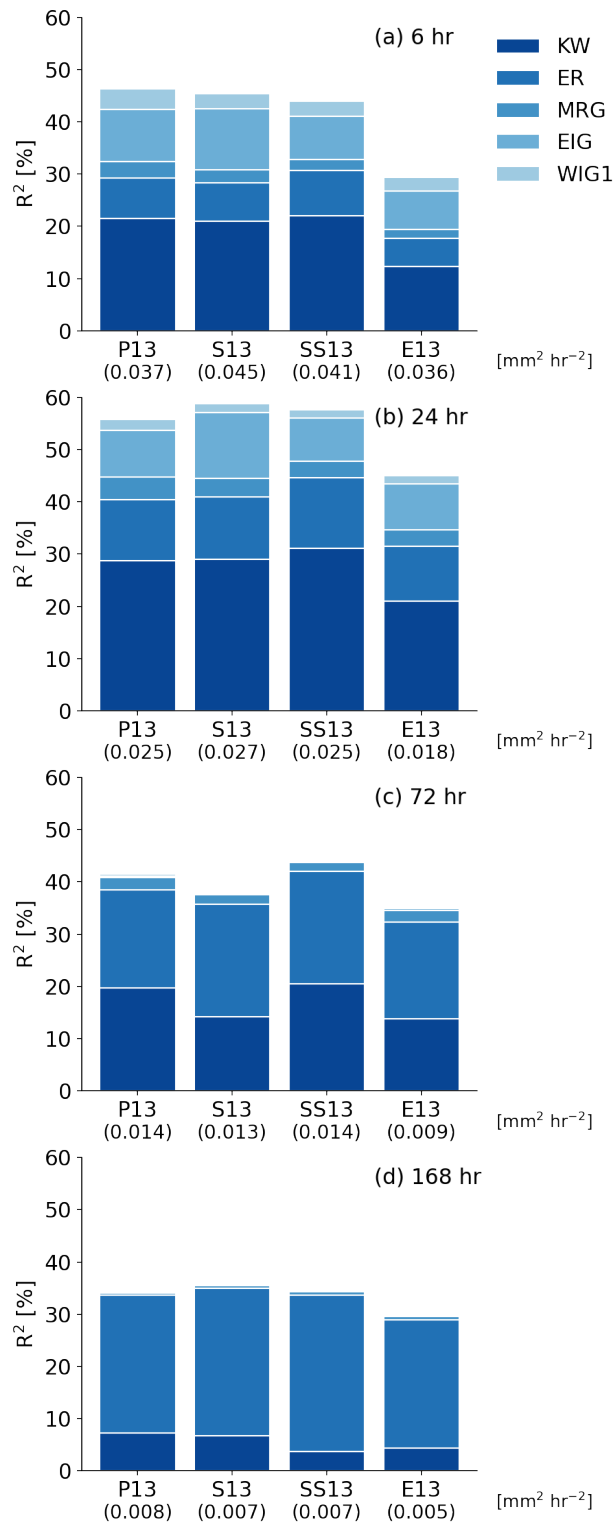
Figure 8.3: Fraction of total precipitation variance explained by each wave type using the WK method [%] on (a) 6-hourly, (b) daily, (c) 3-day and (d) weekly time scales. The numbers on the bottom indicate the total precipitation variance [mm^2 h^{-2}] on the corresponding time scales. All fields are averaged from 0° to 10°N before the computation of variance and correlations.

	P13	S13	SS13	E13
WK method [10^2 mm^2 h^{-2}]				
KW	0.59	0.77	0.76	0.33
ER	0.08	0.18	0.15	0.11
MRG	0.03	0.03	0.02	0.02
EIG	0.29	0.43	0.27	0.22
WIG1	0.1	0.09	0.07	0.06
YP method [m^2 s^{-2}]				
KW	11.1 (6.8)	34.6 (16.1)	22.8 (8.9)	29.6 (14.5)
ER	0.9 (0.1)	0.6 (0.1)	0.3 (0.1)	0.2 (0.04)
MRG	0.4 (0.05)	0.5 (0.09)	0.3 (0.1)	0.3 (0.07)
EIG	2.1 (0.08)	1.0 (0.04)	0.8 (0.04)	0.6 (0.03)
WIG1	0.2 (0.03)	0.1 (0.02)	0.05 (0.02)	0.04 (0.02)

Table 8.1: Wave-related absolute variances of precipitation and horizontal winds for each experiment. For the YP field, wind variances at 200 hPa are represented and corresponding values at 850 hPa in parenthesis. Note that wave signals are obtained using 6-hourly data (section 5.1), so the absolute variances are calculated from the 6-hourly signals.

On the daily time scale (Fig. 8.3b), the sum of the wave contributions is the largest compared to other time scales, which is in line with Schlueter et al. (2019). Again, the differences are mainly between parameterized and explicit shallow convection and KWs govern rainfall variability as seen in Fig. 8.3a. Although the correlation of EIGs to rainfall variability changes only by about 1 % between the two time scales, ERs become more important than EIGs on the daily time scale, leading to R^2 of 11.8, 11.9, 13.6 and 10.6 %.

On the longer time scales (Fig. 8.3c and d), ERs become the major source of rainfall variability, except for the 3-day precipitation in P13 where KWs and ERs are equally important. Although KWs become less important, specifically on the weekly time scale, they are still correlated with rainfall variability, explaining 18.5–21.6 % of the 3-day rainfall variability and 3.7–7.2 % of the weekly rainfall variability. The importance of ERs for rainfall variability on longer time scales agrees with Schlueter et al. (2019), whose research focus was on North Africa from April to October, but in their study KWs lose their importance for rainfall variability on a time scale longer than a day.

b. Horizontal winds

Figure 8.4 shows horizontal wind variability at 200 hPa (left) and 850 hPa (right) on different time scales and how they are correlated with wave-filtered winds (YP). For variance of horizontal winds at 200 hPa (the numbers on the x-axes), P13 shows the largest values for all time scales, specifically compared to E13, while at 850 hPa wind variability of P13 is moderate among the four aquachannel simulations. This may be associated with more organized precipitating systems in P13 that can modulate the upper-level wind fields, while latent heating by short-lived, intense rainfall in explicit deep convection is quickly adjusted in the tropics by gravity waves but

linked to the relatively high variance of the lower-level dynamic fields. The exception is SS13. As the stochastic scheme is designed to take into account missing variability by the deterministic version (Sakradzija et al., 2020), it is unexpected why SS13 presents the low variance of winds at 850 hPa.

Figure 8.4 shows that KWs govern zonal wind variability on all time scales in all simulations, whereas other wave types are weakly correlated with meridional wind variability, and even their total contributions are smaller than the contribution of KWs alone. An exception is the sum of ERs, MRGs and EIGs in P13 on the 6-hourly and daily time scales, the bars of which are slightly higher than the KW ones (Fig. 8.4 a and b). These results qualitatively and quantitatively confirm that the eastward-propagating features in the unfiltered zonal wind fields (Fig. 8.2) are dominated by KWs.

Another interesting aspect is that on all time scales, the variability of zonal winds explained by KWs substantially differs between parameterized and explicit deep convection, rather than shallow convection despite the fact that P13 exhibits the highest wind variability overall. Also, the absolute value of zonal wind variance of KWs is smaller for P13 than for the other simulations in Table 8.1. (Note that wave identification is applied to the 6-hourly dataset in this thesis and smoothing is carried out to unfiltered fields only for the correlation analysis on different time scales, so wave variance refers to the variance of the 6-hourly data.) This means that the zonal wind variability is dominated by KWs with explicit deep convection, but other modes of variability, which are not identified using the YP method, are also important for the zonal wind variability in P13, which contributes to the high variability of zonal winds.

For meridional wind variability, the relative importance of EWs varies with the time scale and altitude of interest. On the 6-hourly and daily time scales (Fig. 8.4a, b, e and f), EIGs contribute to the 200-hPa meridional wind variability the most, compared to ERs and MRGs, explaining 17–21 %, while their importance substantially decreases at 850 hPa, explaining only about 5 % with explicit deep convection and about 11 % with parameterized deep convection. At this level, ERs are most important for P13 and S13 (R^2 = 14–16 %) and MRGs are most important for SS13 and E13 (R^2 = 10–13 %). We speculate that the different relative importance of EWs between the two levels is associated with a Doppler-shift effect. In this latitudinal belt between 0° to 10°N the mean zonal wind at 200 hPa is 13, 7, 6 and 5 m s^{-1} for P13, S13, SS13 and E13, respectively, while the corresponding zonal wind at 850 hPa is almost 0 m s^{-1} for P13 and −2 m s^{-1} for the other runs. The mean zonal wind alters the nature of the wave modes (Dias and Kiladis, 2014), but the results are opposite to Yang et al. (2007a), who found the evident structure of EIGs with the strong easterly mean wind consistent with the notion of Doppler shifting by the easterly wind (see Fig 2. in Yang et al., 2003). We leave the further investigation of a Doppler-shift effect on EIGs for future study.

On the longer time scales (Fig. 8.4c, d, g and h), MRGs gain importance for meridional wind variability, which is not observed in rainfall variability. Also, P13 and S13 show that ERs become less important for meridional wind variability on the 3-day and weekly time scales, which is opposite to their role for rainfall variability. Meanwhile, the importance of ERs for
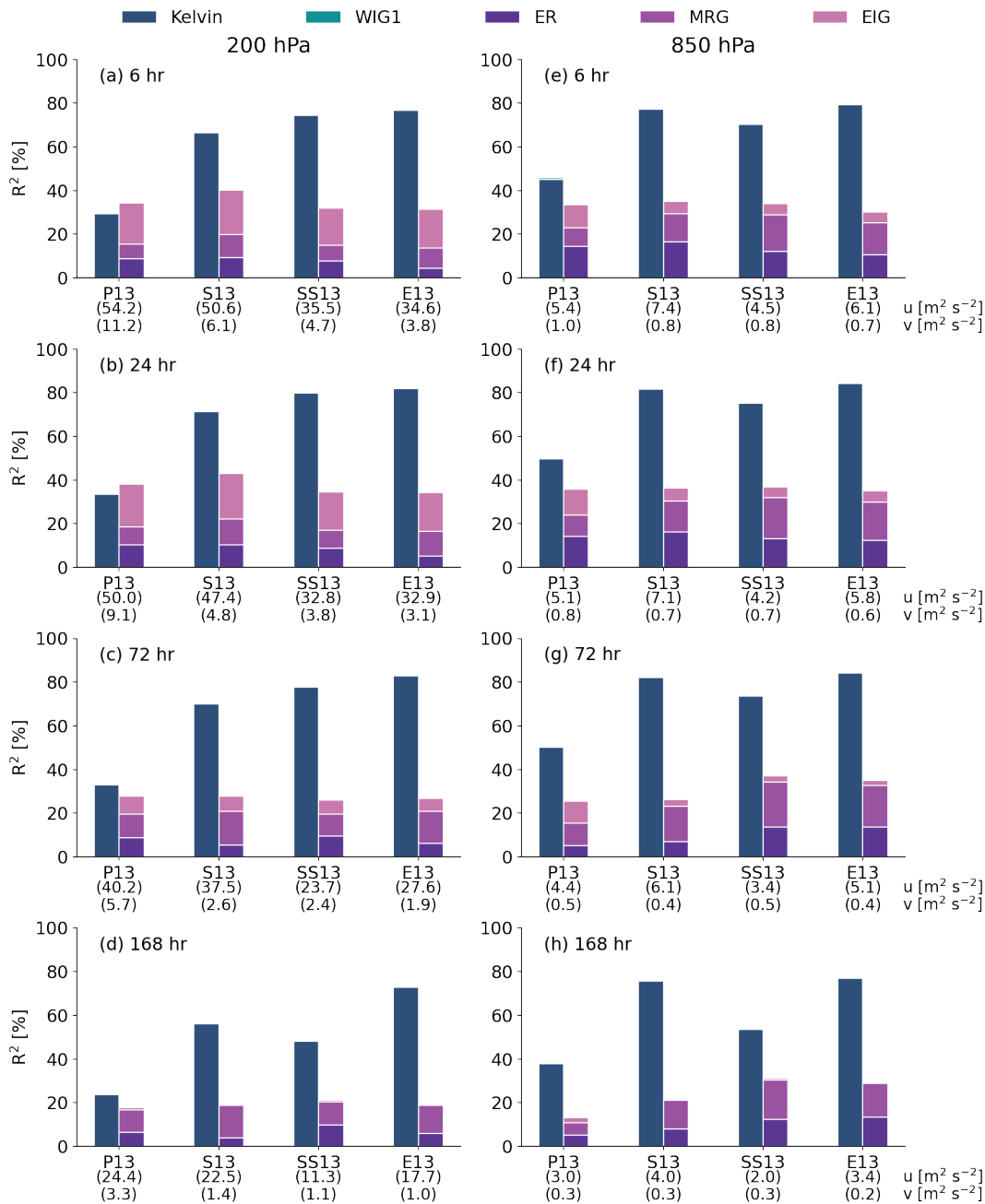
Figure 8.4: Fraction of total variances of zonal wind (left bars in blue hue) and meridional wind (right bars in purple hue) on different time scales at (a–d) 200 hPa and (e–h) 850 hPa explained by each wave type [%] using the YP method. The numbers on the bottom indicate the total variances of (first row) zonal wind and (second row) meridional wind [$m^2 s^{-2}$] on the corresponding time scale. Note that R^2 of < 1 % for WIG1 is too small to be visually shown in the box plots. All fields are averaged from 0° to 10°N before the computation of variance and correlations.

SS13 and E13 does not vary much with different time scales with a small increase of R^2 by 1 % at 200 hPa.

To summarize, rainfall variability and its correlation with EWs on the 6-hourly and daily time scales differ mainly between parameterized and explicit shallow convection. This difference is evident in the KW contribution. On the longer time scales ($\geq$ 3 days), ERs gain importance with a less important role of KWs. In contrast, P13 overall exhibits the largest variability of horizontal winds but the lowest correlation of KWs to zonal wind variability on all time scales, compared to explicit deep convection. What type of waves explains meridional wind variability depends on the vertical level and we observe Doppler-shift effects on EIGs, MRGs and ERs. Finally, EWs identified by the YP method do not show the relatively important role of ERs on the longer time scales. The different importance of waves between the two fields indicates that the larger fraction of wind variability explained by EWs does not necessarily translate into better wave-convection coupling. Furthermore, the unexpected differences between parameterized and explicit shallow convection may be associated with the crucial role of shallow convection for the moisture exchange between the BL and free troposphere, a process that is frequently observed in the early stage of the life cycle of convectively coupled EWs (Mapes et al., 2006; Kiladis et al., 2009).

8.2.2 Kelvin waves

The previous subsection quantified how much of each wave type is correlated with the variability of precipitation and horizontal winds on different time scales, and overall KWs have the strongest correlation with those variabilities. This subsection thus focuses on KWs.

Figure 8.5 shows Hovmöller diagrams of the WK-filtered and YP-filtered KWs that illustrate wave amplitude and phase speeds. (The full spectrum of EWs is shown in Figs. B.10 and B.11.) As expected from the previous discussions, E13 (Fig. 8.5g and h) clearly illustrates a wavenumber-one feature that propagates eastward at the phase speed of 24 m s^{-1} using both the WK and YP approaches. The rainfall signal is aligned with the westerly wind signal at 200 hPa, which corresponds to the easterly wind signal at 850 hPa (Fig. B.12). The mirroring pattern between 200 and 850 hPa suggests a first baroclinic structure of KWs and no Doppler-shift effect on them (Dias and Kiladis, 2014). Together with the mean easterly flow in the lower troposphere (Fig. 7.2d), easterly anomalies of KWs intensify local horizontal winds and thus can induce surface enthalpy fluxes, which in turn can trigger the development of convection. This suggests that the wind-induced surface heat exchange (WISHE) may be important for rainfall associated KWs for E13 (Emanuel, 1987; Neelin et al., 1987). The role of surface enthalpy fluxes for KWs will be discussed further using a composite analysis.

The largest contrast to E13 is found in P13 (Fig. 8.5a and b). The rainfall signals show mainly two different phase speeds with the slow propagation of around 15 m s^{-1} (marked by lines A and B) and the fast propagation of 24 m s^{-1} (marked by line C). The slow propagation is associated with the intense rainfall ($\geq$ 0.75 mm h^{-1}) that lasts up to around 10 days (Fig. 8.1a). Meanwhile,
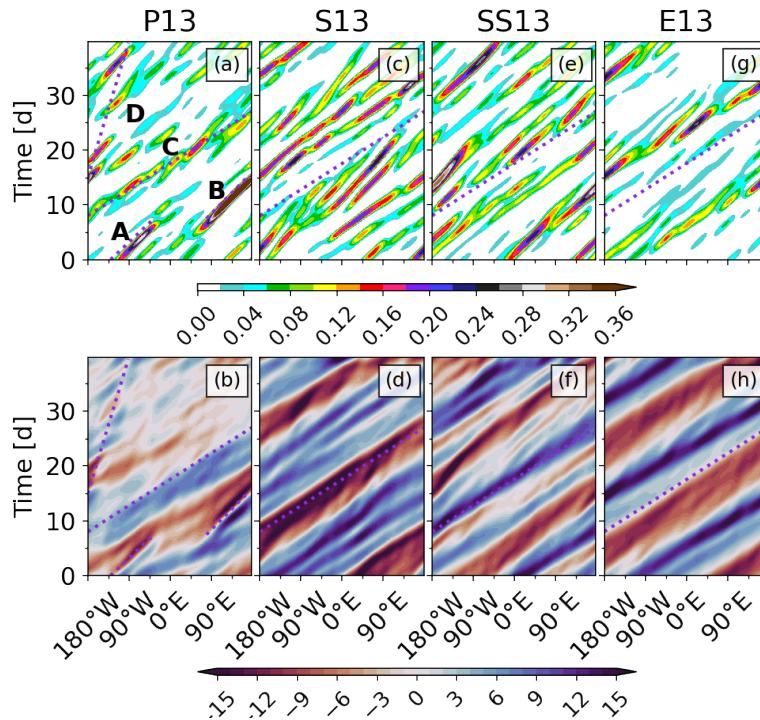
Figure 8.5: Hovmöller diagrams covering the analysis period over 40 days of (top) KW-filtered precipitation averaged over 0–10°N [mm h^{-1}] and (bottom) KW-filtered zonal wind at 200 hPa. The WK and YP methods are applied to precipitation and horizontal wind, respectively. The dotted lines indicate phase speeds. A: 17 m s^{-1}, B: 15 m s^{-1}, C: 24 m s^{-1} and D: 5 m s^{-1}. Note that only line C is illustrated in S13, SS13 and E13.

the fast propagation is associated with moderate rainfall (0.08 mm h^{-1}) and travels through the entire channel domain. The wind signal (Fig. 8.5b) shows that the wave amplitude substantially decreases from the first half to the second half simulation period, leading to R^2 of 41.4 and 18.8 %, respectively (not shown). In the first half of the simulation period, the moderate to strong rainfall signals (lines A–C in P13) remarkably coincide with the upper-level divergence associated with KWs, indicating that rainfall is in phase with KWs. In contrast, the marked rainfall signal (line D) does not show this wind-rainfall relation (discussed below in detail).

The identified KWs in S13 and SS13 (Fig. 8.5c–f) share similar features to those in E13. Both rainfall and wind signals largely exhibit eastward propagation at 24 m s^{-1}, although some slower motions are detected in the rainfall signals in S13 (Fig. 8.5c). The fast propagation is characterized by a zonal wavenumber of one and travels through the entire simulation domain as in E13. However, there are differences from E13. The rainfall and wind signals of KWs exhibit substructures within the wavenumber-one feature, as seen in the unfiltered zonal winds. The wavenumber of these signals ranges from 3 to 5. These values are closer to those of observed KWs than the zonal wave number of one (e.g., Wheeler and Kiladis, 1999; Yasunaga and Mapes, 2012). In S13 and SS13, the enhanced rainfall signals coincide with both upper-level divergence and easterly wind anomalies associated with KWs. The former and latter relations are shown in P13 and E13, respectively. This means that S13 and SS13 generate a mixture of behaviors of KWs between P13 and E13. Another noteworthy feature is that S13 has strong easterly
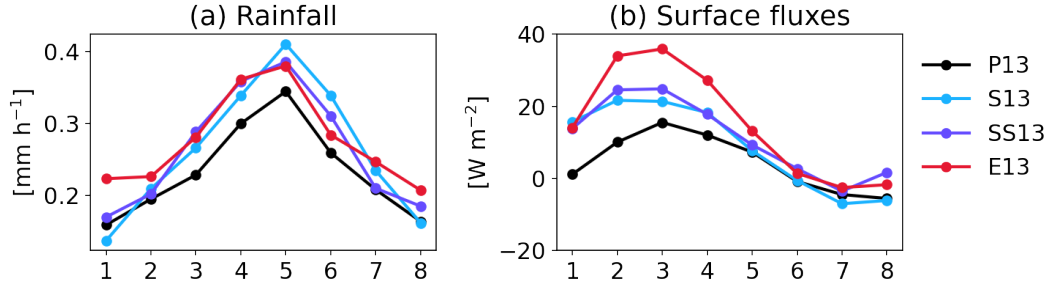
Figure 8.6: Composite of (a) unfiltered rainfall and (b) anomalous surface enthalpy fluxes on the basis of KW phase identified by the YP method. Anomalies of the surface fluxes are obtained by subtracting the horizontal mean between 20°N/S to be consistent with the surface flux analysis for the mean state (section 7.2.1). Composited variables are averaged over 0–10°N. Phases 3 and 5 indicate the upper-level westerly wind anomaly and the maximum upper-level divergence of KWs, respectively. Figure B.3e illustrates how each phase of KWs is composited.

wind anomalies (Fig. 8.5d), marking a sharp upper-level convergence from day 10 to day 30. Correspondingly, the rainfall signal is suppressed along this marked upper-level convergence associated with KWs (Fig. 8.1c and d).

8.3 Composites

Previously, EWs were discussed separately between WK- and YP-filtered fields. Here we link the two fields (WK precipitation and YP winds) using composite analysis. Figure 8.6a shows rainfall modulation in eight phases of KWs that are identified by the YP method. Note that unfiltered rainfall is averaged in each phase on the basis of the KW-filtered wind and Phase 5 indicates the upper-level divergence of KWs (see section 5.2 for more detail). In all four runs, the maximum rainfall is in Phase 5 with values of 0.345, 0.411, 0.386 and 0.380 mm h^{-1} for P13, S13, SS13 and E13, respectively. The minimum rainfall occurs in Phase 1, which indicates the upper-level convergence of KWs, except for E13 where it is in Phase 8, which is one phase prior to Phase 1. The amplitude of the modulation varies with the simulations, showing that the difference between the maximum and minimum rainfall is the greatest for S13 (0.275 mm h^{-1}), followed by SS13 (0.217 mm h^{-1}), which is greater than P13 (0.186 mm h^{-1}), and E13 exhibits the lowest difference of 0.174 mm h^{-1}. These results give the idea that rainfall is strongly modulated through KW dynamics in all simulations, but the strength of wave-convection coupling varies with convective treatment. Somewhat surprisingly, P13 yields the strongest wave-convection coupling. These different amplitudes of rainfall modulation are consistent with the wave-related variance of precipitation when using the WK method (Table 8.1).

Another interesting aspect of the rainfall modulation is that in E13 and SS13 rainfall is substantially greater in Phase 4, i.e., before the upper-level divergence of KWs or convectively active phase, than in Phase 6. Phase 4 indicates the westerly wind anomalies at 200 hPa and corresponding easterly wind anomalies at 850 hPa followed. These easterly wind anomalies can enhance surface fluxes together with the mean easterly flow in the lower troposphere (Fig. 7.2)

and this can lead to increased rainfall through WISHE. This wind-rainfall relation is also evident in the previous section, showing that the enhancement of KW-filtered rainfall is collocated with the KW-filtered westerly wind anomalies at 200 hPa (e.g., Fig. 8.5g and h), indicating that the rainfall signal coincides with the KW-filtered easterly wind anomalies at 850 hPa. (The shape of higher composited rainfall in Phase 4 than in Phase 6 does not change by altering the latitudinal belt, e.g., 0°–10°S or 5°S–5°N, for averaging.)

To assess the role of surface enthalpy fluxes for wave-convection coupling, the surface flux anomalies are composited on the basis of the YP-filtered KWs (Fig. 8.6b). The majority of the simulations (P13, SS13 and E13) show that the maximum positive anomalies of surface fluxes are in Phase 3, where the upper-level westerly and corresponding low-level easterly anomalies are large. Again, the low-level easterly anomalies are superposed with the easterly mean flow in the lower troposphere. This reveals that surface enthalpy fluxes are enhanced at the leading edge of KWs, which can develop convection there. Furthermore, SS13 and E13 exhibit the minimum of the surface flux anomaly in Phase 7, where the low-level wind anomaly by KWs is westerly, so the easterly mean flow opposes the westerly wind anomaly, suppressing surface fluxes there. The largest amplitude of the modulation is observed in E13, followed by S13 and SS13, while P13 exhibits the smallest amplitude. Thus, this suggests the important role of WISHE for convectively coupled KWs with explicit deep convection. It is speculative that it is hard to overcome CIN without a deep convection parameterization, so some support from surface enthalpy fluxes is essential to trigger convection.

So far, we examined how KW dynamics modulate rainfall and surface fluxes. To obtain robust results, we investigate how convectively coupled EWs, identified by the WK method, modulate structures of dynamics and thermodynamics. As the WK method is the most widely used method, we can also compare our results to previous studies who used observations to confirm if the wave modulation in the aquachannel simulations is reasonable.

Figure 8.7 shows the vertical structures of wind and temperature anomalies composited on the basis of the WK-filtered rainfall. Overall, the structures are consistent but clearer with explicit deep convection than with parameterized deep convection. Arguably, the strongest modulation with phases is found in E13 (Fig. 8.7d and h). In the wet Phase 5, strong westerly wind anomalies are observed in the upper troposphere with easterly wind anomalies after the wet phase, indicating the upper-level divergence. Toward lower phases wind structures tilt above and below around 200 hPa, forming an elbow shape. The vertical structure of temperature shows that warm anomalies in the lower troposphere precede the wet phase and during the wet phase warm anomalies at 300 hPa are observed as well as in the BL. In the lower stratosphere, the temperature is tilted with large anomalies ($\pm$ 1.2 K). Overall, these vertical structures of zonal wind and temperature are consistent with the observed KW structures, except that cooling in the BL was in the wet phase (Wheeler et al., 2000; Kiladis et al., 2009; Nakamura and Takayabu, 2022).

The other runs with explicit deep convection (S13 and SS13) closely follow E13 in terms of the vertical structures of zonal wind and temperature (Fig. 8.7b, c, f and g). However, there are
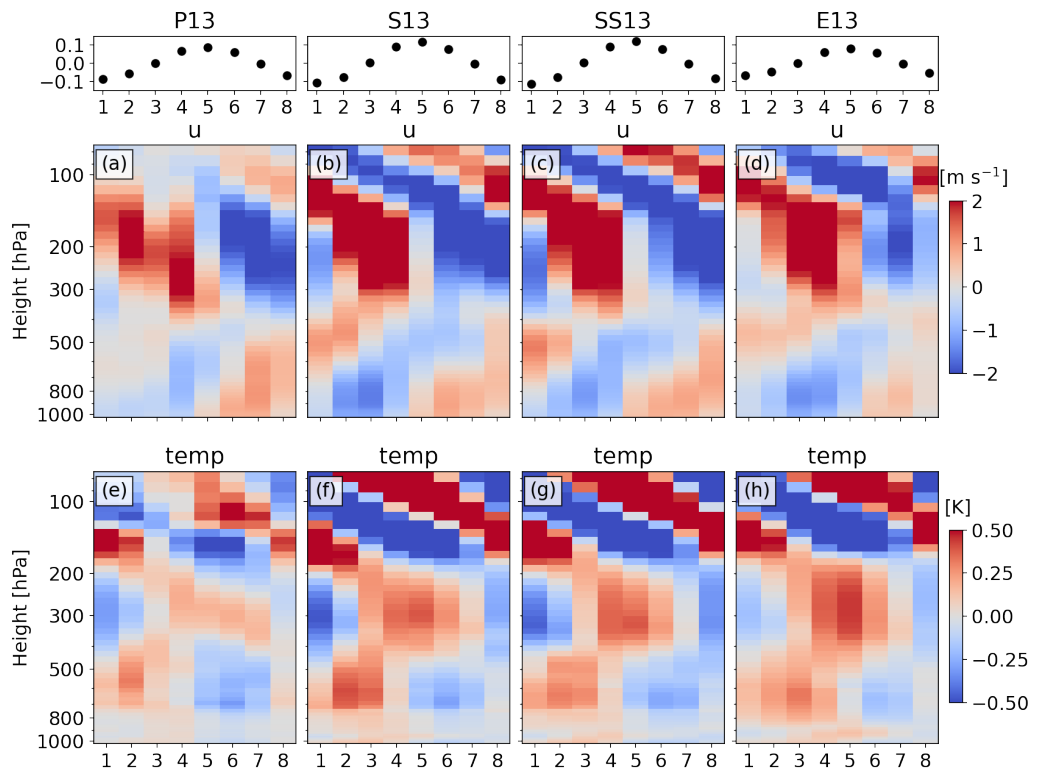
Figure 8.7: Composite of unfiltered (a–d) zonal wind and (e–h) temperature anomalies on the basis of KW wave phase identified by the WK method. Composited variables are averaged over 0–10°N. The associated wave-filtered precipitation anomaly in each phase is shown at the top.

delicate deviations. For S13 and SS13, weak easterly anomalies at 200 hPa (0.1–0.15 m s^{-1}) occur in the wet Phase 5, although the signature of the upper-level divergence is still evident with a sharp contrast of westerly and easterly anomalies with respect to the wet phase. For temperature, differences from E13 are observed below 750 hPa, which is equivalent to 2.5 km, showing that temperature anomalies are rather muted and no warm anomalies are found in the BL during the wet phase but rather weak cold anomalies of 0.02 and 0.05 K for S13 and SS13. These small structural differences in zonal wind and temperature associated with KWs indicate that different shallow convection treatments also impact wave-convection coupling.

The largest differences from E13 are observed in P13 (Fig. 8.7a and e), showing that the modulation of wind and temperature with the wave phase based on KW-filtered rainfall becomes substantially weaker. For zonal wind (Fig. 8.7a), easterly anomalies at 200 hPa in Phase 5 get stronger to 0.28 m s^{-1} compared to S13 (0.16 m s^{-1}) and SS13 (0.09 m s^{-1}), while the westerly and easterly contrast before and after the phase is still observed, marking the upper-level divergence collocated with the wet phase. The dynamical structure faintly depicts the elbow structure, specifically with weak westerly anomalies (< 0.12 m s^{-1}) below 400 hPa (or 7 km) toward lower phases and small wind anomalies in the lower stratosphere ($\pm$ 0.3 m s^{-1}). The temperature structure (Fig. 8.7e) illustrates lower-tropospheric warming before the wet phase and warming at 300 hPa during the wet phase, but warm anomalies are weaker than the other runs. For example, the mid-tropospheric warming of 0.18 K is marked in P13, whereas explicit deep convection exhibits a warming of 0.35–0.45 K. Furthermore, the mid-tropospheric warming is rather concentrated around 300 hPa for P13, while it is more vertically extended between 400 and 200 hPa for explicit deep convection. Temperature anomalies in the tilted structure in the lower stratosphere become substantially weaker from explicit deep convection ($\pm$ 1.2 K) to parameterized deep convection ($\pm$ 0.2 K). Additionally, temperature anomalies below 2.5 km also change weakly with phases, which is seen in S13 and SS13 but differ from E13.

To summarize, the modulation of variables of interest through KWs is largely consistent among the aquachannel simulations and shows some agreement with previous studies using observations. However, some differences are observed due to convective treatment. Evidence of WISHE by KWs is found in SS13 and E13, in which the vertical exchange of heat and moisture is stronger than the other runs by stochastic and explicit shallow convection (Sakradzija et al., 2020). Nonetheless, this relation does not necessarily lead to a strong modulation of rainfall by waves as the largest amplitude of modulation is observed in S13, whereas E13 exhibits the weakest modulation of rainfall. For modulation of zonal winds, explicit deep convection produces a reasonable structure associated with KWs, which is in line with previous studies, while parameterized deep convection generally reduces wind anomalies with wave phase, particularly in the lower stratosphere. The weakened anomalies with parameterized deep convection are also observed for temperature. This may be due to the fact that explicit deep convection can produce more convectively generated momentum fluxes, which is an important factor for stratospheric dynamics (Stephan et al., 2019; Kim and Achatz, 2021). In the lower troposphere, there are differences in temperature anomalies between parameterized and explicit shallow convection, with the former exhibiting reduced anomalies and the latter showing warming in the wet phase,

	P13	S13	SS13	E13
OLR [W m^{-2}]	248.9 ± 23.5	252.6 ± 17.6	252.6 ± 16.1	252.0 ± 14.0
P_{sfc} [hPa]	1029.1 ± 3.0	1029.2 ± 2.9	1029.1 ± 2.7	1029.4 ± 2.7

Table 8.2: The mean of raw fields for OLR, surface pressure (P_{sfc}) for each experiment. The latitudinal belt for the average is between 0°–10°N.

which is opposite to previous studies (Wheeler et al., 2000; Kiladis et al., 2009; Nakamura and Takayabu, 2022). It is speculative that BL warming may be associated with the representation of cold pools, which are not resolved at the horizontal grid spacing of 13 km and they are crucial to form new convection at the leading edge of convectively coupled KWs (Mapes et al., 2006).

8.4   Transition from Kelvin wave to Madden Julian Oscillation

Section 8.2 showed variability explained by EWs related to Matsuno's linear wave solutions. However, we could not identify the distinctive slow-propagating feature in P13 with a speed of about 5 m s^{-1} (aligned with line D in Fig. 8.1a). Furthermore, during the period when this feature is present, the zonal wind signal of KWs is reduced almost by half (Fig. 8.5b). This raises the question if there is an MJO-like disturbance in P13 at the cost of KWs. The competing effect between KWs and the MJO is counterintuitive as some studies, who used narrow filter windows for KWs and MJO, found that KW signals become stronger during the active phase of the MJO (Roundy, 2008; DePasquale et al., 2014; Baranowski et al., 2016). In this section, the structural differences between the MJO-like disturbance and KWs are investigated using composite analysis on the basis of raw fields of OLR and surface pressure to characterize the MJO and KWs, respectively. The focus of the analysis is on P13, where the MJO-like disturbance is present, and E13, where a wavenumber-one KW signal is discernible.

We first present raw fields of OLR and surface pressure in P13 and E13 (Fig. 8.8). In ICON, OLR corresponds to the upward radiative fluxes at the top of the atmosphere, obtained from the radiation scheme. The pattern of OLR shows greater variance for P13 than for E13, with marked low OLR in the former. This leads to a smaller mean value of 248.9 W m^{-2} but a greater standard deviation of 23.5 W m^{-2} for P13, compared to E13 (252.0 ± 14.0 W m^{-2}, Table 8.2). For P13 (Fig. 8.8a), the marked OLR with low values (< 190 W m^{-2}) is aligned with lines A, B and D. The previous section showed that strong KW activity in rainfall and winds were found along with lines A and B for P13 (Fig. 8.5a and b). The discernible decrease in the KW wind signal was observed with line D (Fig. 8.5b). For E13 (Fig. 8.8b), a wavenumber-one feature manifests the raw OLR field, which coincides with KWs.

Differences in surface pressure between the simulations are rather subtle (Table 8.2), as the tropics are characterized by small fluctuations in temperature and pressure. Despite that, most propagating features that we discussed earlier are evident in the patterns of surface pressure (Fig. 8.8c and d). Again, the evidence of the wavenumber-one pattern indicates the activity
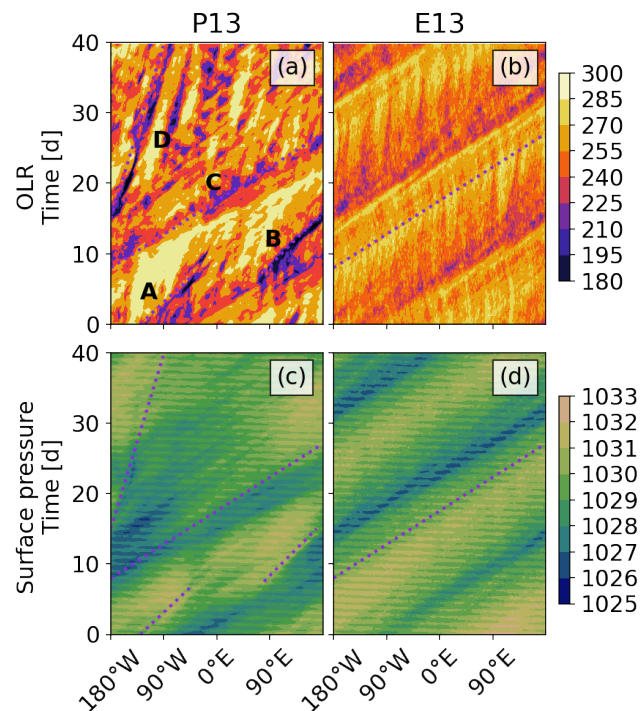
Figure 8.8: As in Fig. 8.1 but for (top) OLR [W m^{-2}] and (bottom) surface pressure [hPa] in P13 and E13. The dotted lines indicate phase speeds. A: 17 m s^{-1}, B: 15 m s^{-1}, C: 24 m s^{-1} and D: 5 m s^{-1}. Note that only line C is illustrated in E13.

related to KWs in E13. This pattern is found in P13 in the first half of the simulation period, but it is less clear in the later period when the slow propagation is present.

Based on the raw fields of OLR and surface pressure, we divide the simulation period of P13 into two periods before and after day 15. We composite variables of interest using the lowest surface pressure and the low OLR at a time step for KWs and the MJO, respectively. The detailed description of the method is found in section 5.4. In the remainder of the study, the first period (0–14 days) in P13 is called an active KW period and the second period (15–40 days) is called an active MJO period. As the KW signals are remarkably persistent in E13, we call the entire 40-day period of E13 a reference KW period.

Figure 8.9a shows the composite field of precipitation on the basis of OLR in P13, which represents the MJO signal. Intense precipitation is in phase with the MJO-like disturbance and the maximum precipitation is off-equatorial, forming a swallowtail pattern. The off-equatorial maximum is in line with previous studies (Maloney and Hartmann, 1998; Zhang and Ling, 2012), which explained that off-equatorial flows associated with Rossby waves induce moisture convergence, leading to the unique rainfall pattern (Salby et al., 1994). The maximum precipitation is observed only in the northern part, leading to antisymmetry in precipitation with respect to the equator. The OLR pattern follows the precipitation pattern, showing that the low values of 150 W m^{-2} are near the maximum rainfall (> 1.8 mm h^{-1}). It is uncertain if the meridional antisymmetric patterns in precipitation and OLR are characteristics features of

the MJO-like disturbance in our case or if the simulation period limits to having fair statistics as the MJO-like disturbance travels only a quarter of the entire domain. The zonal pattern of rainfall also exhibits antisymmetry with respect to the reference longitude of 0°, such that it is greater on the upwind side ($0.47 \, \mathrm{mm \, h^{-1}}$) than on the downwind side ($0.26 \, \mathrm{mm \, h^{-1}}$) of the eastward-propagating disturbance. Similarly, the composite surface pressure (Fig. 8.9d) shows that it is greater on the upwind side by 1.5 hPa than on the downwind side. This leading low surface pressure is observed when enhanced convection associated with the MJO passes over the Maritime Continent and western Pacific (see Fig. 1 in Zhang, 2005).

Figure 8.9b shows the composite precipitation on the basis of surface pressure from E13, which represents the KW signal. Precipitation mostly occurs within the ITCZ, forming a banded structure, and it is higher on the upwind side ($0.65 \, \mathrm{mm \, h^{-1}}$) than on the downwind side ($0.32 \, \mathrm{mm \, h^{-1}}$) with respect to the lowest surface pressure. The composite OLR follows the pattern of precipitation. When we composite rainfall and OLR on the basis of the lowest surface pressure from P13 (Fig. 8.9c), the patterns closely follow those from E13 in terms of the zonally extended band shape and zonal antisymmetry between the upwind and downwind sides. Similarities of KWs between P13 and E13 are also found in surface pressure and PW anomalies (Fig. 8.9e and f). The surface pressure pattern is symmetric with respect to the relative longitude of 0°, which is ahead of intensified rainfall on the upwind side of KWs. A similar phase difference between rainfall and surface pressure was shown in Kim and Zhang (2021). PW anomalies are greater on the upwind side than on the downwind side, indicating that large PW anomalies follow KWs.

To understand structures of dynamics and thermodynamics associated with the MJO-like disturbance and our reference KWs, we composite anomalies of surface enthalpy fluxes F_h, the vertically integrated longwave and shortwave radiative fluxes and horizontal winds at the surface and 200 hPa, which are shown in Fig. 8.10. (Note that Fig. 8.10 focuses on longitudes between 50°W and 50°E to cover more than half a wavelength of KWs while still centering on the reference point.) Here we take the anomaly from the horizontal mean of the latitudinal belt between 20°N/S to avoid the distorted fields due to the closed walls (section 4.2). A east-west contrast of F_h anomalies is discernible with respect to the center of the MJO-like disturbance (Fig. 8.10a). The positive anomalies of F_h ($> 30 \, \mathrm{W \, m^{-2}}$) to the west of the MJO center are collocated with anomalous westerly wind near the surface, while equatorial surface wind anomalies are very small to the east with negative anomalies of F_h ($< -30 \, \mathrm{W \, m^{-2}}$). Surface winds exhibit a hint of a pair of cyclonic Rossby gyres in phase with the MJO-like disturbance and its northern branch is collocated with the intense rainfall ($> 1.8 \, \mathrm{mm \, h^{-1}}$). This surface wind pattern is consistent with low-level wind patterns in the Matsuno-Gill model (Gill, 1980) and the skeleton model (Majda and Stechmann, 2009), which are used to understand the MJO structure.

Composite structures associated with KWs (Fig. 8.10b and c) exhibit a large contrast to those with the MJO-like disturbance. The latitudinal distribution of anomalies of F_h and surface winds resembles the mean state, such that F_h is enhanced in the vicinity of the ITCZ as well as the surface winds (section 7.2.1) and surface easterly wind anomalies blow towards the equator
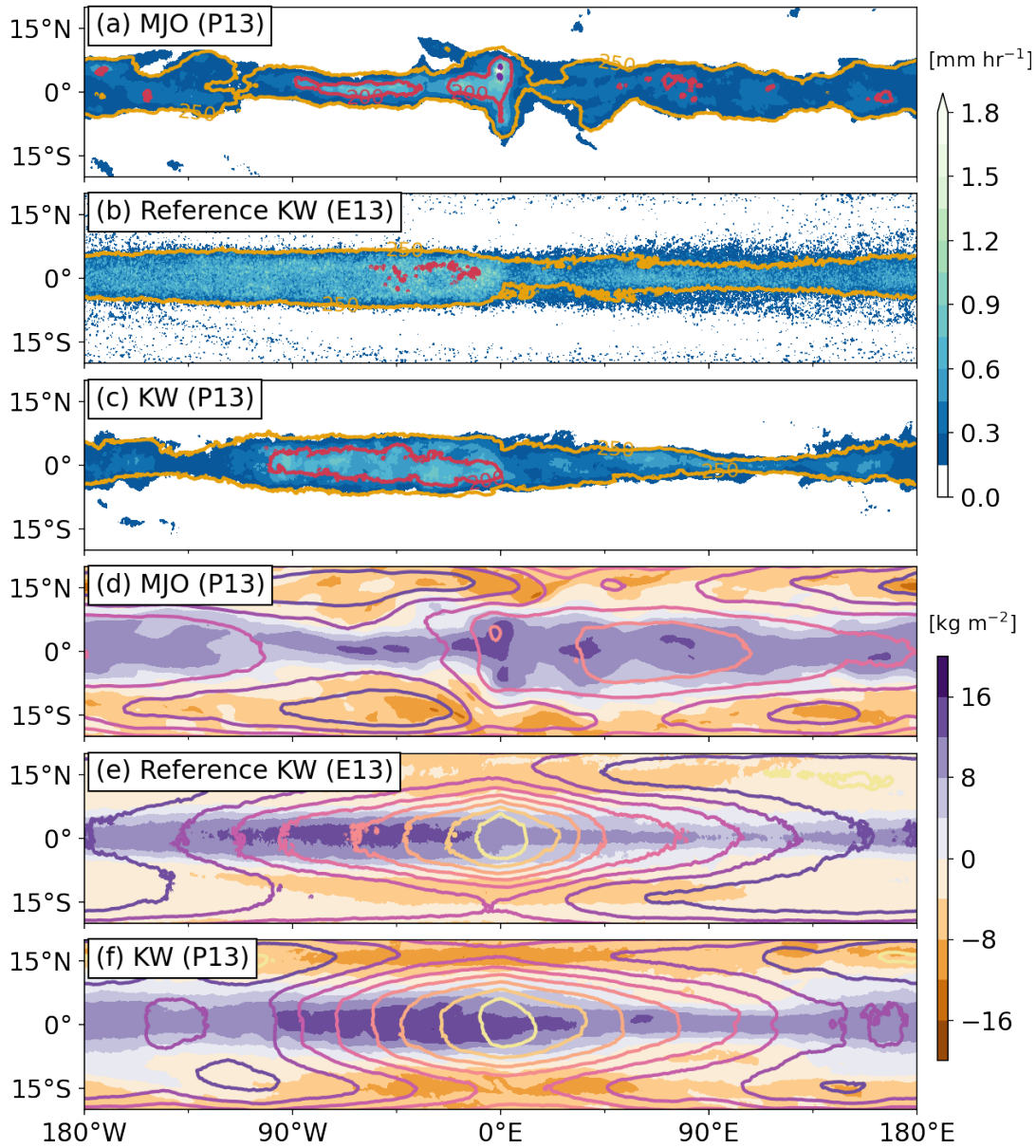
Figure 8.9: Composite fields of (a–c) precipitation [mm h^{-1}] in shading and OLR [W m^{-2}] in contour and (d–f) anomalies of precipitable water (PW) [kg m^{-2}] in shading and surface pressure [hPa] in contour. (a and d) The fields are constructed on the basis of low OLR values and (b, c, e and f) lowest surface pressure at each time step. The contours are every 50 W m^{-2} for OLR and 0.5 hPa for surface pressure. The relative longitude of 0° indicates the basis of the low OLR and the lowest surface pressure at a time step for the MJO and KWs, respectively.
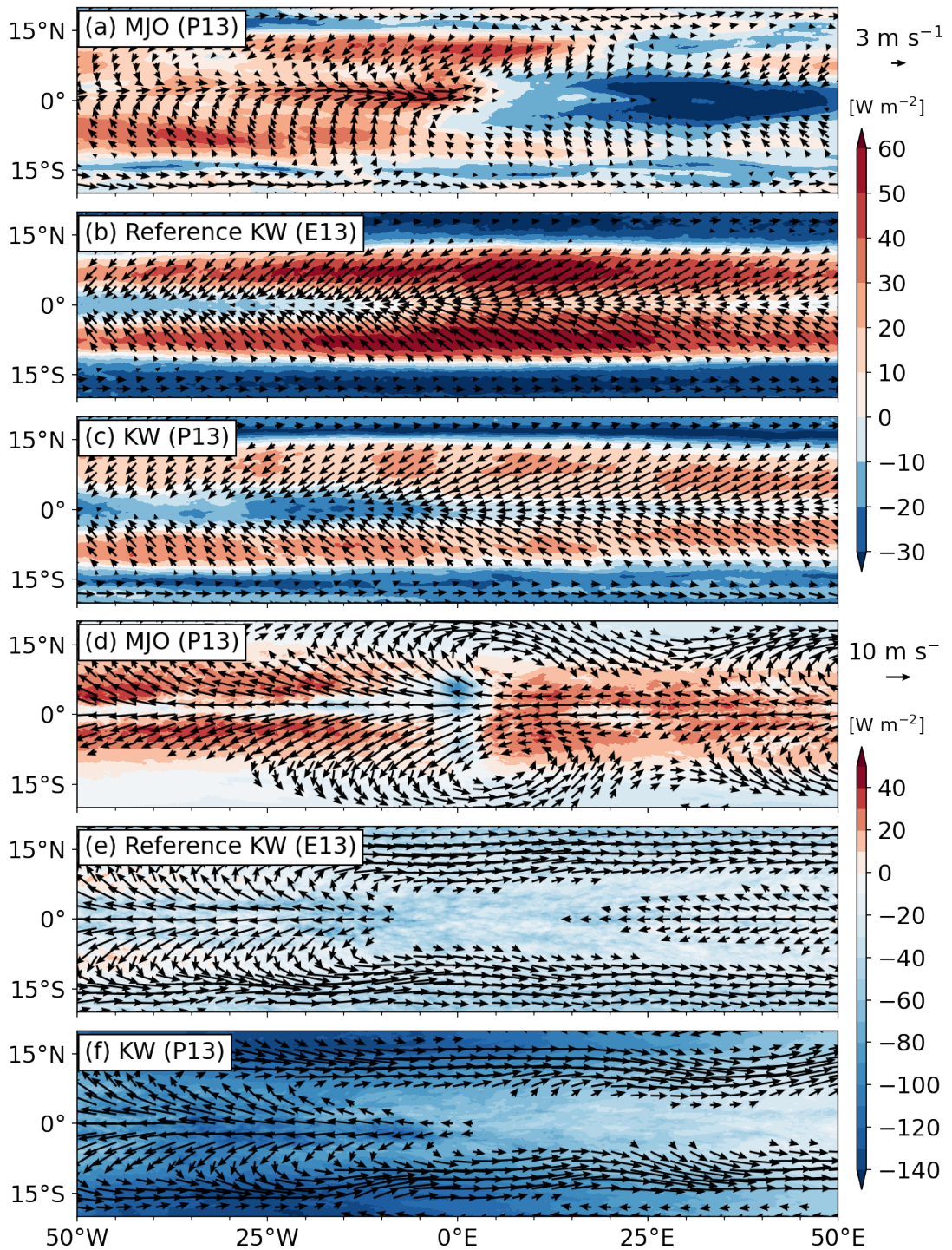
Figure 8.10: As in Fig. 8.9 but for (a–c) anomalies of surface enthalpy fluxes [W m^{-2}] in shading and anomalies of surface horizontal winds [m s^{-1}] in vector and (e–f) anomalies of the vertically integrated radiative fluxes [W m^{-2}] in shading and anomalies of 200-hPa horizontal winds [m s^{-1}] in vector. Surface wind anomalies are illustrated when their speed is greater than 0.5 m s^{-1}. Horizontal winds at 200 hPa are illustrated when their speed is greater than 2 m s^{-1}. Note that the longitudinal extent is between 50°W and 50°E.

(Fig. 7.2). However, there are distinctive features associated with KWs in E13 (Fig. 8.10b). To the east of the reference KW point, anomalies of F_h are positive near the equator with equatorial easterly anomalies near the surface. To the west F_h is suppressed with very small wind anomalies near the surface. Surface wind speed associated with KWs increases by 1.5–2 m s^{-1} from the mean field, specifically between 10°N–10°S (not shown but the surface horizontal wind field is quite similar to its anomaly field). This supports the role of WISHE for KWs discussed in section 8.3.

Figure 8.10d–f shows composite anomalies of the vertically integrated radiative fluxes and horizontal winds at 200 hPa for each case. At the MJO reference point (Fig. 8.10d), total radiative cooling of 16.6 W m^{-2} is observed. In contrast, in the leading edge of the MJO, there is strong total radiative heating of 23.1 W m^{-2} while the tail of the MJO consists of weak radiative cooling at the equator and warming at the off-equator, leading to the total effect of −0.5 W m^{-2} on average. The strong total column radiative heating effect at the leading edge may be associated with the propagation of the MJO-like disturbance by destabilizing atmospheric columns ahead of the MJO reference point. The cloud-radiative feedback, which increases instability ahead of the MJO, is crucial to explain the MJO propagation in moisture modes (Sobel and Maloney, 2013; Adames and Kim, 2016).

The anomalous horizontal winds at 200 hPa (Fig. 8.10d) illustrate a distinct pair of anticyclonic flows around the MJO reference point with the center of this pair located ahead of the reference point. This suggests a vertical tilt in the dynamical structure, as the cyclonic pair at the surface is in phase with the MJO-like disturbance. Also, anomalous easterly flow near the equator is remarkable, given the fact that the background wind near the equator is westerly in the upper troposphere (Fig. 7.2a). Furthermore, this anticyclonic pattern is observed in studies using the Matsuno-Gill model (Rui and Wang, 1990; Gill, 1980).

The patterns by anomalous total column radiative fluxes and upper-level horizontal winds by KWs show sharp contrasts to those by the MJO-like disturbance (Fig. 8.10e and f). The illustrated area is dominated by total column radiative cooling in P13 and E13. For horizontal winds, both P13 and E13 show that strong easterly anomalies near the equator are on the western side, which coincides with the high rainfall (Fig. 8.9b and c). On the eastern side, the upper-level wind anomalies are too weak to be illustrated (≤ 2 m s^{-1}). Around 15°N/S, strong westerly anomalies are dominant at 200 hPa, which is associated with subtropical jets there. In contrast, westerly anomalies in the outer tropics are rather weak for the MJO-like disturbance (Fig. 8.10d). This difference in the upper-level wind structure between the MJO-like disturbance and KWs certainly suggests that anticyclonic gyres (or Rossby wave structure) are essential to developing the MJO-like disturbance. Some theories of the MJO demonstrated an important role of a Rossby wave structure for dynamics of the MJO (e.g., Hendon and Salby, 1994; Wang et al., 2016).

In summary, the composite analysis highlights structural differences between the MJO-like disturbance and KWs. Although the first two weeks of the analysis period are taken from P13

for KWs and the rest from the MJO-like disturbance, the composited patterns of the former show better agreement with those of the KW reference obtained from E13.

Finally, we compare the composite analysis associated with the MJO-like disturbance (Fig. 8.9 and 8.10) to the real-world phenomenon. The off-equatorial rainfall pattern in P13 indicates a swallowtail pattern which is one of the characteristic patterns during the active phase of the MJO (Maloney and Hartmann, 1998; Zhang and Ling, 2012). Evidence is also found in the sharp east-west contrasts in anomalies of surface properties with respect to the reference point. To the west of the point, westerly anomalies are evident near the equator with large positive anomalies of surface enthalpy fluxes and vice versa to the east, which is also observed in reality (see Fig. 8 in Jiang et al., 2020). However, negative anomalies of surface fluxes are observed to the east of the MJO-like disturbance, which is opposite to other studies that attributed the MJO propagation to positive surface flux anomalies preceding the MJO (Fuchs and Raymond, 2017; Sentić et al., 2020; Hudson and Maloney, 2023). The total radiative heating can be an important source of the destabilization in the MJO (Lin and Mapes, 2004; Del Genio and Chen, 2015) and the composited pattern showed that there are positive radiative heating anomalies at the leading edge of the disturbance. The cyclonic and anticyclonic pairs of horizontal winds near the surface and at 200 hPa coincide with the off-equatorial rainfall. This pattern is consistent with that in the Matsuno-Gill model (Gill, 1980) which describes the dynamical patterns in response to heating and is used to explain the dynamical structure of the MJO (Rui and Wang, 1990; Wang et al., 2016; Adames and Wallace, 2015). Also, the Rossby gyres are one of the key components of dynamics in the skeleton model (Majda and Stechmann, 2009) and the Rossby wave structure explains distinctive dynamical structures of the MJO in some studies (Hendon and Salby, 1994; Wang et al., 2016).

8.5   Summary and discussions

The main objective of this study is to document the behavior and structures of EWs that are present in the aquachannel simulations, as the behavior of EWs largely varies depending on model configuration (Lin et al., 2006) even in a simpler setup such as aquaplanet or aquapatch simulations (Blackburn et al., 2013; Blanco et al., 2016; Rios-Berrios et al., 2020). For objective wave identification, we detected EWs from two different angles: (a) by filtering precipitation using the spectral analysis (Wheeler and Kiladis, 1999), which emphasizes the space-time behavior of EWs, and (b) by projecting horizontal winds and geopotential onto theoretical wave patterns (Yang et al., 2003), which emphasizes dynamical structures of EWs (see detail in section 5.1). We also investigated a slow-propagating signal, which could not be identified by the aforementioned methods due to no theoretical pattern present for the signal and the limited time integration of the simulations. We characterized this signal in a subjective manner (see detail in section 5.4) and composited fields of interest on the basis of the characteristics of the signal.

Overall, all four simulations produce KWs remarkably strong amongst all wave types, and variability of zonal wind and rainfall is mostly explained by KWs on all time scales, except for

rainfall variability on longer time scales (≥ 3 days). Yet, there are substantial differences between the simulations. The main findings with respect to prominent features in each simulation are summarized as follows:

P13 Various modes of variability are observed in unfiltered fields of precipitation and horizontal winds: prominent signatures of eastward propagation with a wide range of speeds (5–27 m s^{-1}) and hints of westward propagation. One very fascinating feature in P13 is the MJO-like disturbance that propagates eastward with a speed of 5 m s^{-1}. This disturbance shares similarities with the MJO. The composited precipitation shows a swallowtail pattern, which is characteristic of the active phase of the observed MJO (Maloney and Hartmann, 1998; Zhang and Ling, 2012). The dynamical structures are characterized by low-level cyclonic and upper-level anticyclonic pairs around the center of the MJO-like disturbance, consistent with the Matsuno-Gill model (Gill, 1980). This dynamical structure underpins some of the MJO theories (see Moisture-mode and Trio-interaction theories in Zhang et al., 2020). Anomalies of surface enthalpy fluxes and vertically integrated total radiative heating exhibit a sharp east-west contrast with respect to the MJO center. From the center to the tail of the MJO-like disturbance, enhanced surface fluxes with anomalous westerly surface winds are found while ahead of the disturbance, suppressed surface fluxes and radiative warming are observed. This total radiative warming at the leading edge may be associated with the eastward propagation in our case. These features of surface enthalpy fluxes and radiative fluxes were also reported in a review paper of the MJO (see Fig.8 in Jiang et al., 2020).

E13 Unfiltered fields of precipitation and horizontal winds manifest eastward propagation with a speed of 24 m s^{-1} and with a zonal wavenumber of one. Although the realistic simulations in Chapter 6 showed that total variances of precipitation and wind are greater with explicit convection than with parameterized one, the results using the aquachannel simulations demonstrate that variabilities of rainfall and zonal winds at 200 hPa on all time scales are very low compared to its counterpart (P13). These different results suggest that extratropical forcings and triggering of convection over land can alter the sensitivity of variability to convective treatment. Nevertheless, the wind signals of KWs consistently modulate rainfall, showing that rainfall maximum is in phase with the upper-level divergence of KWs. The upper-level divergence maximum is preceded by low-level easterly anomalies of KWs which coincide with positive surface enthalpy flux anomalies. Considering the mean easterly flow in the lower troposphere, the collocation of anomalous low-level easterly and surface fluxes suggests an important role of WISHE for wave-convection coupling. This means that enhanced surface fluxes may help overcome high CIN to trigger convection. Vertical structures of temperature and zonal wind modulated by KWs largely agree with observed structures (Wheeler et al., 2000; Kiladis et al., 2009; Nakamura and Takayabu, 2022), except for BL warming

in phase with KWs. The BL warming may be due to the poor representation of cold pools with explicit convection at the horizontal grid spacing of 13 km.

S13 & SS13 Patterns of unfiltered precipitation and horizontal winds closely follow those of E13, but some substructures are shown with higher zonal wavenumbers superimposed on a zonal wavenumber-one structure. However, absolute rainfall variability and fraction explained by EWs in S13 and SS13 are more consistent with those in P13 than in E13, meaning that a treatment of shallow convection changes variability associated EWs. These results are striking because the averaged fields of precipitation and horizontal winds differ, mainly between explicit and parameterized deep convection (Chapter 7). It is suggestive that parameterized shallow convection aids in overcoming CIN, which facilitates a vertical transport of moist static energy between the BL and free troposphere and thus enhances convection-wave coupling. More differences from E13 are evident in temperature modulation through KWs. While E13 shows that KWs strongly modulate temperature anomalies throughout the entire column, S13 and SS13 demonstrate that very small temperature anomalies ($\leq 0.2\,\mathrm{K}$) are observed below 2.5 km, which is also manifested in P13. Why parameterized shallow convection reduces wave modulation below 2.5 km remains an open question but suggests further research to systematically compare simulations with different convective treatments.

The simulation period of 40 days limits our analysis to further investigate the slow-moving disturbance. For a more objective analysis, a longer time integration is required for MJO detection (Kiladis et al., 2014). Moreover, the channel geometry prevents extratropical forcings which can initiate EWs (Hoskins and Yang, 2000; Straub and Kiladis, 2003a; Yang et al., 2007b). Nevertheless, various EWs are present in the aquachannel simulations. P13, which follows closely the current ICON-NWP setup, arguably produces the most variable modes, while the other runs show better agreement in wave structure with previous studies. This encourages the utility of aquachannel simulations using the ICON-NWP to study the behavior of EWs.

9 Conclusions

This dissertation has provided a comprehensive understanding of the impact of convective treatment on tropical rainfall and its variability by using the ICON-NWP model as a tool. Although our focus has been on one model in different configurations, untangling the processes behind the observed sensitivities is nontrivial. To achieve this, we used a wide range of diagnostics. For example, a novel approach to understanding the ITCZ behavior was suggested (section 5.5) and complementary wave identification methods were used to obtain deep insights into physical mechanisms (section 5.1). This chapter summarizes the main results by referring back to the research questions proposed in Chapter 3.

As outlined in the literature review, climate and weather models struggle to accurately capture EWs. The main reason behind that is often attributed to convection parameterization, which represents the collective effects of convection (subgrid-scale) on the large-scale environment (grid scale) and thus can poorly simulate multiscale interactions, particularly wave-convection coupling in a model. A recent study demonstrated that explicit deep convection realistically produces rainfall variability associated with EWs compared to parameterized deep convection using the MPAS model (Judt and Rios-Berrios, 2021) in the DYAMOND dataset (Stevens et al., 2019). While they employed a wave filtering tool (section 5.1), we used two complementary methods for robust wave identification (Knippertz et al., 2022): one that characterizes the time-space behavior of rainfall associated with waves (Wheeler and Kiladis, 1999) and the other that projects wind and pressure onto spatial patterns of waves (Yang et al., 2003). In Chapter 6, we used these methods to identify EWs in realistic simulations using the global ICON-NWP model from the DYAMOND project for a direct comparison with the MPAS results. The horizontal resolution of the ICON simulations ranges from 80 km down to 2.5 km and different convective treatments are implemented. The main findings of Chapter 6 are:

> **RQ 1a How do model resolution and convective treatment in ICON impact unfiltered precipitation patterns compared to satellite observations and MPAS?**
> Satellite observations demonstrate that westward propagation in unfiltered precipitation is frequent, which is captured in all ICON simulations. However, the runs produce more widespread precipitation, leading to an overall overestimation of mean rainfall. This overestimation is also found in MPAS (Judt and Rios-Berrios, 2021). There are differences in precipitation patterns between explicit

and parameterized convection. Explicit convection produces clear westward propagation over Africa and the Atlantic and this structure becomes sharper with decreasing horizontal grid spacing, particularly in the 40- and 80-km runs, in which explicitly representing convection is unrealistic. In contrast, parameterized convection favors westward propagation with large-scale patterns over the Maritime Continent and Indian Ocean. Furthermore, averaged rainfall and its variance are less sensitive to horizontal resolution than to convective treatment. However, the westward propagation is muted for parameterized convection in MPAS.

RQ 1b **How sensitive are EWs to model configuration such as model resolution, convective treatment and model type?**

Precipitation signals of KWs, MRGs and ERs are largely consistent in terms of phase speed and variance, remarkably showing little sensitivity to resolution and convective treatment in ICON. However, WIG1-filtered precipitation does not depend on horizontal resolution but on convective treatment between explicit and parameterized convection, such that WIG1-related variance is very small (1 %) with the latter. All results agree with the previous study using MPAS (Judt and Rios-Berrios, 2021), except for the phase speed of KWs.

RQ 1c **Are the identified EWs robust when using two complementary wave identification methods?**

Wind signals of KWs, MRGs and ERs broadly agree with corresponding signals in precipitation with some delicate differences. A composite analysis, which links the two methods, shows that MRGs consistently modulate precipitation and vertical structures of winds and temperature. A large disagreement is found in WIG1, showing that YP-filtered wind signals are very weak irrespective of convective treatment. Our composite analysis reveals that the strong signals in precipitation are not WIG1 but appear to reflect MCSs associated with AEWs, as MCSs share similar wavenumber and frequency to WIG1 and thus, can be isolated as waves through a space-time filter. Moreover, MCSs are better captured with explicit convection (Marsham et al., 2013; Pantillon et al., 2015; Pante and Knippertz, 2019).

To fundamentally understand the EW behavior depending on convective treatment, we explored rainfall and its variability in aquachannel experiments using the ICON-NWP model. The experiments use full-blown physics with the Coriolis force and diurnal cycle to be as realistic as possible but at the same time incorporate prescribed zonally symmetric SSTs and the tropical channel geometry to simplify the problems associated with continents, zonal asymmetries, tropical-extratropical interactions. To assess the impact of convective treatment, different combinations of deep and shallow convection are used for the experiments: P13 with parameterized deep and shallow convection (Bechtold et al., 2008; Tiedtke, 1989), S13 with explicit deep

convection and parameterized shallow convection, SS13 as for S13 but with a stochastic version of shallow convection (Sakradzija et al., 2015, 2020) and E13 with explicit deep and shallow convection. The overall setup remains the same among them (section 4.2).

Before investigating the EW behavior, it is essential to examine the mean state in the simulations. Thus, Chapter 7 explored the mean state with a particular focus on rainfall. As the large uncertainty of tropical rainfall is a main challenge and the reasons for that remain unclear (Rajendran et al., 2013; Fiedler et al., 2020; Tian and Dong, 2020), we presented a suitable diagnostic tool to understand this. The key results of Chapter 7 are:

RQ 2a **How does the mean state differ with altering the treatment of deep and shallow convection in the aquachannel simulations?**

All four aquachannel experiments produce pronounced rainfall at the equator, indicative of an ITCZ, and a Hadley circulation with an ascending branch at the equator and descending branches at 15°N/S. These features are broadly consistent with the mean climate in reality (Webster, 2020a), except for the narrow Hadley cells due to the channel geometry. Despite the similarities between the runs, some differences are found. Explicit deep convection produces 35 % more rainfall than parameterized deep convection and strengthens the Hadley circulation and trade winds, which converge into the ITCZ in the lower branches of the Hadley cells. Meanwhile, the treatment of shallow convection does not have a large impact on the mean state.

RQ 2b **What diagnostic framework is suitable to understand the differences in rainfall between parameterized and explicit convection?**

A novel diagnostic is proposed in this thesis based on Emanuel (2019). Convective updraft mass flux and precipitation efficiency are inconsistent between parameterized and explicit deep convection, as the vertical motion is treated differently in the two cases. The diagnostic presented here formulates these two variables using other consistent variables from the model output, such as surface enthalpy fluxes, radiative cooling and other thermodynamic variables and thus allows for a simple, fair comparison. Estimates of the two variables are directly related to rainfall, thus allowing for a physically consistent analysis of simulations with different convective treatments.

RQ 2c **What processes are responsible for differences in mean rainfall in the ITCZ between the experiments?**

Convective updraft mass flux increases by 29–37 % with explicit deep convection, while precipitation efficiency – somewhat surprisingly – remains almost constant among the four runs. Differences in surface enthalpy fluxes are also discernible, which are enhanced by 20.2–27.7 % with explicit deep convection. According to the conceptual model, this relationship is explained by BLQE, such that strong convective mass flux is balanced by enhancing surface fluxes, which are

associated with strong surface winds related to the strong Hadley circulation. Therefore, the change in rainfall due to convective treatment is seen through the close links among dynamical fields, surface fluxes, and convective mass flux.

Understanding the variability of rainfall and winds is as crucial for studying the tropical atmosphere as it is for understanding its mean state. Chapter 8 examined the variability of rainfall and winds, and how much of it can be explained by EWs in the aquachannel simulations. To identify EWs objectively, the two complementary methods were applied to rainfall and dynamical fields, as previously done in Chapter 6. Composite techniques allowed us to investigate modulations of fields of interest through EWs. With this thorough investigation, we identified the sources of uncertainty associated with EWs due to different treatments of deep and shallow convection. The key results of Chapter 8 with respect to the research questions are as follows:

RQ 3a What characterizes the large-scale variability of rainfall and horizontal winds?

All four aquachannel simulations show prominent features of eastward propagation in unfiltered rainfall and horizontal winds, except for the low-level meridional winds. A wide range of propagation speeds ($5\text{--}27\,\mathrm{m\,s^{-1}}$) and large variance of horizontal winds are found with parameterized deep convection, while explicit deep convection is dominated by a zonal wavenumber-one feature, propagating eastward with a speed of $24\,\mathrm{m\,s^{-1}}$.

RQ 3b How strongly do EWs contribute to variability of rainfall and horizontal winds?

KWs substantially contribute to the variability of rainfall and zonal winds. EIGs explain for the variability of meridional wind at $200\,\mathrm{hPa}$, and MRGs or ERs for 850-hPa wind variability, indicating a Doppler-shift effect. The fraction of zonal wind variability explained by KWs is higher with explicit deep convection than with parameterized deep convection. The fraction of rainfall variability explained by KWs, however, increases from explicit to parameterized shallow convection. It is unanticipated because differences in the mean state are mainly due to the treatment of deep convection. This indicates that parameterized shallow convection enhances the dynamics-rainfall coupling, hypothetically because parameterized shallow convection facilitates an exchange of moist static energy between the BL and free troposphere, overcoming CIN more easily.

RQ 3c How consistent are waves in the aquachannel simulations with their real-world counterparts?

Overall, modulations of rainfall, temperature and zonal winds through KWs are consistent. Yet, there are differences due to convective treatment. Explicit deep convection produces large anomalies of winds and temperature in the lower stratosphere and has the effect of wind-induced surface flux exchange on the

development of convection, which can help trigger convection, except for S13. Explicit shallow convection is essential for temperature anomalies below 2.5 km. Yet, BL warming is in phase with a rainfall maximum of KWs, which is opposite to observations. One fascinating disturbance is found in P13, which is not identified using the wave identification methods but shares similarities with the MJO in terms of swallowtail rainfall pattern, Matsuno-Gill circulation, enhanced surface enthalpy fluxes to the west of the center of the disturbance, and column radiative warming at the leading edge of the disturbance.

This work has provided a comprehensive examination of tropical rainfall and its variability in the context of EWs, using the ICON-NWP model as a tool. The results highlighted the significance of convective treatment on the tropical atmosphere, both in realistic and idealized simulations, and shed light on the underlying mechanisms of different modes of variability in tropical rainfall and dynamics. The use of complementary wave identification methods enabled a robust analysis of these modes of variability, expanding our knowledge and understanding of tropical weather patterns. The composite analysis not only linked the two different wave fields but also revealed differences in structure due to model configuration, which can ultimately help model development. Furthermore, a companion study (Ruckstuhl et al., 2023), which attempts to improve initial conditions for weather forecasting in the tropics, has benefited from our understanding of EWs in aquachannel simulations. In addition, this dissertation has introduced a new tool for the ITCZ diagnostic based on the conceptual framework of Emanuel (2019). The new tool facilitated a more detailed quantification and visualization of the complex behavior of tropical rainfall due to convective treatment and had implications for untangling sources of uncertainty of large discrepancies in ITCZ in climate models (Fiedler et al., 2020; Tian and Dong, 2020). The findings presented in this dissertation helped to clarify the role of EWs in the variability of tropical rainfall, which has significant implications for climate models and weather forecasting. Above all, the results are encouraging to use the ICON-NWP model to gain insight into atmospheric phenomena in the tropics, which are remarkably consistent with their real-world counterparts through a range of convective treatments and resolutions.

Overall, explicit convection does not always excel over parameterized convection to accurately simulate tropical rainfall and its variability, although previous studied expected explicit convection to represent better multi-scale interactions between convection and large-scale circulations (Randall, 2013; Tomassini, 2020). However, understanding the gap between these two different representations of convection provides an opportunity to improve weather and climate models during the exciting phase of the model development from parameterized to explicit convection (Bechtold, 2019; Palmer and Stevens, 2019). Therefore, we have to continue challenging these models with observations and conduct systematic sensitivity tests, for example, by applying the diagnostic tools for wave and mean rainfall that were presented in this dissertation.

10 Outlook

The research presented in this dissertation has shed light on the complexity of tropical rainfall and its variability associated with EWs. The findings of this study have important implications for weather forecasting, climate modeling, and our understanding of the Earth's climate system. However, there are several limitations to the research presented here that need to be addressed to further advance our understanding of tropical rainfall and EWs. Here, we discuss some of these limitations and propose avenues for future research that can build upon the work presented in this dissertation.

While Chapter 6 addressed various wave types in the global realistic simulations, Chapter 8 focused on KWs and the MJO. KWs exhibit the strongest wind signals of the other wave types (Fig. B.2) and have longer predictability than higher-frequency waves such as EIGs. Given these facts, the detailed analysis of KWs provided important information for data assimilation experiments (Ruckstuhl et al., 2023). The focus on KWs leaves open questions how EIGs, the theoretical pattern of which are antisymmetric about the equator, are present despite the zonally symmetric nature of the simulation configuration. Moreover, the Doppler-shift effect was found for EIGs. We will leave the investigation of EIGs for future study.

The composite analysis of the vertical structures on the basis of the WK method was done using 3D fields of temperature and horizontal winds. The apparent heat source (Q1 in Yanai et al., 1973) may be more useful than temperature to relate the heating source to waves (Rios-Berrios et al., 2023), which will be practical to discover the sources of uncertainty that should be addressed during the model development process.

Both realistic and idealized simulations provided an analysis period of 40 days, which restricts wave identification to relatively fast-moving waves. For example, ERs have slower propagation speeds than KWs, such that there were only five marked precipitation signals during the study period (section 6.2.3), providing poor statistics for composite analysis. Nevertheless, the YP method, which is less restricted to a time window than the WK method, can be applied for more robust wave identification since ERs derive from the shallow water equations on a rotating beta plane (Matsuno, 1966). Another limitation was characterizing the MJO, which was unexpected when the idealized runs were planned because its period is 30–90 days and it does not derive from Matsuno's solution. (Many theories for the MJO have been suggested but there is no consensus on it; Zhang et al., 2020). We can tackle this due to the limited time integration by performing P13 for a longer simulation period that can capture the full range of variability.

For realistic simulations, high-resolution climate simulations can be used, such as the Next Generation Earth Modelling Systems (NextGEMS[1]), which plans to simulate the coupled Earth system for 30 years with kilometer horizontal grid spacing. The complementary wave analysis and composite technique used in this thesis (sections 5.1 and 5.2) will help find the sources of uncertainty for wave-convection coupling in these high-resolution climate models. With the completion of the decadal simulations, new avenues for obtaining a better understanding of long-term variability such as the MJO will be opened, making it an exciting time for future research in this field.

Throughout this dissertation, we have gained valuable insights into the dependence of tropical rainfall patterns and variability on resolution and convective treatment using the ICON-NWP model. However, we have also seen that these findings may not necessarily apply to other model types, as demonstrated in Chapter 6 through the comparison with MPAS (Judt and Rios-Berrios, 2021). To expand our understanding of tropical weather patterns and their predictability, we recommend comparing simulations across different models using the wave and ITCZ diagnostics presented in sections 5.1 and 5.5. The DYAMOND simulations from nine models are available upon request[2], and we recommend that future research can make use of these diagnostics in those simulations to better understand the sources of uncertainty for tropical rainfall and EWs. Ultimately, improving global NWP models in the tropics can have significant benefits for weather forecasting in midlatitudes, and we believe that continued efforts in this area will lead to more accurate and reliable weather predictions, also outside of the tropics (Vitart, 2013; Pante and Knippertz, 2019).

Improving predictability for tropical rainfall can be achieved through new data assimilation algorithms optimized for the tropics and better observations in the equatorial region. The Aeolus satellite with the first spaceborne Doppler Wind Lidar onboard, measuring global atmospheric winds up to 30 km in height, was launched in 2018 by the European Space Agency (Reitebuch, 2012). Several studies have already reported positive impacts of assimilating Aeolus wind data into NWP models (Rennie et al., 2021; Garrett et al., 2022; Borne et al., 2023; Martin et al., 2023). Moreover, Ruckstuhl et al. (2023) demonstrates the potential of wind data for data assimilation to improve forecasts of tropical rainfall. By performing data assimilation experiments using P13 as a nature run, they found that upper-level wind errors associated with KWs grow at a surprisingly slow rate, which suggests the possibility of predictability up to 25 days. Rainfall predictability in their experiments is up to 10. (Note that Chapter 8 demonstrated that KWs substantially modulate rainfall.) The key variables for these data assimilation experiments are horizontal winds and specific humidity. This is particularly interesting given the recent launch of the Aeolus satellite by the European Space Agency, indicating the potential for further improvements in tropical rainfall forecasting.

Lastly, conducting aquachannel simulations can provide meaningful information to explore the atmosphere with more affordable computational resources. The simplified nature of these

---

[1] https://nextgems-h2020.eu
[2] https://www.esiwace.eu/services/dyamond-initiative

simulations can also help to identify and understand key processes that may be difficult to isolate in realistic simulations. The results from the aquachannel simulations were convincing as they captured the major atmospheric processes in the tropics, such as the ITCZ, the Hadley circulation and EWs. For those who aim to accurately simulate the Hadley circulation, it should be taken into account that our aquachannel geometry creates somewhat a narrower Hadley circulation than what is observed in the real world (Webster, 2020a) due to the closed walls at 30°N/S. Furthermore, analyzing idealized simulations together with realistic simulations will allow for a more comprehensive understanding of the processes involved. As data from realistic simulations become more easily available, we recommend exploring both types of simulations for future studies to fully exploit their complementary strengths.

Acknowledgements

Bibliography

Adam, O., T. Bischoff, and T. Schneider, 2016: Seasonal and interannual variations of the energy flux equator and ITCZ. Part i: Zonally averaged ITCZ position. *J. Climate*, **29 (9)**, 3219–3230, doi: 10.1175/JCLI-D-15-0512.1.

Adames, Á. F., and D. Kim, 2016: The mjo as a dispersive, convectively coupled moisture wave: Theory and observations. *J. Atmos. Sci.*, **73 (3)**, 913–941, doi: 10.1175/JAS-D-15-0170.1.

Adames, Á. F., and J. M. Wallace, 2014: Three-dimensional structure and evolution of the MJO and its relation to the mean flow. *J. Atmos. Sci.*, **71 (6)**, 2007–2026, doi: 10.1175/ JAS-D-13-0254.1.

Adames, Á. F., and J. M. Wallace, 2015: Three-dimensional structure and evolution of the moisture field in the MJO. *J. Atmos. Sci.*, **72 (10)**, 3733–3754, doi: 10.1175/JAS-D-15-0003. 1.

Angulo-Umana, P., and D. Kim, 2023: Mesoscale convective clustering enhances tropical precipitation. *Science Advances*, **9 (2)**, eabo5317, doi: 10.1126/sciadv.abo5317.

Arakawa, A., 2004: The cumulus parameterization problem: Past, present, and future. *Journal of Climate*, **17 (13)**, 2493–2525, doi: 10.1175/1520-0442(2004)017<2493:RATCPP>2.0.CO;2.

Arakawa, A., and W. H. Schubert, 1974: Interaction of a cumulus cloud ensemble with the large-scale environment, Part i. *J. Atmos. Sci.*, **31 (3)**, 674–701, doi: 10.1175/1520-0469(1974) 031<0674:IOACCE>2.0.CO;2.

Arnold, N. P., and D. A. Randall, 2015: Global-scale convective aggregation: Implications for the Madden-Julian Oscillation. *J. Adv. Model. Earth Syst.*, **7 (4)**, 1499–1518, doi: 10.1002/ 2015MS000498.

Ayesiga, G., C. E. Holloway, C. J. Williams, G.-Y. Yang, and S. Ferrett, 2021: The observed synoptic scale precipitation relationship between Western Equatorial Africa and Eastern Equatorial Africa. *Int. J. Climatol.*, **41**, E582–E601, doi: 10.1002/joc.6711.

Baldauf, M., A. Seifert, J. Förstner, D. Majewski, M. Raschendorfer, and T. Reinhardt, 2011: Operational convective-scale numerical weather prediction with the COSMO model: Description and sensitivities. *Mon. Wea. Rev.*, **139 (12)**, 3887–3905, doi: 10.1175/MWR-D-10-05013.1.

Baranowski, D. B., M. K. Flatau, P. J. Flatau, and A. J. Matthews, 2016: Impact of atmospheric convectively coupled equatorial Kelvin waves on upper ocean variability. *J. Geophys. Res.*, **121 (5)**, 2045–2059, doi: 10.1002/2015JD024150.

Bardachova, T., 2022: Tropical waves and predictability in simulations with a stochastic convection scheme. M.S. thesis, Faculty of Physics, Ludwig Maximilian University of Munich, 66 pp., URL https://www.wavestoweather.de/publications/bardachova_2022.pdf.

Barlow, J., and Coauthors, 2018: The future of hyperdiverse tropical ecosystems. *Nature*, **559 (7715)**, 517–526, doi: 10.1038/s41586-018-0301-1.

Bechtold, P., 2017: Atmospheric moist convection. *Meteorological Training Course Lecture Series, ECMWF*.

Bechtold, P., 2019: Challenges in tropical numerical weather prediction at ECMWF. *Current Trends in the Representation of Physical Processes in Weather and Climate Models*, D. A. Randall, J. Srinivasan, R. S. Nanjundiah, and P. Mukhopadhyay, Eds., Springer, 29–50, doi: 10.1007/978-981-13-3396-5_2.

Bechtold, P., E. Bazile, F. Guichard, P. Mascart, and E. Richard, 2001: A mass-flux convection scheme for regional and global models. *Quart. J. Roy. Met. Soc.*, **127 (573)**, 869–886, doi: 10.1002/qj.49712757309.

Bechtold, P., M. Köhler, T. Jung, F. Doblas-Reyes, M. Leutbecher, M. J. Rodwell, F. Vitart, and G. Balsamo, 2008: Advances in simulating atmospheric variability with the ECMWF model: From synoptic to decadal time-scales. *Quart. J. Roy. Met. Soc.*, **134 (634)**, 1337–1351, doi: 10.1002/qj.289.

Bechtold, P., N. Semane, P. Lopez, J.-P. Chaboureau, A. Beljaars, and N. Bormann, 2014: Representing equilibrium and nonequilibrium convection in large–scale models. *J. Atmos. Sci.*, **71 (2)**, 734–753, doi: 10.1175/JAS-D-13-0163.1.

Becker, T., P. Bechtold, and I. Sandu, 2021: Characteristics of convective precipitation over tropical Africa in storm–resolving global simulations. *Quart. J. Roy. Met. Soc.*, doi: 10.1002/qj.4185.

Benedict, J. J., B. Medeiros, A. C. Clement, and A. G. Pendergrass, 2017: Sensitivities of the hydrologic cycle to model physics, grid resolution, and ocean type in the aquaplanet Community Atmosphere Model. *J. Adv. Model. Earth Syst.*, **9 (2)**, 1307–1324, doi: 10.1002/2016MS000891.

Bengtsson, L., J. Dias, S. Tulich, M. Gehne, and J.-W. Bao, 2021: A stochastic parameterization of organized tropical convection using cellular automata for global forecasts in NOAA's Unified Forecast System. *J. Adv. Model. Earth Syst.*, **13 (1)**, e2020MS002 260, doi: 10.1029/2020MS002260.

Bengtsson, L., and Coauthors, 2019: Convectively coupled equatorial wave simulations using the ECMWF IFS and the NOAA GFS cumulus convection schemes in the NOAA GFS model. *Mon. Wea. Rev.*, **147 (11)**, 4005–4025, doi: 10.1175/MWR-D-19-0195.1.

Bjerknes, J., 1969: Atmospheric teleconnections from the equatorial Pacific. *Mon. Wea. Rev.*, **97 (3)**, 163–172, doi: 10.1175/1520-0493(1969)097<0163:ATFTEP>2.3.CO;2.

Blackburn, M., and Coauthors, 2013: The aqua-planet experiment (APE): Control SST simulation. *J. Met. Soc. Jap.*, **91 (0)**, 17–56, doi: 10.2151/jmsj.2013-A02.

Blanco, J. E., D. S. Nolan, and S. N. Tulich, 2016: Convectively coupled Kelvin waves in aquachannel simulations: 1. Propagation speeds, composite structures, and comparison with aquaplanets. *J. Geophys. Res.*, **121 (19)**, 11–287, doi: 10.1002/2016JD025004.

Borne, M., P. Knippertz, M. Weissmann, A. Martin, M. Rennie, and A. Cress, 2023: Impact of Aeolus wind lidar observations on the representation of the West African monsoon circulation in the ECMWF and DWD forecasting systems. *Quart. J. Roy. Met. Soc.*, doi: 10.1002/qj.4442.

Bretherton, C. S., P. N. Blossey, and M. Khairoutdinov, 2005: An energy-balance analysis of deep convective self-aggregation above uniform SST. *J. Atmos. Sci.*, **62 (12)**, 4273–4292, doi: 10.1175/JAS3614.1.

Bretherton, C. S., and M. F. Khairoutdinov, 2015: Convective self-aggregation feedbacks in near-global cloud-resolving simulations of an aquaplanet. *J. Adv. Model. Earth Syst.*, **7 (4)**, 1765–1787, doi: 10.1002/2015MS000499.

Bretherton, C. S., M. E. Peters, and L. E. Back, 2004: Relationships between water vapor path and precipitation over the tropical oceans. *J. Climate*, **17 (7)**, 1517–1528, doi: 10.1175/1520-0442(2004)017<1517:RBWVPA>2.0.CO;2.

Bretherton, F., 1964: Low frequency oscillations trapped near the equator. *Tellus*, **16 (2)**, 181–185, doi: 10.3402/tellusa.v16i2.8922.

Burpee, R. W., 1972: The origin and structure of easterly waves in the lower troposphere of North Africa. *J. Atmos. Sci.*, **29 (1)**, 77–90, doi: 10.1175/1520-0469(1972)029<0077:TOASOE>2.0.CO;2.

Carlson, T. N., 1969: Some remarks on African disturbances and their progress over the tropical Atlantic. *Mon. Wea. Rev.*, **97 (10)**, 716–726, doi: 10.1175/1520-0493(1969)097<0716:SROADA>2.3.CO;2.

Carpenter, R. L., K. K. Droegemeier, and A. M. Blyth, 1998: Entrainment and detrainment in numerically simulated cumulus congestus clouds. Part ii: Cloud budgets. *J. Atmos. Sci.*, **55 (23)**, 3433–3439, doi: 10.1175/1520-0469(1998)055<3433:EADINS>2.0.CO;2.

Chan, S. C., E. J. Kendon, H. J. Fowler, S. Blenkinsop, N. M. Roberts, and C. A. Ferro, 2014: The value of high-resolution Met office regional climate models in the

simulation of multihourly precipitation extremes. *J. Climate*, **27 (16)**, 6155–6174, doi: 10.1175/JCLI-D-13-00723.1.

Chang, C.-P., Z. Wang, J. McBride, and C.-H. Liu, 2005: Annual cycle of Southeast Asia—Maritime Continent rainfall and the asymmetric monsoon transition. *J. Climate*, **18 (2)**, 287–301, doi: 10.1175/JCLI-3257.1.

Charney, J. G., and A. Eliassen, 1964: On the growth of the hurricane depression. *J. Atmos. Sci.*, **21 (1)**, 68–75, doi: 10.1175/1520-0469(1964)021<0068:OTGOTH>2.0.CO;2.

Chen, S. S., and R. A. Houze, 1997: Diurnal variation and life-cycle of deep convective systems over the tropical Pacific warm pool. *Quart. J. Roy. Met. Soc.*, **123 (538)**, 357–388, doi: 10.1002/qj.49712353806.

Cheng, C.-P., and R. A. Houze, 1979: The distribution of convective and mesoscale precipitation in GATE radar echo patterns. *Mon. Wea. Rev.*, **107 (10)**, 1370–1381, doi: 10.1175/1520-0493(1979)107<1370:TDOCAM>2.0.CO;2.

Cheng, Y.-M., J. Dias, G. Kiladis, Z. Feng, and L. R. Leung, 2023: Mesoscale convective systems modulated by convectively coupled equatorial waves, under review.

Craig, G. C., and B. G. Cohen, 2006: Fluctuations in an equilibrium convective ensemble. part i: Theoretical formulation. *J. Atmos. Sci.*, **63 (8)**, 1996–2004, doi: 10.1175/JAS3709.1.

Del Genio, A. D., and Y. Chen, 2015: Cloud-radiative driving of the Madden-Julian oscillation as seen by the A-Train. *Journal of Geophysical Research: Atmospheres*, **120 (11)**, 5344–5356.

DePasquale, A., C. Schumacher, and A. Rapp, 2014: Radar observations of MJO and Kelvin wave interactions during DYNAMO/CINDY2011/AMIE. *J. Geophys. Res.*, **119 (11)**, 6347–6367, doi: 10.1002/2013JD021031.

Dias, J., M. Gehne, G. N. Kiladis, N. Sakaeda, P. Bechtold, and T. Haiden, 2018: Equatorial waves and the skill of NCEP and ECMWF numerical weather prediction systems. *Mon. Wea. Rev.*, **146 (6)**, 1763–1784.

Dias, J., and G. N. Kiladis, 2014: Influence of the basic state zonal flow on convectively coupled equatorial waves. *Geophys. Res. Lett.*, **41 (19)**, 6904–6913, doi: 10.1002/2014GL061476.

Dias, J., and O. Pauluis, 2011: Modulations of the phase speed of convectively coupled kelvin waves by the itcz. *J. Atmos. Sci.*, **68 (7)**, 1446–1459, doi: 10.1175/2011JAS3630.1.

Dominguez, C., J. M. Done, and C. L. Bruyère, 2020: Easterly wave contributions to seasonal rainfall over the tropical Americas in observations and a regional climate model. *Clim. Dynam.*, **54**, 191–209, doi: 10.1007/s00382-019-04996-7.

Emanuel, K., 2019: Inferences from simple models of slow, convectively coupled processes. *J. Atmos. Sci.*, **76 (1)**, 195–208, doi: 10.1175/JAS-D-18-0090.1.

Emanuel, K. A., 1987: An air-sea interaction model of intraseasonal oscillations in the tropics. *J. Atmos. Sci.*, **44 (16)**, 2324–2340, doi: 10.1175/1520-0469(1987)044<2324:AASIMO>2.0. CO;2.

Emanuel, K. A., 1994: *Atmospheric convection.* Oxford University Press on Demand.

Emanuel, K. A., J. David Neelin, and C. S. Bretherton, 1994: On large-scale circulations in convecting atmospheres. *Quart. J. Roy. Met. Soc.*, **120 (519)**, 1111–1143, doi: 10.1002/qj. 49712051902.

FAO, 2022: FAOSTAT website. Food and Agriculture Organization of the United Nations, accessed 2 March 2023, https://www.fao.org/faostat/en/#home.

Feng, Z., L. R. Leung, J. Hardin, C. R. Terai, F. Song, and P. Caldwell, 2023: Mesoscale convective systems in DYAMOND global convection-permitting simulations. *Geophys. Res. Lett.*, **50 (4)**, e2022GL102 603, doi: 10.1029/2022GL102603.

Feng, Z., and Coauthors, 2021: A global high-resolution mesoscale convective system database using satellite-derived cloud tops, surface precipitation, and tracking. *J. Geophys. Res.*, **126 (8)**, e2020JD034 202, doi: 10.1029/2020JD034202.

Ferreira, A. P., R. Nieto, and L. Gimeno, 2019: Completeness of radiosonde humidity observations based on the Integrated Global Radiosonde Archive. *Earth-Syst. Sci. Data*, **11 (2)**, 603–627, doi: 10.5194/essd-11-603-2019.

Ferrett, S., G.-Y. Yang, S. J. Woolnough, J. Methven, K. Hodges, and C. E. Holloway, 2020: Linking extreme precipitation in Southeast Asia to equatorial waves. *Quart. J. Roy. Met. Soc.*, **146 (727)**, 665–684, doi: 10.1002/qj.3699.

Fiedler, S., and Coauthors, 2020: Simulated tropical precipitation assessed across three major phases of the coupled model intercomparison project (CMIP). *Mon. Wea. Rev.*, **148 (9)**, 3653–3680, doi: 10.1175/MWR-D-19-0404.1.

Fink, A. H., and A. Reiner, 2003: Spatiotemporal variability of the relation between African easterly waves and West African squall lines in 1998 and 1999. *J. Geophys. Res.*, **108 (D11)**, doi: 10.1029/2002JD002816.

Fiolleau, T., and R. Roca, 2013: Composite life cycle of tropical mesoscale convective systems from geostationary and low Earth orbit satellite observations: Method and sampling considerations. *Quarterly Journal of the Royal Meteorological Society*, **139 (673)**, 941–953, doi: 10.1002/qj.2174.

Fuchs, Ž., and D. J. Raymond, 2017: A simple model of intraseasonal oscillations. *J. Adv. Model. Earth Syst.*, **9 (2)**, 1195–1211, doi: 10.1002/2017MS000963.

Gadgil, S., 2003: The Indian monsoon and its variability. *Annu. Rev. Earth Planet. Sci.*, **31 (1)**, 429–467, doi: 10.1146/annurev.earth.31.100901.141251.

Garrett, K., H. Liu, K. Ide, R. N. Hoffman, and K. E. Lukens, 2022: Optimization and impact assessment of Aeolus HLOS wind assimilation in NOAA's global forecast system. *Quart. J. Roy. Met. Soc.*, **148 (747)**, 2703–2716, doi: 10.1002/qj.4331.

Geen, R., S. Bordoni, D. S. Battisti, and K. Hui, 2020: Monsoons, ITCZs, and the concept of the global monsoon. *Rev. Geophys.*, **58 (4)**, e2020RG000 700, doi: 10.1029/2020RG000700.

Gehne, M., and R. Kleeman, 2012: Spectral analysis of tropical atmospheric dynamical variables using a linear shallow-water modal decomposition. *J. Atmos. Sci.*, **69 (7)**, 2300–2316, doi: 10.1175/JAS-D-10-05008.1.

Gehne, M., B. Wolding, J. Dias, and G. N. Kiladis, 2022: Diagnostics of tropical variability for numerical weather forecasts. *Weather and Forecasting*, **37 (9)**, 1661–1680, doi: 10.1175/ WAF-D-21-0204.1.

Gill, A. E., 1980: Some simple solutions for heat-induced tropical circulation. *Quart. J. Roy. Met. Soc.*, **106 (449)**, 447–462, doi: 10.1002/qj.49710644905.

Giorgi, F., 1991: Sensitivity of simulated summertime precipitation over the western United States to different physics parameterizations. *Mon. Wea. Rev.*, **119 (12)**, 2870–2888, doi: 10.1175/1520-0493(1991)119<2870:SOSSPO>2.0.CO;2.

Gleiter, T., T. Janjić, and N. Chen, 2022: Ensemble kalman filter based data assimilation for tropical waves in the MJO skeleton model. *Quart. J. Roy. Met. Soc.*, **148 (743)**, 1035–1056, doi: 10.1002/qj.4245.

Grant, A., 2001: Cloud-base fluxes in the cumulus-capped boundary layer. *Quart. J. Roy. Met. Soc.*, **127 (572)**, 407–421, doi: 10.1002/qj.49712757209.

Hadley, G., 1735: Vi. concerning the cause of the general trade-winds. *Philos. T. R. Soc. Lond.*, **39 (437)**, 58–62, doi: 10.1098/rstl.1735.0014.

Haertel, P. T., and G. N. Kiladis, 2004: Dynamics of 2-day equatorial waves. *J. Atmos. Sci.*, **61 (22)**, 2707–2721, doi: 10.1175/JAS3352.1.

Haertel, P. T., G. N. Kiladis, A. Denno, and T. M. Rickenbach, 2008: Vertical-mode decompositions of 2-day waves and the Madden–Julian oscillation. *J. Atmos. Sci.*, **65 (3)**, 813–833, doi: 10.1175/2007JAS2314.1.

Haiden, T., M. J. Rodwell, D. S. Richardson, A. Okagaki, T. Robinson, and T. Hewson, 2012: Intercomparison of global model precipitation forecast skill in 2010/11 using the SEEPS score. *Mon. Wea. Rev.*, **140 (8)**, 2720–2733, doi: 10.1175/MWR-D-11-00301.1.

Halley, E., 1686: An historical account of the trade winds, and monsoons, observable in the seas between and near the tropicks, with an attempt to assign the physical cause of the said winds. *Philos. T. R. Soc. Lond.*, **16 (183)**, 153–168, doi: 10.1098/rstl.1686.0026.

Haynes, P. H., and M. E. McIntyre, 1987: On the evolution of vorticity and potential vorticity in the presence of diabatic heating and frictional or other forces. *J. Atmos. Sci.*, **44 (5)**, 828–841, doi: 10.1175/1520-0469(1987)044<0828:OTEOVA>2.0.CO;2.

Held, I. M., and A. Y. Hou, 1980: Nonlinear axially symmetric circulations in a nearly inviscid atmosphere. *J. Atmos. Sci.*, **37 (3)**, 515–533, doi: 10.1175/1520-0469(1980)037<0515:NASCIA>2.0.CO;2.

Hendon, H. H., and M. L. Salby, 1994: The life cycle of the Madden–Julian oscillation. *J. Atmos. Sci.*, **51 (15)**, 2225–2237, doi: 10.1175/1520-0469(1994)051<2225:TLCOTM>2.0.CO;2.

Hersbach, H., and Coauthors, 2020: The ERA5 global reanalysis. *Quart. J. Roy. Met. Soc.*, **146 (730)**, 1999–2049.

Hodges, K. I., and C. Thorncroft, 1997: Distribution and statistics of African mesoscale convective weather systems based on the ISCCP Meteosat imagery. *Mon. Wea. Rev.*, **125 (11)**, 2821–2837, doi: 10.1175/1520-0493(1997)125<2821:DASOAM>2.0.CO;2.

Hohenegger, C., L. Kornblueh, D. Klocke, T. Becker, G. Cioni, J. F. Engels, U. Schulzweida, and B. Stevens, 2020: Climate statistics in global simulations of the atmosphere, from 80 to 2.5 km grid spacing. *J. Met. Soc. Jap.*, **98**, 73–91, doi: 10.2151/jmsj.2020-005.

Holton, J. R., 2004: *An introduction to dynamic meteorology*. 4th ed., International Geophysics Series, Elsevier Academic Press,.

Hong, S.-Y., and J. Dudhia, 2012: Next-generation numerical weather prediction: Bridging parameterization, explicit clouds, and large eddies. *Bull. Am. Met. Soc.*, **93 (1)**, ES6–ES9, doi: 10.1175/2011BAMS3224.1.

Hoskins, B. J., and G.-Y. Yang, 2000: The equatorial response to higher-latitude forcing. *J. Atmos. Sci.*, **57 (9)**, 1197–1213, doi: 10.1175/1520-0469(2000)057<1197:TERTHL>2.0.CO;2.

Hou, A. Y., and Coauthors, 2014: The global precipitation measurement mission. *Bull. Am. Met. Soc.*, **95 (5)**, 701–722, doi: 10.1175/BAMS-D-13-00164.1.

Houze, R. A., 1977: Structure and dynamics of a tropical squall–line system. *Mon. Wea. Rev.*, **105 (12)**, 1540–1567, doi: 10.1175/1520-0493(1977)105<1540:SADOAT>2.0.CO;2.

Houze, R. A., 1982: Cloud Clusters and Large-Scale Vertical Motions in the Tropics. *J. Met. Soc. Jap.*, **60 (1)**, 396–410, doi: 10.2151/jmsj1965.60.1_396.

Houze, R. A., 1989: Observed structure of mesoscale convective systems and implications for large-scale heating. *Quart. J. Roy. Met. Soc.*, **115 (487)**, 425–461, doi: 10.1002/qj.49711548702.

Houze, R. A., 2004: Mesoscale convective systems. *Rev. Geophys.*, **42 (4)**, doi: 10.1029/ 2004RG000150.

Houze, R. A., 2018: 100 years of research on mesoscale convective systems. *Meteor. Monogr.*, **59**, 17.1–17.54, doi: 10.1175/amsmonographs-d-18-0001.1.

Houze, R. A., and A. K. Betts, 1981: Convection in GATE. *Rev. Geophys.*, **19 (4)**, 541–576, doi: 10.1029/RG019i004p00541.

Houze, R. A., C.-P. Cheng, C. A. Leary, and J. F. Gamache, 1980: Diagnosis of cloud mass and heat fluxes from radar and synoptic data. *J. Atmos. Sci.*, **37 (4)**, 754–773, doi: 10.1175/1520-0469(1980)037<0754:DOCMAH>2.0.CO;2.

Hsu, C.-W., C. A. DeMott, M. Branson, J. Reeves Eyre, and X. Zeng, 2022: Ocean surface flux algorithm effects on tropical Indo-Pacific intraseasonal precipitation. *Geophys. Res. Lett.*, **49 (7)**, e2021GL096 968, doi: 10.1029/2021GL096968.

Huaman, L., E. D. Maloney, C. Schumacher, and G. N. Kiladis, 2021: Easterly waves in the East Pacific during the OTREC 2019 field campaign. *J. Atmos. Sci.*, **78 (12)**, 4071–4088, doi: 10.1175/JAS-D-21-0128.1.

Hudson, J., and E. Maloney, 2023: The role of surface fluxes in MJO propagation through the Maritime Continent. *J. Climate*, **36 (6)**, 1633–1652, doi: 10.1175/JCLI-D-22-0484.1.

Huffman, G. J., D. T. Bolvin, D. Braithwaite, K. Hsu, R. Joyce, P. Xie, and S.-H. Yoo, 2015: NASA global precipitation measurement (GPM) integrated multi-satellite retrievals for GPM (IMERG). *Algorithm Theoretical Basis Document (ATBD) Version*, **4 (26)**, 30, URL http://pmm.nasa.gov/sites/default/files/document_files/IMERG_ATBD_V4.5.pdf.

Huffman, G. J., and Coauthors, 2007: The TRMM multisatellite precipitation analysis (TMPA): Quasi-global, multiyear, combined-sensor precipitation estimates at fine scales. *J. Hydrometeorol.*, **8 (1)**, 38–55, doi: 10.1175/JHM560.1.

Inoue, K., Á. F. Adames, and K. Yasunaga, 2020: Vertical velocity profiles in convectively coupled equatorial waves and MJO: New diagnoses of vertical velocity profiles in the wavenumber–frequency domain. *J. Atmos. Sci.*, **77 (6)**, 2139–2162, doi: 10.1175/JAS-D-19-0209.1.

Janiga, M. A., C. J. Schreck III, J. A. Ridout, M. Flatau, N. P. Barton, E. J. Metzger, and C. A. Reynolds, 2018: Subseasonal forecasts of convectively coupled equatorial waves and the MJO: Activity and predictive skill. *Mon. Wea. Rev.*, **146 (8)**, 2337–2360, doi: 10.1175/MWR-D-17-0261.1.

Jeevanjee, N., 2017: Vertical velocity in the gray zone. *J. Adv. Model. Earth Syst.*, **9 (6)**, 2304–2316, doi: 10.1002/2017MS001059.

Jiang, X., and Coauthors, 2020: Fifty years of research on the Madden-Julian Oscillation: Recent progress, challenges, and perspectives. *J. Geophys. Res.*, **125 (17)**, e2019JD030 911, doi: 10.1029/2019JD030911.

Johnson, R. H., and P. E. Ciesielski, 2013: Structure and properties of Madden–Julian oscillations deduced from DYNAMO sounding arrays. *J. Atmos. Sci.*, **70 (10)**, 3157–3179, doi: 10.1175/JAS-D-13-065.1.

Johnson, R. H., T. M. Rickenbach, S. A. Rutledge, P. E. Ciesielski, and W. H. Schubert, 1999: Trimodal characteristics of tropical convection. *J. Climate*, **12 (8)**, 2397–2418, doi: 10.1175/1520-0442(1999)012<2397:TCOTC>2.0.CO;2.

Johnson, R. H., and G. S. Young, 1983: Heat and Moisture Budgets of Tropical Mesoscale Anvil Clouds. *J. Atmos. Sci.*, **40 (9)**, 2138 – 2147, doi: 10.1175/1520-0469(1983)040<2138: HAMBOT>2.0.CO;2.

Jones, C., D. E. Waliser, K. Lau, and W. Stern, 2004: Global occurrences of extreme precipitation and the Madden–Julian oscillation: Observations and predictability. *J. Climate*, **17 (23)**, 4575–4589, doi: 10.1175/3238.1.

Judt, F., 2020: Atmospheric predictability of the tropics, middle latitudes, and polar regions explored through global storm–resolving simulations. *J. Atmos. Sci.*, **77 (1)**, 257–276, doi: 10.1175/JAS-D-19-0116.1.

Judt, F., and R. Rios-Berrios, 2021: Resolved convection improves the representation of equatorial waves and tropical rainfall variability in a global nonhydrostatic model. *Geophys. Res. Lett.*, **48 (14)**, e2021GL093 265, doi: 10.1029/2021GL093265.

Jung, H., and P. Knippertz, 2023: Link between the time-space behavior of rainfall and 3D dynamical structures of equatorial waves in global convection-permitting simulations. *Geophys. Res. Lett.*, **50 (2)**, e2022GL100 973, doi: 10.1029/2022GL100973.

Jung, H., P. Knippertz, Y. Ruckstuhl, R. Redl, T. Janjic, and C. Hoose, 2023: Understanding the dependence of mean precipitation on convective treatment in tropical aquachannel experiments. *Weather Clim. Dynam. Discuss.*, **4 (1)**, 249–264, doi: 10.5194/wcd-4-249-2023.

Khairoutdinov, M. F., and K. Emanuel, 2018: Intraseasonal variability in a cloud-permitting near-global equatorial aquaplanet model. *J. Atmos. Sci.*, **75 (12)**, 4337–4355, doi: 10.1175/JAS-D-18-0152.1.

Khairoutdinov, M. F., S. K. Krueger, C.-H. Moeng, P. A. Bogenschutz, and D. A. Randall, 2009: Large-eddy simulation of maritime deep tropical convection. *J. Adv. Model. Earth Syst.*, **1 (4)**, doi: 10.3894/JAMES.2009.1.15.

Khouider, B., and M. W. Moncrieff, 2015: Organized convection parameterization for the ITCZ. *J. Atmos. Sci.*, **72 (8)**, 3073–3096, doi: 10.1175/JAS-D-15-0006.1.

Kikuchi, K., G. N. Kiladis, J. Dias, and T. Nasuno, 2018: Convectively coupled equatorial waves within the MJO during CINDY/DYNAMO: Slow kelvin waves as building blocks. *Clim. Dynam.*, **50**, 4211–4230, doi: 10.1007/s00382-017-3869-5.

Kiladis, G. N., J. Dias, K. H. Straub, M. C. Wheeler, S. N. Tulich, K. Kikuchi, K. M. Weickmann, and M. J. Ventrice, 2014: A comparison of OLR and circulation-based indices for tracking the MJO. *Mon. Wea. Rev.*, **142 (5)**, 1697–1715, doi: 10.1175/MWR-D-13-00301.1.

Kiladis, G. N., C. D. Thorncroft, and N. M. Hall, 2006: Three-dimensional structure and dynamics of African easterly waves. Part i: Observations. *J. Atmos. Sci.*, **63 (9)**, 2212–2230, doi: 10.1175/JAS3741.1.

Kiladis, G. N., M. C. Wheeler, P. T. Haertel, K. H. Straub, and P. E. Roundy, 2009: Convectively coupled equatorial waves. *Rev. Geophys.*, **47 (2)**, doi: 10.1016/B978-0-12-382225-3.00414-X.

Kim, J.-E., and C. Zhang, 2021: Core dynamics of the MJO. *J. Atmos. Sci.*, **78 (1)**, 229–248, doi: 10.1175/JAS-D-20-0193.1.

Kim, Y.-H., and U. Achatz, 2021: Interaction between stratospheric Kelvin waves and gravity waves in the easterly QBO phase. *Geophys. Res. Lett.*, **48 (18)**, e2021GL095 226, doi: 10.1029/2021GL095226.

Knippertz, P., and Coauthors, 2022: The intricacies of identifying equatorial waves. *Quart. J. Roy. Met. Soc.*, **148 (747)**, 2814–2852, doi: 10.1002/qj.4338.

Koutsoyiannis, D., and A. Langousis, 2011: 2.02 - precipitation. *Treatise on Water Science*, P. Wilderer, Ed., Elsevier, Oxford, 27–77, doi: https://doi.org/10.1016/B978-0-444-53199-5.00027-0.

Kwon, Y. C., and S.-Y. Hong, 2017: A mass-flux cumulus parameterization scheme across gray-zone resolutions. *Mon. Wea. Rev.*, **145 (2)**, 583–598, doi: 10.1175/MWR-D-16-0034.1.

Landu, K., L. R. Leung, S. Hagos, V. Vinoj, S. A. Rauscher, T. Ringler, and M. Taylor, 2014: The dependence of ITCZ structure on model resolution and dynamical core in aquaplanet simulations. *J. Climate*, **27 (6)**, 2375–2385, doi: 10.1175/JCLI-D-13-00269.1.

Leary, C. A., and R. A. Houze, 1979: The structure and evolution of convection in a tropical cloud cluster. *J. Atmos. Sci.*, **36 (3)**, 437–457, doi: 10.1175/1520-0469(1979)036<0437:TSAEOC>2.0.CO;2.

LeMone, M. A., E. J. Zipser, and S. B. Trier, 1998: The role of environmental shear and thermodynamic conditions in determining the structure and evolution of mesoscale convective systems during TOGA COARE. *J. Atmos. Sci.*, **55 (23)**, 3493–3518, doi: 10.1175/1520-0469(1998)055<3493:TROESA>2.0.CO;2.

Li, F., W. D. Collins, M. F. Wehner, D. L. Williamson, J. G. Olson, and C. Algieri, 2011: Impact of horizontal resolution on simulation of precipitation extremes in an aqua-planet version of Community Atmospheric Model (CAM3). *TELLUS A*, **63 (5)**, 884–892, doi: 10.1111/j.1600-0870.2011.00544.x.

Li, Y., and S. N. Stechmann, 2020: Predictability of tropical rainfall and waves: Estimates from observational data. *Quart. J. Roy. Met. Soc.*, **146 (729)**, 1668–1684, doi: 10.1002/qj.3759.

Liebmann, B., G. N. Kiladis, L. M. Carvalho, C. Jones, C. S. Vera, I. Bladé, and D. Allured, 2009: Origin of convectively coupled Kelvin waves over South America. *J. Climate*, **22 (2)**, 300–315, doi: 10.1175/2008JCLI2340.1.

Lin, C., and A. Arakawa, 1997: The macroscopic entrainment processes of simulated cumulus ensemble. Part ii: Testing the entraining-plume model. *J. Atmos. Sci.*, **54 (8)**, 1044–1053, doi: 10.1175/1520-0469(1997)054<1044:TMEPOS>2.0.CO;2.

Lin, J.-L., and B. E. Mapes, 2004: Radiation budget of the tropical intraseasonal oscillation. *J. Atmos. Sci.*, **61 (16)**, 2050–2062.

Lin, J.-L., and Coauthors, 2006: Tropical intraseasonal variability in 14 IPCC AR4 climate models. Part i: Convective signals. *J. Climate*, **19 (12)**, 2665–2690, doi: 10.1175/JCLI3735.1.

Lorenz, E. N., 1963: Deterministic nonperiodic flow. *J. Atmos. Sci.*, **20 (2)**, 130–141, doi: 10.1175/1520-0469(1963)020<0130:DNF>2.0.CO;2.

Loschnigg, J., and P. J. Webster, 2000: A coupled ocean–atmosphere system of SST modulation for the Indian Ocean. *J. Climate*, **13 (19)**, 3342–3360, doi: 10.1175/1520-0442(2000)013<3342:ACOASO>2.0.CO;2.

Madden, R. A., and P. R. Julian, 1971: Detection of a 40–50 day oscillation in the zonal wind in the tropical Pacific. *J. Atmos. Sci.*, **28 (5)**, 702–708, doi: 10.1175/1520-0469(1971)028<0702:DOADOI>2.0.CO;2.

Madden, R. A., and P. R. Julian, 1972: Description of global-scale circulation cells in the tropics with a 40–50 day period. *J. Atmos. Sci.*, **29 (6)**, 1109–1123, doi: 10.1175/1520-0469(1972)029<1109:DOGSCC>2.0.CO;2.

Majda, A. J., and S. N. Stechmann, 2009: The skeleton of tropical intraseasonal oscillations. *Proc. Natl. Acad. Sci.*, **106 (21)**, 8417–8422, doi: 10.1073/pnas.0903367106.

Maloney, E. D., and D. L. Hartmann, 1998: Frictional moisture convergence in a composite life cycle of the Madden–Julian oscillation. *J. Climate*, **11 (9)**, 2387–2403, doi: 10.1175/1520-0442(1998)011<2387:FMCIAC>2.0.CO;2.

Mapes, B., S. Tulich, J. Lin, and P. Zuidema, 2006: The mesoscale convection life cycle: Building block or prototype for large-scale tropical waves? *Dyn. Atmos. Oceans.*, **42 (1)**, 3–29, doi: 10.1016/j.dynatmoce.2006.03.003.

Mapes, B. E., and R. A. Houze, 1995: Diabatic divergence profiles in western Pacific mesoscale convective systems. *J. Atmos. Sci.*, **52 (10)**, 1807–1828, doi: 10.1175/1520-0469(1995) 052<1807:DDPIWP>2.0.CO;2.

Marshall, J., and R. A. Plumb, 2016: *Climate and climate variability*, chap. 12, 259–294. Academic Press.

Marsham, J. H., N. S. Dixon, L. Garcia-Carreras, G. M. Lister, D. J. Parker, P. Knippertz, and C. E. Birch, 2013: The role of moist convection in the West African monsoon system: Insights from continental–scale convection–permitting simulations. *Geophys. Res. Lett.*, **40 (9)**, 1843–1849, doi: 10.1002/grl.50347.

Martin, A., M. Weissmann, and A. Cress, 2023: Investigation of links between dynamical scenarios and particularly high impact of Aeolus on numerical weather prediction (NWP) forecasts. *Weather Clim. Dynam.*, **4 (1)**, 249–264, doi: 10.5194/wcd-4-249-2023.

Matsuno, T., 1966: Quasi-geostrophic motions in the equatorial area. *J. Met. Soc. Jap.*, **44 (1)**, 25–43, doi: 10.2151/jmsj1965.44.1_25.

Medeiros, B., L. Nuijens, C. Antoniazzi, and B. Stevens, 2010: Low-latitude boundary layer clouds as seen by CALIPSO. *J. Geophys. Res.*, **115 (D23)**, doi: 10.1029/2010JD014437.

Medeiros, B., D. L. Williamson, and J. G. Olson, 2016: Reference aquaplanet climate in the Community Atmosphere Model, Version 5. *J. Adv. Model. Earth Syst.*, **8 (1)**, 406–424, doi: 10.1002/2015MS000593.

Mellor, G. L., and T. Yamada, 1982: Development of a turbulence closure model for geophysical fluid problems. *Rev. Geophys.*, **20 (4)**, 851–875, doi: 10.1029/RG020i004p00851.

Milliff, R. F., and R. A. Madden, 1996: The existence and vertical structure of fast, eastward-moving disturbances in the equatorial troposphere. *J. Atmos. Sci.*, **53 (4)**, 586–597, doi: 10.1175/1520-0469(1996)053<0586:TEAVSO>2.0.CO;2.

Mlawer, E. J., S. J. Taubman, P. D. Brown, M. J. Iacono, and S. A. Clough, 1997: Radiative transfer for inhomogeneous atmospheres: RRTM, a validated correlated-k model for the longwave. *J. Geophys. Res. Atmos.*, **102 (D14)**, 16 663–16 682, doi: 10.1029/97JD00237.

Möbis, B., and B. Stevens, 2012: Factors controlling the position of the Intertropical Convergence Zone on an aquaplanet. *J. Adv. Model. Earth Syst.*, **4 (4)**, doi: 10.1029/2012MS000199.

Muller, C., and Y. Takayabu, 2020: Response of precipitation extremes to warming: what have we learned from theory and idealized cloud-resolving simulations, and what remains to be learned? *Environ. Res. Lett.*, **15 (3)**, 035 001, doi: 10.1088/1748-9326/ab7130.

Nakamura, Y., and Y. N. Takayabu, 2022: Convective Couplings with Equatorial Rossby Waves and Equatorial Kelvin Waves. Part i: Coupled Wave Structures. *J. Atmos. Sci.*, **79 (1)**, 247–262, doi: 10.1175/JAS-D-21-0080.1.

Narsey, S., C. Jakob, M. S. Singh, M. Bergemann, V. Louf, A. Protat, and C. Williams, 2019: Convective precipitation efficiency observed in the tropics. *Geophys. Res. Lett.*, **46 (22)**, 13 574–13 583, doi: 10.1029/2019GL085031.

Naumann, A. K., B. Stevens, and C. Hohenegger, 2019: A moist conceptual model for the boundary layer structure and radiatively driven shallow circulations in the trades. *J. Atmos. Sci.*, **76 (5)**, 1289–1306, doi: 10.1175/JAS-D-18-0226.1.

Neale, R. B., and B. J. Hoskins, 2000: A standard test for AGCMs including their physical parametrizations: I: The proposal. *Atmos. Sci. Let.*, **1 (2)**, 101–107, doi: 10.1006/asle.2000. 0019.

Neelin, J. D., I. M. Held, and K. H. Cook, 1987: Evaporation-wind feedback and low-frequency variability in the tropical atmosphere. *J. Atmos. Sci.*, **44 (16)**, 2341–2348, doi: 10.1175/1520-0469(1987)044<2341:EWFALF>2.0.CO;2.

Nesbitt, S. W., R. Cifelli, and S. A. Rutledge, 2006: Storm morphology and rainfall characteristics of TRMM precipitation features. *Mon. Wea. Rev.*, **134 (10)**, 2702–2721, doi: 10.1175/MWR3200.1.

Nolan, D. S., S. N. Tulich, and J. E. Blanco, 2016: ITCZ structure as determined by parameterized versus explicit convection in aquachannel and aquapatch simulations. *J. Adv. Model. Earth Syst.*, **8 (1)**, 425–452, doi: 10.1002/2015MS000560.

Oh, J.-H., W.-T. Kwon, and S.-B. Ryoo, 1997: Review of the researches on Changma and future observational study (KORMEX). *Adv. Atmos. Sci.*, **14 (2)**, 207–222, doi: 10.1007/ s00376-997-0020-2.

Ortega, S., P. J. Webster, V. Toma, and H.-R. Chang, 2017: Quasi-biweekly oscillations of the south asian monsoon and its co-evolution in the upper and lower troposphere. *Clim. Dynam.*, **49**, 3159–3174, doi: 10.1007/s00382-016-3503-y.

Paccini, L., C. Hohenegger, and B. Stevens, 2021: Explicit versus parameterized convection in response to the Atlantic Meridional Mode. *J. Climate*, **34 (9)**, 3343–3354, doi: 10.1175/ JCLI-D-20-0224.1.

Palmer, C., 1952: Reviews of modern meteorology—5. tropical meteorology. *Quart. J. Roy. Met. Soc.*, **78 (336)**, 126–164, doi: 10.1002/qj.49707833603.

Palmer, T., and B. Stevens, 2019: The scientific challenge of understanding and estimating climate change. *Proc. Natl. Acad. Sci.*, **116 (49)**, 24 390–24 395, doi: 10.1073/pnas.1906691116.

Pante, G., and P. Knippertz, 2019: Resolving Sahelian thunderstorms improves mid-latitude weather forecasts. *Nat. Commun.*, **10**, 3487, doi: 10.1038/s41467-019-11081-4.

Pantillon, F., P. Knippertz, J. H. Marsham, and C. E. Birch, 2015: A parameterization of convective dust storms for models with mass–flux convection schemes. *J. Atmos. Sci.*, **72 (6)**, 2545–2561, doi: 10.1175/JAS-D-14-0341.1.

Parker, D. J., and Coauthors, 2008: The amma radiosonde program and its implications for the future of atmospheric monitoring over africa. *Bull. Am. Met. Soc.*, **89 (7)**, 1015–1028, doi: 10.1175/2008BAMS2436.1.

Parker, T. J., G. J. Berry, M. J. Reeder, and N. Nicholls, 2014: Modes of climate variability and heat waves in Victoria, southeastern Australia. *Geophys. Res. Lett.*, **41 (19)**, 6926–6934, doi: 10.1002/2014GL061736.

Peatman, S. C., J. Schwendike, C. E. Birch, J. H. Marsham, A. J. Matthews, and G.-Y. Yang, 2021: A Local-to-Large scale view of Maritime Continent rainfall: Control by ENSO, MJO, and equatorial waves. *J. Climate*, **34 (22)**, 8933–8953, doi: 10.1175/JCLI-D-20-0909.1.

Plant, R., and G. C. Craig, 2008: A stochastic parameterization for deep convection based on equilibrium statistics. *J. Atmos. Sci.*, **65 (1)**, 87–105, doi: 10.1175/2007JAS2263.1.

Prein, A. F., and Coauthors, 2015: A review on regional convection-permitting climate modeling: Demonstrations, prospects, and challenges. *Rev. Geophys.*, **53 (2)**, 323–361, doi: 10.1002/2014RG000475.

Privé, N. C., and R. M. Errico, 2013: The role of model and initial condition error in numerical weather forecasting investigated with an observing system simulation experiment. *TELLUS A*, **65 (1)**, 21 740, doi: 10.3402/tellusa.v65i0.21740.

Rajendran, K., A. Kitoh, and J. Srinivasan, 2013: Effect of SST variation on ITCZ in APE simulations. *J. Met. Soc. Jap.*, **91**, 195–215, doi: 10.2151/jmsj.2013-A06.

Randall, D. A., 2013: Beyond deadlock. *Geophys. Res. Lett.*, **40 (22)**, 5970–5976, doi: 10.1002/2013GL057998.

Raschendorfer, M., 2001: The new turbulence parameterization of LM. *COSMO newsletter*, **1**, 89–97.

Raymond, D., Ž. Fuchs, S. Gjorgjievska, and S. Sessions, 2015: Balanced dynamics and convection in the tropical troposphere. *J. Adv. Model. Earth Syst.*, **7 (3)**, 1093–1116, doi: 10.1002/2015MS000467.

Raymond, D. J., 1995: Regulation of moist convection over the west Pacific warm pool. *J. Atmos. Sci.*, **52 (22)**, 3945–3959, doi: 10.1175/1520-0469(1995)052<3945:ROMCOT>2.0.CO;2.

Reed, R. J., and E. E. Recker, 1971: Structure and properties of synoptic-scale wave disturbances in the equatorial western Pacific. *J. Atmos. Sci.*, **28 (7)**, 1117–1133, doi: 10.1175/1520-0469(1971)028<1117:SAPOSS>2.0.CO;2.

Reitebuch, O., 2012: *The spaceborne wind lidar mission ADM-Aeolus*, 815–827. Springer Berlin Heidelberg, doi: 10.1007/978-3-642-30183-4_49.

Rennie, M. P., L. Isaksen, F. Weiler, J. de Kloe, T. Kanitz, and O. Reitebuch, 2021: The impact of Aeolus wind retrievals on ECMWF global weather forecasts. *Quart. J. Roy. Met. Soc.*, **147 (740)**, 3555–3586, doi: 10.1002/qj.4142.

Retsch, M.-H., C. Hohenegger, and B. Stevens, 2017: Vertical resolution refinement in an aqua-planet and its effect on the ITCZ. *J. Adv. Model. Earth Syst.*, **9 (6)**, 2425–2436, doi: 10.1002/2017MS001010.

Retsch, M. H., T. Mauritsen, and C. Hohenegger, 2019: Climate change feedbacks in aquaplanet experiments with explicit and parametrized convection for horizontal resolutions of 2,525 up to 5 km. *J. Adv. Model. Earth Syst.*, **11 (7)**, 2070–2088, doi: 10.1029/2019MS001677.

Riehl, H., 1945: Waves in the easterlies and the polar front in the tropics. vol. 17, miscellaneous reports, department of meteorology, university of chicago. University of Chicago Press.

Riehl, H., 1954: Tropical meteorology. Tech. rep., McGraw-hill.

Riley, E. M., B. E. Mapes, and S. N. Tulich, 2011: Clouds associated with the Madden–Julian oscillation: A new perspective from CloudSat. *J. Atmos. Sci.*, **68 (12)**, 3032–3051, doi: 10.1175/JAS-D-11-030.1.

Rios-Berrios, R., G. H. Bryan, B. Medeiros, F. Judt, and W. Wang, 2022: Differences in Tropical Rainfall in Aquaplanet Simulations With Resolved or Parameterized Deep Convection. *J. Adv. Model. Earth Syst.*, e2021MS002902, doi: 10.1029/2021MS002902.

Rios-Berrios, R., F. Judt, G. Bryan, B. Medeiros, and W. Wang, 2023: Three-dimensional structure of convectively coupled equatorial waves in aquaplanet experiments with resolved or parameterized convection. *J. Climate*, **36 (9)**, 2895–2915, doi: 10.1175/JCLI-D-22-0422.1.

Rios-Berrios, R., B. Medeiros, and G. Bryan, 2020: Mean climate and tropical rainfall variability in aquaplanet simulations using the model for prediction across scales–atmosphere. *J. Adv. Model. Earth Syst.*, **12 (10)**, e2020MS002 102, doi: 10.1029/2020MS002102.

Rosenthal, S. L., 1965: Some preliminary theoretical considerations of tropospheric wave motions in equatorial latitudes. *Mon. Wea. Rev.*, **93 (10)**, 605–612, doi: 10.1175/1520-0493(1965)093<0605:SPTCOT>2.3.CO;2.

Rotunno, R., J. B. Klemp, and M. L. Weisman, 1988: A theory for strong, long-lived squall lines. *J. Atmos. Sci.*, **45 (3)**, 463–485, doi: 10.1175/1520-0469(1988)045<0463:ATFSLL>2.0.CO;2.

Roundy, P. E., 2008: Analysis of convectively coupled Kelvin waves in the Indian Ocean MJO. *J. Atmos. Sci.*, **65 (4)**, 1342–1359, doi: 10.1175/2007JAS2345.1.

Roundy, P. E., 2012: Observed structure of convectively coupled waves as a function of equivalent depth: Kelvin waves and the Madden–Julian oscillation. *J. Atmos. Sci.*, **69 (7)**, 2097–2106, doi: 10.1175/JAS-D-12-03.1.

Roundy, P. E., and W. M. Frank, 2004: Effects of low-frequency wave interactions on intraseasonal oscillations. *J. Atmos. Sci.*, **61 (24)**, 3025–3040, doi: 10.1175/JAS-3348.1.

Ruckstuhl, Y., T. Janjic, H. Jung, P. Knippertz, and R. Redl, 2023: The influence of data assimilation on tropical waves and precipitation, in preparation.

Rui, H., and B. Wang, 1990: Development characteristics and dynamic structure of tropical intraseasonal convection anomalies. *J. Atmos. Sci.*, **47 (3)**, 357–379, doi: 10.1175/1520-0469(1990)047<0357:DCADSO>2.0.CO;2.

Sakradzija, M., and C. Hohenegger, 2017: What determines the distribution of shallow convective mass flux through a cloud base? *J. Atmos. Sci.*, **74 (8)**, 2615–2632, doi: 10.1175/JAS-D-16-0326.1.

Sakradzija, M., A. Seifert, and T. Heus, 2015: Fluctuations in a quasi-stationary shallow cumulus cloud ensemble. *Nonlinear Processes Geophys.*, **22 (1)**, 65–85, doi: https://doi: 10.5194/npg-22-65-2015.

Sakradzija, M., F. Senf, L. Scheck, M. Ahlgrimm, and D. Klocke, 2020: Local impact of stochastic shallow convection on clouds and precipitation in the tropical Atlantic. *Mon. Wea. Rev.*, **148 (12)**, 5041–5062, doi: 10.1175/MWR-D-20-0107.1.

Salby, M. L., R. R. Garcia, and H. H. Hendon, 1994: Planetary-scale circulations in the presence of climatological and wave-induced heating. *J. Atmos. Sci.*, **51 (16)**, 2344–2367, doi: 10.1175/1520-0469(1994)051<2344:PSCITP>2.0.CO;2.

Satoh, M., and Coauthors, 2017: Outcomes and challenges of global high-resolution non-hydrostatic atmospheric simulations using the K computer. *Prog Earth Planet Sci.*, **4 (13)**, 1–24, doi: 10.1186/s40645-017-0127-8.

Schlemmer, L., P. Bechtold, I. Sandu, and M. Ahlgrimm, 2017: Uncertainties related to the representation of momentum transport in shallow convection. *J. Adv. Model. Earth Syst.*, **9 (2)**, 1269–1291, doi: 10.1002/2017MS000915.

Schlueter, A., A. H. Fink, P. Knippertz, and P. Vogel, 2019: A systematic comparison of tropical waves over northern Africa. Part i: Influence on rainfall. *J. Climate*, **32 (5)**, 1501–1523, doi: 10.1175/JCLI-D-18-0173.1.

Schneider, T., T. Bischoff, and G. H. Haug, 2014: Migrations and dynamics of the intertropical convergence zone. *Nature*, **513 (7516)**, 45–53, doi: 10.1038/nature13636.

Schrodin, R., and E. Heise, 2002: A new multi-layer soil model. *COSMO Newsletter*, **2**, 149–151.

Schumacher, C., and R. A. Houze, 2003: Stratiform rain in the tropics as seen by the TRMM precipitation radar. *J. Climate*, **16 (11)**, 1739–1756, doi: 10.1175/1520-0442(2003)016<1739:SRITTA>2.0.CO;2.

Schumacher, C., and R. A. Houze, 2006: Stratiform precipitation production over sub-saharan Africa and the tropical East Atlantic as observed by TRMM. *Quart. J. Roy. Met. Soc.*, **132 (620)**, 2235–2255, doi: 10.1256/qj.05.121.

Schumacher, C., R. A. Houze, and I. Kraucunas, 2004: The tropical dynamical response to latent heating estimates derived from the TRMM precipitation radar. *J. Atmos. Sci.*, **61 (12)**, 1341–1358, doi: 10.1175/1520-0469(2004)061<1341:TTDRTL>2.0.CO;2.

Schwendike, J., P. Govekar, M. J. Reeder, R. Wardle, G. J. Berry, and C. Jakob, 2014: Local partitioning of the overturning circulation in the tropics and the connection to the Hadley and walker circulations. *J. Geophys. Res.*, **119 (3)**, 1322–1339, doi: 10.1002/2013JD020742.

Scinocca, J. F., and N. A. McFarlane, 2004: The variability of modeled tropical precipitation. *J. Atmos. Sci.*, **61 (16)**, 1993–2015, doi: 10.1175/1520-0469(2004)061<1993:TVOMTP>2.0.CO;2.

Seifert, A., 2008: A revised cloud microphysical parameterization for COSMO-LME. *COSMO Newsletter*, **7**, 25–28.

Selz, T., and G. C. Craig, 2015: Simulation of upscale error growth with a stochastic convection scheme. *Geophys. Res. Lett.*, **42 (8)**, 3056–3062, doi: 10.1002/2015GL063525.

Selz, T., M. Riemer, and G. C. Craig, 2022: The transition from practical to intrinsic predictability of midlatitude weather. *J. Atmos. Sci.*, **79 (8)**, 2013–2030.

Senf, F., A. Voigt, N. Clerbaux, A. Hünerbein, and H. Deneke, 2020: Increasing resolution and resolving convection improve the simulation of cloud-radiative effects over the north Atlantic. *J. Geophys. Res. Atmos.*, **125 (19)**, e2020JD032 667, doi: 10.1029/2020JD032667.

Sentić, S., Ž. Fuchs-Stone, and D. J. Raymond, 2020: The Madden-Julian Oscillation and mean easterly winds. *J. Geophys. Res.*, **125 (10)**, e2019JD030 869, doi: 10.1029/2019JD030869.

Seo, K.-H., H.-J. Lee, and D. M. Frierson, 2016: Unraveling the teleconnection mechanisms that induce wintertime temperature anomalies over the Northern Hemisphere continents in response to the MJO. *J. Atmos. Sci.*, **73 (9)**, 3557–3571, doi: 10.1175/JAS-D-16-0036.1.

Siebesma, A., and J. Cuijpers, 1995: Evaluation of parametric assumptions for shallow cumulus convection. *Journal of Atmospheric Sciences*, **52 (6)**, 650–666, doi: 10.1175/1520-0469(1995)052<0650:EOPAFS>2.0.CO;2.

Skamarock, W. C., J. B. Klemp, M. G. Duda, L. D. Fowler, S.-H. Park, and T. D. Ringler, 2012: A multiscale nonhydrostatic atmospheric model using centroidal Voronoi tesselations and C-grid staggering. *Mon. Wea. Rev.*, **140 (9)**, 3090–3105, doi: 10.1175/MWR-D-11-00215.1.

Slingo, J., and Coauthors, 1996: Intraseasonal oscillations in 15 atmospheric general circulation models: results from an AMIP diagnostic subproject. *Climate Dynamics*, **12 (5)**, 325–357, doi: 10.1007/BF00231106.

Sobel, A., and D. Kim, 2012: The MJO-Kelvin wave transition. *Geophys. Res. Lett.*, **39 (20)**, doi: 10.1029/2012GL053380.

Sobel, A., and E. Maloney, 2013: Moisture modes and the eastward propagation of the MJO. *J. Atmos. Sci.*, **70 (1)**, 187–192, doi: 10.1175/JAS-D-12-0189.1.

Sobel, A. H., J. Nilsson, and L. M. Polvani, 2001: The weak temperature gradient approximation and balanced tropical moisture waves. *J. Atmos. Sci.*, **58 (23)**, 3650–3665, doi: 10.1175/1520-0469(2001)058<3650:TWTGAA>2.0.CO;2.

Stensrud, D. J., 2007: *Convective parameterizations*, 185–259. Cambridge University Press, doi: 10.1017/CBO9780511812590.007.

Stephan, C. C., C. Strube, D. Klocke, M. Ern, L. Hoffmann, P. Preusse, and H. Schmidt, 2019: Gravity waves in global high-resolution simulations with explicit and parameterized convection. *J. Geophys. Res. Atmos.*, **124 (8)**, 4446–4459, doi: 10.1029/2018JD030073.

Stephan, C. C., N. Žagar, and T. G. Shepherd, 2021: Waves and coherent flows in the tropical atmosphere: New opportunities, old challenges. *Quart. J. Roy. Met. Soc.*, **147 (738)**, 2597–2624, doi: doi.org/10.1002/qj.4109.

Stern, M. E., 1963: Trapping of low frequency oscillations in an equatorial "boundary layer". *Tellus*, **15 (3)**, 246–250, doi: 10.3402/tellusa.v15i3.8847.

Stevens, B., and S. Bony, 2013: What are climate models missing? *Science*, **340 (6136)**, 1053–1054, doi: 10.1126/science.1237554.

Stevens, B., H. Brogniez, C. Kiemle, J.-L. Lacour, C. Crevoisier, and J. Kiliani, 2018: Structure and dynamical influence of water vapor in the lower tropical troposphere. Springer, 199–225 pp., doi: 10.1007/978-3-319-77273-8_10.

Stevens, B., and Coauthors, 2019: DYAMOND: The DYnamics of the atmospheric general circulation modeled on non-hydrostatic domains. *Prog Earth Planet Sci.*, **6 (1)**, 61, doi: 10.1186/s40645-019-0304-z.

Stevens, B., and Coauthors, 2020: The added value of large-eddy and storm-resolving models for simulating clouds and precipitation. *J. Met. Soc. Jap.*, **98 (2)**, 395–435, doi: 10.2151/jmsj.2020-021.

Straub, K. H., and G. N. Kiladis, 2002: Observations of a convectively coupled kelvin wave in the eastern pacific ITCZ. *J. Atmos. Sci.*, **59 (1)**, 30–53, doi: 10.1175/1520-0469(2002)059<0030:OOACCK>2.0.CO;2.

Straub, K. H., and G. N. Kiladis, 2003a: Extratropical forcing of convectively coupled Kelvin waves during austral winter. *J. Atmos. Sci.*, **60 (3)**, 526–543, doi: 10.1175/1520-0469(2003)060<0526:EFOCCK>2.0.CO;2.

Straub, K. H., and G. N. Kiladis, 2003b: The observed structure of convectively coupled Kelvin waves: Comparison with simple models of coupled wave instability. *J. Atmos. Sci.*, **60 (14)**, 1655–1668, doi: 10.1175/1520-0469(2003)060<1655:TOSOCC>2.0.CO;2.

Suematsu, T., and H. Miura, 2022: Changes in the eastward movement speed of the Madden–Julian oscillation with fluctuation in the Walker circulation. *J. Climate*, **35 (1)**, 211–225, doi: 10.1175/JCLI-D-21-0269.1.

Sundqvist, H., 1978: A parameterization scheme for non-convective condensation including prediction of cloud water content. *Quart. J. Roy. Met. Soc.*, **104 (441)**, 677–690, doi: 10.1002/qj.49710444110.

Takasuka, D., M. Satoh, and S. Yokoi, 2019: Observational evidence of mixed Rossby-gravity waves as a driving force for the mjo convective initiation and propagation. *Geophys. Res. Lett.*, **46 (10)**, 5546–5555, doi: 10.1029/2019GL083108.

Takayabu, Y. N., 1994a: Large-scale cloud disturbances associated with equatorial waves Part i: Spectral features of the cloud disturbances. *J. Met. Soc. Jap.*, **72 (3)**, 433–449, doi: 10.2151/jmsj1965.72.3_433.

Takayabu, Y. N., 1994b: Large-scale cloud disturbances associated with equatorial waves Part ii: Westward-propagating inertio-gravity waves. *J. Met. Soc. Jap.*, **72 (3)**, 451–465, doi: 10.2151/jmsj1965.72.3_451.

Takayabu, Y. N., K. Lau, and C. Sui, 1996: Observation of a quasi-2-day wave during TOGA COARE. *Mon. Wea. Rev.*, **124 (9)**, 1892–1913, doi: 10.1175/1520-0493(1996)124<1892:OOAQDW>2.0.CO;2.

Tao, W.-K., and M. W. Moncrieff, 2009: Multiscale cloud system modeling. *Rev. Geophys.*, **47 (4)**, doi: 10.1029/2008RG000276.

Thompson Jr, R. M., S. W. Payne, E. E. Recker, and R. J. Reed, 1979: Structure and properties of synoptic-scale wave disturbances in the intertropical convergence zone of the eastern Atlantic. *J. Atmos. Sci.*, **36 (1)**, 53–72, doi: 10.1175/1520-0469(1979)036<0053:SAPOSS>2.0.CO;2.

Tian, B., and X. Dong, 2020: The double-ITCZ bias in CMIP3, CMIP5, and CMIP6 models based on annual mean precipitation. *Geophys. Res. Lett.*, **47 (8)**, e2020GL087 232, doi: 10.1029/2020GL087232.

Tiedtke, M., 1989: A comprehensive mass flux scheme for cumulus parameterization in large-scale models. *Mon. Wea. Rev.*, **117 (8)**, 1779–1800, doi: 10.1175/1520-0493(1989)117<1779:ACMFSF>2.0.CO;2.

Tomassini, L., 2020: The interaction between moist convection and the atmospheric circulation in the tropics. *Bull. Am. Met. Soc.*, **101 (8)**, E1378–E1396, doi: 10.1175/BAMS-D-19-0180.1.

Bibliography

Trenberth, K. E., D. P. Stepaniak, and J. M. Caron, 2000: The global monsoon as seen through the divergent atmospheric circulation. *J. Climate*, **13 (22)**, 3969–3993, doi: 10.1175/ 1520-0442(2000)013<3969:TGMAST>2.0.CO;2.

Tulich, S. N., and G. N. Kiladis, 2012: Squall lines and convectively coupled gravity waves in the tropics: Why do most cloud systems propagate westward? *J. Atmos. Sci.*, **69 (10)**, 2995–3012, doi: 10.1175/JAS-D-11-0297.1.

Vitart, F., 2013: *Evolution of ECMWF sub-seasonal forecast skill scores over the past 10 years*. 694, ECMWF, 28 pp., doi: 10.21957/tb4x2lkhv.

Vogel, P., P. Knippertz, A. H. Fink, A. Schlueter, and T. Gneiting, 2020: Skill of global raw and postprocessed ensemble predictions of rainfall in the tropics. *Weather and Forecasting*, **35 (6)**, 2367–2385, doi: 10.1175/WAF-D-20-0082.1.

Wang, B., 2002: Rainy season of the Asian–Pacific summer monsoon. *J. Climate*, **15 (4)**, 386–398, doi: 10.1175/1520-0442(2002)015<0386:RSOTAP>2.0.CO;2.

Wang, B., F. Liu, and G. Chen, 2016: A trio-interaction theory for Madden–Julian oscillation. *Geosci. Lett.*, **3**, 1–16.

Wang, P. X., B. Wang, H. Cheng, J. Fasullo, Z. Guo, T. Kiefer, and Z. Liu, 2017: The global monsoon across time scales: Mechanisms and outstanding issues. *Earth-Sci. Rev.*, **174**, 84–121, doi: 10.1016/j.earscirev.2017.07.006.

Wang, W., 2022: Forecasting convection with a 'scale-aware' tiedtke cumulus parameterization scheme at kilometer scales. *Weather and Forecasting*, **37 (8)**, 1491–1507, doi: 10.1175/ WAF-D-21-0179.1.

Webster, P. J., 1987: *The elementary monsoon*, 3–32. Wiley.

Webster, P. J., 2020a: *Climatology of the Tropical Atmosphere and Upper Ocean*, chap. 1, 1–34. John Wiley & Sons.

Webster, P. J., 2020b: *Dynamics of the Tropical Atmosphere and Oceans*. Wiley-Blackwell.

Webster, P. J., and R. Lukas, 1992: TOGA COARE: The coupled ocean–atmosphere response experiment. *Bull. Am. Met. Soc.*, **73 (9)**, 1377–1416, doi: 10.1175/1520-0477(1992)073<1377: TCTCOR>2.0.CO;2.

Webster, P. J., V. O. Magana, T. Palmer, J. Shukla, R. Tomas, M. Yanai, and T. Yasunari, 1998: Monsoons: Processes, predictability, and the prospects for prediction. *J. Geophys. Res.*, **103 (C7)**, 14 451–14 510, doi: 10.1029/97JC02719.

Wedi, N. P., and Coauthors, 2020: A baseline for global weather and climate simulations at 1 km resolution. *J. Adv. Model. Earth Syst.*, **12 (11)**, e2020MS002 192, doi: 10.1029/ 2020MS002192.

Weisman, M. L., and J. B. Klemp, 1986: *Characteristics of Isolated Convective Storms*, 331–358. American Meteorological Society, doi: 10.1007/978-1-935704-20-1_15.

Weisman, M. L., and R. Rotunno, 2004: "a theory for strong long-lived squall lines" revisited. *J. Atmos. Sci.*, **61 (4)**, 361–382, doi: 10.1175/1520-0469(2004)061<0361:ATFSLS>2.0.CO; 2.

Weisman, M. L., W. C. Skamarock, and J. B. Klemp, 1997: The resolution dependence of explicitly modeled convective systems. *Mon. Wea. Rev.*, **125 (4)**, 527–548, doi: 10.1175/ 1520-0493(1997)125<0527:TRDOEM>2.0.CO;2.

Wheeler, M., and G. N. Kiladis, 1999: Convectively coupled equatorial waves: Analysis of clouds and temperature in the wavenumber–frequency domain. *J. Atmos. Sci.*, **56 (3)**, 374–399, doi: 10.1175/1520-0469(1999)056<0374:CCEWAO>2.0.CO;2.

Wheeler, M., G. N. Kiladis, and P. J. Webster, 2000: Large-scale dynamical fields associated with convectively coupled equatorial waves. *J. Atmos. Sci.*, **57 (5)**, 613–640, doi: 10.1175/ 1520-0469(2000)057<0613:LSDFAW>2.0.CO;2.

Wheeler, M., and H. Nguyen, 2015: Equatorial waves. *Encyclopedia of Atmospheric Sciences*, G. R. North, J. Pyle, and F. Zhang, Eds., second edition ed., Academic Press, Oxford, 102–112, doi: 10.1016/B978-0-12-382225-3.00414-X.

Wheeler, M., and K. M. Weickmann, 2001: Real-time monitoring and prediction of modes of coherent synoptic to intraseasonal tropical variability. *Mon. Wea. Rev.*, **129 (11)**, 2677–2694, doi: 10.1175/1520-0493(2001)129<2677:RTMAPO>2.0.CO;2.

Williamson, D. L., and Coauthors, 2013: The aqua-planet experiment (APE): response to changed meridional SST profile. *J. Met. Soc. Jap.*, **91 (0)**, 57–89.

Woolnough, S. J., 2019: Chapter 5 - The Madden-Julian Oscillation. *Sub-Seasonal to Seasonal Prediction*, A. W. Robertson, and F. Vitart, Eds., Elsevier, 93–117, doi: 10.1016/ B978-0-12-811714-9.00005-X.

Yanai, M., S. Esbensen, and J.-H. Chu, 1973: Determination of bulk properties of tropical cloud clusters from large-scale heat and moisture budgets. *J. Atmos. Sci.*, **30 (4)**, 611–627, doi: 10.1175/1520-0469(1973)030<0611:DOBPOT>2.0.CO;2.

Yang, G.-Y., S. Ferrett, S. Woolnough, J. Methven, and C. Holloway, 2021: Real-time identification of equatorial waves and evaluation of waves in global forecasts. *Weather and Forecasting*, **36 (1)**, 171–193, doi: 10.1175/WAF-D-20-0144.1.

Yang, G.-Y., B. Hoskins, and J. Slingo, 2003: Convectively coupled equatorial waves: A new methodology for identifying wave structures in observational data. *J. Atmos. Sci.*, **60 (14)**, 1637–1654, doi: 10.1175/1520-0469(2003)060<1637:CCEWAN>2.0.CO;2.

Yang, G.-Y., B. Hoskins, and J. Slingo, 2007a: Convectively coupled equatorial waves. Part i: Horizontal and vertical structures. *J. Atmos. Sci.*, **64 (10)**, 3406–3423, doi: 10.1175/JAS4017.1.

Yang, G.-Y., B. Hoskins, and J. Slingo, 2007b: Convectively coupled equatorial waves. Part iii: Synthesis structures and their forcing and evolution. *J. Atmos. Sci.*, **64 (10)**, 3438–3451, doi: 10.1175/JAS4019.1.

Yasunaga, K., and B. Mapes, 2012: Differences between more divergent and more rotational types of convectively coupled equatorial waves. Part ii: Composite analysis based on space–time filtering. *J. Atmos. Sci.*, **69 (1)**, 17–34, doi: 10.1175/JAS-D-11-034.1.

Yihui, D., and J. C. Chan, 2005: The East Asian summer monsoon: an overview. *Meteorol. Atmos. Phys.*, **89 (1)**, 117–142, doi: 10.1007/s00703-005-0125-z.

Ying, Y., and F. Zhang, 2017: Practical and intrinsic predictability of multiscale weather and convectively coupled equatorial waves during the active phase of an MJO. *J. Atmos. Sci.*, **74 (11)**, 3771–3785, doi: 10.1175/JAS-D-17-0157.1.

Yoneyama, K., and C. Zhang, 2020: Years of the maritime continent. *Geophysical Research Letters*, **47 (12)**, e2020GL087 182, doi: 10.1029/2020GL087182.

Yuan, J., and R. A. Houze, 2010: Global variability of mesoscale convective system anvil structure from A-Train satellite data. *Journal of Climate*, **23 (21)**, 5864–5888, doi: 10.1175/2010JCLI3671.1.

Yuan, X., 2004: Enso-related impacts on Antarctic sea ice: a synthesis of phenomenon and mechanisms. *Antarctic Science*, **16 (4)**, 415–425, doi: 10.1017/S0954102004002238.

Zagar, N., E. Andersson, and M. Fisher, 2005: Balanced tropical data assimilation based on a study of equatorial waves in ECMWF short-range forecast errors. *Quart. J. Roy. Met. Soc.*, **131 (607)**, 987–1011, doi: 10.1256/qj.04.54.

Žagar, N., N. Gustafsson, and E. Källén, 2004: Variational data assimilation in the tropics: The impact of a background-error constraint. *Quart. J. Roy. Met. Soc.*, **130 (596)**, 103–125, doi: 10.1256/qj.03.13.

Žagar, N., F. Lunkeit, F. Sielmann, and W. Xiao, 2022: Three-Dimensional Structure of the Equatorial Kelvin Wave: Vertical Structure Functions, Equivalent Depths, and Frequency and Wavenumber Spectra. *J. Climate*, **35 (7)**, 2209–2230, doi: 10.1175/JCLI-D-21-0342.1.

Žagar, N., M. Rennie, and L. Isaksen, 2021: Uncertainties in kelvin waves in ECMWF analyses and forecasts: Insights from Aeolus observing system experiments. *Geophys. Res. Lett.*, **48 (22)**, e2021GL094 716, doi: 10.1029/2021GL094716.

Žagar, N., J. Tribbia, J. Anderson, and K. Raeder, 2009: Uncertainties of estimates of inertia–gravity energy in the atmosphere. Part ii: Large-scale equatorial waves. *Mon. Wea. Rev.*, **137 (11)**, 3858–3873, doi: 10.1175/2009MWR2816.1.

Zängl, G., D. Reinert, P. Rípodas, and M. Baldauf, 2015: The ICON (ICOsahedral Non–hydrostatic) modelling framework of DWD and MPI–M: Description of the non–hydrostatic dynamical core. *Quart. J. Roy. Met. Soc.*, **141 (687)**, 563–579, doi: 10.1002/qj.2378.

Zavala-Garay, J., C. Zhang, A. Moore, and R. Kleeman, 2005: The linear response of ENSO to the Madden–Julian oscillation. *J. Climate*, **18 (13)**, 2441–2459, doi: 10.1175/JCLI3408.1.

Zhang, C., 2005: Madden-Julian oscillation. *Rev. Geophys.*, **43 (2)**, doi: 10.1029/2004RG000158.

Zhang, C., 2013: Madden–Julian oscillation: Bridging weather and climate. *Bull. Am. Met. Soc.*, **94 (12)**, 1849–1870, doi: 10.1175/BAMS-D-12-00026.1.

Zhang, C., Á. Adames, B. Khouider, B. Wang, and D. Yang, 2020: Four theories of the Madden-Julian oscillation. *Rev. Geophys.*, **58 (3)**, e2019RG000 685, doi: 10.1029/2019RG000685.

Zhang, C., and J. Ling, 2012: Potential vorticity of the Madden–Julian oscillation. *J. Atmos. Sci.*, **69 (1)**, 65–78, doi: 10.1175/JAS-D-11-081.1.

Zhou, Y., S. Wang, and J. Fang, 2022: Diurnal Cycle and Dipolar Pattern of Precipitation over Borneo during an MJO event: Lee Convergence and Offshore Propagation. *J. Atmos. Sci.*, **79 (8)**, 2145–2168, doi: 10.1175/JAS-D-21-0258.1.

Zipser, E., 1977: Mesoscale and convective–scale downdrafts as distinct components of squall-line structure. *Mon. Wea. Rev.*, **105 (12)**, 1568–1589, doi: 10.1175/1520-0493(1977) 105<1568:MACDAD>2.0.CO;2.

Zipser, E. J., 2003: Some views on "hot towers" after 50 years of tropical field programs and two years of TRMM data. *Cloud Systems, Hurricanes, and the Tropical Rainfall Measuring Mission (TRMM)*, W.-K. Tao, and R. Adler, Eds., Springer, 49–58, doi: 10.1007/978-1-878220-63-9_5.

Zuluaga, M. D., and R. A. Houze, 2013: Evolution of the population of precipitating convective systems over the equatorial Indian Ocean in active phases of the Madden–Julian Oscillation. *J. Atmos. Sci.*, **70 (9)**, 2713–2725, doi: 10.1175/JAS-D-12-0311.1.

Appendices

A   Theory of equatorial waves

The shallow water equations on a rotating system using the beta plane approximation can be written as:

$$\frac{\partial u'}{\partial t} - \beta y v' = -\frac{\partial \Phi'}{\partial x},$$
$$\frac{\partial v'}{\partial t} + \beta y u' = -\frac{\partial \Phi'}{\partial y}, \tag{A.1}$$
$$\frac{\partial \Phi'}{\partial t} + g h_e \left(\frac{\partial u'}{\partial x} + \frac{\partial v'}{\partial y} \right) = 0$$

where f is the Coriolis parameter $f = \beta y$, g is the gravitational acceleration, h_e is the equivalent depth, u' and v' are the zonal and meridioanl winds, respectively, and Φ' is the geopotential. The primes denote that the fields are linearized with respect to the basic state.

Using the wave ansatz, u', v' and Φ' can be expressed as:

$$\begin{pmatrix} u' \\ v' \\ \Phi' \end{pmatrix} = \begin{pmatrix} \hat{u}(y) \\ \hat{v}(y) \\ \hat{\Phi}(y) \end{pmatrix} \exp\left[i(kx - \omega t) \right] \tag{A.2}$$

with k being the zonal waves number and ω the frequency.

$$\frac{\sqrt{g h_e}}{\beta} \left(\frac{\omega^2}{g h_e} - k^2 - \frac{k}{\omega} \beta \right) = 2n + 1; n = 0, 1, 2, \dots \tag{A.3}$$

where n is the number for meridional mode. The formula relates ω and k which is called a dispersion relationship. The detailed derivation of the solution is shown in Appendix A. Solutions of Eq. A.3 can be obtained with some approximations. For example, the term $\omega^2/g h_e$ can be neglected at low frequencies. Then, the dispersion relation becomes

$$\omega_{\text{Rossby}} \approx \frac{-\beta k}{k^2 + (2n + 1)\beta / \sqrt{g h_e}}. \tag{A.4}$$

This wave class corresponds to equatorial Rossby (ER) waves. On a resting atmosphere, i.e., no background wind, they always propagate westward because ω is of the opposite sign to k.

At high frequencies, the term $k/\omega\beta$ in Eq. A.3 can be neglected, resulting in

$$\omega_{\text{IG}} \approx \pm \left[(2n + 1)\beta \sqrt{g h_e} + k^2 g h_e \right]^{1/2}. \tag{A.5}$$

These wave classes corresponding to the roots represent the inertio-gravity (IG) wave types. The positive and negative roots are called eastward inertio-gravity (EIG) and westward inertio-gravity (WIG) waves, respectively.

Note that the aforementioned solutions are for $n \geq 1$. For $n = 0$, the dispersion relation can be obtained directly from Eq. A.3 as

$$\omega_{n=0} = k \sqrt{gh_e} \left[\frac{1}{2} \pm \frac{1}{2} \left(1 + \frac{4\beta}{k^2 \sqrt{gh_e}} \right)^{1/2} \right].$$
(A.6)

The negative root corresponds to mixed-Rossby gravity (MRG) waves, while the positive root corresponds to an eastward inertio-gravity (EIG) waves with $n = 0$.

Kelvin waves (KWs) have no meridional wind component from theory, so the disperion relationship can be obtained by setting the meridional wind component to zero (Appendix A). Thus, the solution for KWs follows as

$$\omega_{KW} = k \sqrt{gh_e}.$$
(A.7)

This solution corresponds to Eq. A.3 with $n = -1$. The phase speed of KW ($= \omega/k$) is identical to the group speed ($= \partial\omega/\partial k$).

$\hat{v}(y)$ is obtained using the Hermite polynomial of nth order H_n as follows:

$$\hat{v}(y) = \exp\left(-\beta y^2 / 2 \sqrt{gh_e}\right) H_n \left((\beta/gh_e)^{1/2} y \right).$$
(A.8)

The first five Hermite polynomials are

$$H_0(x) = 1,$$
$$H_1(x) = 2x,$$
$$H_2(x) = 4x^2 - 2,$$
$$H_3(x) = 8x^3 - 12x,$$
$$H_4(x) = 16x^4 - 48x + 12$$
(A.9)

B   Supplementary figures
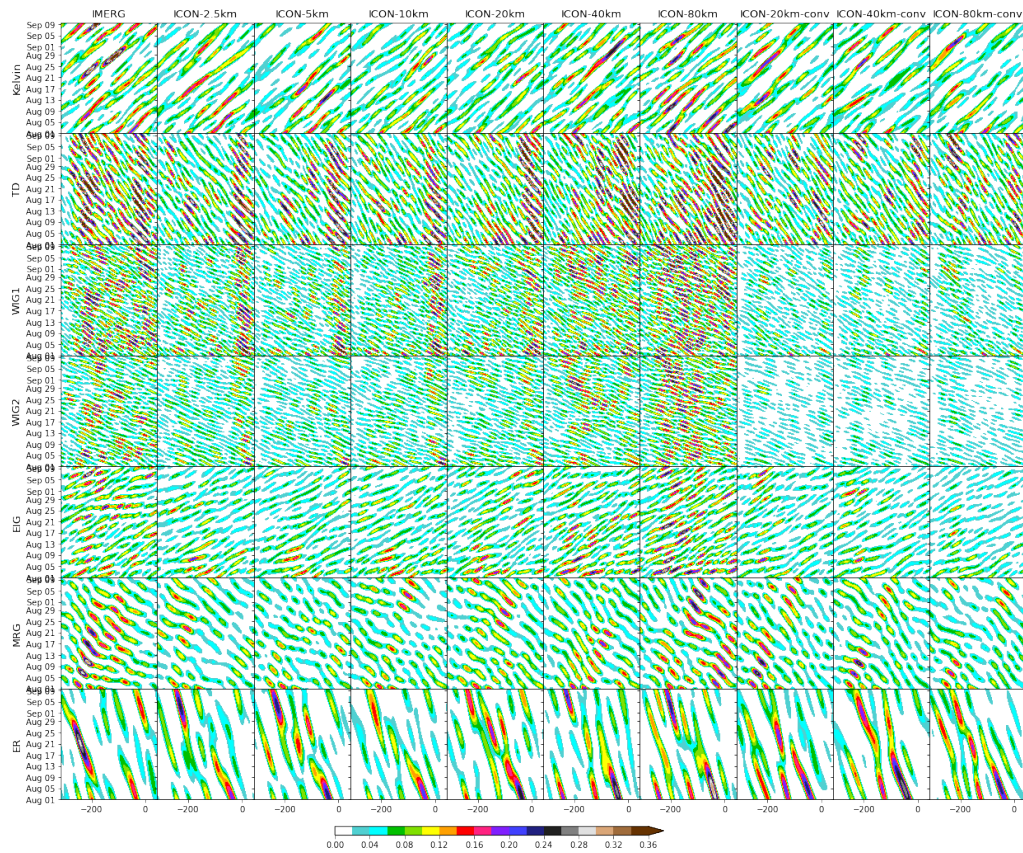
Figure B.1: Similar to Figure 6.2 but only for filtered rainfall in all 9 simulations and 7 different equatorial waves. TD indicates tropical disturbances, WIG2 *n* = 2 westward inertio-gravity wave, EIG *n* = 0 eastward inertio-gravity wave. Reprinted from Jung and Knippertz (2023), supplementary material. ©The Authors, CC BY 4.0 ⓒⓘ.
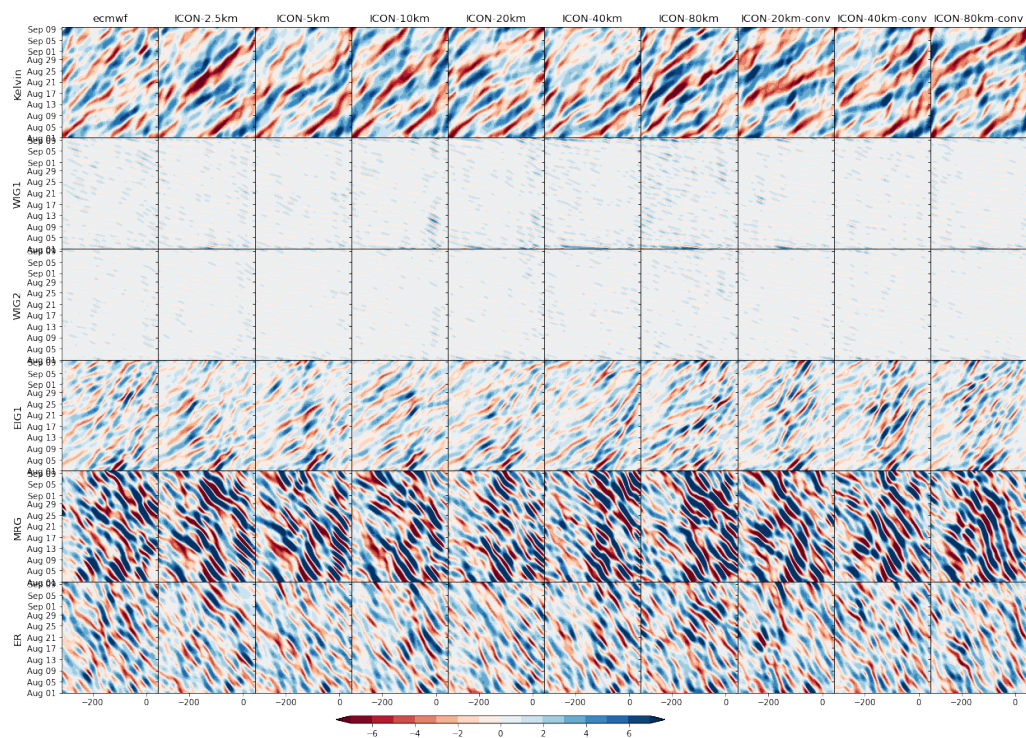
Figure B.2: Similar to Figure 6.2 but only for filtered upper-level winds [m s^{-1}] for all 9 simulations and 6 different equatorial waves. WIG2 indicates $n = 2$ westward inertio-gravity wave and EIG $n = 0$ eastward inertio-gravity wave. TD cannot be isolated by the YP method as it does not have a theoretical wave structure. Reprinted from Jung and Knippertz (2023), supplementary material. ©The Authors, CC BY 4.0 ⓒⓘ.
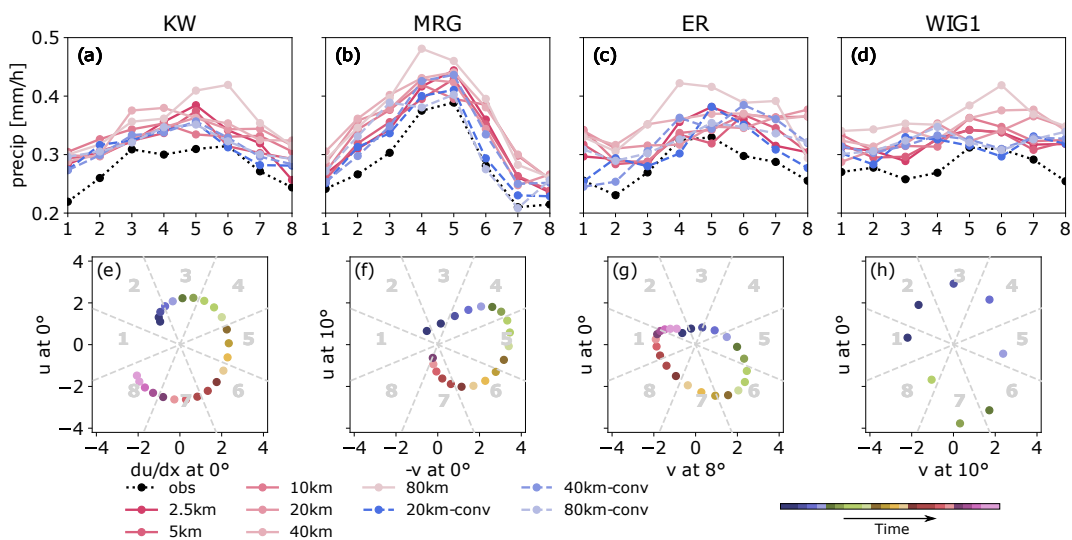
Figure B.3: Composite of unfiltered rainfall on the basis of (a) KW, (b) MRG, (c) ER and (d) WIG1 wave phase identified by the YP method. Unfiltered rainfall is averaged over 5–15°N. (e–h) Exemplary visualization of how a composite analysis is constructed for each wave at a longitude at every 6 hour, and representative variables are denoted on the abscissa and ordinate axes. Reprinted from Jung and Knippertz (2023), supplementary material. ©The Authors, CC BY 4.0 ⓒⓘ.
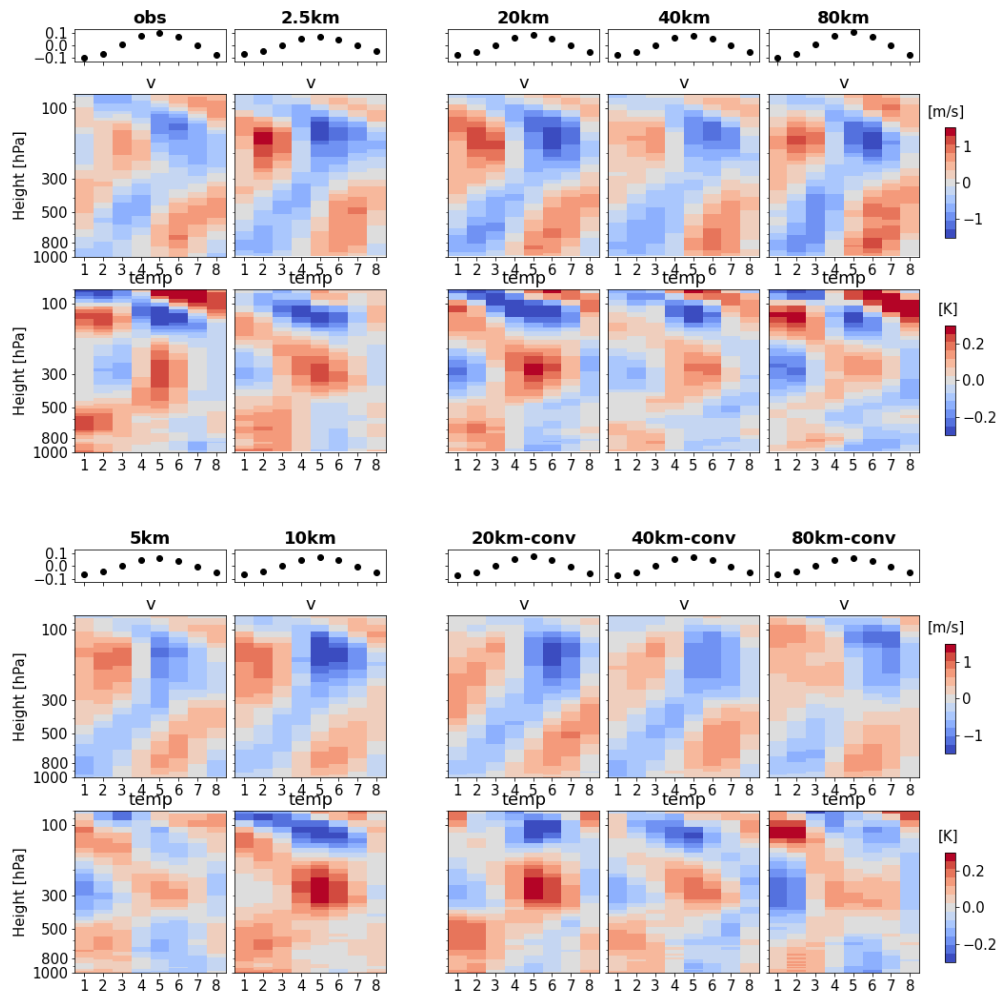
Figure B.4: Composite of unfiltered horizontal wind and temperature anomalies on the basis of MRG wave phase identified by the WK method. The scatter plots in the uppermost describe normalized wave-filtered rainfall variability in each phase. Reprinted from Jung and Knippertz (2023), supplementary material. ©The Authors, CC BY 4.0 ©①.
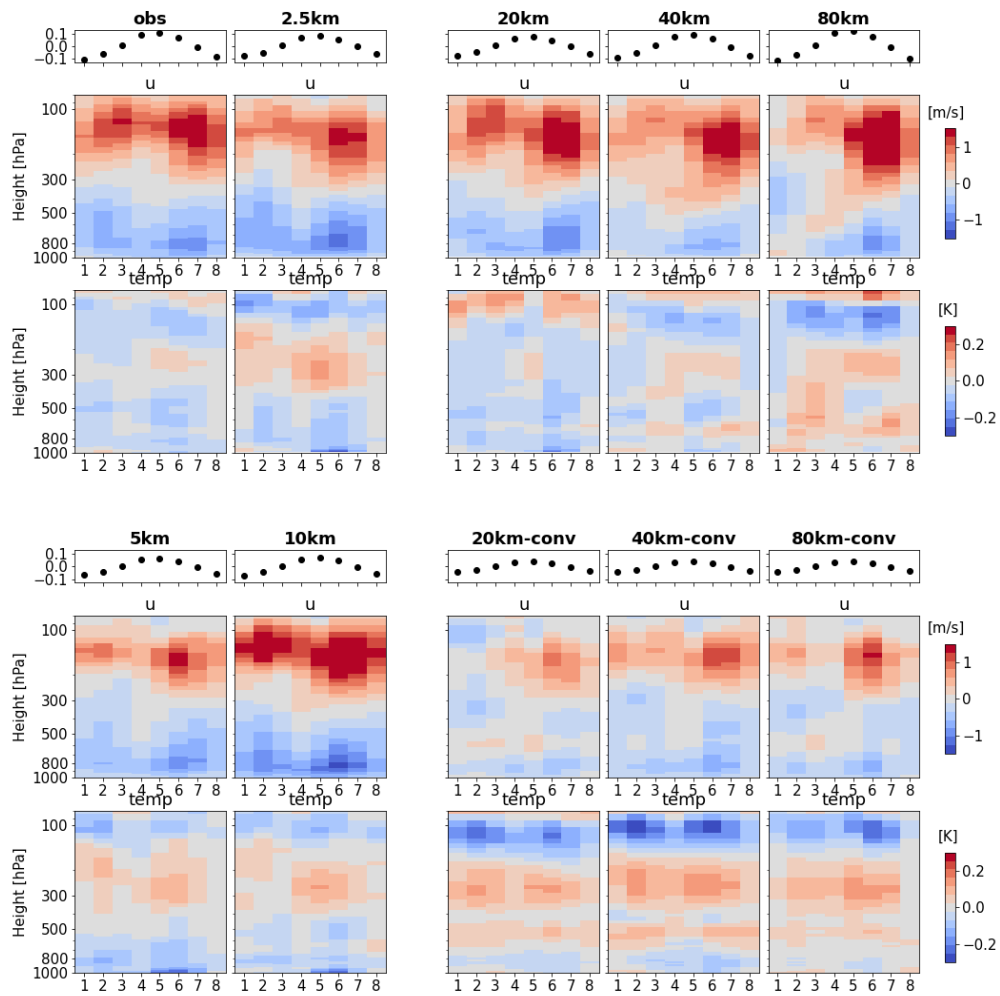
Figure B.5: As in Fig. B.4 but for WIG1 waves. Reprinted from Jung and Knippertz (2023), supplementary material. ©The Authors, CC BY 4.0 ⓒⓘ.
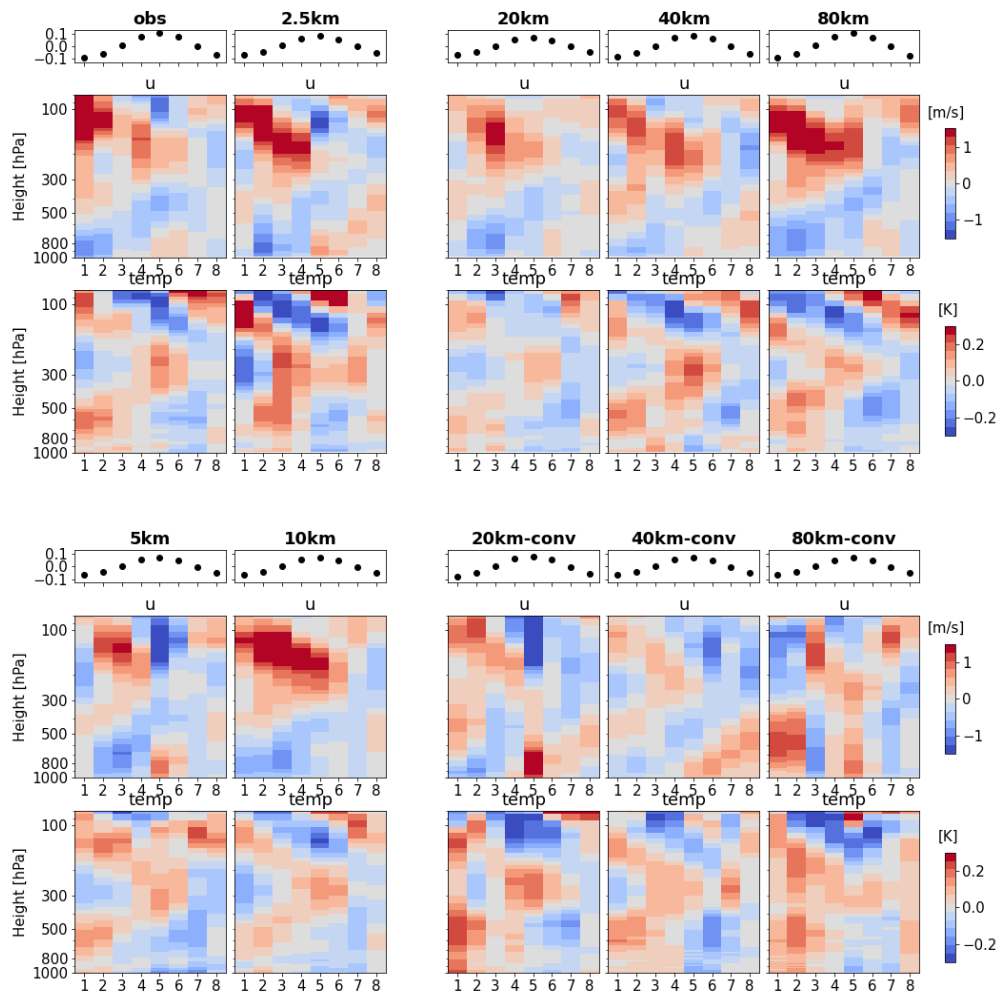
Figure B.6: As in Fig. B.4 but for KWs. Reprinted from Jung and Knippertz (2023), supplementary material. ©The Authors, CC BY 4.0 ©①.
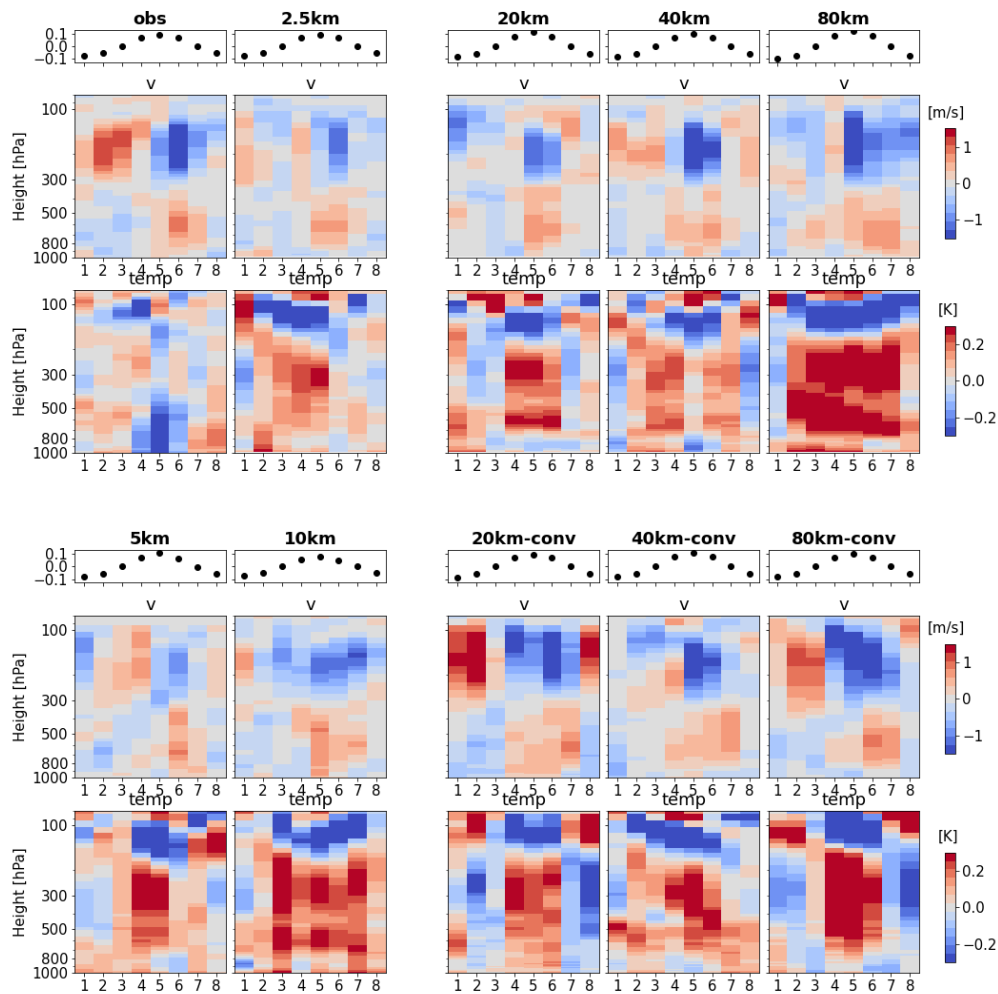
Figure B.7: As in Fig. B.4 but for ER waves. Reprinted from Jung and Knippertz (2023), supplementary material. ©The Authors, CC BY 4.0 ⓒⓘ.
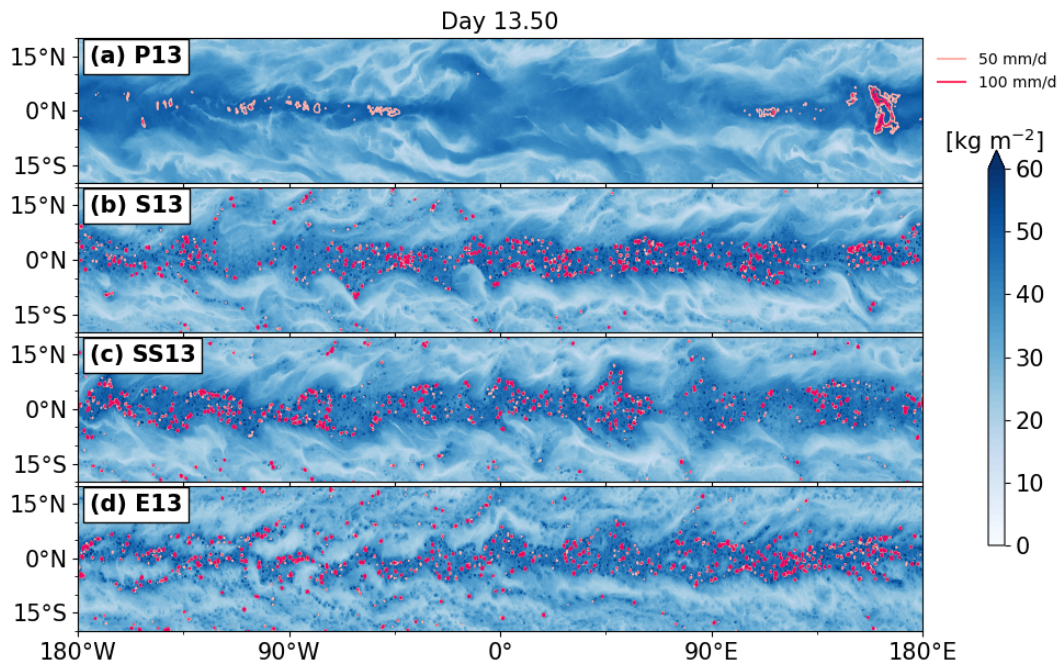
Figure B.8: Snapshot of PW [kg m^{-2}] in shading and precipitation rate [mm d^{-1}] in contour at day 13.5 for (a) P13, (b) S13, (c) SS13 and (d) E13. The light pink and dark pink contours are equivalent to precipitation rates of 50 and 100 mm d^{-1}, respectively. P13 displays a large-scale organized system of precipitation, while the other runs show localized precipitation with high intensity.
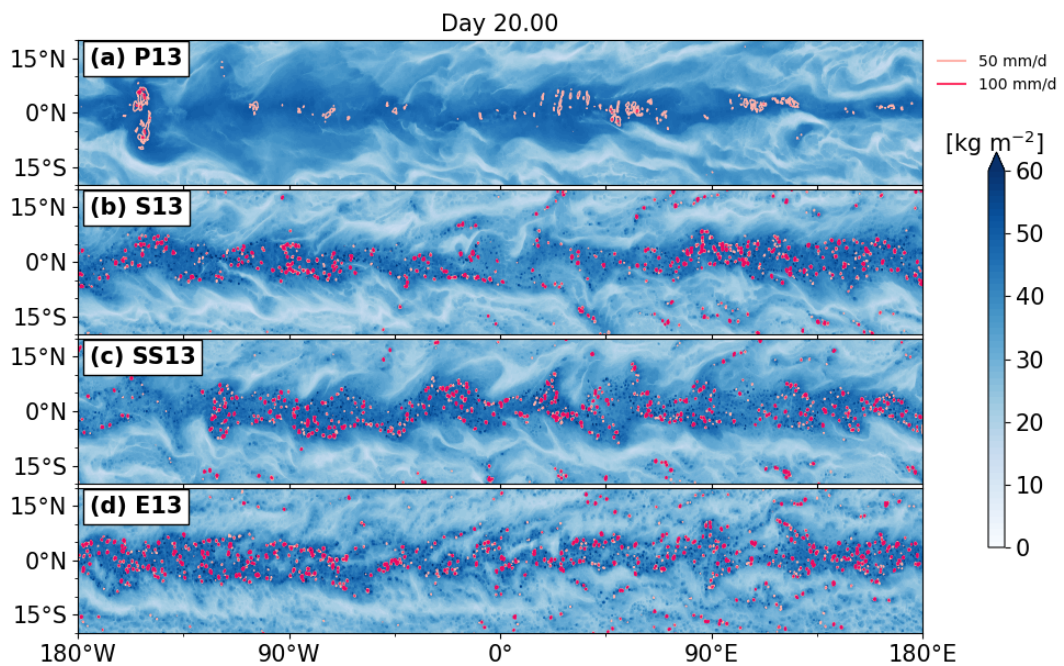
Figure B.9: As in Fig. B.9 but at day 20. P13 displays that the large-scale system propagates eastward, appearing around at 140°W and there is evidence of imprints of gravity waves between 20° and 60°E.
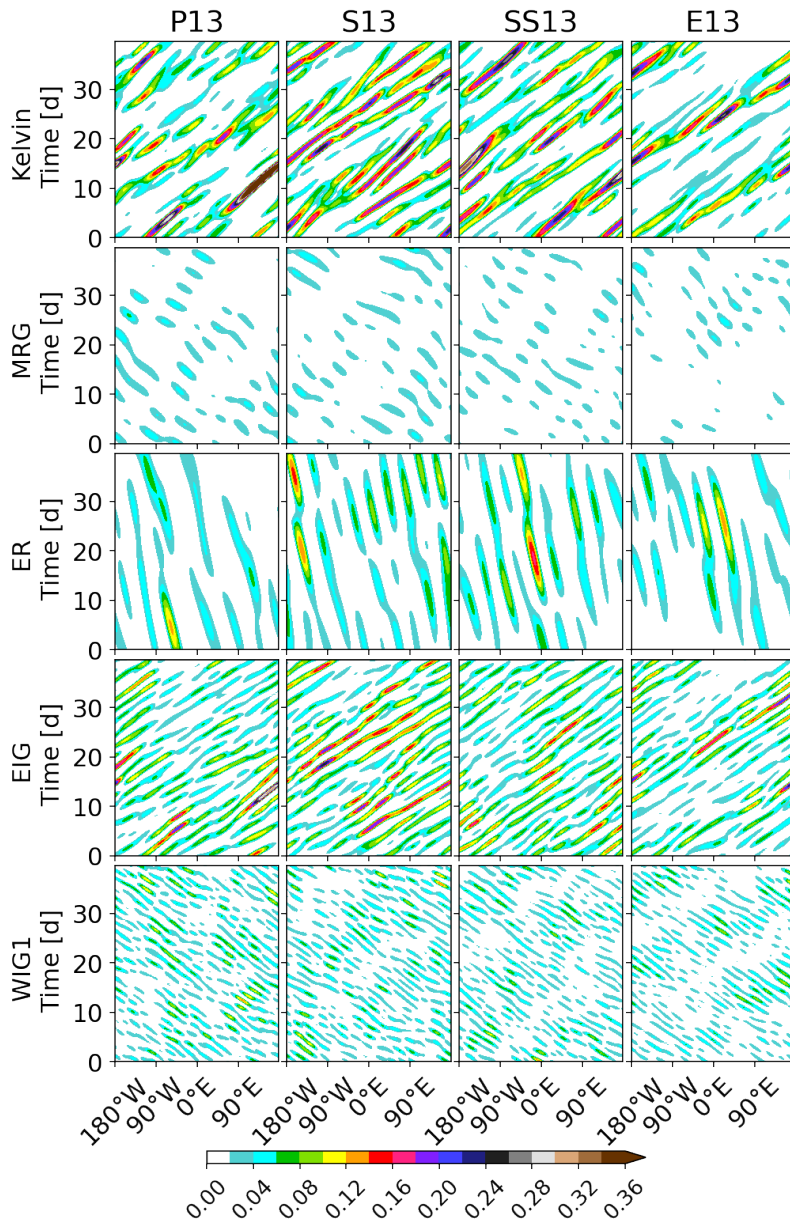
Figure B.10: Similar to Figure 6.2 but only for filtered upper-level winds [m s^{-1}] for all 9 simulations and 6 different equatorial waves. WIG2 indicates $n = 2$ westward inertio-gravity wave and EIG $n = 0$ eastward inertio-gravity wave. TD cannot be isolated by the YP method as it does not have a theoretical wave structure.
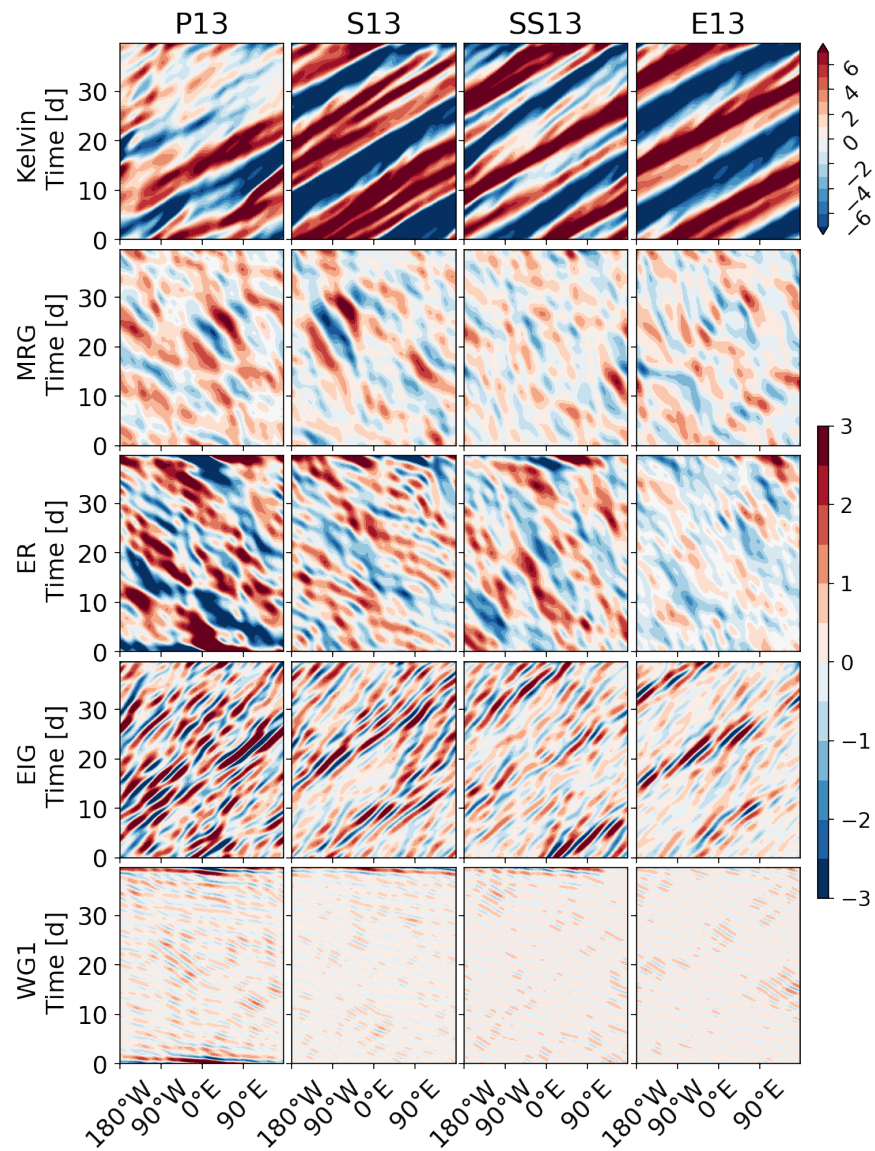
Figure B.11: Similar to Figure 6.2 but only for filtered 200-hPa winds [m s^{-1}] for all 9 simulations and 6 different equatorial waves. WIG2 indicates $n = 2$ westward inertio-gravity wave and EIG $n = 0$ eastward inertio-gravity wave. TD cannot be isolated by the YP method as it does not have a theoretical wave structure.
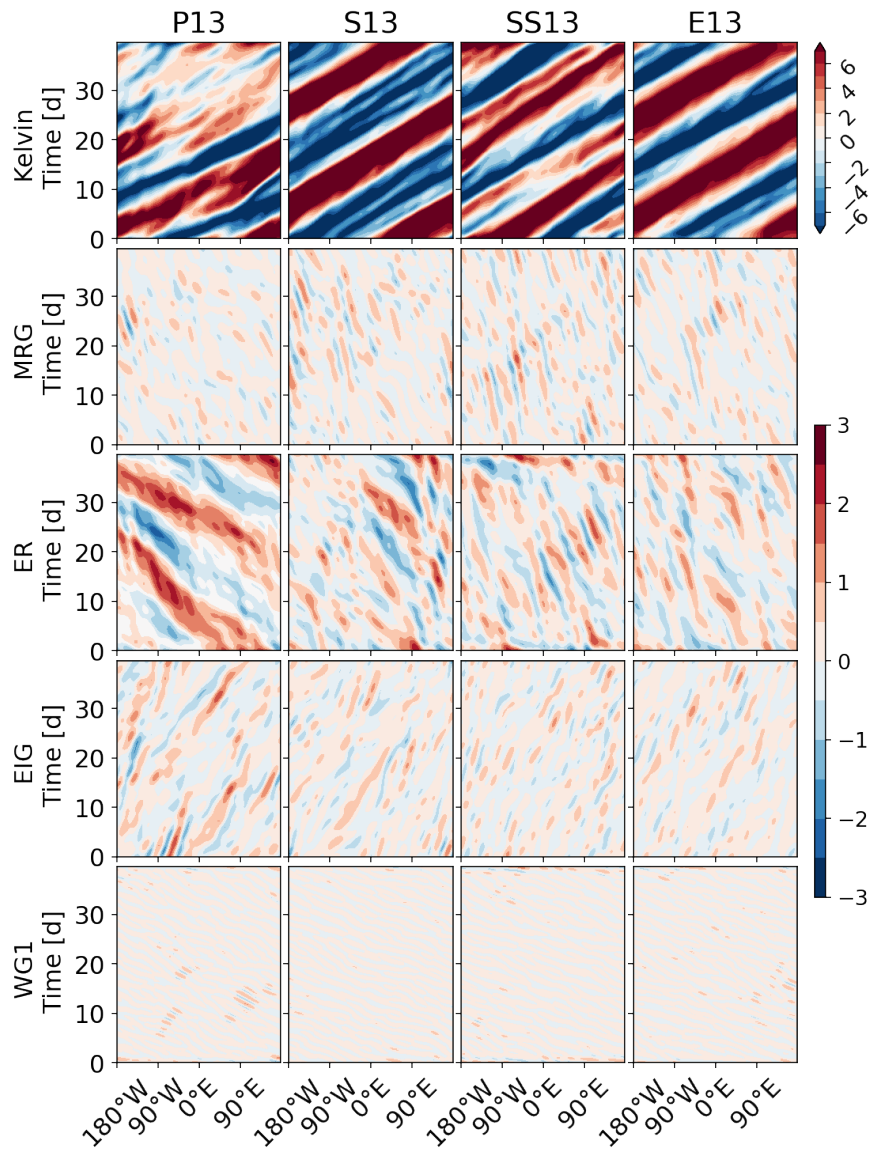
Figure B.12: As in Fig. B.11 but for filtered 850-hPa winds [m s^{-1}].